

Ultracold collisions in traps

Control of ultracold two-body collisions by trapping potentials
and by magnetic fields near Feshbach resonances

DISSERTATION

zur Erlangung des akademischen Grades
doctor rerum naturalium
(Dr. rer. nat.)
im Fach Physik

eingereicht an der
Mathematisch-Naturwissenschaftlichen
Fakultät I
Humboldt-Universität zu Berlin

von
Sergey Grishkevich
geboren am 30.05.1980 in Chargev

Präsident der Humboldt-Universität zu Berlin:
Prof. Dr. Dr. h.c. Christoph Marksches

Dekan der Mathematisch-Naturwissenschaftlichen
Fakultät I:
Prof. Dr. rer. nat. habil. Lutz-Helmut Schön

Gutachter:

1. Prof. Dr. Peter Schmelcher
2. Prof. Dr. Tommaso Calarco
3. PD Dr. Alejandro Saenz

eingereicht am: 17.08.2009
Tag der mündlichen Prüfung: 22.10.2009

Abstract

The ultracold atomic and molecular physics as it is accessible, e. g., in Bose-Einstein condensates of dilute gases was investigated. In such systems two-body collisions are dominant and their detailed study is one of the central topics of this work. They were done considering elementary chemical reactions as photoassociation, and magnetic Feshbach resonances. Additionally, studies of atoms in optical lattice sites were carried out. The many-body systems were not only considered within the usually adopted mean-field approach but also beyond that in order to simulate the fully correlated motion.

A collision of two particles is in general a multi-channel problem. However, in many cases it cannot be treated completely for practical reasons. In order to overcome this problem the single-channel schemes are usually adopted. A number of effective single-channel schemes were developed in this work in order to approximate such collisions. The applicability of these schemes was verified comparing to multi-channel solutions in the presence of a resonant magnetic field.

An interesting aspect in ultracold physics is that atoms can bind together to form ultracold and even Bose-Einstein condensed molecules. Molecules may be achieved by, e. g., Feshbach resonances or photoassociation. In this work the influence of a tight isotropic harmonic trap on photoassociation of two ultracold atoms forming a homonuclear dimer was investigated. To this end, different photoassociation schemes were considered with respect to their experimental realizability and their possible manipulation by external confinement. For the first time, realistic molecular potentials were consistently accounted for in the photoassociation problem in a trap.

An important progress in physics at ultracold energies was the loading of the ultracold gas into an optical periodic lattice formed with the aid of standing light waves. In this work, a theoretical approach was developed that allows for a full numerical description of an atomic pair trapped in a three-dimensional optical lattice. This approach includes the possible coupling between center-of-mass and relative motion coordinates in a configuration-interaction manner and uses realistic interatomic potentials. The developed method was applied to model experimental data, where radio-frequency association was used to create molecules from fermionic and bosonic atoms in a three dimensional cubic optical lattice. A very recent application of this approach allowed to compare the Bose-Hubbard model which is frequently used in solid state physics with the exact solution for different multi-well lattices. The applicability range of the Bose-Hubbard model was examined and

corrections were determined. An exact treatment of polar molecules in traps, atom-ion collisions, quantum dots, atoms in effective one and two dimensional geometries, systems in double-well and triple-well potentials become possible within the framework of the developed theory with minor extensions. The dynamic properties involving the solution of the time-dependent Schrödinger equation can also be accounted for straightforwardly.

For simulating the fully correlated motion in ultracold many-body systems a B -spline based configuration-interaction approach was developed. In this approach the two-body interparticle interaction was described by the pseudopotential. It turned out that with this choice of the two-body model potential the presently developed many-body approach does not converge. The reasons are not yet fully explained in literature. The two-body studies done in this work should be a good basis to understand the consequences of applied approximations as well as for further many-body research.

Zusammenfassung

Die ultrakalte Atom- und Molekülephysik, zu welcher man zum Beispiel bei der Bose-Einstein-Kondensation von verdünnten Gasen Zugang hat, wurde untersucht. In solchen Systemen dominieren Zwei-Körper-Stöße und ihre detaillierte Untersuchung ist eines der zentralen Themen dieser Arbeit. Diese wurden durchgeführt unter Berücksichtigung von elementaren chemischen Reaktionen, Photoassoziation und magnetischen Feshbach-Resonanzen. Weiterhin wurden Untersuchungen von Atomen in optischen Gittern durchgeführt. Die Viel-Teilchen-Systeme wurden nicht nur mit dem üblichen mean-field Ansatz behandelt, sondern auch darüber hinausgehend, um die voll korrelierte Bewegung zu simulieren.

Ein Stoß von zwei Teilchen ist ein Viel-Kanal-Problem. In vielen Systemen kann dies auf Grund von praktischen Limitationen jedoch nicht vollständig berücksichtigt werden. Um diesem Problem zu begegnen, werden häufig Ein-Kanal-Näherungen verwendet. Es wurden mehrere effektive Ein-Kanal-Näherungen in dieser Arbeit entwickelt, um solche Stöße zu approximieren. Die Anwendbarkeit dieser Näherungen wurde unter Zuhilfenahme der Viel-Kanal-Lösungen in Anwesenheit eines resonanten Magnetfelds überprüft.

Ein interessanter Aspekt im Bezug auf die ultrakalte Physik ist, dass Atome eine Bindung eingehen können um ultrakalte und sogar Bose-Einstein kondensierte Moleküle zu bilden. Moleküle können durch Feshbach-Resonanzen oder Photoassoziation erreicht werden. Der Einfluss einer engen isotropen harmonischen Falle auf den Prozess der Photoassoziation von zwei ultrakalten Atomen, die ein homonuklearen Dimer bilden, wurde untersucht. Hiefür wurden verschiedene Photoassoziationsszenarien im Bezug auf ihre experimentelle Realisierbarkeit und ihre mögliche Beeinflussung durch externen Einschluss betrachtet. Zum ersten Mal wurden für das Photoassoziationsproblem in einer Falle realistische molekulare Potentiale in konsistenter Weise berücksichtigt.

Ein wichtiger Fortschritt in der Physik der ultrakalten Energien war das Laden von ultrakalten Gas in optische periodische Gitter, welche mit der Hilfe von stehenden Lichtwellen gebildet werden. In dieser Arbeit wurde ein theoretischer Ansatz entwickelt, der die volle numerische Beschreibung von atomaren Paaren in einem dreidimensionalen optischen Gitter ermöglicht. Dieser Ansatz beinhaltet die mögliche Kopplung zwischen der Bewegung

in Schwerpunkts- und Relativkoordinaten mit Hilfe einer Konfigurations-Wechselwirkungs-Methode und verwendet außerdem realistische interatomare Potentiale. Die entwickelte Methode wurde angewendet, um experimentelle Daten zu modellieren, bei denen Radiofrequenz-Assoziation benutzt wurde, um Moleküle herzustellen aus fermionischen und bosonischen Atomen in einem dreidimensionalen kubischen optischen Gitter. Eine aktuelle Anwendung dieses Ansatzes ermöglichte den Vergleich zwischen dem Bose-Hubbard-Modell, welches häufig in der Festkörperphysik verwendet wird, mit der exakten Lösung für verschiedene Gitter von Potentialtöpfen. Eine exakte Behandlung von polaren Molekülen in Fallen, Atom-Ionen-Stöße, Quantenpunkte, Atome in effektiven ein- und zweidimensionalen Geometrien und Systeme in zwei und drei Potentialtöpfen ist im Rahmen der entwickelten Theorie mit nur kleinen Erweiterungen möglich. Die dynamischen Eigenschaften, welche die Lösung der zeitabhängigen Schrödinger-Gleichung beinhalten, können ebenso auf direkte Art und Weise berücksichtigt werden.

Um die voll korrelierte Bewegung in ultrakalten Vielteilchen-Systemen zu simulieren, wurde eine *B*-spline basierte Konfigurations-Wechselwirkungs-Methode entwickelt. In diesem Ansatz wurde die Zwei-Körper-Wechselwirkung zwischen den Teilchen durch ein Pseudopotential beschrieben. Es erwies sich dabei, dass mit dieser Wahl des Zwei-Körper-Modellpotentials das entwickelte Programm nicht konvergiert. Die Gründe hierfür wurden noch nicht vollständig erklärt in der Literatur. Die Zwei-Körper-Studien, welche in dieser Arbeit betrieben wurden, sind eine gute Basis für das Verständnis der Auswirkungen verwendeter Näherungen und weiterhin für die zukünftige Viel-Körper-Forschung.

Dedicated

To the memory of my grandfather.

PUBLICATION LIST

A) articles in fully peer-reviewed journals

1. S. Grishkevich and A. Saenz (2007): Influence of a tight isotropic harmonic trap on photoassociation in ultracold homonuclear alkali gases. *Phys. Rev. A* 76, 022704, 1-18.
2. S. Grishkevich, and A. Saenz (2009): Theoretical description of two ultracold atoms in a single site of a three-dimensional optical lattice using realistic interatomic interaction potentials. *Phys. Rev. A* 80, 013403, 1-17.
3. Ph.-I. Schneider, S. Grishkevich, and A. Saenz (2009): Ab initio determination of Bose-Hubbard parameters for two ultracold atoms in an optical lattice using a three-well potential. *Phys. Rev. A* 80, 013404, 1-13.

B) in preparation

1. S. Grishkevich, Ph.-I. Schneider, Y. Vanne, and A. Saenz (2009): Mimicking multi-channel scattering with single-channel approaches. arXiv:0909.4448 (2009)
2. S. Grishkevich, and A. Saenz (2009): Theoretical approach for two ultracold atoms in 3D optical lattice of \sin^2/\cos^2 form using realistic interatomic interaction potentials.

C) published contributions to academic conferences

1. S. Grishkevich and A. Saenz (2007): Exact Theoretical Description of Two Ultracold Atoms in 3D Optical Lattices. *J. Phys.-Conference series* 88, 012042.

This thesis is mainly based on the following above-mentioned papers:

A1, A2, B1, B2

Contents

1	Introduction	1
1.1	Bose-Einstein condensate	1
1.2	Photoassociation and magnetic Feshbach resonances	3
1.3	Optical lattices	5
1.4	State of research	7
1.5	Outline	11
2	Investigation of ultracold many-body systems	13
2.1	Mean-field approach	14
2.1.1	Approximate wave function	14
2.1.2	Approximate Hamiltonian	14
2.1.3	Ginzburg-Gross-Pitaevskii equation (GGPE)	15
2.1.4	Solutions of the GGPE vs further approximations	16
2.2	Beyond mean field	20
2.3	Two-body approaches	22
2.4	Conclusion	26
3	Collision of two atoms in the presence of a magnetic field	27
3.1	Atomic properties	27
3.2	Molecular properties	30
3.3	Multi-channel Feshbach resonance	33
3.3.1	Channel definitions	33
3.3.2	The coupled-channel equations	34
3.3.3	Multi-channel solutions	35
3.4	Conclusion	41
4	Multi-channel approach vs single-channel approximation	43
4.1	Single-channel approximation	44
4.2	Comparison based on wave functions	46
4.2.1	Short range	46
4.2.2	Long range	51

4.3	Conclusion	53
5	Photoassociation	55
5.1	The system	56
5.2	Photoassociation in a harmonic isotropic trap	59
5.2.1	Photoassociation in a trap	59
5.2.2	Sum rule	64
5.2.3	Enhancement and suppression factor f^v	65
5.2.4	Constant regime	66
5.2.5	Cut-off regime	69
5.3	Influence of atomic interaction	71
5.3.1	$I^v(\omega)$ for a repulsive interaction	71
5.3.2	Combined influence of trap and atomic interaction	77
5.4	Pseudopotential approximation in a harmonic trap	80
5.4.1	I^v in pseudopotential approximation	83
5.5	Conclusion and discussion	88
6	Reaching the absolute lowest state via photoassociation	97
6.1	Reaching the lowest state of ${}^6\text{Li}$ - ${}^{87}\text{Rb}$	98
6.2	Conclusion	102
7	Theoretical approach for two atoms in a 3D optical lattice	105
7.1	Trapping potential	106
7.1.1	Outline of the exact theoretical description	106
7.2	Spherical harmonics approach (SHA)	108
7.2.1	Center-of-mass and relative motion coordinate systems	108
7.2.2	Hamiltonians and trial functions	109
7.2.3	Description of the trapping potential	112
7.2.4	Expansion of the trap with spherical harmonics	115
7.2.5	Alternative lattice potential \cos^2	119
7.2.6	Overlap and Hamiltonian matrices	121
7.3	Symmetry of the system	126
7.4	Conclusion	131
8	Anharmonicity and coupling effects in optical lattices	133
8.1	Model system	133
8.1.1	Trap parameters	133
8.1.2	Interatomic interaction potential	134
8.1.3	Manipulation of the interatomic interaction	135
8.1.4	Computational details	137
8.2	Numerical results	138

8.2.1	Energy spectrum of the ^{87}Rb - ^{40}K system	138
8.2.2	Comparison with ^6Li - ^{133}Cs and ^6Li - ^7Li dimers	143
8.2.3	Wave-function analysis	145
8.3	Conclusion	154
9	Ultracold heteronuclear molecules in a 3D optical lattice	157
9.1	Comparison to experiment	157
9.1.1	Reasons for deviation between theory and experiment .	160
9.2	Comparison to a previous theoretical investigation	162
9.3	Conclusion	167
10	Summary and outlook	169
A	Rayleigh-Ritz-Galerkin approach	175
B	B splines	177
C	Pseudopotential approximation with B splines	181
D	Born-Oppenheimer approximation	185
E	Auxiliary relations	189
	Bibliography	195
	List of Figures	211
	List of Tables	213

Chapter 1

Introduction

1.1 Bose-Einstein condensate

Within a year, which spanned 1924 to 1925, Satyendra Nath Bose and Albert Einstein predicted a new, fifth, state of matter [1], now known as Bose-Einstein condensate (BEC). This state appears in a system of indistinguishable bosons. Bose particles, in contrast to Fermi particles, have a tendency governing their association: they transit to the most populated state. If conditions are such that the only energetically favorable level is the lowest possible state of the system, bosons will condense into this state. In this case, particles lose their individuality and the whole system will behave as one “macroscopic atomic cloud”, which inherits the quantum properties of its microscopic constituents, such as wave-particle duality.

Seventy years after this theoretical finding, in 1995, in the laboratory of the Joint Institute for Laboratory Astrophysics (JILA), Eric Cornell, Carl Wieman, and their colleagues obtained a BEC from dilute alkali atoms of rubidium [2] in a magnetic trap. The conditions of creation were extreme. In a dilute gas of atoms, the condensation is possible when the temperature is of order from 1 nK to 1 μ K and the densities are between 10^{14} cm^{-3} and 10^{15} cm^{-3} . These conditions were achieved through the combination of two cooling techniques: laser cooling [3] and evaporative cooling [4]. Soon after, the condensation of other alkali-metal elements [5–8], hydrogen [9, 10], metastable helium [11, 12], ytterbium [13] and chromium [14] were realized experimentally. The molecular condensation of composite bosons made of two fermions has also been observed in $^6\text{Li}_2$ [15, 16] and $^{40}\text{K}_2$ [17, 18] systems.

After the experimental observations of BEC, ultracold atomic and molecular physics has attracted a lot of interest. The atomic condensates exhibit many qualitatively new features. The condensate cloud is a single, wave-like

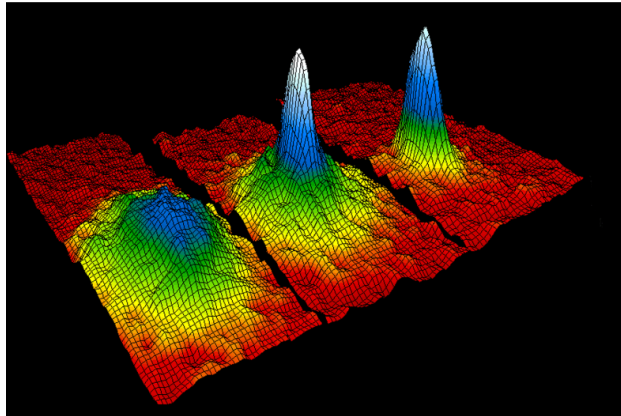


Figure 1.1: Three-dimensional rendition of the Bose-Einstein condensate obtained by E. A. Cornell and C. E. Wieman. From left to right, the evolution of an atomic cloud towards the degenerated state, passing through increasingly lower temperatures is shown. In the last image, rightmost, practically all the atoms are condensed [2].

“super-atom”. Its physics can be explained by quantum mechanics, which describes the wave-like behavior of atoms as well as photons of light. Clouds of condensed atoms can be manipulated just like electromagnetic waves, and the interference phenomena, as in waves, can also be observed [19], verifying the spatial [20, 21] and temporal [22] coherence of condensates. Since a condensate is a coherent wave, an “atom laser” becomes possible. Such a device may be exploited in a similar manner to optical lasers, suggesting a new field of atom optics. Atom lasers might be used holographically to “paint” integrated circuits at the nano scale, while interferometers based on atom lasers could provide the basis of a new method of making precision measurements. The analogy with optics has been strengthened through a number of experiments producing simple atom-laser outputs from condensates [23].

The condensation phenomena includes superfluidity, first observed in ^4He [24], and superconductivity, first observed in mercury cooled by liquid helium. In fact, the original scientific motive for creating and studying BEC stemmed from the belief that the mechanism underlying BEC is the same mechanism that is responsible for the effects of superconductivity and superfluidity. In the broadest sense, those electrical currents that flow without resistance in a superconducting metal and those liquid currents that persist without viscosity in superfluid helium are essentially Bose condensates. But liquids and solids are rather dense and strongly interacting systems. It is difficult to characterize them theoretically in a precise manner. The BEC of dilute atomic gases may be well-characterized model system, a system that

might illuminate the counter-intuitive behavior of superfluid liquids and superconducting solids. Indeed, the pioneering paper by Bogoliubov in 1947 provided the starting point for a microscopic theory of superfluidity [25]. This theory attributes the superfluidity phenomena to BEC. Furthermore, it was able to “directly photograph” the Bogoliubov transformation [26]. Moreover, BEC has provided physicists with a new basis for exploring many aspects of superfluidity, including frictionless current [27] and vortices [28]. In particular, increasing interest and effort has been directed to the study of superfluidity and related phenomena concerning BEC loaded in an optical lattice, such as Landau-Zener tunneling [29], the Josephson effect [30] and dynamical instability [31].

The use of BECs in spectroscopy applications has many advantages. The general rule of thumb in spectroscopy is “colder equals more accurate.” Colder atoms move more slowly, which means they can be probed longer, with correspondingly narrower resonance lines. In addition, systematic errors are often more easily controlled at lower temperatures. These advantages could someday lead to a better atomic clock [32, 33].

1.2 Photoassociation and magnetic Feshbach resonances

A further interesting aspect of BEC and ultracold atomic system is that atoms can be bound together to form ultracold and even Bose-Einstein condensed molecules [15, 16, 34]. Ultracold molecules can be obtained from ultracold atoms by sweeping a magnetic field around a Feshbach resonance [34–36]. When atoms are placed in a static magnetic field B , the scattering process of atoms changes drastically. For particular values of the field, the interaction between atoms undergoes a sudden variation in magnitude and sign. This indicates the presence of a magnetic Feshbach resonance (MFR). Emergence of molecules in a mixture of cold gas atoms is illustrated in Figure 1.2. MFR does not appear to be universal scheme for creating molecules. One of the alternative schemes is photoassociation (PA), where two ultracold or Bose-condensed atoms absorb a photon and form a molecule in ground or excited state [38, 39] as is shown in Figure 1.3. Although it was demonstrated that this process generates cold molecules, the yield is small compared to the one obtained by means of MFRs. The advantage of PA compared to MFRs is, however, its assumed wider range of applicability, since there is no need for the occurrence of suitable resonances and thus no requirement for specific magnetic properties of the atoms involved [40]. PA is also a powerful

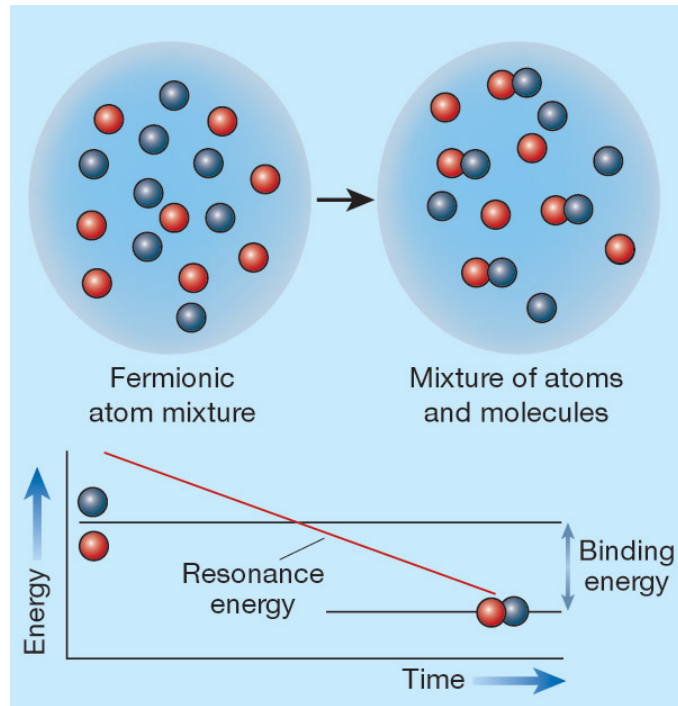


Figure 1.2: Emergence of molecules in a mixture of cold gas atoms. The atoms exist in two different spin states (represented by red and blue dots) at a certain energy, but can be made to pair up through a Feshbach resonance. Varying the magnetic field applied to the system changes the energy of the resonance. When the resonance's energy reaches the energy level of the atomic mixture, colliding atoms can be converted to resonant-state molecules. As the resonance energy decreases further, the molecules finally reach a lower-energy state, which is lower than the atomic state by the amount of molecular binding energy. (Figure and caption are taken from [37])

tool for the investigation of atomic and molecular diatomic properties at low temperatures, especially in the ground-state. The absorption of the photon typically occurs at large internuclear distances, and thus the PA spectrum provides important information about the long-range part of the molecular potential curves as well as the collisional properties of atoms [41–44].

Due to a recent formation of ultracold molecules at even the lowest possible energy level, the possibility of producing tightly bound molecular BEC nears. Formation of tightly bound ultracold molecules in low vibrational levels of ground electronic states is already achieved in many alkali dimers: for example, in heteronuclear KRb [45], RbCs [46], LiCs [47], or homonuclear Cs₂ [48]. The studies of such systems are needed for a better scientific understanding of fundamental issues of the control of elementary reaction

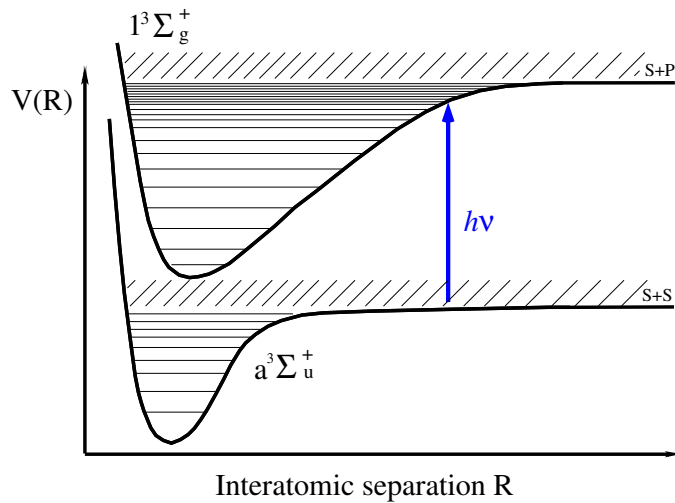


Figure 1.3: Sketch of the photoassociation process for two homonuclear alkali atoms in free space (not to scale). With the aid of a laser, photoassociation is induced from two free ground-state atoms interacting via the $a^3\Sigma_u^+$ state into some vibrational level of the $1^3\Sigma_g^+$ state. Due to hyperfine interaction, two free ground-state alkali atoms can also interact via a coherent admixture of singlet and triplet states. Due to fine and hyperfine interactions the excited state is also a coherent admixture of many potential curves.

to provide insight into how matter can be arranged into a complex structure. Besides this principal aspect of physics, the ultracold molecules are also desirable for other applications. For instance, the strong dipole-dipole interactions between molecules may be used for realization of different spin models [49, 50]. They may be also used as qubits for quantum computation [51] and for precision measurements [52], since for the lowest possible state of the system, perturbations are maximally suppressed.

1.3 Optical lattices

A further important advance in ultracold physics was the loading of ultracold gas into an optical lattice (OL), formed with the aid of standing light waves [54–56]. Optical lattice potentials formed by superimposing orthogonal standing waves are schematically shown in Figure 1.4. Atoms in OLs are well-suited as systems for theoretical and experimental studies: practically any lattice geometry may be achieved with optical potentials. Apart from limitations set by the diffraction limit, they can have practically any desired shape and can form any kind of OL: regular, disordered, modulated, etc. The optical potentials also provide accessibility to low-dimensional physics [57–

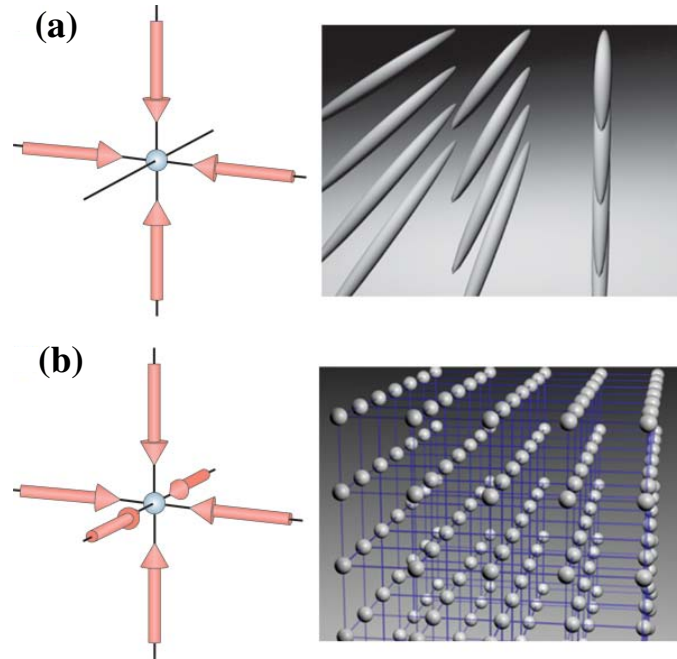


Figure 1.4: Optical lattice potentials formed by superimposing orthogonal standing waves. (a) For a 2D optical lattice, the atoms are confined to an array of tightly confining 1D potential tubes. (b) In the 3D case, the optical lattice can be approximated by a 3D simple cubic array of tightly confining harmonic oscillator potentials at each lattice site. (figure and caption are taken from [53])

60]. If the intensity is tuned such that only one direction is weakly confined, the system turns into arrays of almost independent one-dimensional tubes; if confinement in two directions is weak, then the system behaves like layers of independent two-dimensional pancakes. The variation of the laser intensity allows switching of the system from a tunneling-dominated regime to interaction-dominated ones. While different kinds of chemical elements, their isotopes, or atoms in different electronic or spin states already cover quite a range of interaction strengths, further control of the tuning of the atom-atom interactions in OLs can be achieved using MFRs or optical Feshbach resonances [61]. OLs may also provide good systems for realization of quantum computing [62]. The observation of bosonic superfluid-Mott insulator transition in pure Bose systems [54, 56, 63], in disordered Bose systems [64], or in Bose-Fermi mixtures [65], is hoped to provide a source of efficient systems for preparing a quantum register with a fixed number of atoms per lattice site.

The OL resembles, in some sense, the periodicity of a crystal poten-

tial [53, 66, 67]. Therefore, it is an almost perfect realization of various kinds of Hubbard models. The Hubbard model has its origin in the description of electrons in solids [68]. However, the additional advantage of OLs is that many parameters such as the lattice depth and the interaction strength can be controlled, and the characteristics of the system can be observed with high accuracy [69]. In contrast to a real solid, the OL does not allow dissipation to phonons [70]. Another important phenomenon is the *disorder* which plays a central role in condensed matter physics. One of the signatures of disorder is Anderson localization [71]. Controlled disorder, or pseudo-disorder, might be created in an OL by several lattices with incommensurate periods of spatial oscillations [72, 73]. According to theoretical predictions [74–76], the prospects of detecting signatures of Anderson localization in weak nonlinear interactions and quasi-disorder in BEC are quite promising. This allows to study Anderson-Bose glasses and the crossover to Mott-type localization.

1.4 State of research

Many-body studies

Although the usually adopted mean-field theory often provided a satisfactory description of experiments, the beyond-mean-field approaches were also interesting. The goal for this work was to develop an approach to give a description for the many-body system beyond the mean-field for simulating fully correlated motion. As the first stage, the standard mean-field approach to ultracold many-body systems had to be closely examined. After that, the B -spline-based configuration-interaction approach was developed. It turned out that this approach fails to converge. The most likely reason was the choice of the two-body interactions in a pseudopotential form. The conducted mean-field investigations and the observed divergence showed the importance of the correct choice for the theoretical description of interatomic interactions. These facts motivated further detailed microscopic studies of two-body collisions in different levels of approximation.

Photoassociation in tight traps

The BEC is achieved in a trap, thus PA and MFR experiments in ultra-cold atomic gases are performed in the presence of a trap potential. In most cases these traps are rather shallow, so that the corresponding harmonic trap frequency ω is of the order of 100 Hz [77]. For such a frequency, the influence of the trap on, e.g., the PA rate, is expected to be negligible. This may, however, change for very tight traps. In fact, it was pointed out that the

atom-molecule conversion process is more efficient, if PA is performed under tight trapping conditions as they are, e. g., accessible in OLs [78]. The advantage of using tight confinement has stimulated further theoretical investigations, and recently some proposals were made that discuss the possibility of using the trapping potential itself for the formation of molecules [79, 80]. The study of PA in tight OLs is of interest by itself, since it is possible to achieve tailored Mott insulator (MI) states containing a large number of almost identical lattice sites, each filled with exactly two atoms [55]. The trap frequency of a lattice site in which molecules are produced via PA can be of the order of 100 kHz [81].

Surely, the influence of a tight trap on PA in ultracold gases represents an important scientific problem. The objective of this thesis was the evaluation of different PA schemes with respect to their experimental realizability and the possibility of manipulating them by external confinement. Although some theoretical works exist on this topic (e. g., [82]), no systematic analysis had been done. Therefore, a systematic investigation of the influence of tight traps on the PA rate was desirable. In alternative theoretical studies such a systematic investigation was even impossible due to the use of simplified atom-atom interaction potentials. The present work overcame this problem by adopting realistic molecular potentials. While the validity regime of the pseudopotential approximation has already been discussed with respect to the energy levels for trapped atoms (e. g., [83]), it was not immediately evident whether this simplified model for the atomic interaction is appropriate for the description of photoassociation in a harmonic trap. The range of applicability of the pseudopotential description of the PA process was checked using the present approach. As will be shown in this work this approach even led to new findings.

Photoassociation in resonant regimes

Photoassociation may also be used for reaching the absolute lowest state of the system. The tightly bound ultracold molecules in low vibrational levels of ground electronic states are difficult to obtain. Standard cooling techniques developed for atoms are not suitable for molecules, due to their complex spectral structure. The most successful scheme to access the lowest vibrational levels is the optical Stimulated Raman Adiabatic Passage (STIRAP) [84–87]. This scheme is realized by means of PA transition via an intermediate excited state. This method is efficient for the production of molecules but is relatively complex from both points of view theory and experiment. The intermediate excited state used in STIRAP has a very sophisticated structure [40] especially in heteronuclear systems [88], therefore the identification

of a favorable intermediate state is not easy. The situation is worse, if several intermediate passages are required [78]. The direct transition of two ultracold atoms at lower levels is preferable. The dump photoassociation (DPA) process is conceptually simple. A complicated set of excited electronic states is omitted from consideration; a single laser pulse of a definite frequency creates molecules. The absolute DPA rate (Γ_{\downarrow}) needed is very small to apply the process in practice. However, it can be significantly increased using a MFR. The use of the Feshbach-optimized photoassociation (FOPA) [89] improves the transitions into deeply bound levels. It has even been calculated in this work (Section (5.3.2), that tight confinement and strong interaction give, independently and equally, several orders of enhancement of the PA rate to excited states (Γ_{\uparrow}). The increase was consistently observed for some specific range of final states. The enhancement of Γ_{\uparrow} around the resonance has also been measured experimentally [90, 91].

It can be concluded that processes like, e. g., DPA or PA should be preferably considered in a resonant regime of strong interaction, which is accessible with the aid of MFRs. In general, the correct theoretical description of a MFR requires a multi-channel scattering treatment. Since the multi-channel method can be computationally demanding and can even be impractical for certain applications, the task of this thesis was the development of various effective, single-channel schemes approximating multi-channel scattering. To this end, the complete multi-channel problem of describing the two-body collisions in the presence of a resonant magnetic field had to be solved. The applicability of the schemes had to be verified using multi-channel solutions. Furthermore, it had to be checked whether the developed single-channel approaches permit changing the interatomic interactions in a correct way for the studies of, e. g., PA process. The single-channel approximation especially along with the substitution of the real potential by a pseudopotential was intensively used in theory [40, 69, 92, 93]. In most of studies single-channel approximation was used mainly for approximating the long-range solutions. Whether the short-range part of the approximate solution may be also used for calculating various observables was however not clear. A detailed comparison of both short-range and long-range parts of the multi-channel solutions against various single-channel ones was considered as a new investigation that could be done in this work. Finally, this study was promising to give a better understanding for the consequences of applied approximations unavoidable in many-body research.

Optical lattices

In order to describe the behavior of atoms in an OL, the latter is usually considered as an array of harmonic traps. In such an approach, some important features of the OL can be lost. For example, the correct sinusoidal potential exhibits an energy band with a spread of transition energies while the harmonic potential possesses a discrete equidistant spectrum. Nevertheless, the experiment of Stöferle *et al.* [94] showed good agreement with a simplified theoretical description, based on the harmonic approximation. In their analysis, Stöferle *et al.* compared the measured binding energies of confinement-induced molecules and real molecules to the ones predicted by a simplified theory, where two atoms are trapped in a harmonic potential and interact *via* a δ -function pseudopotential. Within such a model an analytical solution exists in the case of two identical atoms (in the same quantum states) [95]. However, another experiment that adopted higher resolution spectroscopy and considered a heteronuclear system was interpreted as clearly indicating a breakdown of the harmonic approximation [96].

The interest in anharmonicity and coupling effects also came from the side of the theory some time ago [97]. Due to complexity of the problem the results of these investigations appeared only very recently in parallel [98] or after [99] the present work. The approaches considered in these alternative studies have vital limitations and cannot be straightforwardly extended for further investigation of, e. g., multi-well lattices or long-range interactions. From the theoretical point of view, the description of just two atoms in an OL is very laborious beyond the harmonic approximation. The anharmonic part of the OL potential leads to a coupling of center-of-mass (COM) and relative (REL) motion and requires therefore to solve the full six-dimensional problem. Even within the harmonic approximation, the different trapping potentials experienced by the two atoms lead to a coupling of COM and REL motion [79, 100]. This situation occurs, e. g., for heteronuclear atom pairs or two atoms of the same kind but in different electronic states [101]. The task of this thesis was thus to study atoms in real OL sites beyond the harmonic approximation and also including COM and REL motion coupling. To this end, a theoretical approach had to be developed that allows for a full numerical description of an atomic pair trapped in a 3D OL. This approach had to include the possible coupling between COM and REL motion coordinates in a configuration-interaction manner, and had to use realistic interatomic potentials. In order to investigate the influence of the atomic interaction strength, its value could be varied using the single-channel approach already developed at an earlier stage of the present work. The generality of the conclusions was also checked for different systems. After a systematic in-

vestigation of the effects of anharmonicity and coupling of COM and REL motion, a comparison was made to both the experimental data [96] and a subsequent theoretical analysis [98] performed independently in parallel to the present work.

1.5 Outline

The thesis is organized in the following way. The investigation of ultracold many-body systems is presented in Chapter 2. The investigations made in this chapter highlight the importance of two-body collisions in ultracold dilute atomic gases. At the end of the Chapter 2, the review of the two-body approaches is tailored for understanding the physics relevant to the present thesis. Chapter 3 presents the solution of the full multi-channel problem for two ultracold atoms colliding in a magnetic field. The analysis of the solutions is based on wave functions in different asymptotic bases. The obtained multi-channel solutions are used in the next Chapter 4 in order to carry out the comparison to alternative effective single-channel approaches. Single-channel approaches will be used for all systems considered in this work, in order to investigate the influence of interatomic interaction. Furthermore, in Chapter 5, the influence of a tight isotropic harmonic trap on a PA transition to an excited state in ultracold homonuclear alkali-metal gases is investigated using realistic atomic interaction potentials. In combination with the trap, the influence of the interaction between atoms is also investigated. A comparison with simplified models describing the atomic interaction, such as the pseudopotential approximation, is additionally carried out in Chapter 5. PA is studied further in Chapter 6 for the transition to the lowest state. The two-body study is continued in Chapters 7, 8, and 9. However in those chapters, an anharmonic trap is considered. Chapter 7 provides the mathematical description of the developed theoretical approach for an exact treatment of a pair of ultracold atoms interacting through a central potential that is trapped in a 3D optical lattice. Also, the full consideration of the lattice symmetry is presented in Chapter 7. In Chapter 8, the developed theoretical approach is used for a detailed analysis of anharmonicity and coupling of COM and REL coordinates. In Chapter 9, the theoretical predictions of the approach are checked against the experimental data and against subsequent theoretical studies. Chapter 10 summarizes the results of the thesis. In Appendix A the mathematical description of the variational Rayleigh-Ritz-Galerkin approach is given. This method is used to solve most of the equations in the thesis. The equations are solved numerically using an expansion of the radial parts in B splines, introduced in Appendix B. The numerical approach for

the pseudopotential approximation with B splines is given in Appendix C as a complement to Chapter 5. Calculations of the present thesis assume the Born-Oppenheimer approximation for describing realistic interatomic potentials to be valid. This approximation is considered in Appendix D. Finally, Appendix E collects auxiliary relations that are used in Chapter 7.

Chapter 2

Investigation of ultracold many-body systems

The interest in the theory of dilute ultracold atomic gases has been rapidly growing since the experimental realization of Bose-Einstein condensates. Although the mean-field theory usually adopted often provides a satisfactory description of experiments, the beyond-mean-field approaches are also interesting. Besides the use in describing thermally excited samples, a more detailed understanding of the correlated motion appears to be especially important if, e. g., processes as the creation of molecules from atoms (by magnetic Feshbach resonances or photoassociation) are considered. Another example is ultracold samples with long-range interactions, as one finds for polar molecules. Furthermore, the confinement of the particles in a rather small spatial volume should increase the importance of the particle interactions. The confinement may be realized by tight optical traps. In this chapter, the attempt is made to provide a beyond-mean-field description for ultracold atomic gases. For this purpose a B-spline based configuration-interaction (CI) method was developed. As a first step, one-particle wave-functions are obtained within the Hartree-Fock approximation. The resulting Hartree-Fock orbitals are then used in the subsequent CI calculation. The second approximation usually adopted in the description of ultracold dilute gases was used, i. e., the pseudopotential model representing the interparticle interaction by a delta function. It turns out that, with this approximation, the CI approach does not converge, supporting a corresponding earlier finding in [102].

The mean-field investigations made in this chapter highlight the importance of two-body collisions in ultracold dilute atomic gases. The observed divergence shows the importance of the correct choice for the theoretical description of the interaction between two particles. In order to understand the reasons for the non-convergence and investigate two-body physics governing

many-body behavior, the collisions between two particles should be investigated in more detail using different levels of approximation and preferably considering also specific applications. To this end, in this work the investigations for the two-body interactions are done considering realistic interatomic potentials. At the end of this chapter, the review of the two-body approaches is tailored for understanding the physics relevant to the present thesis.

2.1 Mean-field approach

2.1.1 Approximate wave function

The mean-field theory builds on the simplest possible approximation to a many-body wave function. The function is presented as a product of one-particle wave functions. Another additional aspect is included in the many-body wave function, namely the fact that the symmetry of the particles must be taken into account. Hence, the wave function in a mean-field theory is a symmetrized product of the single-particle wave functions. This is a good approximation because, in a fully condensed state, all particles are in the same single-particle state $\phi(\mathbf{r})$. Therefore, the wave function of the N -particle system might be written as

$$\Psi(\mathbf{r}_1, \mathbf{r}_2, \dots, \mathbf{r}_N) = S \left(\prod_{i=1}^N \phi(\mathbf{r}_i) \right) \quad (2.1)$$

where the S symbol means the symmetrization of the term inside brackets and the single-particle wave function $\phi(\mathbf{r}_i)$ is normalized in the usual way

$$\int d\mathbf{r} |\phi(\mathbf{r}_i)|^2 = 1 \quad . \quad (2.2)$$

2.1.2 Approximate Hamiltonian

The Hamiltonian of the many-body system is

$$\hat{H} = \sum_{i=1}^N \left[\frac{\mathbf{p}_i^2}{2m} + \hat{V}_{\text{trap}}(\mathbf{r}_i) \right] + \sum_{i<j} \hat{V}_{\text{int}}(\mathbf{r}_i - \mathbf{r}_j) \quad . \quad (2.3)$$

At the low temperature and density conditions present in a trapped BEC, all scattering events occur at extremely low energy. Consequently, the atoms rarely come close enough to each other to sample the complex nature of the inter-atomic potential. The atom-atom interaction is therefore well characterized by the s -wave scattering length, and the interaction potential may be

written in the form

$$\hat{V}_{\text{int}}(\mathbf{r} - \mathbf{r}') = U_0 \delta(\mathbf{r} - \mathbf{r}') \quad . \quad (2.4)$$

This full potential is commonly approximated heuristically by a simplified binary collision pseudo-potential treating them as the hard-sphere collisions. In Equation (2.4) U_0 is the effective interaction strength related to the s -wave scattering length a_{sc} by $U_0 = \frac{4\pi a_{\text{sc}}}{m}$ where m is the atomic mass, \mathbf{r} and \mathbf{r}' are the positions of the two particles.

The symmetry that is being adapted in the most of experiments with atomic clouds is the so-called the ‘‘cigar-shaped’’ symmetry. This symmetry is a consequence of the trapping potential given by operator

$$\hat{V}_{\text{trap}} = \frac{m}{2}(\omega_\rho^2 \rho^2 + \omega_z^2 z^2) \quad (2.5)$$

in cylindrical coordinates. In Equation (2.5) ω_ρ and ω_z are respective transverse and longitudinal harmonic frequencies.

2.1.3 Ginzburg-Gross-Pitaevskii equation (GGPE)

The incorporation of Equations (2.1), (2.3) and (2.4) results in the Hartree-Fock equation (HFE)

$$-\frac{1}{2m}\nabla^2\phi(\mathbf{r}) + V(\mathbf{r})\phi(\mathbf{r}) + U_0\frac{N-1}{2}|\phi(\mathbf{r})|^2\phi(\mathbf{r}) = E_n\phi(\mathbf{r}), \quad (2.6)$$

where $E_n = E/N$. This is the basic, zero-temperature equation of the MFT, which describes the properties of the trapped atomic cloud. It can also be rewritten in the form of the commonly adopted Ginzburg-Gross-Pitaevskii (GGP) equation. The GGPE is used as a limit of HFE in a system with a big number of particles. The GGPE was originally derived from the statistical consideration when it is possible to make the replacement $N - 1 \approx N$ in the interaction term for the Hamiltonian. The time-independent GGPE has the following form

$$-\frac{1}{2m}\nabla^2\psi(\mathbf{r}) + V_{\text{trap}}(\mathbf{r})\psi(\mathbf{r}) + U_0|\psi(\mathbf{r})|^2\psi(\mathbf{r}) = \mu\psi(\mathbf{r}) \quad (2.7)$$

where $\mu = \frac{\delta E}{\delta N}$ is the chemical potential and $\psi(\mathbf{r}) = N^{1/2}\phi(\mathbf{r})$ is the wave function of the condensed state. Equation (2.7) has the form of the Schrödinger equation. One part of it is the external potential V_{trap} and the other is the non-linear term $U_0|\psi(\mathbf{r})|^2$ that takes into account the mean field

produced by the other particles. The eigenvalue is the chemical potential and not the energy per particle as it is for the usual linear Schrödinger equation. The chemical potential is equal to the energy per particle for the non-interacting particles, if they are all in the same state. This is not the case for interacting particles.

2.1.4 Solutions of the GGPE vs further approximations

The transformed GGPE

$$-\frac{1}{2m}\nabla^2\phi(\mathbf{r}) + V_{\text{trap}}(\mathbf{r})\phi(\mathbf{r}) + g|\phi(\mathbf{r})|^2\phi(\mathbf{r}) = \mu\phi(\mathbf{r}) \quad . \quad (2.8)$$

is more convenient to study because the parameter

$$g = \frac{4\pi a_{\text{sc}}}{m}N \quad (2.9)$$

incorporates both interaction and number of particles. Then g is the only variable parameter for the system in a given trap. In the absence of an analytical solution, Equation (2.8) is solved numerically in the cylindrical coordinate system. The wave function $\phi(\mathbf{r})$ is obtained by expressing the radial and axial components as linear products of B splines (Appendix B) and an exponential angular part with quantum number \mathbf{m} ,

$$\phi(\mathbf{r}) = \sum_i^{n_\rho} \sum_j^{n_z} C_{ij} B_{i,k_\rho}(\rho) B_{j,k_z}(z) e^{i\mathbf{m}\phi}. \quad (2.10)$$

The GGPE is solved numerically using the following iterative procedure. The solution of Equation (2.7) obtained for no interaction situation is used for the construction of the interaction term. Then the GGPE with this interaction term is solved, yielding the value for the first iteration. This solution is used to construct the new interaction term. The procedure is repeated until convergence is reached.

Numerical solutions of the GGPE can be used in order to check available approximations. One of these approximations is the Thomas-Fermi approximation (TFA). It implies that the interaction is so strong or that the number of particles is so large, that the kinetic energy term in the GGPE can be ignored. The solution is then trivial and is given as

$$\phi(\mathbf{r}) = \sqrt{\frac{1}{U_0 N} [\mu - V_{\text{trap}}(\mathbf{r})]} \quad (2.11)$$

where the chemical potential is $\mu = \frac{1}{2} \left(\frac{15}{8\pi} \lambda \frac{8\pi a_{\text{sc}} N}{a_\rho} \right)^{2/5} \omega_\rho$ with $\lambda = \omega_z/\omega_\rho$.

Another sometimes invoked approximation is based on the variational principle (VP). It gives an upper bound for the ground state energy. The assumption about the ground state is

$$\phi(\mathbf{r}) = \sqrt{\tilde{\omega}_\rho \sqrt{\tilde{\omega}_z}} \left(\frac{m}{\pi} \right)^{3/4} e^{-m(\tilde{\omega}_\rho^2 \rho^2 + \tilde{\omega}_z^2 z^2)/2} \quad (2.12)$$

treating the effective frequencies $\tilde{\omega}_\rho$ and $\tilde{\omega}_z$ as the variable parameters. The substitution of (2.12) into the GGP energy functional yields the ground state energy

$$E(\tilde{\omega}_\rho, \tilde{\omega}_z) = \frac{\tilde{\omega}_\rho}{2} + \frac{\omega_\rho^2}{2\tilde{\omega}_\rho} + \frac{\tilde{\omega}_z}{4} + \frac{\omega_z^2}{4\tilde{\omega}_z} + \sqrt{\frac{m\tilde{\omega}_z}{2\pi}} N a_{\text{sc}} \tilde{\omega}_\rho \quad . \quad (2.13)$$

The minimization of energy with respect to $\tilde{\omega}_\rho$ leads to $\tilde{\omega}_\rho = \omega_\rho/\Delta$ with

$$\Delta = \sqrt{1 + \zeta^5 \sqrt{\frac{\tilde{\omega}_z}{\omega_\rho} \frac{1}{32\pi^3}}} \quad (2.14)$$

where $\zeta = (8\pi N a_{\text{sc}}/a_\rho)^{1/5}$.

Figure 2.1 shows the wave functions of the GGPE against TFA and VP. This figure clearly shows the correctness of the numerical results. As is also

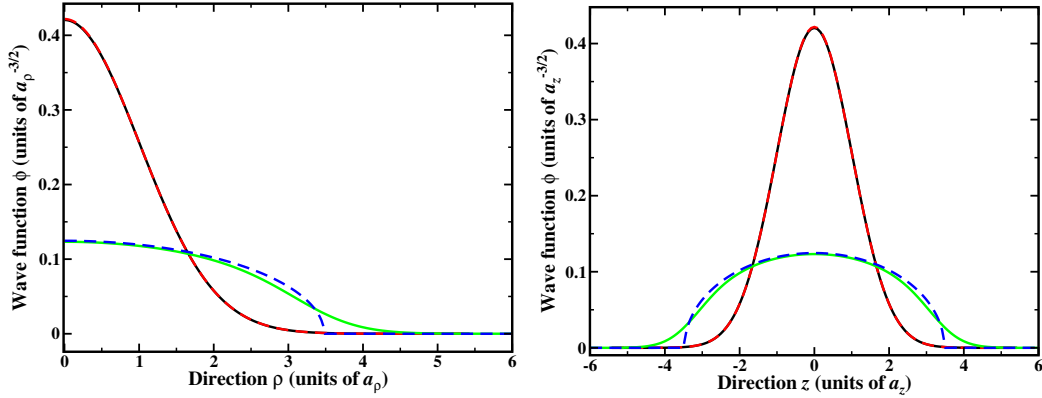


Figure 2.1: Numerical solution of the GGPE (black and green solids) together with the TFA for 20000 atoms (blue dashes) and the VP with Gaussians for 10 atoms (red dashes). The calculations are done for ^{87}Rb atoms in an isotropic trap of $\omega_\rho = \omega_z = 2\pi \times 100\text{kHz}$ interacting repulsively with $a_{\text{sc}} = 1a_0$.

evident from Figure 2.1, as the number of particles increases, the repulsion

between atoms tends to lower the central density, which expands the cloud of atoms towards the regions where the trapping potential is higher.

An important feature is the difference between systems interacting with either repulsive or with attractive forces. If interaction between particles is attractive ($a_{sc} < 0$), then the solution of GGPE is metastable. In this case, if the number of particles in the condensate is sufficiently large, it becomes unstable and collapses. However, this case will not be considered in this work.

Using the GGPE, it is possible to discuss various ground-state properties of the system: the form of the atomic cloud, the role of the interatomic potential, and the velocity distribution. An important question is the role of the interatomic potential. At first sight it is expected to be negligible for such a dilute system like the BEC. However, the interaction has a deep influence on how the GGPE is solved.

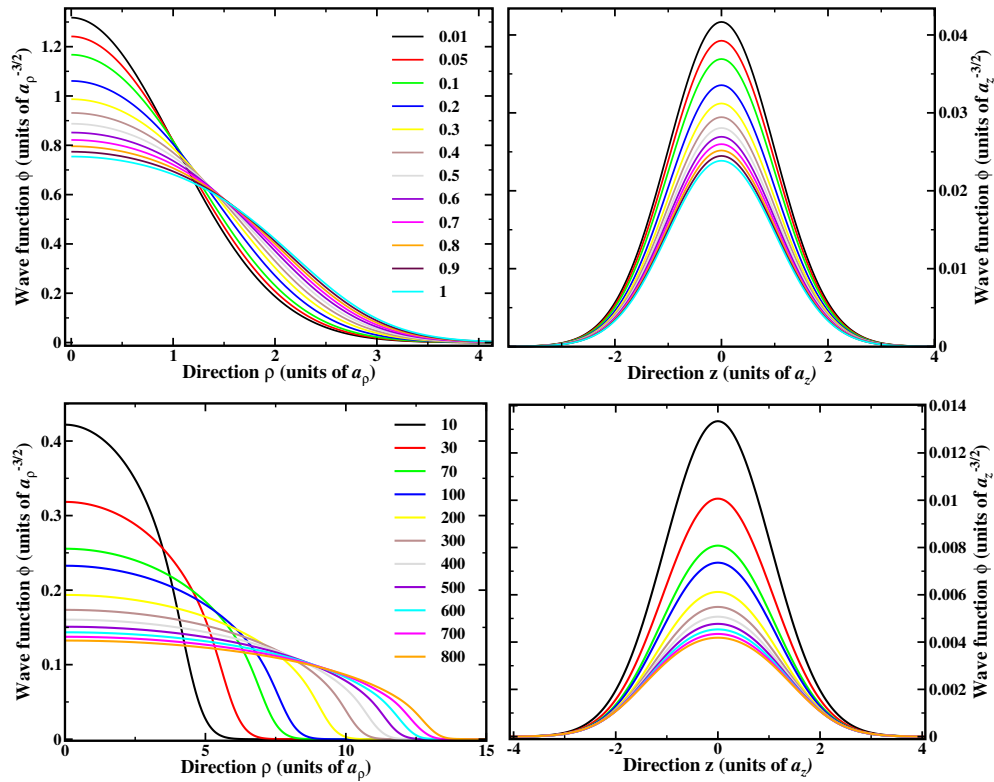


Figure 2.2: The ground state wave functions of the radial and the transverse motion of 20000 ^{87}Rb atoms in the pancake-shaped harmonic trap of frequencies $\omega_\rho = 2\pi \times 100\text{Hz}$ and $\omega_z = 2\pi \times 10\text{kHz}$. The variable parameter (2.9) is indicated in the figure.

In order to understand how the behavior of the condensate changes as

2.1 Mean-field approach

the interaction strength varies, further solutions of the GGPE are considered here. Figure 2.2 shows the wave functions of the radial and longitudinal motion for the pancake-shaped geometry of the trap. Figure 2.3 shows the chemical potential as a function of g -factor (2.9). Figure 2.4 shows the wave

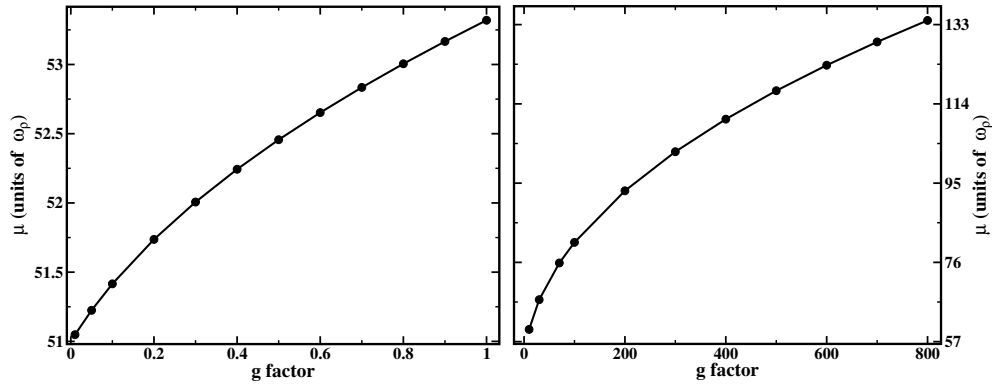


Figure 2.3: The chemical potential μ as a function of the g -factor for the solutions of Figure 2.2

functions of the radial and longitudinal motion for the cigar-shaped geometry of the trap. Figure 2.5 shows the chemical potential as a function of the g -factor (2.9). As is evident from Figure 2.2 and Figure 2.4, an increase

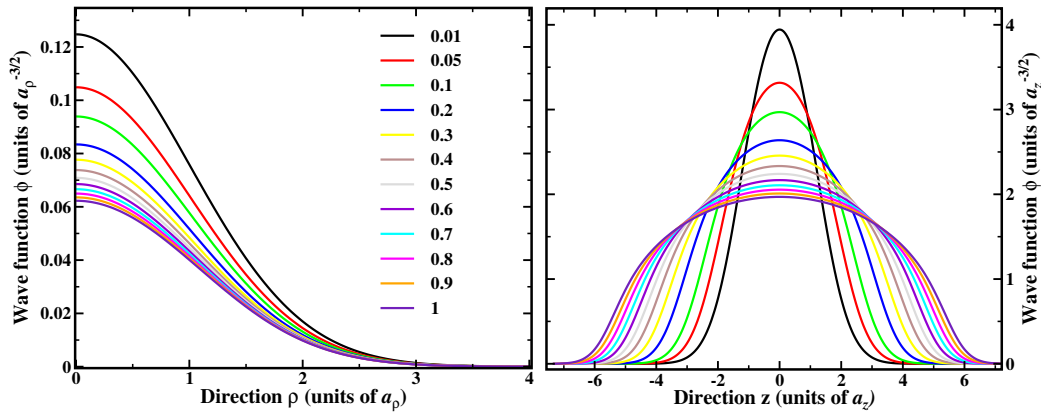


Figure 2.4: The ground state wave functions of the radial and the transverse motion of 20000 ^{87}Rb atoms in the cigar-shaped harmonic trap of frequencies $\omega_\rho = 2\pi \times 10\text{kHz}$ and $\omega_z = 2\pi \times 100\text{Hz}$. The variation parameter (2.9) is indicated in the figure.

in interaction between particles lowers the central density (it becomes rather flat) expanding the cloud of atoms towards regions where the trapping potential is higher. The final result is that the system is still fully condensed, but

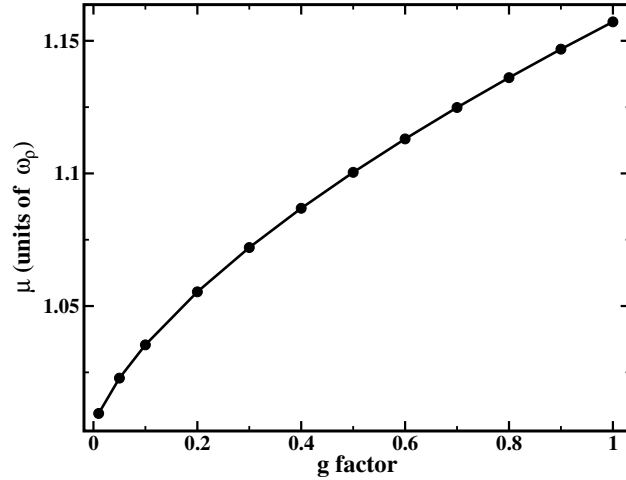


Figure 2.5: The chemical potential μ as a function of the g -factor for the solutions of Figure 2.4

the structure of its wave function can be strongly affected by the interatomic forces.

The GGPE is valid if the gas of atoms is dilute. BEC satisfies this condition. The diluteness parameter is na_{sc}^3 where n is the density of the sample. As long as this parameter is small, the mean-field description should be accurate. The GGPE is formulated in the limit of zero temperature and so corrections are expected as the temperature of the gas increases. In order to investigate the effects of the density and finite temperature the beyond-mean-field (BMF) description is required.

2.2 Beyond mean field

One of the possible beyond-mean-field approaches is CI based on mean-field solutions. The single-particle solutions of the GGPE can be used to form a configuration for N atoms. The superposition of different configurations forms the basis for the description of a many-body system. This approach is very laborious. If the number of one-particle states is M then the number of possible configurations is $\frac{M!}{N!(M-N)!}$. Even with only a few particles and states, this amount quickly becomes extremely large, leading to a problem which cannot be solved in practice. However, since in BEC the number of excited atoms surrounding the condensate is expected to be small, the amount of necessary basis states is also expected to be small.

This problem of large basis can be also partly solved, if the symmetry

of the system is properly taken into account, if an appropriate selection of most important configurations is implemented, and if large-scale diagonalization techniques are adopted. However, there is an even more vital problem concerning CI method. If the pseudopotential model representing the interparticle interaction by a delta function is used, then the CI approach does not converge, as was found in [102]. Figure 2.6 shows the convergence check of the presently developed CI method for three and five particles as a function of the maximum orbital energy ε_{\max} of configurations. At first sight it

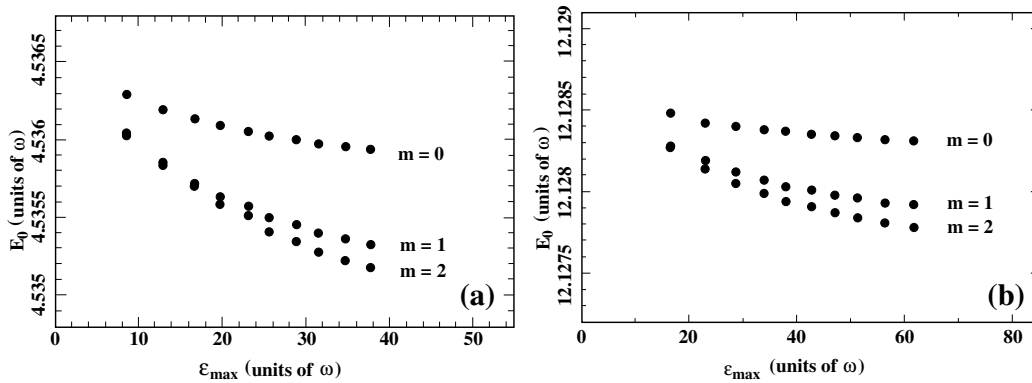


Figure 2.6: Convergence of the CI expansion for a) three ^{87}Rb atoms in a $2\pi \times 1$ kHz isotropic harmonic trap and b) five ^{87}Rb atoms in anisotropic harmonic trap with $\omega_\rho = 2\pi \times 1$ kHz and $\omega_z = 2\pi \times 10$ kHz. In both cases $a_{\text{sc}} = 100 a_0$. Each curve shows convergence of the total ground-state energy as a function of the maximum orbital energy for various values m .

seems that the convergence is slowly establishing. But this is not true. The divergency can be found if higher values of ε_{\max} are considered. The numerical realization must be further improved in order to see this. The theoretical study of Esry and Green [102] considers the same approach to investigate BEC beyond mean field, but in the harmonic isotropic trap. In this study, the use of a large basis is possible because there is spherical symmetry and selection of the most important configurations can be adopted. Figure 2.7 shows the CI convergence check for three particles done by Esry and Green. As is evident from the Figure 2.7 (especially Figure 2.7(b)), CI diverges with orbital quantum numbers l . It turned out that the reason for divergence is the choice of the model potential in the form of the delta function. However, the exact reason has not yet been explained and the solution to this problem has not yet been found. Some problems due to the replacement of the “true” two-body interaction potential by a pseudopotential are already known. For example, for the s -wave scattering of two atoms the pseudopotential must be

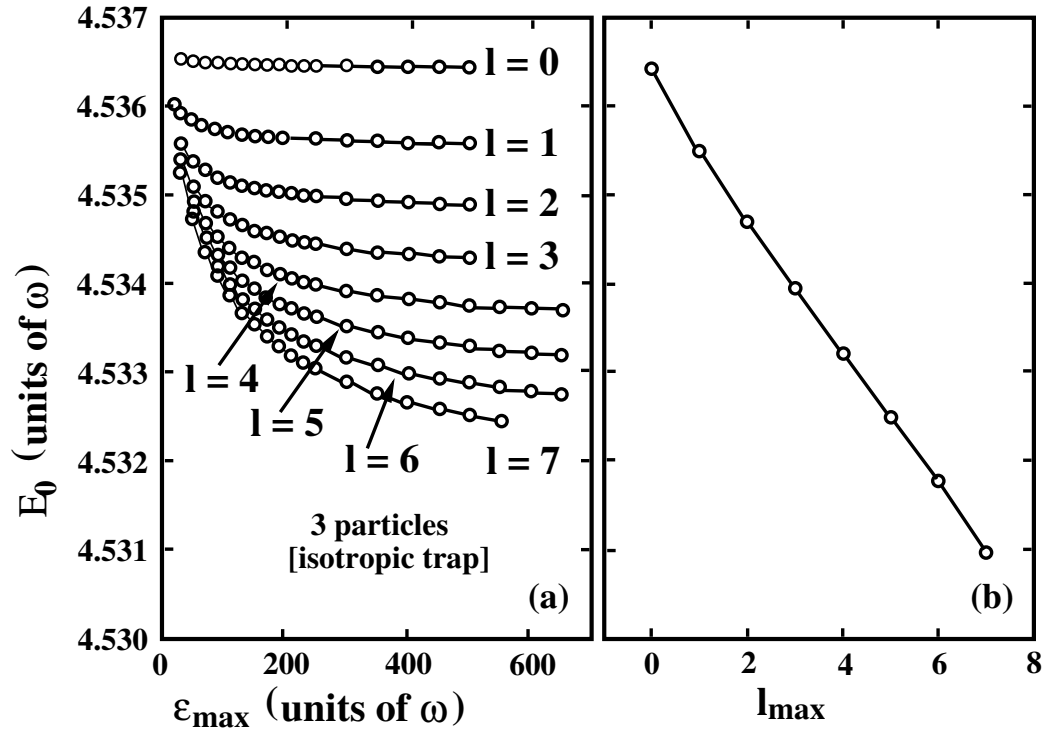


Figure 2.7: Esry and Green's convergence check a) shows the same as Figure 2.6(a) but convergence is done relative to l quantum number and b) is the extrapolation of the curves in a) to $\varepsilon_{\max} \rightarrow \infty$.

adopted in a regularized form [103], if only the relative motion is considered. It may occur that a similar type of regularization for the s -wave scattering as well as for higher partial wave scatterings [104] is required also in the present problem.

2.3 Two-body approaches

The mean-field study shows that two-body collisions are dominant in ultracold dilute atomic gases. The observed divergence also shows that the correct choice of the interparticle interaction description is important. These facts have motivated the detailed study of two-body physics presented in this thesis. In the following section the review of the two-body approaches is tailored to the understanding of the physics relevant for the present research. For coherency, the approaches listed here will be reconsidered in the corresponding chapters.

Multi-channel approach

The complete theoretical treatment of two-body collisions, either in free space or in the presence of a resonant magnetic field, requires a multi-channel scattering treatment. Such a treatment allows the interactions, including the hyperfine, the exchange, or the Zeeman ones, to be properly taken into account. The space of states describing the spatial and spin degrees of freedom of two scattering atoms then may be divided into two subspaces. One subspace, \mathcal{P} , contains the open channel and the other, \mathcal{Q} , contains the closed channels [105]. Open and closed channels may be defined by considering atomic collisions. If the threshold energy of a channel either lies below or equals the total energy available to the system (the kinetic energy of two atoms prior to the interaction) the channel is considered to be open, otherwise it is closed. These subspaces form two orthogonal components which together span the full Hilbert space of both scattering and bound wavefunctions. The state vector is then

$$|\Psi\rangle = \hat{P}|\Psi\rangle + \hat{Q}|\Psi\rangle \quad (2.15)$$

with \hat{P} and \hat{Q} being the projection operators onto subspaces \mathcal{P} and \mathcal{Q} respectively. Consequently, the Schrödinger equation is split into coupled equations

$$(E - H_{PP})\Psi_P = H_{PQ}\Psi_Q \quad , \quad (2.16)$$

$$(E - H_{QQ})\Psi_Q = H_{QP}\Psi_P \quad (2.17)$$

where $\Psi_P = P\Psi$, $\Psi_Q = Q\Psi$, $H_{PP} = PHP$, $H_{QQ} = QHQ$, $H_{PQ} = PHQ$. Equations (2.16) and (2.17) describe system of coupled-channel second-order differential equations. The number of differential equations is equal to the number of open and closed channels.

It is important to note that the multi-channel approach considered in the present work is formulated in relative motion coordinates. This implies that the center-of-mass and relative motion of two atoms may be decoupled and effects due to coupling may be neglected.

Single-channel approach for two untrapped atoms

In many systems the complete multi-channel description cannot be considered due to practical limitations. In order to overcome this problem, the single-channel schemes may be used. In this work, the complete multi-channel problem is given in Chapter 3, describing collisions in off-resonant and on-resonant magnetic fields. In order to approximate these collisions, the effective single-channel schemes are developed and discussed in detail in Chapter 4.

In a single-channel approach the value of the interaction strength and its character can be varied artificially by a controlled manipulation of the Hamiltonian

$$H_{\text{free}} = \frac{1}{2\mu} \frac{d^2}{dR^2} - \frac{J(J+1)}{2\mu R^2} - V_{\text{int}}(R) \quad (2.18)$$

In Equation (2.18), J denotes the rotational quantum number, and μ the reduced mass. Since the present study is concerned with collisions in an ultracold regime, they can be restricted to just the s -wave type. Therefore, Equation (2.18) is considered only for the case $J = 0$. In Equation (2.18), the inter-atomic potential $V_{\text{int}}(R)$ and the mass μ in the kinetic energy term may be modified in the framework of the single-channel approximation. The inter-atomic potential $V_{\text{int}}(R)$ can be varied in numerous ways that are investigated in detail in Chapter 4. In the present work the applicability of the variational approaches obtained with Hamiltonian (2.18) are verified using multi-channel solutions.

Two atoms in a harmonic trap

Experiments with ultracold atomic gases are performed in a trap. In most cases, the trap can be approximated by means of a harmonic potential. In the present work, the influence of a tight, isotropic harmonic trap on the photoassociation of two ultracold ground state atoms forming a homonuclear excited molecule is investigated by solving the single-channel Hamiltonian

$$H_{\omega} = \frac{1}{2\mu} \frac{d^2}{dR^2} - \frac{J(J+1)}{2\mu R^2} - V_{\text{int}}(R) - \frac{1}{2}\mu\omega^2 R^2 \quad (2.19)$$

This Hamiltonian differs from the one in Equation (2.18) by the presence of harmonic potential with the frequency ω . Again, the problem is handled using only relative coordinates. The spherical symmetry and harmonicity of the trap allows the separation of the center-of-mass and the radial internal motion [95]. The eigenfunctions of the center-of-mass motion are the harmonic-oscillator states.

The Schrödinger equation with Hamiltonian (2.19) for collisions of two homonuclear atoms in the same state in harmonic traps possesses analytical solutions [106], if V_{int} is approximated by the regularized contact pseudopotential

$$V_{\text{int}}(R) = \frac{4\pi}{2\mu} a_{\text{sc}} \delta^3(\vec{R}) \frac{\partial}{\partial R} R \quad (2.20)$$

provides an approximation of the atom-atom interaction $V_{\text{int}}(R)$ [95]. In the photoassociation study results with this simplified model for the atomic interaction are compared against the ones obtained using realistic potentials.

Two atoms in an optical lattice

If three independent laser fields are turned on along three spatial directions and create the standing light waves, a three-dimensional lattice potential will be generated. The form of the optical lattice potential can be given by the equation

$$\hat{V}_{\text{trap},j} = \sum_{c=x,y,z} V_c^j \sin^2(k_c c_j) \quad , \quad (2.21)$$

where V_c^j is the potential depth acting on the particle j along the direction c equal to the product of the laser intensity I_c , the polarizability of the particle j . $k_c = 2\pi/\lambda_c$ is the wave vector, and λ_c is the wavelength of the laser creating the lattice potential along the coordinate c . The optical lattice period is $\lambda_c/2$.

Due to the interparticle interaction potential, two atoms in an 3D optical lattice of the form (2.21) should be investigated in center-of-mass and relative motion coordinates. The anharmonicity of the optical lattice leads to a coupling of center-of-mass and relative motion. In fact, even within the harmonic approximation, different trapping potentials experienced by the two atoms lead to a coupling of center-of-mass and relative motion [79, 100]. This situation occurs, e. g., for heteronuclear atom pairs, or for two atoms of the same kind but in different electronic states [101].

After transition from absolute coordinates to center-of-mass and relative motion coordinates, and after performing the Taylor expansion of the sinusoidal trapping potential (2.21) around the origin, the transformation of the Hamiltonian from absolute coordinates into the center-of-mass and relative coordinate systems leads to a Hamiltonian of the form

$$\hat{H} = \hat{h}_{\text{COM}} + \hat{h}_{\text{REL}} + \hat{W} \quad (2.22)$$

with

$$\hat{h}_{\text{COM}} = \hat{t} + \hat{v}_{\text{OL}} \quad (2.23)$$

$$\hat{h}_{\text{REL}} = \hat{T} + \hat{V}_{\text{OL}} + \hat{V}_{\text{int}} \quad . \quad (2.24)$$

In the present formulation only the truly non-separable terms (represented by products of center-of-mass and relative coordinates) are left in the coupling term \hat{W} . All separable terms of the optical lattice potential \hat{v}_{OL} and \hat{V}_{OL} , kinetic energy operators \hat{t} and \hat{T} , and \hat{V}_{int} are included into the center-of-mass and relative Hamiltonians \hat{h}_{COM} and \hat{h}_{REL} respectively as is given by Equations (2.23) and (2.24). An approach to solve the problem with Hamiltonian (2.22) is presented in Chapter 7.

2.4 Conclusion

A numerical approach was developed that allows the treatment of BEC beyond mean field in a harmonic anisotropic trap. The mean-field solutions are used in order to construct configurations which in turn can be used as a basis for beyond-mean-field calculations. If the interparticle interaction is represented by a pseudopotential, the configuration-interaction approach breaks down. The exact reason is, however, not yet known.

Unfortunately, the theoretical microscopic investigation of ultracold many-body systems is feasible only within the framework of the pseudopotential approximation. The mean-field study shows that two-body collisions are dominant in ultracold dilute atomic gases. However, in order to understand the physics of the condensate, even a complete knowledge concerning two-body collisions is not sufficient. Nevertheless, a good knowledge of two-body collisions should help in understanding the consequences of approximations which must be done when many-body systems are considered.

For the delta potential and where the two atoms are placed in a harmonic trap, the Schrödinger equation possesses an analytical solution [95]. This analytical solution may be used for comparison with the exact CI solution in order to understand and fix the divergency problem. There are many-body studies planned for the future and so this problem will not be considered in the thesis anymore. For these studies, the divergency problem must be solved and the numerical approach developed here must also be further improved for a better convergence.

Chapter 3

Collision of two atoms in the presence of a magnetic field

In ultracold alkali atom gases, the interaction between atoms can be varied across a wide range by changing the strength of the magnetic field in the vicinity of a Feshbach resonance. The complete theoretical treatment of magnetic Feshbach resonances requires a multi-channel scattering treatment. Knowledge of the atomic and molecular structures is important for this treatment. In this chapter, the full multi-channel problem is solved numerically for the Feshbach resonances in collisions between generic ultracold ${}^6\text{Li}$ and ${}^{87}\text{Rb}$ atoms in the absolute ground-state mixture in the presence of a static magnetic field. The radial wave functions for the atomic and molecular basis of the ground-state collisional wave function are analyzed in detail in off-resonant and on-resonant points. The solutions obtained in this chapter will be adopted in the Chapter 4 in order to develop approximate single-channel schemes that will be used afterwards in the thesis.

3.1 Atomic properties

The atomic structure of alkali atoms plays an important role for the description of ultracold atomic gases. In order to understand the collision properties of two atoms, in both the field-free case and within a field, the atomic structure must be considered.

The ground-state of alkali atoms consists of one valence electron in an outer shell, and a core with closed electronic shells. This structure makes alkali atoms hydrogen-like two-particle systems. For a hydrogen atom, the non-relativistic Schrödinger equation can be solved analytically. The solutions are one-electron functions also called atomic orbitals. Due to the

spherical symmetry of the core potential, they can be given as

$$\Psi_{n,l,m_l}(r_e, \theta, \phi) = R_{n,l}(r_e)Y_{l,m_l}(\theta, \phi) \quad . \quad (3.1)$$

Here the principal quantum number n , the angular momentum quantum number l , and the magnetic quantum number m_l , uniquely define the atomic orbital. $R_{n,l}$ is the radial part, where r_e is the relative distance between the valence electron and the point-like core. Spherical harmonics Y_{l,m_l} are the solutions for the spherical part. The quantum numbers n, l and m_l are integers and can have the following values: $n = 1, 2, 3, \dots$, $l < n$, $m_l = 0, \dots, \pm l$. For alkalis, the shell electrons are tightly bound in a spherically symmetric core. Because the field of the core is spherically symmetric, the orbits of the valence electron are still characterized by the same quantum numbers.

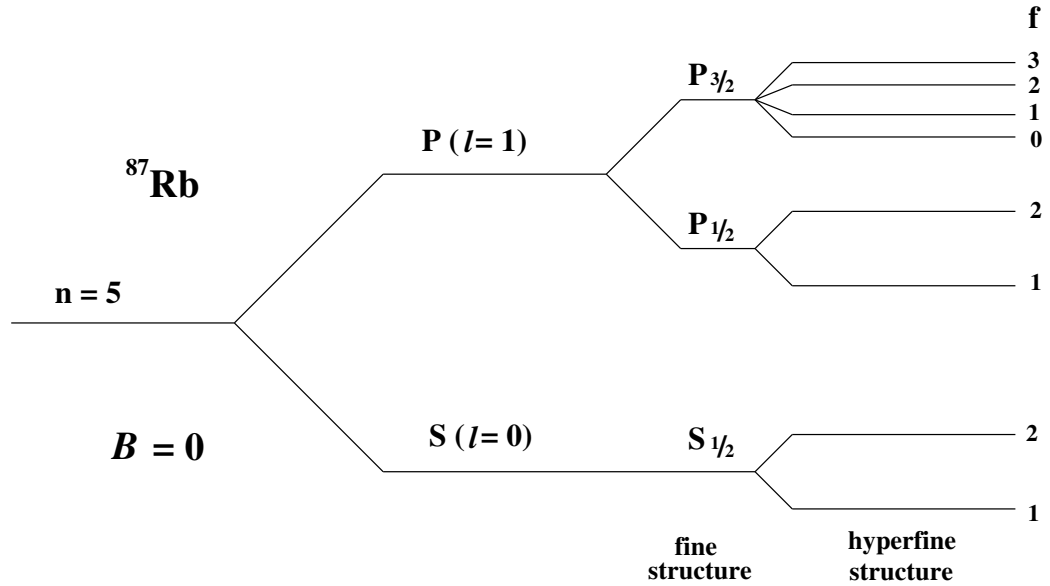


Figure 3.1: An energy level diagram (not to scale) showing the various levels of the valence electron in atomic ^{87}Rb in the absence of the external field.

In the presence of a magnetic field, \vec{B} , the electronic energy levels split into $2l + 1$ sublevels, which can be associated with the different m_l numbers. The energy due to the interaction is $-\vec{\mu} \cdot \vec{B}$. The magnetic dipole moment, $\vec{\mu}$, is produced by the motion of the electron around an orbital path (in a classical picture). The component of $\vec{\mu}$ in the direction of \vec{B} can only take on the integer m_l values. So, the splitting of different $\{l, n\}$ levels in the field is $m_l \mu_B B$ where μ_B is the Bohr magneton (magnetic moment of the electron). If an electron is in the state with $l = 0$, then its orbital motion is not influenced by the magnetic field.

Electrons also possess an internal degree of freedom called spin \vec{s} . The orbital motion of the valence electron is coupled to the spin, $s = \frac{1}{2}$, resulting in a fine structure in the splitting of energy levels. The overall angular momentum of the electron is $\vec{j} = \vec{s} + \vec{l}$. Each j state is $(2j+1)$ -fold degenerate in the absence of an external field. For alkali atoms, the splitting between the two possible levels with the same l , i. e., $l - \frac{1}{2}$ and $l + \frac{1}{2}$ is $\Delta E_{\text{fs}} = a^{\text{fs}}(l + \frac{1}{2})$ where a^{fs} is the fine structure constant. However, this spin-orbit interaction is absent for $l = 0$.

The core of the atom also has a spin determined by the number of protons and neutrons in the nucleus. The nuclear spin \vec{i} interacts with the valence electron spin, leading to hyperfine splitting. If the valence electron is in the state with $l = 0$, its orbital motion does not produce any magnetic field at the nucleus. The coupling arises solely due to the magnetic field produced by the electronic spin. Two spins are combined to a total angular momentum $\vec{f} = \vec{s} + \vec{i}$ where each f state is $(2f + 1)$ -fold degenerate. In a Hamiltonian the coupling is represented by a term V^{hf} of the form

$$\hat{V}^{\text{hf}} = a^{\text{hf}} \vec{s} \cdot \vec{i} \quad (3.2)$$

where a^{hf} is the hyperfine constant. The quantum number f has two possibilities $f = i + \frac{1}{2}$ and $f = i - \frac{1}{2}$. The splitting between the f levels is $\Delta E_{\text{hf}} = a^{\text{hf}}(i + \frac{1}{2})$. The hyperfine quantum numbers can be used to label energy levels of the atom in a magnetic field. The energy level diagram for various levels of the ^{87}Rb demonstrating the atomic structure in the absence of the external field is shown as an example in Figure 3.1.

An atom in the presence of a magnetic field \vec{B} experiences Zeeman interaction due to coupling between the magnetic field and magnetic moments produced by electronic and nuclear spin. If a magnetic field is taken in the z direction, the Zeeman interaction is described by operator

$$\hat{V}^{\text{Z}} = g\mu_{\text{B}}B\hat{s}_z - \frac{\mu}{i}B\hat{i}_z \quad (3.3)$$

where μ is the magnetic moment of the nucleus, μ_{B} is the Bohr magneton, $g \approx 2$ is the electron factor, and $B = B_z$. Figures 3.2 (a) and (b) show the energy spectrum of the hyperfine states for the individual atoms ^6Li and ^{87}Rb as a function of magnetic field.

The interaction with nucleus $\frac{\mu}{i}B\hat{i}_z$ is three orders of magnitude smaller than the interaction with the electron, $g\mu_{\text{B}}B\hat{s}_z$, and for most applications may be neglected. The resulting Hamiltonian contains the hyperfine and

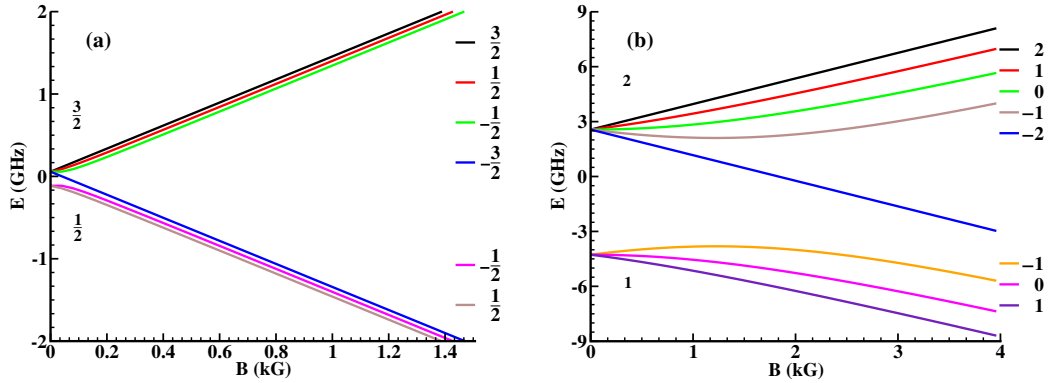


Figure 3.2: Ground-state energies of the hyperfine states for ${}^6\text{Li}$ (a) and ${}^{87}\text{Rb}$ (b) in a magnetic field. The energy curves are labeled by the $B = 0$ hyperfine quantum numbers. The diagrams remain the same for all atoms with corresponding values of the nuclear spin, taking into account difference in scaling due to a change in the hyperfine splitting constant a^{hf} .

Zeeman interactions in Equations (3.2) and (3.3). It conserves the total angular momentum, and therefore only couples states with the same total angular momentum. This reflects the invariance of the interactions relative to the magnetic axis.

3.2 Molecular properties

Ultracold alkali atom gases are dilute systems, in the sense that the dominant effects of interaction are due to two-body collisions. It is possible to calculate properties of a condensate by relying on the knowledge about two-body scattering at low energies, as has been discussed in Chapter 2.

At small atomic separations when atoms are close to each other, the interatomic interaction has a complicated form. To simplify calculations at such distances, the Born-Oppenheimer (BO) approximation is usually adopted. Generally, the electronic spin states for an ultracold atomic pair in certain hyperfine states are superpositions of the electronic triplet and singlet contributions. Consequently, the interaction contains both triplet and singlet terms. The radial interaction between two atoms can be written as

$$\hat{V}_{0,1}(R) = V_0(R)\hat{P}_0 + V_1(R)\hat{P}_1 \quad (3.4)$$

where \hat{P}_0 and \hat{P}_1 are the projection operators on the maximally symmetric singlet ($S = 0$) and triplet ($S = 1$) subspaces respectively. In the van der

Waals limit, the singlet and triplet potentials differ by twice the exchange energy, which is very well represented by the Smirnov and Chibisov form

$$V_{\text{exch}}(R; J_0, \alpha) = J_0 R^{\frac{7}{2\alpha}-1} e^{-\alpha R} \quad . \quad (3.5)$$

In Equation (3.5), the atomic ionization energy is $-\alpha^2/2$, and J_0 is a normalization constant. Example potentials for the singlet $X^1\Sigma_g^+$ and triplet $a^3\Sigma_g^+$ states of a homonuclear system are shown in Figure 3.3.

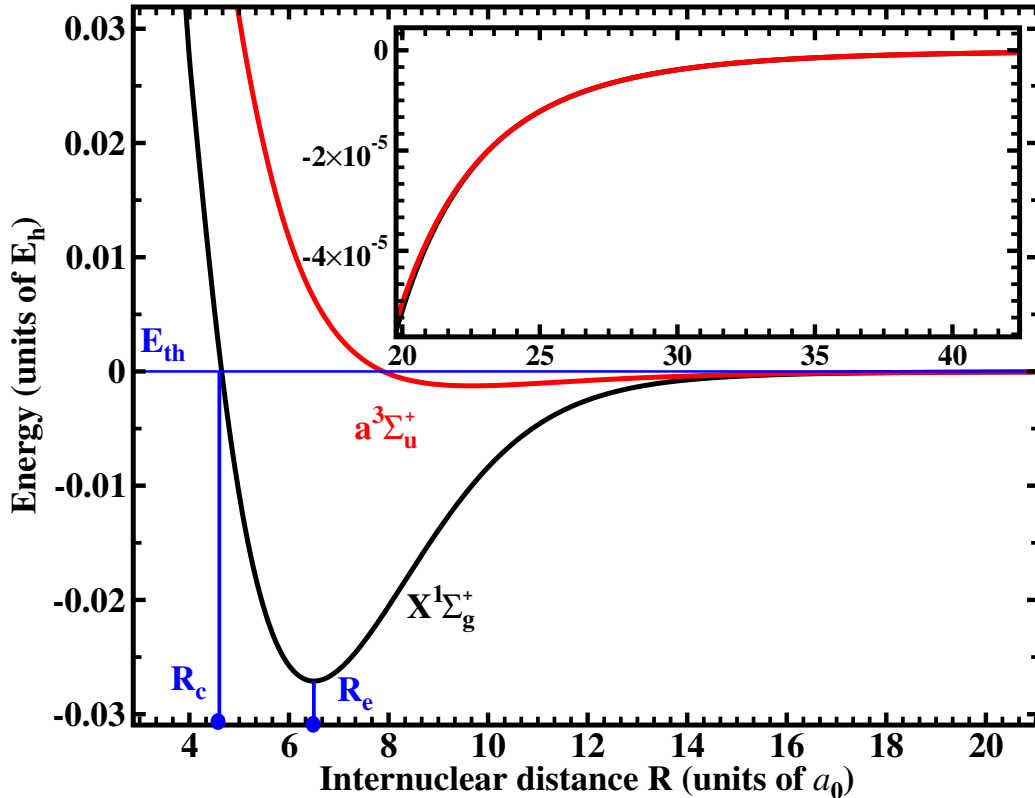


Figure 3.3: The electrostatic interaction potential of two homonuclear atoms in the singlet (black) and triplet (red) state. The inset shows the long-range part of the potential, where the van der Waals interaction is dominant. The equilibrium distance is denoted by R_e , the distance between the $V(R_e)$, and the threshold energy E_{th} is equal to the well depth. The choice of the absolute value for the threshold energy is arbitrary and can be defined by adding or subtracting a constant value. The inner wall of the potential crosses E_{th} at point R_c .

At larger internuclear distances, there is an attractive van der Waals interaction $\hat{V}_{\text{vdW}}(R)$ due to Coulomb forces

$$\hat{V}_{\text{vdW}}(R) = - \sum_n \frac{C_n}{R^n} \quad (3.6)$$

where C_n are the van der Waals coefficients and n is an integer whose value depends on the symmetry of the electronic state. Figure 3.3, inset, shows the part of the interparticle interaction potential in the BO approximation where the van der Waals interaction is dominant.

In general, the atom-atom interaction potential for the short-range distance is only known numerically. The computation of the interatomic interaction potential is very laborious. Nevertheless, using the fact that the motion of nuclei is much slower than the motion of the electrons, it is possible to separate the two motions and simplify the interaction. Such an approach is called the Born-Oppenheimer approximation [107]. This approximation is considered in Appendix D.

If the interatomic potential is known with sufficiently high accuracy, all bound-state and scattering properties can be obtained by numerical integration of the second-order Schrödinger equation [100]. The potential curve can also be refined if experimental data on the positions of the bound states or photoassociation intensities are available.

Calculations of the present thesis assume the Born-Oppenheimer approximation to be valid. Furthermore, the use of a numerically defined realistic interatomic potentials for the calculations reproduces the physics of the interaction almost perfectly. This makes the introduced model suitable as a reference for other approaches (e. g., the pseudopotential approximation discussed in Section 5.4) widely used in ultracold physics.

Without the center-of-mass kinetic energy the total Hamiltonian for two colliding ground-state alkali atoms in the presence of a magnetic field B becomes

$$\hat{H}_B = \hat{T}_\mu + \sum_{j=1}^2 (\hat{V}_j^{\text{hf}} + \hat{V}_j^Z) + \hat{V}_{0,1} \quad (3.7)$$

where \hat{T}_μ is the kinetic energy of the relative motion and μ (not to be confused with magnetic moment $\vec{\mu}$) is the reduced mass. Hyperfine \hat{V}_j^{hf} and Zeeman \hat{V}_j^Z operators for individual atoms constituting the molecule were defined in Equations (3.2) and (3.3) in Section 3.1.

For the interactions in question, the system of two colliding atoms is invariant under independent rotations of spin and orbital coordinates around the axis that runs through the overall center of mass parallel to the magnetic field. Therefore, the projection M_F of the total spin angular momentum $\vec{F} = \vec{f}_1 + \vec{f}_2$ and of the orbital angular momentum \vec{l} along this axis are separately conserved during the collision. Since $\hat{V}_{0,1}$ depends only on $|\vec{R}|$ but not on its direction, \vec{l} is even conserved as a 3D vector. As a consequence, M_F and the rotational quantum numbers l and m_l are good quantum numbers.

Two other interactions are present: the direct interaction between the

electronic spins via their magnetic moments and the spin-orbit interaction of the spins of the valence electrons [107]. These interactions are much weaker and can be safely neglected.

3.3 Multi-channel Feshbach resonance

The physics of magnetic Feshbach resonances is explained in the following section on the basis of the concrete example of two atoms ${}^6\text{Li}$ and ${}^{87}\text{Rb}$ both in the ground state colliding in the presence of a magnetic field.

3.3.1 Channel definitions

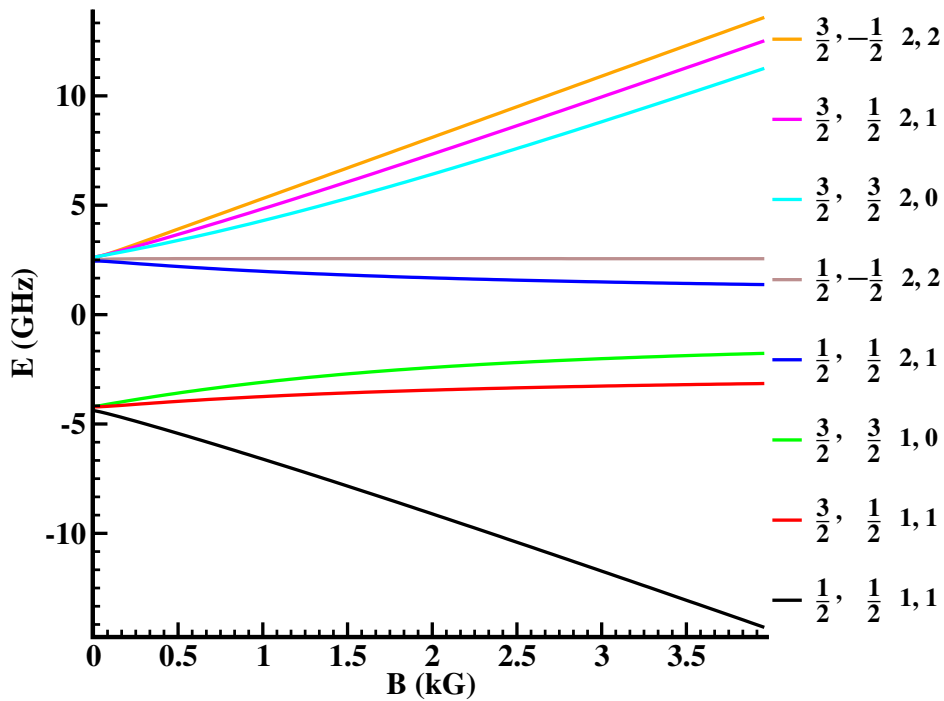


Figure 3.4: The dependence of the collision thresholds E_χ on magnetic field for ${}^6\text{Li}$ - ${}^{87}\text{Rb}$ system for the manifold of states with total angular momentum projection along the magnetic field $M_F = \frac{3}{2}$.

The space of states describing the spatial and spin degrees of freedom of two scattering atoms may be divided into two subspaces. One subspace contains the open channel and the other contains the closed channels [105]. These subspaces form two orthogonal components which together span the

full Hilbert space of both scattering and bound wavefunctions. In the vicinity of the resonance, the strong coupling between the open channel and one of the closed channels originates from the near degeneracy of a closed-channel vibrational Feshbach resonant level with the dissociation-threshold energy of the open channel [36].

If two atoms are far apart from each other, the central interaction (3.4) may be neglected and the two-body system may be described by the eigenstates of each atom introduced in Section 3.1. The quantum number f is not conserved for $B \neq 0$. Nevertheless, the pair f and m_f may be used to label atomic levels because the energy eigenvalues corresponding to different f intersect at rather large magnitudes of magnetic field. The collision channel of two atoms $|\chi\rangle$ is then written as a direct product of the respective one-atom states $|\chi\rangle = |f_{6\text{Li}}, m_{f_{6\text{Li}}}\rangle |f_{87\text{Rb}}, m_{f_{87\text{Rb}}}\rangle$. The sum of the hyperfine and Zeeman energies for an atom pair in an eigenstate of this atomic basis is the threshold energy $E_\chi(B)$ of the collision. Figure 3.4 shows the collision thresholds $E_\chi(B)$ for states with the angular momentum projections $M_F = m_{f_{6\text{Li}}} + m_{f_{87\text{Rb}}} = \frac{3}{2}$. The total energy available to the system is the kinetic energy prior to the interaction, i. e., if the atoms are far apart. If the threshold energy of a channel lies below or equals the total energy available to the system the channel is considered as open, otherwise it is closed.

3.3.2 The coupled-channel equations

As the atoms approach each other during a collision their $|\chi\rangle$ states are mixed by the strong molecular exchange interaction (3.5). The exchange potential couples states with the same magnetic component of the total angular momentum, M_F . The function

$$|\Psi\rangle = \frac{\psi_{\text{open}}(R)}{R} |\text{open}\rangle + \sum_{\chi, \text{closed}} \frac{\psi_\chi(R)}{R} |\chi\rangle \quad (3.8)$$

takes into account all coupled states. In Equation (3.8) the first state on the right-hand side corresponds to the open channel in the collision, and the second term to the closed channels. Equation (3.8) is valid, if only one open channel occurs at the resonance. The function $\Psi(R)$ is a solution of the stationary Schrödinger equation with the Hamiltonian (3.7)

$$\hat{H}_B |\Psi\rangle = E |\Psi\rangle \quad . \quad (3.9)$$

Due to ultracold conditions that are of most interest in this work, only the s -wave collisions may be considered. Then the substitution of Equation (3.8)

into Equation (3.9) leads to the system of coupled-channel second-order differential equations

$$\left[-\frac{1}{2\mu} \frac{\partial^2}{\partial R^2} + E_\chi(B) + V_+(R) \right] \psi_\chi(R) - V_-(R) \sum_{\chi'} W_{\chi'\chi}(B) \psi_{\chi'}(R) = E \psi_\chi(R) \quad (3.10)$$

with

$$V_+(R) = \frac{V_0(R) + V_1(R)}{2}, \quad V_-(R) = \frac{V_0(R) - V_1(R)}{2} . \quad (3.11)$$

The advantage of introducing the V_+ and V_- terms is that their long-range asymptotic behavior is equal to V_{vdW} and $\frac{1}{2}V_{\text{exch}}$ respectively (Equations (3.6) and (3.5)). For a given magnetic field B , the channel threshold energies E_χ and the elements $W_{\chi'\chi}$ of the coupling matrix are fixed, and the $V_-(R)$ term describes how strongly different channels are coupled.

3.3.3 Multi-channel solutions

Choice of the proper basis

Depending on the distance between two particles, the set of interacting states is best considered according either to the atomic basis (AB) or to the molecular basis (MB). The basis of asymptotically free states or atomic basis is convenient for describing the long-range part of the wave function. At such large values of interatomic separation, the exchange interaction V_{exch} is vanishingly small and the hyperfine states of a diatomic system are uncoupled. For the short-range part, the triplet/singlet basis, or molecular basis, is more suitable. It is introduced when the interatomic separation is smaller than the distance where the exchange interaction prevails over the hyperfine interaction. The exchange interaction does not couple states that have well-defined singlet or triplet electronic spin components. In this basis, however, these states are coupled by the hyperfine interaction because it is not diagonal.

One of the possible choices of the MB basis in the regime of strong molecular interaction is $|\xi\rangle = |S, M_S\rangle |m_{i_1}, m_{i_2}\rangle$, where S and M_S are the total electronic spin of the system and its projection along the magnetic field respectively, where m_{i_1} and m_{i_2} are the nuclear spin projections of the individual atoms. The transformation between states ψ_χ and ϕ_ξ is straightforward. Equation (3.8) can be written as

$$|\Psi\rangle = \sum_{\xi} \frac{\phi_\xi(R)}{R} |\xi\rangle , \quad (3.12)$$

Table 3.1: Atomic and molecular basis states of the ${}^6\text{Li}$ - ${}^{87}\text{Rb}$ dimer for the manifold of states with total angular momentum projection along the magnetic field $M_F = \frac{3}{2}$.

atomic index $ \chi\rangle$	AB	molecular index $ \xi\rangle$	MB
$ a_1\rangle$	$ 1/2, 1/2\rangle 1, 1\rangle$	$ S_1\rangle$	$ 0, 0\rangle 1, 1/2\rangle$
$ a_2\rangle$	$ 3/2, 1/2\rangle 1, 1\rangle$	$ S_2\rangle$	$ 0, 0\rangle 0, 3/2\rangle$
$ a_3\rangle$	$ 3/2, 3/2\rangle 1, 0\rangle$	$ T_1\rangle$	$ 1, -1\rangle 1, 3/2\rangle$
$ a_4\rangle$	$ 1/2, 1/2\rangle 2, 1\rangle$	$ T_2\rangle$	$ 1, 0\rangle 0, 3/2\rangle$
$ a_5\rangle$	$ 1/2, -1/2\rangle 2, 2\rangle$	$ T_3\rangle$	$ 1, 0\rangle 1, 1/2\rangle$
$ a_6\rangle$	$ 3/2, 3/2\rangle 2, 0\rangle$	$ T_4\rangle$	$ 1, 1\rangle -1, 3/2\rangle$
$ a_7\rangle$	$ 3/2, 1/2\rangle 2, 1\rangle$	$ T_5\rangle$	$ 1, 1\rangle 0, 1/2\rangle$
$ a_8\rangle$	$ 3/2, -1/2\rangle 2, 2\rangle$	$ T_6\rangle$	$ 1, 1\rangle 1, -1/2\rangle$

with

$$\phi_\xi(R) = \sum_\chi \psi_\chi(R) \langle \xi | \chi \rangle \quad . \quad (3.13)$$

Table 3.1 lists all atomic and molecular basis states of the ${}^6\text{Li}$ - ${}^{87}\text{Rb}$ system for the case of $M_F = \frac{3}{2}$ and s -wave collisions. The functions ψ/R and ϕ/R are the true wave functions. However, it is convenient to discuss ψ and ϕ instead of the true wave functions. In present work this will be done in the following where ψ and ϕ are for simplicity called wave functions.

Method and boundary conditions

The multi-channel Equations (3.10) are solved numerically using an R -matrix method [108] based on implementation by . The R -matrix method is a general and quite powerful *ab initio* approach to a wide class of atomic and molecular collision problems. The essential idea is to divide the space into two or possibly more physical regions. In each of these regions the time-independent Schrödinger equation is solved using techniques specifically selected and optimized to describe the important physical properties in that region. The solutions and their derivatives are then matched at the boundaries.

The technical details of the calculations with the present ${}^6\text{Li}$ - ${}^{87}\text{Rb}$ dimer are as follows. The ${}^6\text{Li}$ - ${}^{87}\text{Rb}$ dimer in $M_F = \frac{3}{2}$ state has eight states, as presented in Table 3.1. This leads to eight coupled equations of the form given in Equations (3.10). In order to consider the problem numerically, the spatial part of the wave function given by Equation (3.8) is expanded with B

splines (Appendix B). The potential curves for the singlet and triplet states of the ${}^6\text{Li}$ - ${}^{87}\text{Rb}$ were obtained using information from [109, 110] and references therein. In [109], the refined potential parameters were constructed using multi-channel calculations based on experimentally observed resonances.

The wave function (3.8) must obey the appropriate boundary conditions. It is necessary that the functions $\psi_\chi(R)$ vanish at the origin so as to prevent divergence. Another constraint is that functions of the closed channels must vanish as $R \rightarrow \infty$. The fulfillment of these boundary conditions permits solution of the system (3.10), leaving just one parameter in the solution, e. g., the normalization of the entrance channel. Accordingly, the open channel function is normalized to the radial asymptotic solution of two particle scattering on a spherically symmetric potential. This asymptotic solution is

$$\psi_{\text{open}}(R)|_{R \rightarrow \infty} = \sin(k \cdot R + \arctan[-k \cdot a_{\text{sc}}]) \quad (3.14)$$

with a phase δ_0

$$\tan[\delta_0] = -k \cdot a_{\text{sc}} \quad , \quad (3.15)$$

and $k = \sqrt{2\mu E}$. For the present study the normalization constant in Equation (3.14) may be set to any arbitrary value; here it is one. However, for calculating observables like cross-sections the norm plays a role. The kinetic energy E of two atoms when they are far apart is set to arbitrarily chosen small value 50 Hz. Since this energy is very far from $s \rightarrow p$ atomic transition, the collisions are limited to the s -wave type only. The choice of a small but finite energy is justified because, under ultracold conditions, two particles collide with a low but non-zero energy. Furthermore, the non-zero energy helps avoid non-physical numerical artifacts in the definition of the phase δ_0 for the asymptotic function (3.14). In Equation (3.14), a_{sc} denotes the s -wave scattering length. a_{sc} is defined in the zero collision limit and characterizes the interaction between two atoms. The sign of a_{sc} determines the type of interaction (repulsive or attractive), and the absolute value determines the interaction strength.

In order to normalize the incoming channel function its asymptotic form is matched to the solution (3.14). The value of the scattering length is automatically determined by this matching procedure. A variation of the magnetic field around a resonance changes the interaction between atoms and correspondingly the value of the scattering length. In the range of the B -field variation from 1064 G to 1282.6 G the ${}^6\text{Li}$ - ${}^{87}\text{Rb}$ system possesses two s -wave resonances, a broad one at $B_0 = 1066.92 \text{ G}$ and a narrow one at $B_0 = 1282.576 \text{ G}$. Figure 3.5 shows the results of the multi-channel calculations for the scattering length as a function of the magnetic field around these two resonances.

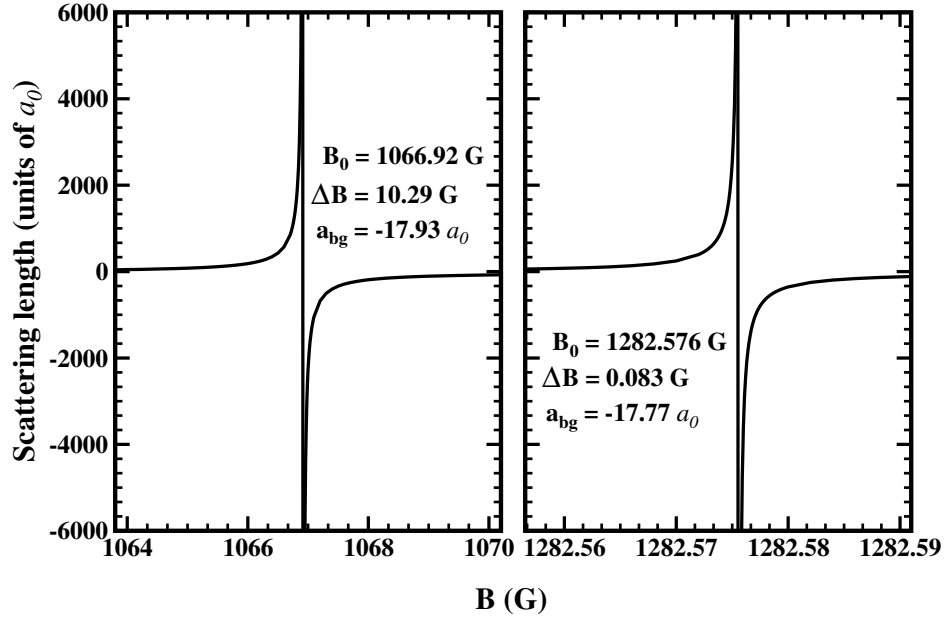


Figure 3.5: Broad and narrow resonances for the collision of the ${}^6\text{Li}-{}^{87}\text{Rb}$ dimer for finite energy 50 Hz. The magnetic Feshbach resonance parameters B_0 (resonance position), ΔB (resonance width) and a_{bg} (background scattering length) are directly specified in the figure.

Solutions in the atomic basis (AB)

Figure 3.6 presents results of the multi-channel calculations for the ${}^6\text{Li}-{}^{87}\text{Rb}$ system in a magnetic field if $E = 50$ Hz. Figures 3.6(a) and (c) show the radial functions of the eight channels in the AB for non-resonant magnetic field at large and short distances respectively. Similarly, Figures 3.6(b) and (d) show the same for the resonant magnetic field when the absolute value of scattering length is very large, chosen here as $a_{\text{sc}} = -65450 a_0$.

In the case of an off-resonant field the function of the incoming channel has the largest amplitude at both large and small distances, as is evident from Figures 3.6(a) and (c). The amplitude of the closed channel functions vanishes at larger separation, as Figure 3.6(a) shows. However, at small distances, the closed channels have non-zero amplitudes even in the B -field-free case; they are slightly excited during the collision and possess a background contribution to the scattering process. Therefore, the two-body collision is a multi-channel process even in free-space.

Near resonance, the closed channel $|a_3\rangle$ is strongly excited during the collision, as is clear from Figures 3.6(b) and (d). This occurs because the energy of the $|a_3\rangle$ state approaches the total energy available to the system

3.3 Multi-channel Feshbach resonance

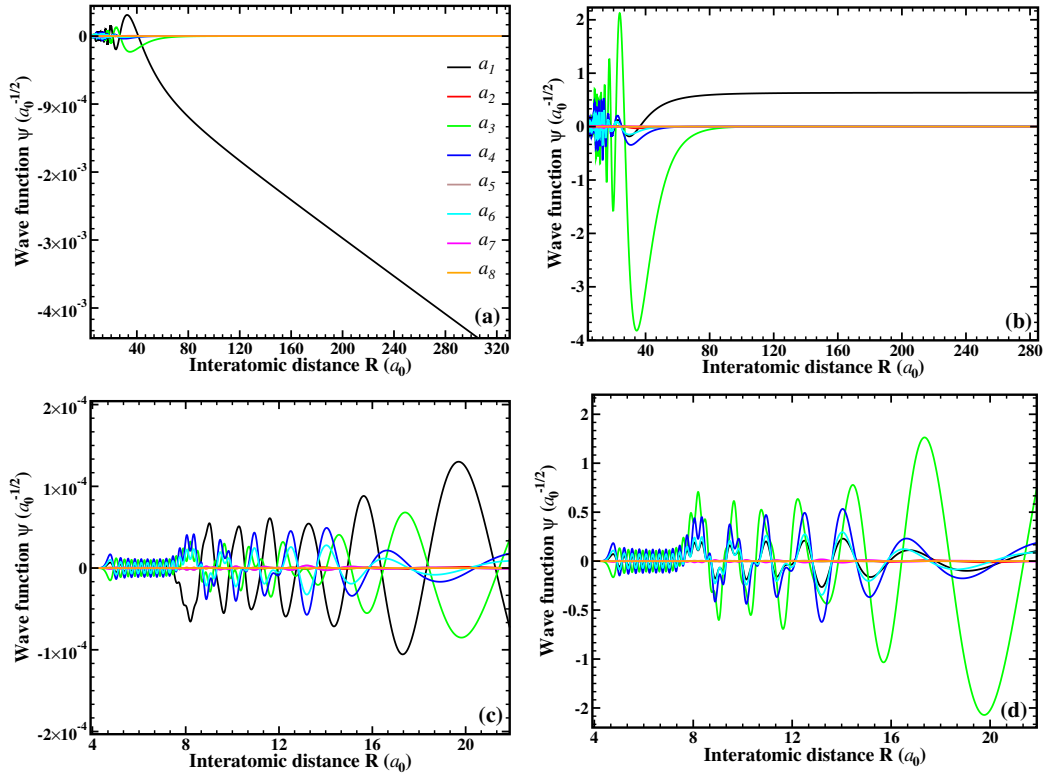


Figure 3.6: The $\psi_\chi(R)$ functions for the solution of the coupled channel Equation (3.10) for the ${}^6\text{Li}$ - ${}^{87}\text{Rb}$ collision with finite energy 50 kHz in an off-resonance field (a) and (c) and in resonance (b) and (d). The atomic labels are indicated in the legend of (a).

at the resonant value of B . The amplitude of the closed channel $|a_3\rangle$ is much larger than the amplitude of the open channel. However, the $|a_3\rangle$ state is not the only one that is resonantly enhanced. The amplitudes of other states are also changed and some of them are even sizeable. Hence, the atomic states are strongly coupled, and there is no possibility of exciting any of the closed channels permanently. Therefore, it is difficult to pick out a single closed channel whose bound state goes into resonance.

The AB is better suited to describe the atomic system when two particles are far apart and do not experience the influence of the complicated short-range potential. With less separation, if the exchange interaction is strong, the MB is preferable and will now be discussed.

Solutions in the molecular basis (MB)

Figure 3.7 shows the radial functions in the MB obtained from the atomic solutions presented in Figure 3.6. The arrangement of figures is the same.

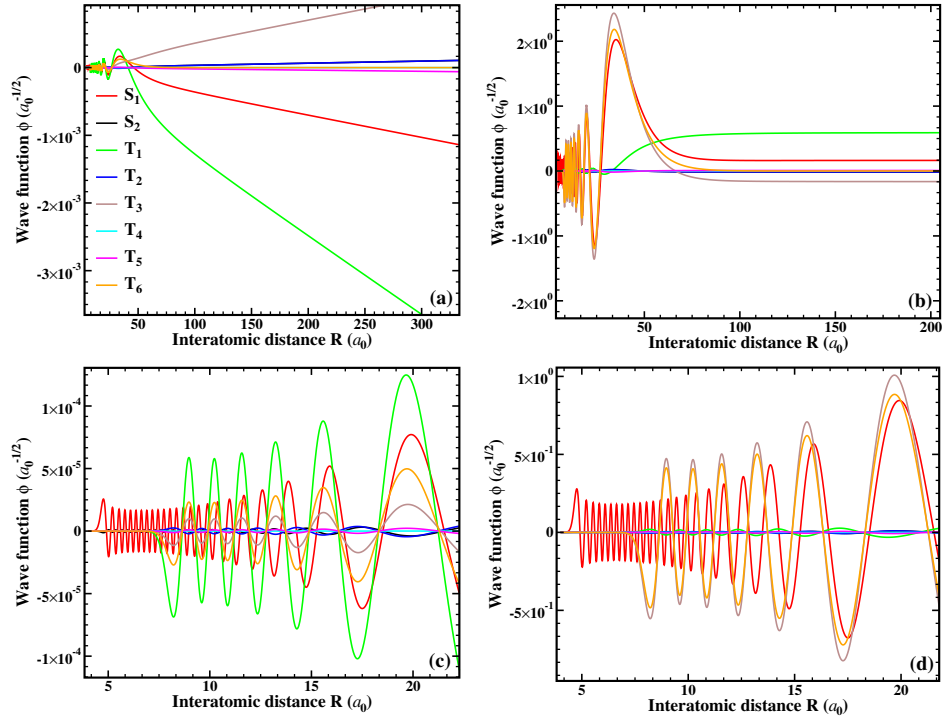


Figure 3.7: The ϕ_ξ functions of Equation (3.12) The same as Figure 3.6 but in molecular basis $|\xi\rangle = |S, M_S\rangle |m_{i_1}, m_{i_2}\rangle$.

Transformation of one basis to another is done with the help of Equation (3.12) and (3.13). From the comparison of Figures 3.7(a) and (b) with Figures 3.6(a) and (b), it is noticeable that molecular functions are asymptotically similar to the atomic incoming channel function. This is expected because the only contribution in the expansion of Equation (3.13) at large distance comes from the non-vanishing, incoming atomic state. At short distance, however, the MB gives a more appropriate description. In this case, the molecular functions ϕ_ξ have a regular structure, as is evident from Figures 3.7(c) and (d). Furthermore, since there is a clear separation into the singlet and triplet states, the appropriate singlet and triplet functions tend to zero at different interatomic separation, in contrast to the atomic functions ψ_χ . The singlet functions extend to smaller interatomic distance than the triplet ones since the repulsive inner wall of the singlet state is located close to zero (Figure 3.3).

In the far-off-resonant regime the triplet state $|T_1\rangle$ has the largest amplitude, as is seen from Figure 3.7(a) and (c). The contribution of the singlet state $|S_1\rangle$ and two triplet states $|T_6\rangle$ and $|T_3\rangle$ is also sizeable. Near resonance the states $|S_1\rangle$, $|T_6\rangle$ and $|T_3\rangle$ are essentially enhanced as shown in

Figures 3.7(d) and (b). There can be no single molecular state that would be dominant in the collision. Furthermore, channels in MB can no longer be classified into closed and open because all molecular states contribute to both. The dominant triplet state $|T_1\rangle$ almost completely vanishes at the resonance.

It is noteworthy that the atomic functions and singlet molecular functions at distances less than $\sim 7a_0$ have identical oscillatory structure. This indicates the distance at which the exchange term becomes relevant.

3.4 Conclusion

Depending on the distance between two particles, the set of interacting states is best considered either according to the atomic basis or to the molecular basis. While the atomic basis is convenient for the description of the long-range part of the wave function, the triplet/singlet molecular basis is suitable for the short-range part. The presence of hyperfine interaction mixes different channels, therefore the closed channels are slightly excited during the collision and make a background contribution to the scattering process. Hence, even in the field-free case the multichannel calculations must be carried out in order to describe the collisions correctly. If a magnetic field is applied on the two atoms, the amplitude of different channels changes. Near resonance the amplitudes of some of them are resonantly enhanced, changing from very small, almost negligible values to very large, dominant ones.

Chapter 4

Multi-channel approach vs single-channel approximation

The multi-channel method considered in the previous chapter is the fully correct, theoretical description of two atom collisions in a resonant B field. In this case the effects of the hyperfine and exchange interactions and the interaction with the magnetic field are taken into account properly. Using multi-channel solutions it is possible to correctly predict, e. g., absolute rates of the photoassociation process. However, the multi-channel approach is very laborious. Depending on the system, the number of channels can be very large. Although many of them may not be directly relevant for a particular investigation, the multi-channel approach requires that they must all be considered together because of mutual inter-channel coupling. The multi-channel method can be computationally demanding and can even become impractical if the center-of-mass and relative motion of two atoms have to be considered in a coupled way. This is the case, if atoms are placed in an anharmonic optical lattice. Then the approach must incorporate not only the magnetic field but also a six-dimensional trapping potential. Therefore, it is desirable to outline the possibilities for further approximations and to find out the range of their applicability. One of the possible approximations may be the single-channel one. In this case the collision properties of two atoms are described by a single interatomic interaction potential, that can for some cases even be substituted by a pseudopotential. The complicated multi-channel picture is reduced to one parameter, namely, the scattering length, whose variation may be related to variation of the magnetic field. This approximation is very common in theory. Furthermore, the theoretical microscopic investigation of ultracold many-body systems is presently feasible only within the framework of the single-channel pseudopotential approximation. This chapter considers the comparison of the exact multi-channel

solutions with single-channel approximation in order to clarify the applicability or limitations of the single-channel approach. The generic results are again presented using heteronuclear ${}^6\text{Li}$ - ${}^{87}\text{Rb}$ in an ultracold regime.

4.1 Single-channel approximation

In a single-channel approach the value of the interaction strength and its character can be varied artificially by a manipulation of the Hamiltonian

$$\hat{H} = -\frac{1}{2\mu} \frac{\partial^2}{\partial R^2} + V(R) \quad . \quad (4.1)$$

In Equation (4.1), the inter-atomic potential $V(R)$ or the mass μ in the kinetic energy term may be modified. Both methods lead to a shift of the least bound energy level relative to the potential threshold. The scattering length is sensitive to the position of the least bound level and can be changed in a wide range. The value of the scattering length and the norm of the wave function are determined in the same way as is done for the incoming channel of the multi-channel approach (Section 3.3), using the asymptotic solution given by Equation (3.14).

The atom-atom interaction potential, $V(R)$, can be varied in numerous ways. The strong-repulsive inner wall, the exchange part, and the long-range van der Waals part may be modified separately in a controllable manner. These procedures including the mass variation will be called the v -variation, where $v = \{\{v' = \{w, J, s\}, \mu\}$ denotes the appropriate single-channel modification. Namely, the indices w , J and s stand for the van der Waals, the exchange and the inner part of the potential respectively, and μ denotes the mass variation where the kinetic energy operator is modified. The Schrödinger equation with the Hamiltonian (4.1) for variable potential and kinetic energy is

$$\left(-\frac{1}{2\mu} \frac{\partial^2}{\partial R^2} + V_{X^1\Sigma^+}^{v'}(R) \right) \varphi^v(R) = E^v \varphi^v(R) \quad . \quad (4.2)$$

To ensure the absence of non-physical artifacts the variation of the potential $V_{X^1\Sigma^+}(R)$ must result in smooth final curves. The variations are defined as follows

$$V_{X^1\Sigma^+}^w(R; w) = V_{X^1\Sigma^+}(R) \cdot f_d(R; \Delta, R_0) - w \cdot \frac{C_6}{R^6} \cdot f_u(R; \Delta, R_0), \quad (4.3)$$

$$V_{X^1\Sigma^+}^J(R; J) = V_{X^1\Sigma^+}(R) + V_{\text{exch}}(R; J_0, \alpha) - V_{\text{exch}}(R; J, \alpha), \quad (4.4)$$

$$V_{X^1\Sigma^+}^s(R; s) = V_{X^1\Sigma^+}(R + s \cdot (R - R_e)/(R_c - R_e)) \quad , \quad (4.5)$$

where $J_0 = 0.0125$ and $\alpha = 1.184$ are universal numbers, $V_{X^1\Sigma^+}(R)$ is the original non-modified potential. The equilibrium distance R_e and threshold crossing point R_c were designated in Figure 3.3. A smooth variation of the long-range $V_{X^1\Sigma^+}^w(R; w)$ potential is achieved by the tuning functions f_u and f_d . These functions are used in order to merge the short-range and long-range parts of the potential at the boundary points. The tuning functions are defined as

$$\begin{aligned} f_d(R; \Delta, R_0) &= \left(1 + e^{\frac{\gamma(R-R_0)}{\Delta}}\right)^{-1} \quad \text{and} \\ f_u(R; \Delta, R_0) &= \left(1 + e^{\frac{\gamma(R_0-R)}{\Delta}}\right)^{-1} . \end{aligned} \quad (4.6)$$

In Equation (4.6) $\gamma = 6.9$ ensures $f_\alpha = 0.001$ or 0.999 for $R = R_0 \pm \Delta$. The properties of these functions are such that

$$\begin{aligned} f_d(R; \Delta, R_0) &\approx 0 \quad \text{for} \quad R < R_0 - \Delta \quad , \\ f_u(R; \Delta, R_0) &\approx 0 \quad \text{for} \quad R > R_0 + \Delta \quad . \end{aligned} \quad (4.7)$$

Figure 4.1 shows the functions in Equation (4.6) for the particular values $\Delta = 6$ and $R_0 = 30a_0$. For the present study the parameters of the tuning functions are chosen as $\Delta = 6$ and $R_0 = 30a_0$ which are also the values used in the present study. In Equation (4.2) w , J and s are the corresponding variational parameters. Figures 4.2(a)-(c) show the results of the proposed manipulations for the singlet potential and Figure 4.2(d) also sketches the mass variation.

As it was found before (Section 3.3.3), using exact treatment of MFRs, the $a_{sc}(B)$ dependence exhibits two resonances (one broad and one narrow) for some magnetic field values (Figure 3.5). In a simplified MFR picture, the resonances occur because the position of a closed-channel bound state approaches the total energy available in a system. The crossing of the resonance position indicates the possibility for the molecule creation or dissociation. Furthermore, in the multi-channel case the number of bound states is constant across the resonance and the number of closed-channel potentials is more than one. The single-channel description differs from this picture. A Hamiltonian variation in the single-channel approach leads to potential resonances. They can be found considering the change of the scattering length as a function of the variation parameter $a_{sc}(v)$. For example, the variation of the inner-wall of the BO potential as the s parameter ranges from -0.4 to 0.1 results in three potential resonances, as is shown in Figure 4.3(a). They occur because the potential becomes less attractive, and less capable of supporting the same number of bound states, or more attractive to support extra bound states. The solution of the Schrödinger equation with a

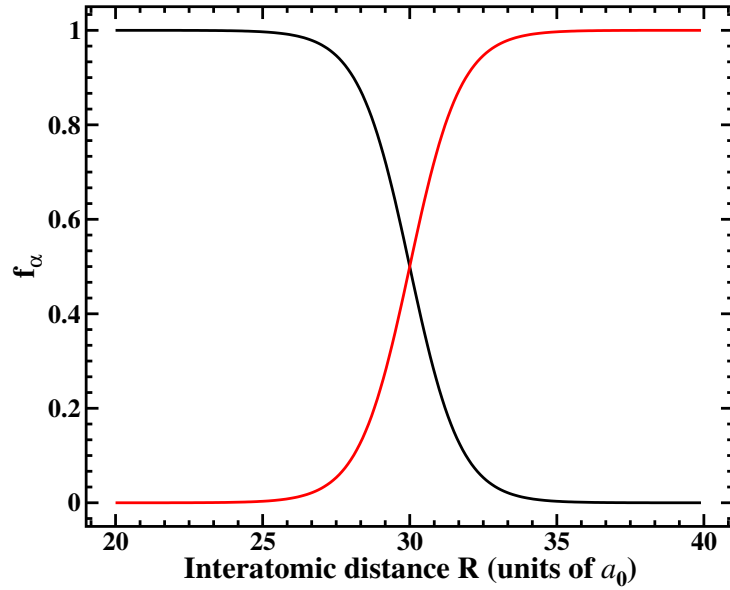


Figure 4.1: The tuning functions f_d (black) and f_u (red) in Equation (4.6) for $\Delta = 6$ and $R_0 = 30a_0$.

modified BO potential may result in a different number of vibrational bound states compared to the non-modified potential. The crossing of resonances in Figure 4.3(a) as s increases indicates an increase of this number. Only in the range $s \in [-0.338, -0.331]$ the number is the same as for the original non-perturbed potential.

Natural questions arise, if the branches for the resonant curves of single-channel approach, like the ones obtained by the s -variation (Figure 4.3(a)), are compared. Namely, it is important to determine which branch of the resonant curve must be chosen for the proper comparison with the multi-channel solutions, and whether the number of bound states should be a conserved quantity in order to properly represent a MFR. To answer these questions, the following analysis considers several branches of the potential resonances for all kinds of the variations introduced above.

4.2 Comparison based on wave functions

4.2.1 Short range

The single-channel and multi-channel approaches may be compared by investigating the wave functions. The multi-channel basis AB or MB will be taken for the comparison depending on the considered distance. It can be

4.2 Comparison based on wave functions

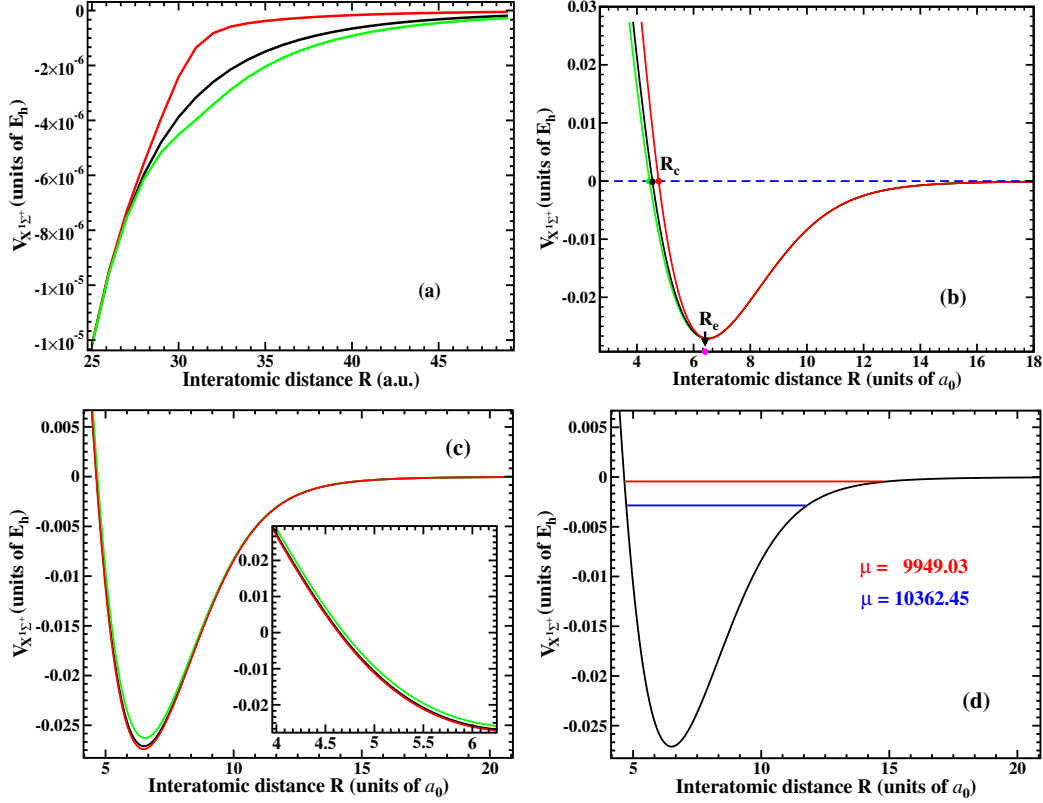


Figure 4.2: The potentials of the ${}^6\text{Li}-{}^{87}\text{Rb}$ used in the single-channel approach. (a) $V_{X^1\Sigma^+}^w$ with the original coefficient $C_6 = 2545.0 a_0$ (black) and modified $C_6 = 692.9 a_0$ (red), $C_6 = 3758.9 a_0$ (green). (b) $V_{X^1\Sigma^+}^s$ with resulting $a_{\text{sc}} = -\infty$ (green), $a_{\text{sc}} = 0$ (black), $a_{\text{sc}} = +\infty$ (red). (c) $V_{X^1\Sigma^+}^J$ with the variational parameter $J=0$ (black), $J=-0.0148786$ (green), $J=0.0051633$ (red). (The inset shows the inner-wall on an enlarged scale.) (d) Sketch of the mass variation. If the mass is increased then the bound level is raised and vice versa.

assumed that the shift from one basis to another may be done at distance R_{sh} , where the exchange interaction is equal to the hyperfine interaction.

The wave function is changed more, if the scattering length has a larger value. Therefore at resonance, the deviations between exact and approximate solutions are expected to be most pronounced. The value $a_{\text{sc}} = -65450 a_0$ is arbitrarily chosen for the present study. This large value of the scattering length is a good representation for the case $a_{\text{sc}} = -\infty$.

The ${}^6\text{Li}-{}^{87}\text{Rb}$ possesses two singlet states in the case of $M_F = \frac{3}{2}$, as is summarized in Table 3.1. At resonance ($a_{\text{sc}} = -65450 a_0$), the singlet state $|S_1\rangle$ has a sizable amplitude and the singlet $|S_2\rangle$ almost vanishes, as

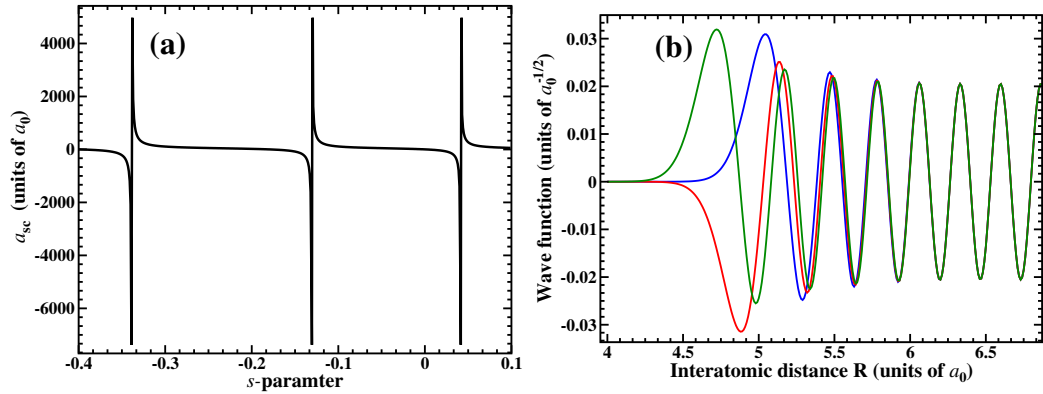


Figure 4.3: (a) Change of the scattering length with inner-wall variation for the $X^1\Sigma^+$ state of the ${}^6\text{Li}-{}^{87}\text{Rb}$. (b) The single-channel functions φ^s for $a_{\text{sc}} = -65450 a_0$ and three different s parameters. $s = -0.338646$ (blue), $s = -0.130566$ (red), $s = 0.041383$ (green).

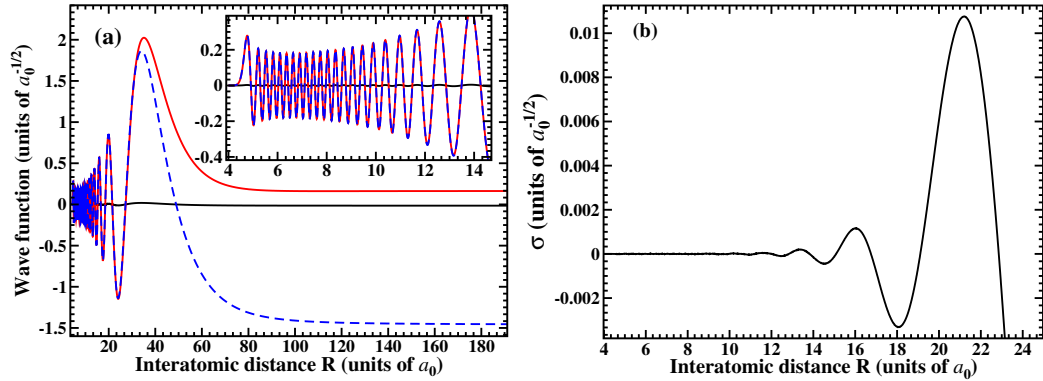


Figure 4.4: Comparison of two multi-channel singlet states $|S_1\rangle$ and $|S_2\rangle$ at resonance when $a_{\text{sc}} = 65450 a_0$. (a) ϕ_{S_1} (red solid), ϕ_{S_2} (black solid), ϕ_{S_2} multiplied to the constant of Equation (4.9) (blue dashes). (The inset shows the small R range on an enlarged scale.) (b) deviation σ as defined in Equation (4.8).

is evident from Figure 3.7(d). Consequently, for this particular case the contribution of the $|S_2\rangle$ state to the collision process is small. This is not necessarily the case for other scattering situations. However, it appears that the states $|S_1\rangle$ and $|S_2\rangle$ at short range differ only by a constant coefficient and do not undergo any structural changes under any collisional conditions. A multiplication of the ϕ_{S_2} function by a proper constant matches it with ϕ_{S_1} function at short interatomic distances. The result of such a procedure is shown in Figure 4.4(a). As is evident from the figure, the difference between the functions is noticeable only beyond $\approx 30 a_0$. In order to quantify this

difference the deviation

$$\sigma(R) = \phi_{S_1}(R) - C^{S_{1,2}}(R_a)\phi_{S_2}(R) \quad (4.8)$$

$$\text{with } C^{S_{1,2}} = \frac{\phi_{S_1}(R_a)}{\phi_{S_2}(R_a)} \quad (4.9)$$

is introduced, where $C^{S_{1,2}}$ is the matching constant and R_a can be any point before $30 a_0$ except those points where the functions are zero. The exclusion of zeroes helps to avoid numerical errors. Figure 4.4(b) shows the function $\sigma(R)$ of Equation (4.8). As is evident from this figure, the mismatch between the two singlets increases beyond R_{sh} . Before R_{sh} the difference reduces and vanishes. If the σ function is divided by the ϕ_{S_1} wave function at the same points excluding zeroes, then it can be seen that the maximum relative disagreement between the functions amounts to around 0.1% before the R_{sh} point. However, this simple analysis is not given here due to space reasons. Eventually, the two singlets do not differ structurally at distances up to R_{sh} to within a good degree of accuracy. Hence, the use of one of the singlet functions is sufficient for a comparison with the single-channel solutions.

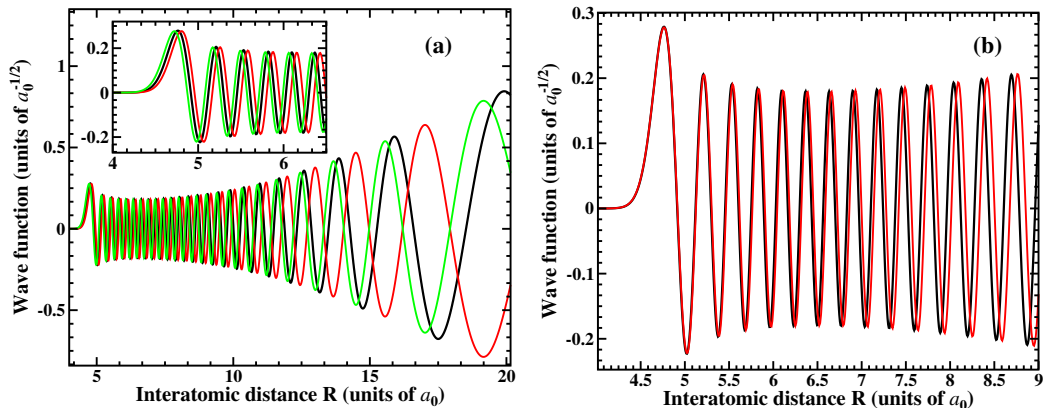


Figure 4.5: Comparison of the single-channel functions with multi-channel singlet state $|S_1\rangle$ at resonance when $a_{\text{sc}} = 65450 a_0$. (a) ϕ_{S_1} (black), $\tilde{\varphi}^J$ (red), $\tilde{\varphi}^s$ (green). (The inset shows the small R range on an enlarged scale.) (b) ϕ_{S_1} (black), $\tilde{\varphi}^\mu$ (red).

A single-channel wave function and a multi-channel one have different amplitudes. In order to compare them, the matching procedure that was applied for the singlets in Equations (4.8)-(4.9) is adopted here. Figure 4.5 shows different $\tilde{\varphi}^v = C^v \cdot \varphi^v$ solutions together with the ϕ_{S_1} function for the same scattering length $a_{\text{sc}} = -65450 a_0$. C^v is the matching constant for v

variation defined as

$$\sigma^v(R) = \phi_{S_1}(R) - C^v(R_a)\varphi^v(R) \quad (4.10)$$

$$\text{with } C^v = \frac{\phi_{S_1}(R_a)}{\varphi^v(R_a)} \quad (4.11)$$

As is evident from Figure 4.5(a), the $\tilde{\varphi}^s$ and $\tilde{\varphi}^J$ functions deviate from ϕ_{S_1} . In both cases the deviations increase with interatomic distance. While the inner-wall modification results in a shift of the nodal structures towards smaller values of R , the modification of the exchange potential shifts it towards larger R . The mass variation results in a slightly different behavior. A noticeable shift of $\tilde{\varphi}^\mu$ relative to ϕ_{S_1} is observed at around $7a_0$. It increases with interatomic distance, as is evident from Figure 4.5(b). The behavior of the single-channel functions can be understood, if the classical turning points of the least bound state are considered. The inner wall of the BO potential is very steep and the outer part of the potential is sloping. Therefore, a slight mass modification shifts the classical inner turning point R_{inn} negligibly while the outer turning point R_{out} is shifted non-negligibly. A similar behavior is observed, if the $V_{X^1\Sigma^+}^s$ and $V_{X^1\Sigma^+}^J$ potentials are used. Since for the $V_{X^1\Sigma^+}^s$ potential the inner wall is directly modified, the shift of $\tilde{\varphi}^s$ occurs already when the oscillations start, as is evident from Figure 4.5(a). Finally, since $V_{X^1\Sigma^+}^J$ is modified relative to the non-perturbed potential in a wide range of the interatomic distance, the shift of the $\tilde{\varphi}^J$ function is observed throughout the whole range of R .

In contrast to these methods, the manipulation of the van der Waals part of the BO potential yields an almost perfect agreement between single-channel and multi-channel wave functions at short range. Figure 4.6 presents the comparison of the functions $\tilde{\varphi}^w$ and ϕ_{S_1} . In order to get $a_{\text{sc}} = -65450 a_0$ the C_6 coefficients had to be significantly changed from the original value $2543.0 a_0$ resulting in $C_6 = 692.9 a_0$ and $C_6 = 3758.9 a_0$. These values correspond to the points in different branches of the $a_{\text{sc}}(w)$ curve. Nevertheless, the agreement of the functions $\tilde{\varphi}^w$ and ϕ_{S_1} is perfect, as is evident from Figure 4.6(a). The deviation σ^w is shown in Figure 4.6(b). The analysis of σ^w relative to the function ϕ_{S_1} shows that the w variation results in less than $\sim 1\%$ deviation from the exact solution at a distance around R_{sh} . Before R_{sh} this deviation reduces and vanishes.

To conclude the comparison at short range, it was shown that the single-channel approach based on the variation of the inner wall, the exchange part and the mass results in a qualitative disagreement with the real multi-channel solution in the MB at short range (Figure 4.5). In contrast, the variation of the long-range van der Waals part of the BO potential results in

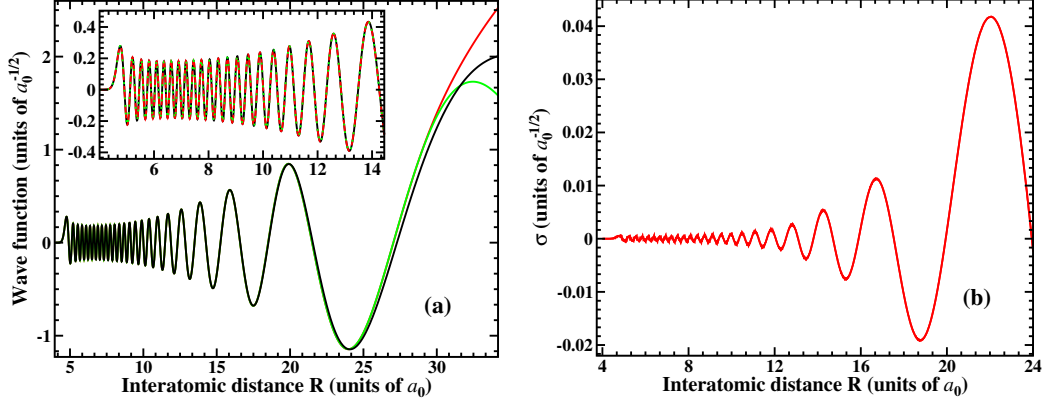


Figure 4.6: Comparison of the single-channel functions with the multi-channel singlet state $|S_1\rangle$ at resonance when $a_{sc} = 65450 a_0$. (a) ϕ_{S_1} (black), $\tilde{\varphi}^w$ with $C_6 = 692.9 a_0$ (red), $\tilde{\varphi}^w$ with $C_6 = 3758.9 a_0$ (green). (The inset shows the small R range on an enlarged scale.) (b) deviation σ^w defined in Equation (4.10).

a qualitative agreement with the real multi-channel solution in MB for the same short distances (Figure 4.5). However, a correction constant must be incorporated in order to match the amplitudes quantitatively.

4.2.2 Long range

In order to check the validity of the variational methods at larger distances another multi-channel basis is adopted. If the two particles are far apart, the MB becomes inappropriate. Instead, the AB must be used (Section 3.3.3). At a long-range distance, the only non-zero channel is the open one ψ_{open} . It is thus the one that must be compared with the $\tilde{\varphi}^v$ solutions. Since the amplitudes of functions ψ_{open} and $\tilde{\varphi}^v$ at long-range are the same, a matching procedure is not needed for this comparison. Figure 4.7 shows the comparison of $\tilde{\varphi}^w$ with ψ_{open} . The w variation, appropriate at short distance, breaks down at long range, as can be concluded from the Figure 4.7. The nodal structure of the single-channel functions does not match that of the exact solution. For $C_6 = 692.9 a_0$ the modification of the BO potential is so strong that the last node disappears. Nevertheless, as the overall sign is undefined, one should plot only the proper (flipped) wave function. If the function for $C_6 = 692.9 a_0$ is flipped then it merges with ψ_{open} only at a distance around $100 a_0$, as is demonstrated in Figure 4.7. This behavior makes the w-variation method useless at long-range distance. In contrast to w variation the use of $V_{X^1\Sigma^+}^s$, $V_{X^1\Sigma^+}^\mu$, and $V_{X^1\Sigma^+}^j$ potentials leads to a perfect agreement with the multi-channel function at distances beyond R_{sh} . Figure 4.8 demonstrates the

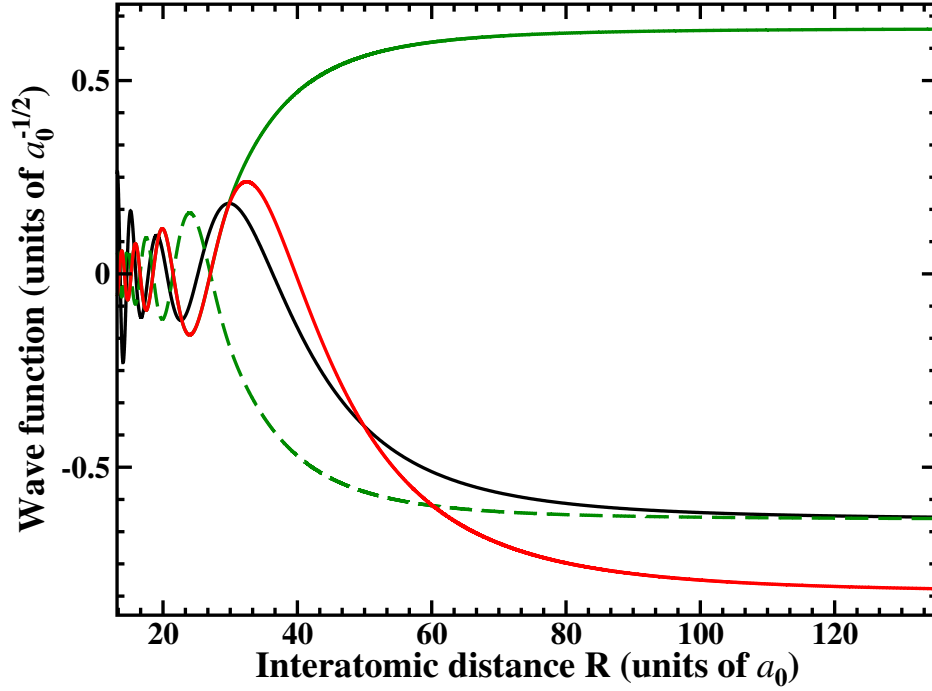


Figure 4.7: Comparison of the single-channel functions with the open incoming channel at resonance for $a_{sc} = 65450 a_0$. ψ_{open} (black solid), $\tilde{\varphi}^w$ with $C_6 = 3758.9 a_0$ (red solid), $\tilde{\varphi}^w$ with $C_6 = 692.9 a_0$ (green solid), $-\tilde{\varphi}^w$ with $C_6 = 692.9 a_0$ (green dashes).

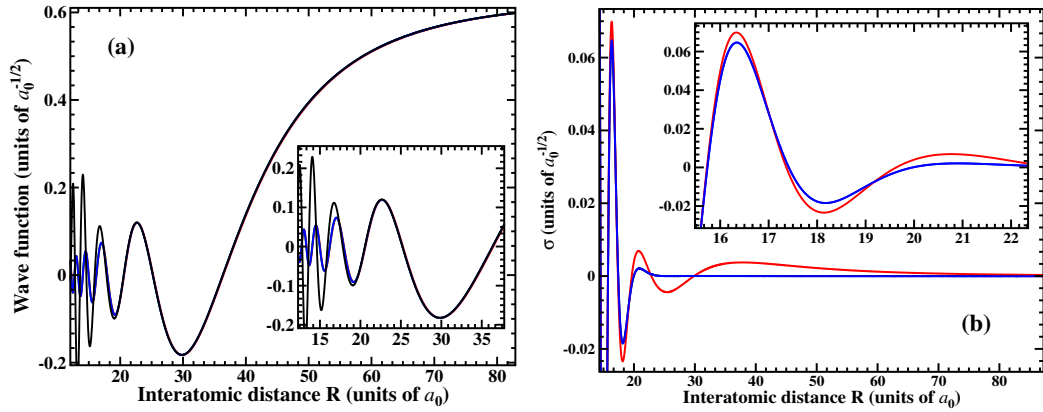


Figure 4.8: Comparison of the single-channel functions with open incoming channel at resonance when $a_{sc} = 65450 a_0$. (a) ψ_{open} (black), φ^J (green), φ^s (blue), φ^m (red). (b) σ^v values in Equation (4.10) σ^m (red), σ^J (blue), σ^s (black). The insets show the intermediate R range on an enlarged scale.

result of the comparison. As before the error at around R_{sh} is $\sim 1\%$. Beyond

R_{sh} the difference reduces and vanishes. It is worth noting, that the mass variation gives the largest deviation in comparison to the two other methods. The function matches the exact solution at distances beyond $70 a_0$.

For the case of s , m and J variation any branches of the resonant curve $a_{\text{sc}}(v)$ (e. g., $a_{\text{sc}}(s)$ in Figure 4.3) can be chosen to get the correct long-range behavior. Figure 4.3(b) presents the φ^s functions for three different values of s but the same $a_{\text{sc}} = -65450 a_0$. At smaller distances the oscillations are different, but after around $6 a_0$ the functions merge and stay the same beyond this point.

4.3 Conclusion

The choice of a suitable v variation depends upon which interatomic distance is under consideration. For R smaller than R_{sh} , the variational schemes obtained by manipulating the mass or the short-range part of the BO potential lead to wave functions that disagree in the nodal structure with the appropriate exact solution. None of the single-channel wave functions give correct amplitudes. In order to find the correction factor at short distances, the multi-channel solution must be available. On the other hand, the variation of the long-range part of the BO potential, via variation of a van der Waals coefficient, results in quantitative agreement of the single-channel solution with the full solution at short range. At long-range, the m , J , s -variational schemes give correct behaviors of the wave functions, while the w variation fails. For these distances, the multiplication by a correction constant is not needed. In the intermediate range (around $R \sim 20 a_0 = R_{\text{sh}}$ where $\Delta E^{\text{hf}} \approx 10^{-6} E_h$ for ${}^6\text{Li}$ - ${}^{87}\text{Rb}$), exchange and hyperfine interactions have comparable magnitude. None of the single-channel schemes gives perfect matching with the multi-channel solutions, neither in MB nor in AB. Therefore, the short range and the asymptotic part of a single-channel wave function do not result in quantitative and qualitative agreement at R_{sh} with either of the two multi-channel bases. However deviations are of the order of 1% and may be negligible for most practical purposes.

Chapter 5

Photoassociation

Atomic condensates exhibit many qualitatively new features. Besides their relevance to fundamental quantum-statistical questions, a further interesting aspect is that the atoms can bind together to form ultracold, and even Bose-Einstein condensed molecules [15, 16, 34]. One of the schemes for achieving a molecular ultracold gas is based on magnetic Feshbach resonances. An alternative scheme is photoassociation, where two ultracold or Bose condensed atoms absorb a photon and form a bound molecule. The advantage of PA compared to MFR is its believed wider range of applicability, since there is no need for the occurrence of suitable resonances and thus no requirement for special magnetic properties of the atoms involved. However, the yield of the PA process is generally small, but it may increase, if the interaction between atoms becomes strong. The MFR may be also adopted for manipulation of the interatomic interaction over a wide range of values. This advantage of MFR in combination with PA may be used for the efficient creation of ultracold molecules, even in the lowest possible ground state.

The atom-molecule conversion process differs, depending on whether it occurs in free space or in a trapping potential. In fact, it was pointed out that the atom-molecule conversion process is more efficient, if PA is performed under tight trapping conditions as they are, e. g., accessible in optical lattices [78]. In this chapter, a systematic investigation is made of the influence of a tight isotropic harmonic trap on the PA process of two alkali atoms forming a homonuclear excited molecule. Realistic atom-atom interaction potentials are adopted. This also allows checking the range of applicability of the single-channel δ -function (pseudopotential) approximation (defined in Section 2.3) for the description of the PA process. The validity regime of the pseudopotential approximation has been discussed with respect to the energy levels for trapped atoms in [83]. Whether this simplified model for the atomic interaction is appropriate for the description of photoassociation

in a harmonic trap is, however, not immediately evident.

Photoassociation in tight traps has been studied theoretically before [82]. The energy-independent pseudopotential approximation was adopted, and only photoassociation into long-range states discussed. Since the present work uses realistic atomic interaction potentials, transitions to all final vibrational states can be considered. This permits the identification of two different regimes with respect to the influence of a tight trap on the photoassociation rate, as well as (approximate) rules where a transition from one regime to the other is to be expected.

In this chapter, this systematic analysis is done for a generic ${}^6\text{Li}_2$ dimer. The generality of the conclusions drawn about ${}^6\text{Li}_2$ are checked considering alternative dimers in diverse electronic states. The possible limitations of the adopted harmonic trapping potential for realistic traps that will not lead to pure harmonic confinement, as well as limitations due to the ignoring of higher order structures of the excited states, are discussed.

5.1 The system

Photoassociation of two identical atoms confined in an isotropic harmonic trap and interacting through a two-body BO potential $V_{\text{int}}(R)$ is considered. The spherical symmetry and harmonicity of the trap allows to separate the center-of-mass and the radial internal motions [95]. The eigenfunctions of the center-of-mass motion are the harmonic-oscillator states. Thus the problem reduces to solving the Schrödinger equation for the radial internal motion

$$\left[\frac{1}{2\mu} \frac{d^2}{dR^2} - \frac{J(J+1)}{2\mu R^2} - V_{\text{int}}(R) - \frac{1}{2}\mu\omega^2 R^2 + E \right] \Psi(R) = 0. \quad (5.1)$$

In Equation (5.1) J denotes the rotational quantum number, ω is the harmonic trap frequency, and μ is the reduced mass that is equal to $m/2$ in the present case of particles with identical mass m .

While Equation (5.1) yields in the trap-free case ($\omega = 0$) both bound (vibrational) and continuum (dissociative) states, the harmonic-trap potential changes the energy spectrum to a purely discrete one, as is sketched in Figure 5.1. Considering the concrete example of two ${}^6\text{Li}$ atoms where the $a^3\Sigma_u^+$ state supports the 10 vibrational bound states $v' = 0$ to 9, $v' = 10$ ($J' = 0$) denotes the first state that results from the trap-induced continuum discretization. This (first trap-induced) state describes the initial state of two spin-polarized ${}^6\text{Li}$ atoms interacting via the $a^3\Sigma_u^+$ potential curve, if a sufficiently cold atomic gas in an (adiabatically turned-on) harmonic trap is considered. In the present work photoassociation (by means of a suitably

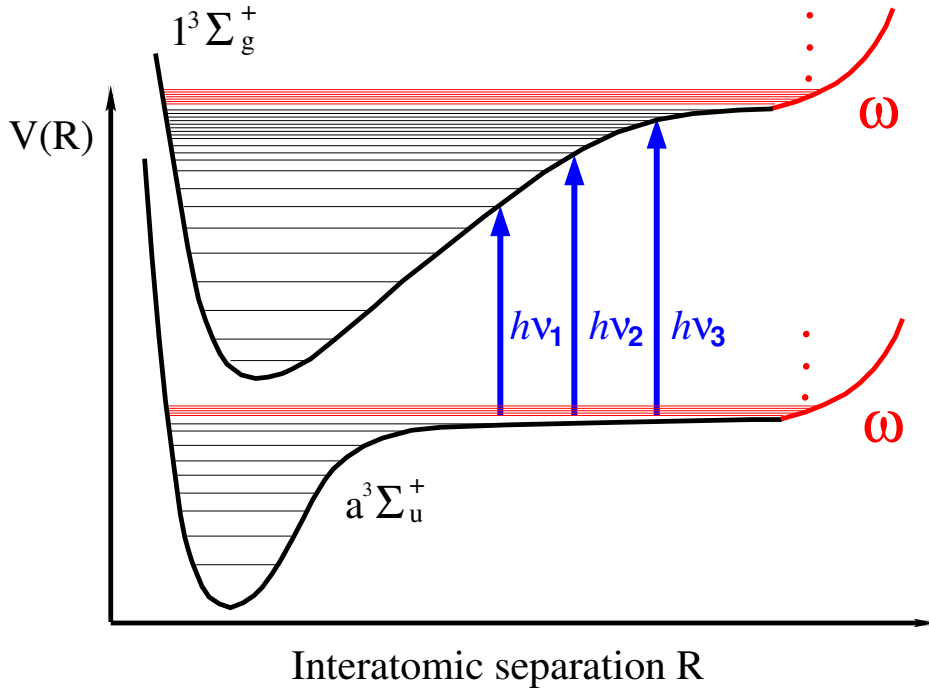


Figure 5.1: Sketch of the photoassociation process for ${}^6\text{Li}_2$ in the presence of a trap (not to scale). With the aid of a laser photoassociation is induced from the first trap-induced bound state ($v' = 10$) of the $a^3\Sigma_u^+$ state into some vibrational level v of the $1^3\Sigma_g^+$ state. Different laser frequencies ν_i couple the same initial state to different final states.

tuned laser) from this initial state to one of the vibrational states v of the $1^3\Sigma_g^+$ potential is investigated as a function of the trap frequency ω .

The photoassociation processes most relevant to experiments on ultra-cold alkali atoms correspond to transitions from two free ground-state atoms (interacting via the ground triplet or singlet potential) to the different vibrational levels of the first excited triplet or singlet state [111–113]. Due to hyperfine interaction, two alkali atoms can also interact via a coherent admixture of singlet and triplet states. This work starts by considering the photoassociative transition between the two triplet states $a^3\Sigma_u^+$ and $1^3\Sigma_g^+$ for ${}^6\text{Li}$. A corresponding experiment is, e. g., reported in [77]. The generality of the conclusions drawn from this specific example are then tested by considering also other atoms (${}^7\text{Li}$ and ${}^{39}\text{K}$) or modifying artificially the interaction strength, as is discussed in Section 5.3.1.

For the short-range part of the $a^3\Sigma_u^+$ molecular potential of Li_2 the data in [114] are used, including the van der Waals coefficients cited therein. In the case of the $1^3\Sigma_g^+$ state data for interatomic distances between $R = 4.66 a_0$

and $R = 7.84 a_0$ are taken from [115] and are extended with *ab initio* values from [116] for distances between $R = 3.25 a_0$ and $R = 4.50 a_0$ and between $R = 8.0 a_0$ and $R = 30.0 a_0$. The van der Waals coefficients from [117] are used. For a Σ to Σ molecular dipole transition the selection rule is $J = J' \pm 1$. Assuming ultracold atomic gases the atoms interact initially in the $J' = 0$ state of the $a^3\Sigma_u^+$ potential. The dipole selection rule leads then to transitions to the $J = 1$ states of $1^3\Sigma_g^+$. With the given potential-curve parameters a solution of Equation (5.1) in the absence of a trap ($\omega = 0$) yields for the fermionic ${}^6\text{Li}$ atoms 10 and 100 vibrational bound states for the $a^3\Sigma_u^+$ ($J' = 0$) and the $1^3\Sigma_g^+$ ($J = 1$) states, respectively. In the case of the bosonic ${}^7\text{Li}$ atoms there are 11 and 108 vibrational bound states for the $a^3\Sigma_u^+$ ($J' = 0$) and the $1^3\Sigma_g^+$ ($J = 1$) states, respectively.

The electronic dipole moment $D(R)$ for the transition $a^3\Sigma_u^+ \rightarrow 1^3\Sigma_g^+$ of Li was calculated with a configuration-interaction (CI) method for the two valence electrons using the code described in [118]. The core electrons were described with the aid of the Klapish model potential with the parameters given in [119] and polarization was considered as discussed in [120]. The resulting $D(R)$ (and its value in the separated atom limit) is in good agreement with literature data [116, 117, 121, 122].

In the limit of zero collision energy the interaction between two atoms can be characterized by their s -wave scattering length a_{sc} (Chapter 2). Its sign determines the type of interaction (repulsive or attractive) and its absolute value the interaction strength. For a given potential curve the s -wave ($J' = 0$) scattering length can be determined using the fact that at large distances the scattering wave function describing the relative motion (for $\omega = 0$ and very small collision energies) reaches its known asymptotic behavior [123]. Using this feature and the adopted potential curves the scattering length values $a_{\text{sc}} = -2030 a_0$ and $a_{\text{sc}} = -30 a_0$ are obtained for ${}^6\text{Li}$ and ${}^7\text{Li}$, respectively. These values agree well with the experimental ones: $a_{\text{sc}} = (-2160 \pm 250) a_0$ (${}^6\text{Li}$) and $a_{\text{sc}} = (-27.6 \pm 0.5) a_0$ (${}^7\text{Li}$) [124].

The interaction of two ultracold ${}^6\text{Li}$ atoms is strongly, the one of ${}^7\text{Li}$ weakly attractive, as is reflected by the large and small but negative scattering lengths. In the case of two identical fermionic ${}^6\text{Li}$ atoms the asymmetry requirement of the total wave function excludes s -wave scattering. Thus the present results are more applicable for two ${}^6\text{Li}$ atoms in different hyperfine states (where the admixture of a singlet potential would, however, usually modify the scattering length), but are actually meant as a realistic example for a very large negative scattering length, i. e., strong attraction. In order to further check the generality of the results also the formation of ${}^{39}\text{K}_2$ is investigated as an example for a small repulsive interaction. In this case photoassociation starting from two potassium atoms interacting via the *sin-*

glet $X^1\Sigma_g^+$ ground state and transitions into the $A^1\Sigma_u^+$ state are considered. This process is not only experimentally relevant [125], but is at the same time an even further check of the generality of the conclusions obtained from the investigation of the transitions between *triplet* states in Li_2 .

The data for constructing the relevant potential curves for $^{39}\text{K}_2$ are taken from [126, 127]. The resulting potential curve for the $X^1\Sigma_g^+$ state yields a scattering length $a_{\text{sc}} \approx +90 a_0$. This is in reasonable agreement with the experimental value given in [128] where a_{sc} is found to be lying between $+90 a_0$ and $+230 a_0$.

Instead of selecting additional atomic pairs that could represent examples for other values of the scattering length, the sensitivity of the *s*-wave interaction on the position of the least bound state is used to generate *artificially* a variable interaction strength. The scattering length is thus modified by a variation of the particle mass, as was discussed in Chapter 4 for a heteronuclear system. The strong mass dependence of the scattering length for lithium is already evident from its change from $-2030 a_0$ to $-30 a_0$ for the isotopes ^6Li and ^7Li , respectively.

5.2 Photoassociation in a harmonic isotropic trap

5.2.1 Photoassociation in a trap

In order to compute the photoassociation spectrum the vibrational wave functions $\Psi(R)/R$ are determined for the initial and final molecular states from Equation (5.1) with the corresponding BO interaction potentials $V_{\text{int}}(R)$. The Equation (5.1) is solved numerically using an expansion in *B* splines. For the investigation of the influence of the trap on the photoassociation rate Equation (5.1) is solved for $\omega \neq 0$.

The strength of the photoassociation transition to final state *v* is given by the rate [129]

$$\Gamma_v(\omega) = 4\pi^2 \mathcal{I} I^v(\omega) \quad (5.2)$$

where \mathcal{I} is the laser intensity and

$$I^v(\omega) = \left| \int_0^\infty \Psi^v(R; \omega) D(R) \Psi^{10'}(R; \omega) dR \right|^2. \quad (5.3)$$

In view of the already discussed relevant dipole-selection rule the final state possesses $J = 1$ and in the following $J' = 0$ and $J = 1$ is tacitly assumed. In

Equation (5.3) $\Psi^v(R)/R$ and $\Psi^{10'}(R)/R$ are the vibrational wave functions of the final and initial states, respectively. Since the radial pair density is proportional to $|\Psi|^2$, it is convenient to discuss Ψ instead of the true vibrational wave function $\Psi(R)/R$. This will be done in the following where Ψ is for simplicity called vibrational wave function. Finally, $D(R)$ is the (R -dependent) electronic transition dipole matrix element between the $a^3\Sigma_u^+$ and the $1^3\Sigma_g^+$ state of Li_2 introduced in Section 5.1. $D(R)$ is practically constant for $R > 25 a_0$. Equation (5.3) is only valid within the dipole approximation. The latter is supposed to be applicable, if the photon wavelength is much larger than the extension of the atomic or molecular system. The shortest photoassociation laser wavelength corresponds to the transition to the highest-lying vibrational state and is thus approximately the one of the atomic ($2^2\text{S} \rightarrow 2^2\text{P}$ transition), $\lambda = 12680 a_0$. Although the spatial extent of some of the final vibrational states (and of course the initial state in the case of shallow traps) has a similar or even larger extent, beyond dipole approximation effects are neglected in this work.

The key quantity describing the photoassociation rate to different vibrational states v or for variable trap frequency ω is $I^v(\omega)$ on whose calculation and discussion this work concentrates. It is important to note that also in the case of more elaborate laser-assisted association schemes like stimulated Raman processes that involve (virtual) transitions to the v states the transition rate is proportional to $I^v(\omega)$.

According to Equation (5.3) the photoassociation rate depends for transitions between long-range states on the Franck-Condon factors between the initial and final nuclear wave functions, if $D(R)$ is practically constant for large R . In the case of alkali atoms the interaction potentials of the electronic states can be very long ranged and can support numerous rovibrational bound states. Figure 5.2 shows, e. g., the classical outer turning points R_{out} of the 100 ($J = 0$) vibrational bound states of ${}^6\text{Li}_2$ supported by the final-state electronic potential curve $1^3\Sigma_g^+$. The orthogonality of the states is achieved by the occurrence of v' nodes. As v' increases the wavefunctions consist of a highly oscillatory short range part with small overall amplitude that covers the range of the $v' - 1$ wavefunction and a large outermost lobe. The $1^3\Sigma_g^+$ state is very long ranged, since its leading van der Waals term is $-C_3/R^3$. The initial electronic state $a^3\Sigma_u^+$ with leading $-C_6/R^6$ van der Waals term is shorter ranged. Figure 5.3 shows the initial vibrational state for ${}^6\text{Li}$ as a function of the trap frequency. This first trap-induced bound state possesses v nodes (here $v = 10$) that are located in the R range of the last trap-free bound state ($v = 9$). The overall amplitude in this about $25 a_0$ long interval is very small and most of the wavefunction is distributed over the harmonic trap.

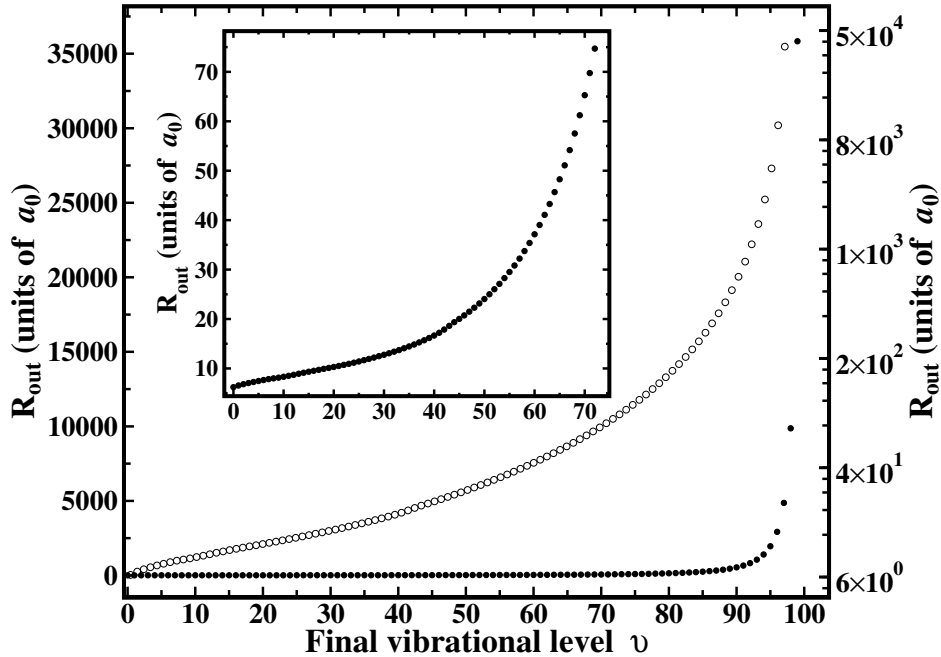


Figure 5.2: The classical outer turning points of the vibrational levels of the $1^3\Sigma_g^+$ state of ${}^6\text{Li}_2$ are shown on a linear (solid circles, left scale and insert) and on a logarithmic scale (empty circles, right scale).

The squared transition dipole moments $I^v(\omega)$ are shown for ${}^6\text{Li}$ in Figure 5.4(a) for three different trap frequencies ω . As mentioned before, the final vibrational levels with $v > 99$ are trap-induced bound states and exist only due to the continuum discretization in the presence of a trap. If the trap would be turned-off (adiabatically) after photoassociation to such a level, the trap induced dimer would immediately dissociate (without the need for any (radiative or non-radiative) coupling to some dissociative state).

For a fixed trap frequency the photoassociation rate generally increases as a function of the final vibrational level v , but for small v an oscillatory behavior is visible. These oscillations are a consequence of the nodal structure of the initial-state wave functions describing the atom pair. The 10 nodes (for the shown example of ${}^6\text{Li}$) of the initial-state wave function lead to exactly 10 dips in the photoassociation spectrum. Their exact position depends on the interference with the nodal structure of the final-state wave functions. The oscillatory structure of $I^v(\omega)$ ends at about $v = 55$ and beyond that point the rate increases by orders of magnitude, before a sharp decrease is observed close to the highest lying vibrational bound state ($v = 99$). The absence of oscillatory behavior is a clear signature that for those transitions

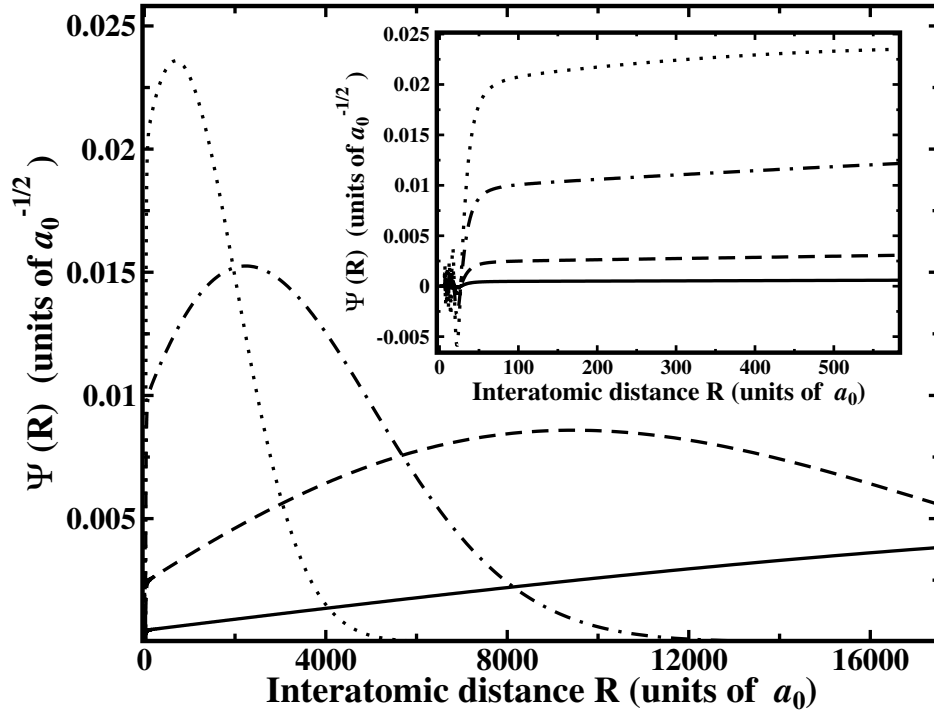


Figure 5.3: Wave functions of the initial $a^3\Sigma_u^+$ state of ${}^6\text{Li}_2$ for trap frequencies $\omega = 2\pi \times 1\text{kHz}$ (solid), $\omega = 2\pi \times 10\text{kHz}$ (dashes), $\omega = 2\pi \times 100\text{kHz}$ (chain), and $\omega = 2\pi \times 500\text{kHz}$ (dots). (The insert shows the small R range on an enlarged scale.)

(in the present example for transitions into states with $\nu > 55$) the Franck-Condon factors are effectively determined by the overlap of the outermost lobe of the initial state with the one of the final state.

The comparison of $I^\nu(\omega)$ for the different trap frequencies shown in Figure 5.4(a) indicates a systematic trend. The transition probabilities to most of the vibrational bound states increases with increasing trap frequency. This is in accordance with simple confinement arguments, since a tighter trap confines the atoms in the initial state to a smaller spatial region. Due to the special properties of harmonic traps, this confinement translates directly into a corresponding confinement of the pair density. The probability for atom pairs to have the correct separation for the photoassociative transition is thus expected to increase for tighter confinements, since a larger Franck-Condon overlap of the now more compact initial state with the bound molecular final state is expected. However, for the vibrational final states close to and above the (trap-free) dissociation threshold a completely different behavior is found. In this case the photoassociation rate decreases with increasing trap frequency, as can be seen especially from the insert of Figure 5.4(a). In

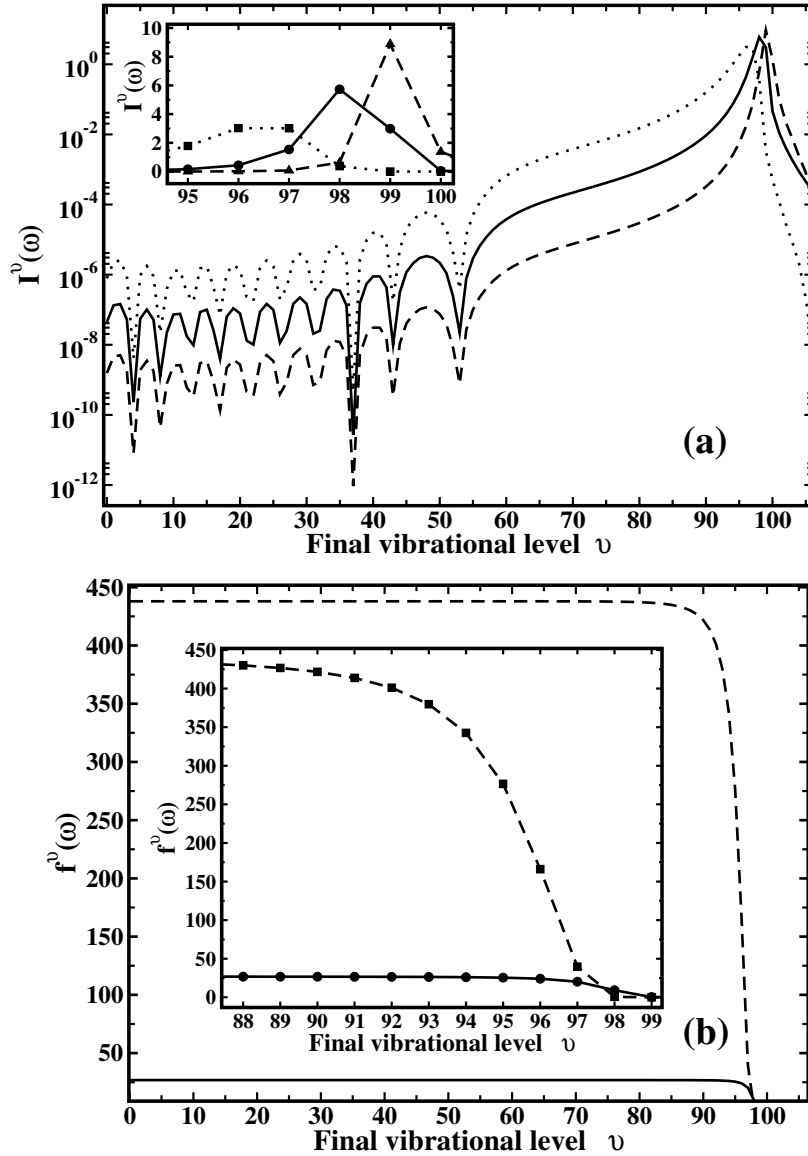


Figure 5.4: (a) The squared dipole transition moments $I^\nu(\omega)$ describing transitions from the trap-induced ($\nu' = 10$) initial $a^3\Sigma_u^+$ state to the vibrational manifold (ν) of the $1^3\Sigma_g^+$ state of ${}^6\text{Li}_2$ are shown for the trap frequencies $\omega = 2\pi \times 1\text{kHz}$ (dashes), $\omega = 2\pi \times 10\text{kHz}$ (solid), and $\omega = 2\pi \times 100\text{kHz}$ (dots). The insert shows the transitions to $\nu = 95$ to 100 on an enlarged scale. For a better visibility (marked explicitly with different symbols in the insert) the discrete transitions are plotted as continuous lines. (b) The ratio $f^\nu(\omega)$ (defined in Equation (5.5)) is shown for $\omega = 2\pi \times 10\text{kHz}$ (solid) and $\omega = 2\pi \times 100\text{kHz}$ (dashes) as a function of the final vibrational level ν . (As in (a) the discrete points are connected by lines to guide the eye.) The insert shows the transitions to $\nu = 88$ to 99 on a magnified scale.

fact, a sharp cut-off of the transition rate is observed. The transitions to the states that possessed the largest photoassociation rate for small trap frequencies are almost completely suppressed for large trap frequencies. Clearly, the simple assumption “a tighter trap leads to a higher photoassociation rate due to an increased spatial confinement” is only partly true. The fact that this assumption cannot be valid for all final states can be substantiated by means of a general sum-rule that is derived and discussed in the following subsection.

5.2.2 Sum rule

Performing a summation (including for $\omega = 0$ an integration over the dissociative continuum) over all final vibrational states (using closure) yields

$$\tilde{I}(\omega) = \sum_{v=0}^{\infty} I^v(\omega) = \int_0^{\infty} \Psi^{10'}(R; \omega) D^2(R) \Psi^{10'}(R; \omega) dR. \quad (5.4)$$

While the electronic transition dipole moment $D(R)$ depends clearly on R for small internuclear separations, it reaches its asymptotic value (the sum of the electronic dipole transition moments of two separated atoms, D_{at}) at some R value that is much smaller than the typical spatial extend of the final vibrational states with the largest transition amplitudes. (In the example of Li_2 this asymptotic limit is reached at about $25 a_0$.) If the largest photoassociation amplitudes result from transitions to final states whose wave functions are mostly located outside this R range, the integral in Equation (5.4) is dominated by the R regime in which $D(R)$ is constant. In this case D^2 can be taken out of the integral and normalization of the initial wave function assures $\tilde{I}(\omega) \approx \tilde{I} = D_{\text{at}}^2$.

Consequently, for all trap frequencies that are too small to confine the atoms into a spatial volume that is comparable to the atomic volumes (leading to $D(R) \neq D_{\text{at}}$) and thus for all traps relevant to this work (and presently experimentally achievable) the total dipole transition moment \tilde{I} is to a good approximation independent of the trap frequency ω . Therefore, changing the trap frequency can only redistribute transition probabilities between different final vibrational states. Increasing the transition rate to one final state must be compensated by a decrease of the transition probability to one or more other vibrational states.

A conservative estimate of the minimum and maximum influence of a harmonic trap on the photoassociation rate is obtained from $\tilde{I}_{\text{min}} = D_{\text{min}}^2$ and $\tilde{I}_{\text{max}} = D_{\text{max}}^2$, respectively, where D_{min} (D_{max}) is the minimum (maximum) value of the molecular electronic transition dipole moment.

The sum-rule values obtained numerically for the trap frequencies shown in Figure 5.4(a) are $\tilde{I}(\omega = 2\pi \times 1 \text{ kHz}) = 11.127222$, $\tilde{I}(\omega = 2\pi \times 10 \text{ kHz}) = 11.12723$, and $\tilde{I}(\omega = 2\pi \times 100 \text{ kHz}) = 11.1273$. This may be compared to the value $\lim_{R \rightarrow \infty} |D(R)|^2 = D_{\text{at}}^2 = |D_{2\text{s}-2\text{s}} + D_{2\text{s}-2\text{p}}|^2 = |D_{2\text{s}-2\text{p}}|^2 = 11.1272213$ obtained from the calculation described in Section 5.1. Clearly, the sum-rule (5.4) can also be used as a test for the correctness of numerical calculations. The very small deviations from the predicted sum-rule value may, however, not only be a result of an inaccuracy of the present numerical approach, but also reflect the (small) R dependence of $D(R)$ that allows some ω dependence of the total photoassociation rate. This interpretation is supported by the fact that the numerically found deviations monotonously increase with increasing frequency ω . Larger values of ω lead to a spatially more confined $\Psi^{10'}(R; \omega)$ which in turn probes more of the R -dependent part of $D(R)$. Since $D(R)$ approaches $D(R = \infty) = D_{\text{at}}$ from above, a small increase of \tilde{I} is expected for increasing trap frequencies. As is evident from Figure 5.4 (a) (especially the insert), the sum-rule fulfillment is achieved by a drastic decrease of the photoassociation rate to the highest lying final states. This compensates the trap-induced increased rate to the lower lying states. Since the rate to the highest lying states is orders of magnitude larger than the one to the low-lying states, the reduced transition probability of a small number of states can easily compensate the substantial increase by orders of magnitude observed for the large number of low-lying states.

From Equation (5.4) it is clear that in those cases where most of the contribution to the sum rule stems from the R range where $D(R)$ is practically constant, there is also no influence of the initial-state wave function. Taking D out of the integral yields always the self-overlap of the initial-state wave function and thus unity. This is important, since it indicates that the sum-rule value is also (approximately) independent of the atom-atom interaction potential.

5.2.3 Enhancement and suppression factor f^v

In order to quantify the effect of a tight harmonic trap on the photoassociation rate and to get rid of its variation as a function of the final-state vibrational level v (that is due to the nodal structure and clearly visible in Figure 5.4(a) especially for smaller v) the ratio

$$f^v(\omega) = \frac{I^v(\omega)}{I^v(\omega_{\text{ref}})}. \quad (5.5)$$

may be introduced. It describes the relative enhancement ($f^v(\omega) > 1$) or suppression ($f^v(\omega) < 1$) of the photoassociation rate to a specific final state

v at a given trap frequency ω with respect to the reference frequency ω_{ref} . Although it may appear to be most natural to choose the trap-free case as reference ($\omega_{\text{ref}} = 0$), a finite value offers some advantages. First, a different normalization applies to $\omega = 0$ and $\omega \neq 0$, since in one case it is free-to-bound transitions, while it is bound-to-bound transitions otherwise. Second, from a numerical point of view it is more convenient to treat both cases the same way and to avoid the variation of the box boundary R_{max} that would otherwise be necessary for the trap-free case. Finally, it may be argued that a non-zero trap reference state is in fact more relevant to typical photoassociation experiments with ultracold alkali atoms, since most of them are anyhow performed in traps. In the present work $\omega_{\text{ref}} = 2\pi \times 1 \text{ kHz}$ was chosen. This value is sufficiently small to represent typical shallow traps in which the influence of the trap on photoassociation is supposedly (at least to a good approximation) negligible. On the other hand, it allows to calculate the transition dipole moments with reasonable numerical efforts and thus sufficient accuracy.

The ratio $f^v(\omega)$ is shown for two different trap frequencies ω in Figure 5.4(b). For most of the vibrational final states a simple constant regime is observed, i. e., the ratio $f^v(\omega)$ is independent of v for all except the highest lying states. This constant regime is followed by a relatively sharp cut-off beyond which the ratio $f^v(\omega)$ is very small. In the constant regime a 100 kHz trap leads to an enhancement by almost 3 orders of magnitude.

Comparing the results for different ω one notices that in the range of final states where a constant behavior (with respect to v) is observed, a tighter trap leads to an increased photoassociation rate, trap-induced enhanced photoassociation (EPA). Due to the cut-off this is, however, not true, if the last vibrational states are considered. Since the range of constant behavior shrinks with increasing trap frequency, there is an increasing range of vibrational states for which a tighter trap leads to a smaller photoassociation rate compared to a shallower trap. In this case trap-induced suppressed photoassociation (SPA) occurs. This effect is especially visible from the insert of Figure 5.4(a). The physical origin of the two different regimes (constant vs. cut-off) and their ω dependence is discussed separately in the following two subsections.

5.2.4 Constant regime

Since in the constant regime the ratio $f^v(\omega)$ is completely independent of the final state level v , its value (for a given ω) and constancy (as a function of v) must be a consequence of the influence of the trap on the initial state. The initial-state wave function for a ${}^6\text{Li}$ atom pair was shown for three different

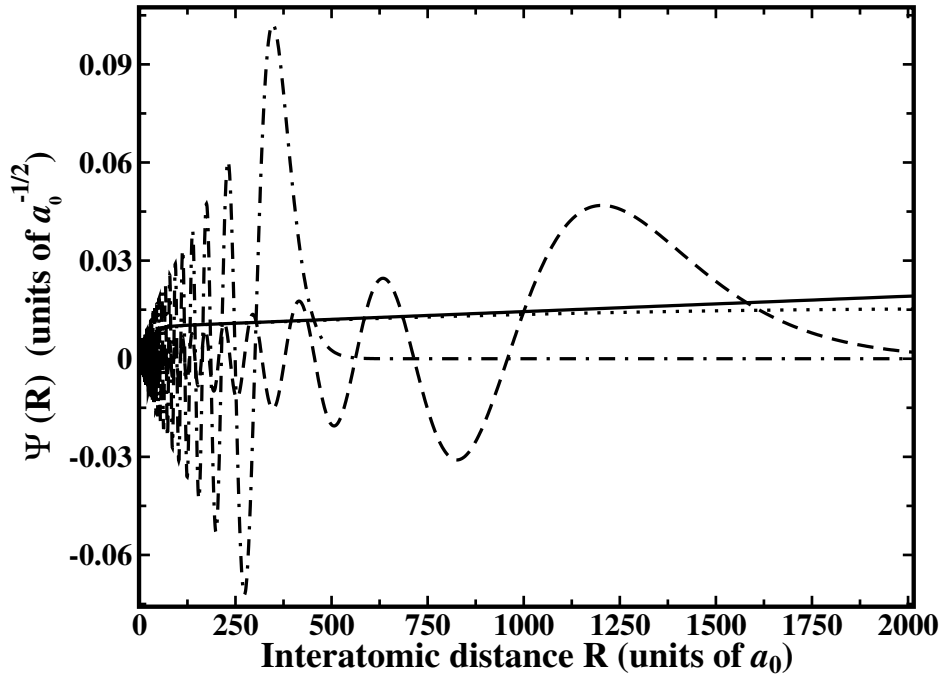


Figure 5.5: Illustration of the constant photoassociation regime. The initial-state wave function $\Psi^{10'}(R; \omega = 100)$ (dots) and an approximation to it, $\sqrt{f_c(\omega = 100)} \cdot \Psi^{10'}(R; \omega = 1)$ (solid), are shown together with the final-state vibrational wave functions for $v = 88$ (chain) and $v = 94$ (dashes).

trap frequencies in Figure 5.3. A view on the complete wave function reveals directly the confinement of the wave function to a smaller spatial volume, if the trap frequency is increased. However, on this scale the variation of the wave function at a specific value of R appears to be quite complicated. Thus it is not at all clear why the enhancement factor f^v has for so many states a constant value. A closer look at smaller internuclear separations (insert of Figure 5.3) reveals that besides the initial oscillatory part confined to the effective range of the atom-atom interaction potential there is a relatively large R interval in which the wave functions for the different trap frequencies vary linearly with R . In this case the slope is very small and the wave function is thus almost constant. If the Franck-Condon integral is determined only by the value of the initial-state wave function in this R window, it produces an almost undistorted image of the final-state wave function.

However, for the ratio $f^v(\omega)$ this final-state dependence disappears. The reason is that in the R range where the initial-state wave function is almost constant, its variation with the trap frequency is also R independent, as can be seen from the insert of Figure 5.3. In other words, one finds $\Psi^{10'}(R; \omega) =$

$C(\omega) \cdot \Psi^{10'}(R; \omega_{\text{ref}})$. If no final-state dependence occurs, the constant $C(\omega)$ is related to the ratio f via $f_c(\omega) = C^2(\omega)$. The validity of this argument for the occurrence of a constant ratio f can thus be checked (and visualized) in the following way. Together with the correct wave function $\Psi^{10'}(R; \omega)$ the approximate one, $\sqrt{f_c(\omega)} \cdot \Psi^{10'}(R; \omega_{\text{ref}})$, is plotted where $f_c(\omega)$ is the value of the factor f in the constant regime. A convenient way to determine $f_c(\omega)$ follows from the observation that the constant regime always starts at $v = 0$. Thus $f_c(\omega) = f^{v=0}(\omega)$ is the most straightforward way of $f_c(\omega)$ determination. In Figure 5.5 the correct wave function $\Psi^{10'}(R; \omega)$ is plotted together with the approximate wave function $\sqrt{f_c(\omega)} \cdot \Psi^{10'}(R; \omega_{\text{ref}})$ for the trap frequency $\omega = 2\pi \times 100\text{kHz}$. The agreement between the two wave functions is clearly good in the shown range of R values, but it is better for small R , since at about $R = 500 a_0$ the two wave functions start to disagree. Below $R = 500 a_0$ the two wave functions agree completely with each other, even in the very short R range where they possess an oscillatory behavior.

The key for understanding the occurrence of the constant regime is that a variation of the trap frequency modifies the spatial extent of the initial-state wave function, but leaves its norm and nodal structure preserved. As a consequence, the wave function changes qualitatively only in the large R range, while in the short range only the amplitude varies (by factor $C(\omega)$). The reason for this behavior is that at small R the wave function is practically shielded from the trap potential by the dominant atom-atom interaction.

Figure 5.5 shows also two final-state wave functions ($v = 88$ and 94). According to Figure 5.4(b) the transition to $v = 88$ belongs still to the constant regime ($f^{88}(\omega) \approx f_c(\omega)$), though to its very end. The transition to $v = 94$ does on the other hand not belong to this regime, since for the considered trap frequency $f^{94}(\omega) < f_c(\omega)$. As is evident from Figure 5.5, a constant ratio $f^v(\omega)$ is observed as long as the final-state wave function v is completely confined within an R range in which the approximation $\Psi^{10'}(R; \omega) \approx C(\omega) \cdot \Psi^{10'}(R; \omega_{\text{ref}})$ is well fulfilled. This is (for $\omega = 2\pi \times 100\text{kHz}$) the case for $v = 88$ for which the wave function is confined within $R < 600 a_0$, but not for $v = 94$ whose outermost lobe has its maximum at about $1350 a_0$. Since the R range in which the initial-state wave function can be approximated in the here discussed fashion decreases with increasing trap frequency, the range of v values for which $f^v(\omega) \approx f_c(\omega)$ is valid diminishes with increasing trap frequency.

The following rule of thumb is found to determine those vibrational levels v for which the relation $f^v(\omega) \approx f_c(\omega)$ starts to break down. For trap frequencies ω_1 and ω_2 (with $\omega_2 > \omega_1$) one may define a difference Δ that

quantifies the deviation of $C \cdot \Psi^{10'}(R; \omega_1)$ and $\Psi^{10'}(R; \omega_2)$ as

$$\Delta(R) = C \cdot \Psi^{10'}(R; \omega_1) - \Psi^{10'}(R; \omega_2) \quad (5.6)$$

where $C = \sqrt{f_c(\omega_2)}$. For example, in Figure 5.5 the difference $\Delta(R)$ is the distance between the solid curve and the dotted one. The relation $f^v(\omega) \approx f_c(\omega)$ breaks down for those final states v whose classical turning point lies beyond R_0 . R_0 itself is determined by $\Delta(R > R_0) \gtrsim 10^{-3}$. In other words, if the last lobe of the final wave function overlaps substantially with a region where the deviation defined by Δ is larger than about 10^{-3} , a clear deviation from the constant regime is to be expected.

5.2.5 Cut-off regime

Once the constant regime of the ratio f^v (for a given trap frequency) is left, f^v is steadily decreasing with v , as is apparent from Figure 5.4 (b). The photoassociation rate displays then a rather sharp cut-off behavior (insert of Figure 5.4 (a)). The most loosely bound vibrational states of the final electronic state have in the trap-free case the largest rate but possess a very small one in very tight traps. For those high-lying states the wave functions have a very highly oscillatory behavior for short R values and a large lobe close to the classical turning point. This outermost lobe determines the Franck-Condon integral, if the initial-state wave function is sufficiently smooth in this R range. In Figure 5.6 the initial-state wave function is shown together with the ones for $v = 96$ and 98 (for $\omega = 2\pi \times 100\text{kHz}$).

It is evident from Figure 5.6 that for $v = 96$ the overlap of the initial wave function with the last lobe of the final state is very large. In fact, for this trap frequency the overlap reaches its maximum for $v = 96$ and 97 (Figure 5.4 (a)), despite the fact that the trap-induced relative enhancement factor $f^v(\omega)$ is small (Figure 5.4 (b)). In the case of $v = 98$ the transition rate is not only clearly smaller than for $v = 96$ or 97 , but it is also much smaller than the rate obtained for the same level at much lower trap frequencies (10 or 1 kHz). Clearly, one has $f^{v=98}(\omega) < 1$ and thus for $\omega = 2\pi \times 100\text{kHz}$ the level $v = 98$ represents an example for a trap-induced suppressed rate (SPA) in contrast to the usually expected enhanced photoassociation in a trap (EPA, $f^v(\omega) > 1$). From Figure 5.6 it is clear that the reason for the small transition rate to $v = 98$ is due to the fact that the outermost lobe of the $v = 98$ state lies mostly outside the R range in which the initial-state wave function is non-zero. The least bound state (in the trap free case), $v = 99$, possesses an even smaller photoassociation rate, since in this case the outermost lobe lies practically completely outside the non-zero R range

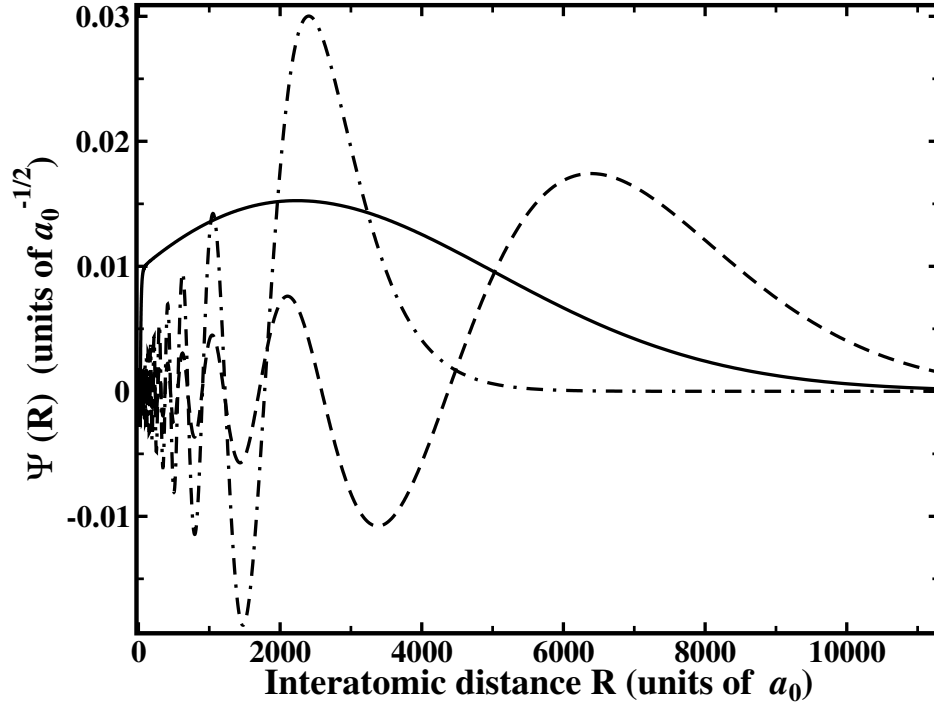


Figure 5.6: Illustration of the cut-off photoassociation regime for a 100 kHz trap. The initial-state wave function $\Psi^{10'}(R; 100)$ (solid) is shown together with the two final-state wavefunctions for $v = 96$ (chain) and $v = 98$ (dashes).

of the initial-state wave function. Due to the imperfect cancellation of the oscillating contributions from the inner lobes, the photoassociation rate for $v = 99$ is very small, but non-zero.

Increasing the trap frequency even more will confine the initial-state wave function to a smaller R range and thus SPA occurs for smaller v values. The origin of the suppression is in fact a quite remarkable feature, since from Figure 5.6 it is clear that the trap has practically no influence on the final states, even if one considers the highest-lying ones that have very tiny binding energies. This is still true, if the spatial extent of the final state is much larger than the one of the trap potential. This may be interpreted as a shielding of the trap potential by the molecular (atom-atom interaction) potential. The reason for the different shielding experienced by the initial and the final states is not only due to the fact that the former lies above the dissociation threshold, since then the photoassociation rate should dramatically increase, if transitions into the purely trap-induced bound states of the final electronic state are considered. This is, however, not the case as can be seen for the states $v > 99$ in Figure 5.4(a). The different shielding

is due to the inherently different long-range behaviors of the two electronic potential curves describing the initial ($a^3\Sigma_u^+$) and the final ($1^3\Sigma_g^+$) state. If one introduces the crossing point R_c of the long range part of the van der Waals potential with the one of the inverted harmonic trap, it is defined by equating C_n/R_c^n and $\frac{1}{2}\mu\omega^2 R_c^2$ where C_n is the corresponding leading van der Waals coefficient. At the point R_c the trap potential starts to dominate. For example, in the case of the trap frequency $\omega = 2\pi \times 10\text{kHz}$ one finds $R_c \approx +825 a_0$ and $R_c \approx +17700 a_0$ for $a^3\Sigma_u^+$ and $1^3\Sigma_g^+$ of Li_2 , respectively.

5.3 Influence of atomic interaction

5.3.1 $I^v(\omega)$ for a repulsive interaction

In order to check the main conclusions of the results obtained for $^6\text{Li}_2$ also the formation of $^{39}\text{K}_2$ is investigated. While for ^6Li a photoassociation process between *triplet* states was considered, a transition between the $X^1\Sigma_g^+$ and the $A^1\Sigma_u^+$ states is chosen for ^{39}K . In contrast to the large negative scattering length of two ^6Li atoms interacting via the $a^3\Sigma_u^+$ potential two ^{39}K ground-state atoms interact via a small positive *s*-wave scattering length. The obtained results for the squared transition dipole moments $I^v(\omega)$ are qualitatively very similar to the results obtained for $^6\text{Li}_2$. This includes the existence of a constant regime of $f^v(\omega)$ followed by a pronounced decrease for the highest-lying vibrational states, the cut-off. The rule of thumb for predicting the range of v values for which a constant ratio f^v is observed does also work in this case. $^{39}\text{K}_2$ shows thus trap-induced suppressed photoassociation for the highest lying states with a sharp cut-off in the $I^v(\omega)$ spectrum very much like $^6\text{Li}_2$. Therefore, the results are not explicitly shown for space reasons.

For a more systematic investigation of the influence of the scattering length a_{sc} and thus the type of interaction (sign of a_{sc}) and its strength (absolute value of a_{sc}) the mass of the Li atoms is varied. The mass variation allows for an in principle continuous (though non-physical) modification of a_{sc} from very large positive to negative values, as was discussed in Chapter 4. With increasing mass an increasing number of bound states (N^v) is supported by the same potential curve. Since a_{sc} is sensitive to the position of the least bound state, even a very small mass variation has a very large effect, if a formerly unbound state becomes bound. For example, an increase of the mass of ^6Li by 0.3% changes a_{sc} from $-2030 a_0$ to about $+850 a_0$. The (for ^6Li unbound) 11th vibrational state becomes weakly bound. A further increase of the mass increases its binding energy until it reaches the value for ^7Li .

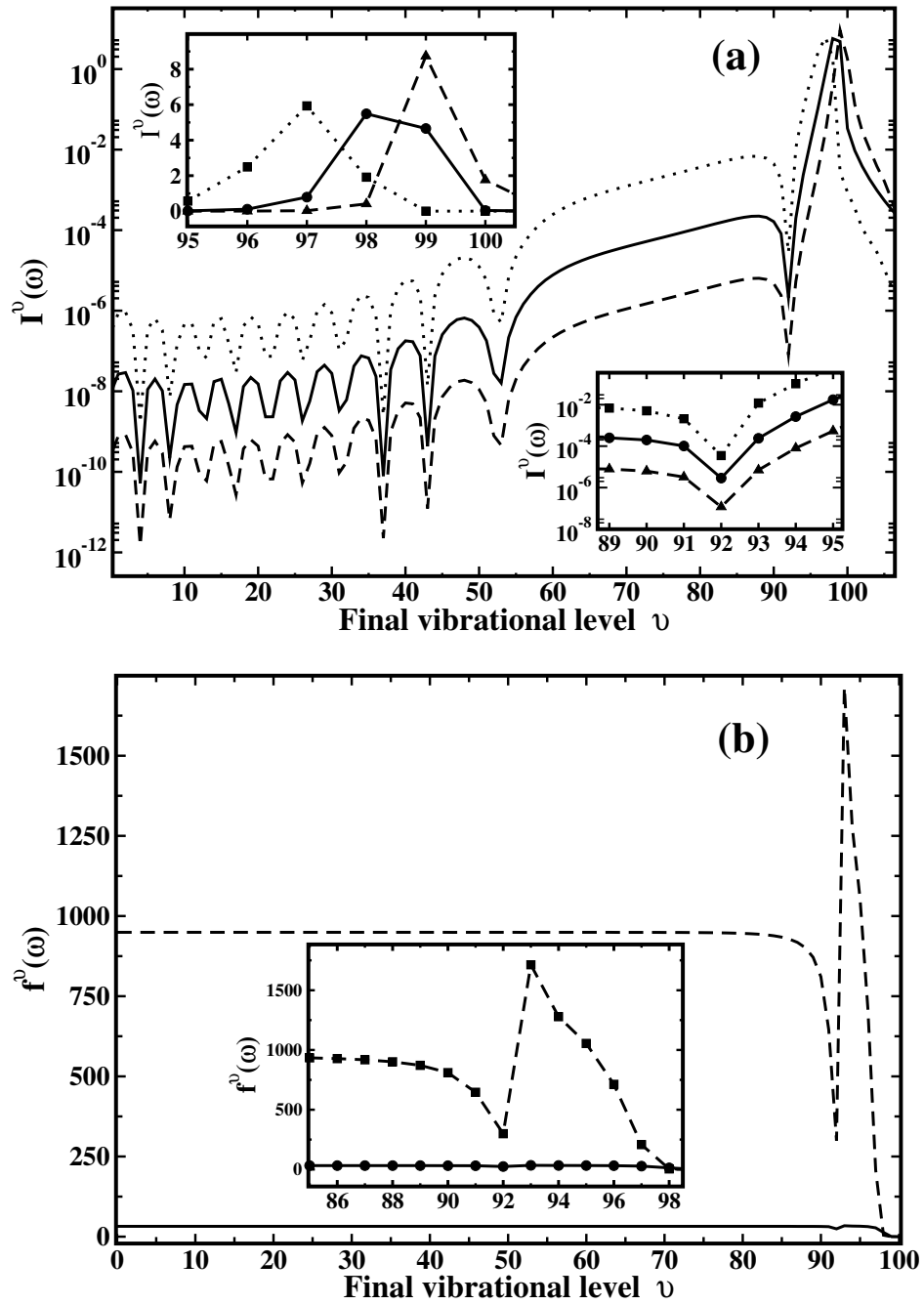


Figure 5.7: As Figure 5.4 but the scattering length is artificially changed to $a_{sc} = +850 a_0$ (text for details). The additional insert in the right bottom corner of (a) shows the range $v = 89$ to $v = 95$ on an enlarged scale.

It is also possible to modify a_{sc} from $-2030 a_0$ to $+850 a_0$ by lowering the mass of ${}^6\text{Li}$. A larger mass variation is required (about 18 %) but the number of bound states remains unchanged. In this case the large positive value of a_{sc} indicates that the 10th bound state is, however, only very weakly bound and a further small decrease of the mass will shift it into the dissociative continuum.

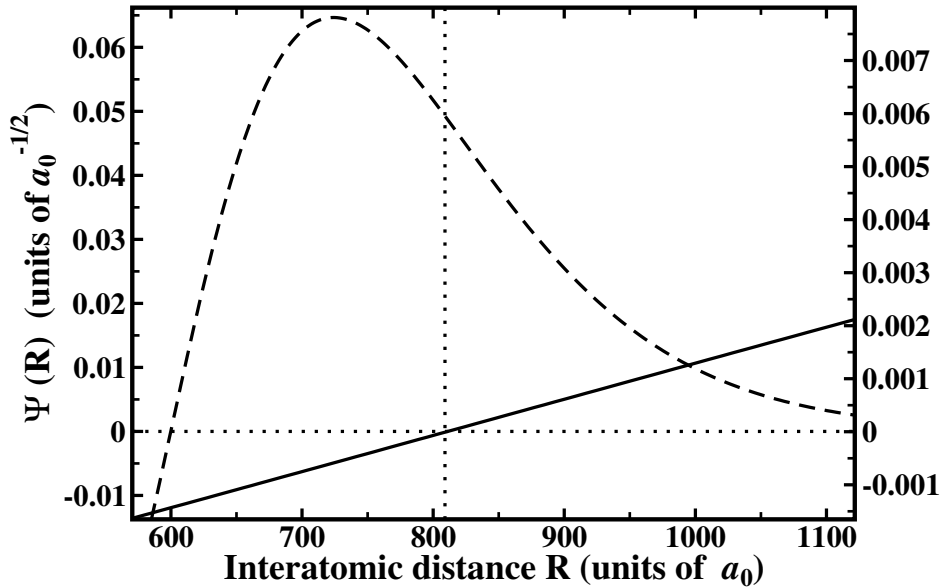


Figure 5.8: For ${}^6\text{Li}_2$ (the scattering length in the initial channel is modified to $a_{\text{sc}} = +850 a_0$) and for a 100 kHz trap the outermost lobe of the final-state wave function ($v = 92$, long dashes, left scale) is shown together with the initial-state wave function ($v' = 10$, solid, right scale). Auxiliary horizontal and vertical dotted lines are given to assist the eye in identifying regions with a positive or negative overlap of the wavefunctions.

In Figure 5.7 (a) $I^v(\omega)$ is shown for $a_{\text{sc}} = +850 a_0$ (achieved by a 0.3% increase of the mass) and three different trap frequencies as an example for a large positive scattering length and thus strong repulsive interaction. The overall result is again very similar to the one obtained for a large negative scattering length. A tighter trap increases the transition rate for most of the states, but there is a sharp cut-off for large v . The position of this cut-off moves to smaller v as the trap frequency is increased. However, for a large positive value of a_{sc} an additional feature appears in the transition spectrum: a photoassociation window visible as a pronounced dip in the I^v spectrum for large v . For the given choice of a_{sc} this minimum occurs for $v = 92$.

The occurrence of the dip for $a_{\text{sc}} \gg 0$ has been predicted and explained for the trap-free case in [93, 129] and was experimentally confirmed [130]. Fig-

Figure 5.8 shows the last lobe of the final-state vibrational wave function $\Psi^{92}(R)$ together with the initial-state wave function, both for $\omega = 2\pi \times 100$ kHz. The key for understanding the occurrence of the dip for large positive scattering lengths and its absence for negative ones is the change of sign of the initial-state wave function as a consequence of the repulsive atom-atom interaction. In fact, in the trap-free case the position of this node agrees of course with the scattering length. As can be seen from Figure 5.8, the tight trap moves the nodal position to a smaller value, but this shift is comparatively small (about 5%) even in the case of a 100 kHz trap. For negative values of a_{sc} this node appears to be absent, since in this case only the extrapolated wave function intersects the R axis, but this occurs at the non-physical interatomic separation $R_x = a_{\text{sc}} < 0$. As a result of the sign change occurring for $a_{\text{sc}} > 0$ the overlap of the initial-state wave function with a final state for which the mean position of the outermost lobe agrees with the nodal position (R_x) vanishes. The probability for a perfect agreement of those two positions is of course rather unlikely, but as can be seen from Figure 5.7(a) and [129] where also an approximation for $I^v(\omega = 0)$ was derived, the cancellation can be very efficient.

It should be emphasized that of course also for $a_{\text{sc}} < 0$ a number of dips occur as was discussed in the context of Figure 5.4. The difference between those dips and the one discussed for $a_{\text{sc}} \gg 0$ is the occurrence of the latter outside the molecular regime. While the other dips are a direct consequence of the short-range part of the atom-atom interaction potential and thus confined (for Li_2) to $v < 55$ corresponding to $R < 30 a_0$, the dip occurring for $a_{\text{sc}} \gg 0$ can be located anywhere outside the molecular regime. This is even more apparent from Figure 5.9 where the I^v spectra for four different positive values of a_{sc} are shown together with the one for the (physical) value $a_{\text{sc}} = -2030 a_0$ (all for $\omega = 2\pi \times 100$ kHz). The values $a_{\text{sc}} = +2020 a_0, +350 a_0, +115 a_0,$ and $+50 a_0$ were obtained by a mass increase of $\sim 0.3\%, \sim 0.8\%, \sim 2\%,$ and $\sim 6\%$, respectively. In agreement with the explanation given above, the position of the dip moves continuously to larger values of v as the scattering length increases, since the position R_x of the last node of the initial state lies close to a_{sc} . Also the positions of the other dips depend on a_{sc} , but their dependence is much weaker and involves a much smaller R interval. Clearly, the positions of the dips become more stable if they occur at smaller v .

Noteworthy, the positions of the first 10 dips agree perfectly for $a_{\text{sc}} = -2030$ and $+2020 a_0$. In fact, both spectra are on a first glance in almost perfect overall agreement, except the occurrence of the additional dip for $v = 92$. According to the discussion of the sum rule in Section 5.2.2 the total sum \tilde{I} should be (approximately) independent of the atomic interaction and

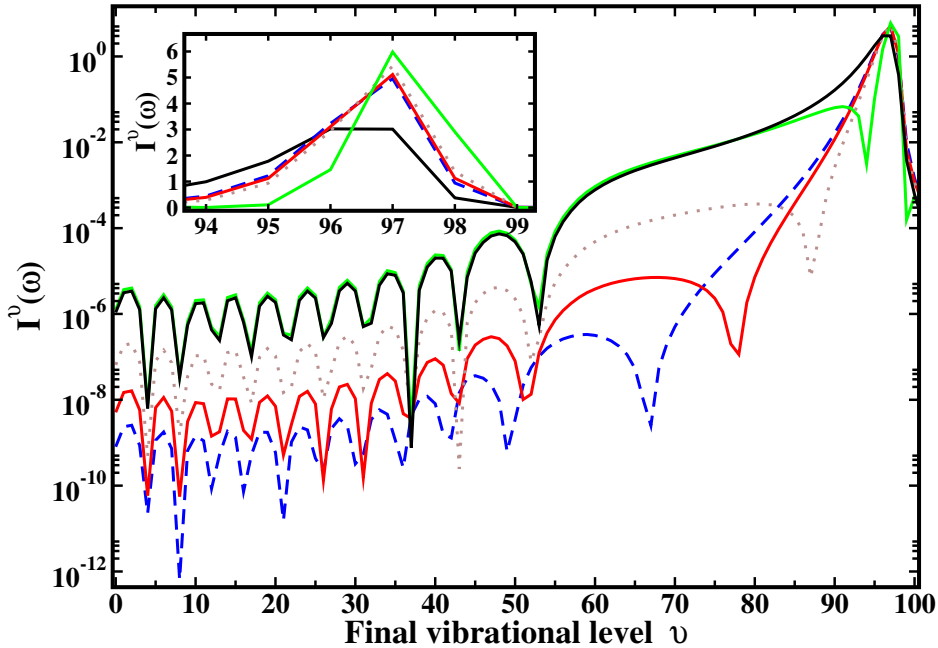


Figure 5.9: Dependence of the squared dipole transition moments $I^{\nu}(\omega)$ on the scattering length a_{sc} for transitions from the first trap-induced ($v' = 11$) initial $a^3\Sigma_u^+$ state to the vibrational manifold (v) of the $1^3\Sigma_g^+$ state of Li_2 in a $\omega = 2\pi \times 100$ kHz trap. Using masses slightly larger than the one of ${}^6\text{Li}$ $a_{\text{sc}} = +50 a_0$ (blue dashes), $a_{\text{sc}} = +115 a_0$ (red), $a_{\text{sc}} = +350 a_0$ (brown dots), and $a_{\text{sc}} = +2020 a_0$ (green) were yielded. For comparison, the result with the physical mass ($a_{\text{sc}} = -2030 a_0$, black) is also shown. The insert shows the transitions to $v = 94$ to 99 on an enlarged scale.

thus a_{sc} . This is also confirmed numerically for the present examples. The insert of Figure 5.9 reveals how the sum-rule is fulfilled. The due to the additional dip missing transition probability is compensated by an enhanced rate to the neighbor states with larger v .

In all shown cases with $a_{\text{sc}} > 0$ there exist 11 bound states in contrast to the 10 states of ${}^6\text{Li}$ ($a_{\text{sc}} = -2030 a_0$). As mentioned in the beginning of this section, it is also possible to change the sign of a_{sc} while preserving the number of nodes. The corresponding I^{ν} spectra (again for $\omega = 2\pi \times 100$ kHz) are shown in Figure 5.10. The same values of a_{sc} as in Figure 5.9 ($+2020 a_0$, $+350 a_0$, $+115 a_0$, and $+50 a_0$) are now obtained by a decrease of the mass by $\sim 18\%$, $\sim 17.5\%$, $\sim 16\%$, and $\sim 13\%$, respectively. A comparison of the two Figures 5.9 and 5.10 demonstrates that the position of the outermost dip (for $a_{\text{sc}} \gg 0$) depends for a given ω solely on a_{sc} , while the other dips (in the molecular regime) differ when changing the total number of bound states from 10 to 11. A comparison of the results obtained for $a_{\text{sc}} = -2030 a_0$

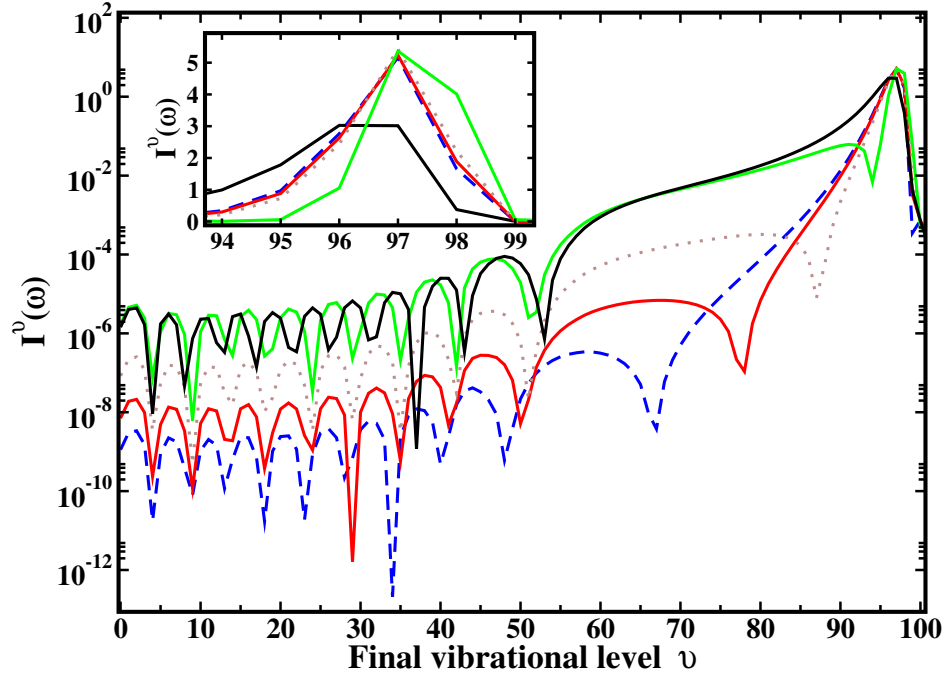


Figure 5.10: As Figure 5.9, but for a variation of a_{sc} by means of a reduction of the mass with respect to the one of ${}^6\text{Li}$. In this case, the number of bound states remains unchanged and the transition starts from the $v' = 10$ $a^3\Sigma_u^+$ state.

and $+2020 a_0$ with 10 bound states in both cases shows that most of the nodes in the molecular regime are shifted with respect to each other in such a way that the v range hosting 10 dips for $a_{sc} = -2030 a_0$ contains 9 dips for $a_{sc} = +2020 a_0$.

Turning back to Figure 5.7 and the question of the influence of a tight trap on the photoassociation rate for $a_{sc} \gg 0$ one notices that the position of the additional dip appears to be practically independent of ω . As was explained in the context of Figure 5.8, the reason is that the position of the outermost node depends only weakly on ω . For the shown example this shift is even for a 100 kHz trap small compared to the separation of the outermost lobes between neighboring v states. Therefore, the shift is not sufficient to move the dip position away from $v = 92$. However, if a_{sc} is, e. g., increased to $+2020 a_0$ the crossing point R_x shifts in a 100 kHz trap to about $1500 a_0$ and changes thus by $\approx 25\%$. In this case the dip position moves from $v = 95$ to 94 . It is therefore important to take the effects of a tight trap into account, if they are used for the determination of a_{sc} using photoassociation spectroscopy the way discussed in [93, 130].

In order to focus on the effect of the tight trap it is again of interest to

consider the ratio $f^v(\omega)$ introduced in Section 5.2.3. For small but positive values of a_{sc} the ratio f^v is structurally very similar to the case $a_{\text{sc}} = -2030 a_0$ shown in Figure 5.4(b). A uniform constant regime covering almost all v states is followed by a sharp cut-off whose position shifts to smaller v as ω increases. A similar behavior is encountered for $a_{\text{sc}} = +850 a_0$ and $\omega = 10$ kHz as shown in Figure 5.7(b). However, for a tighter trap (100 kHz) a new feature appears. In this case the relative enhancement at the dip position ($v = 92$) is smaller than in the constant regime, but larger for the neighbor states. The enhancement factor for $v = 92$ is only $\approx 25\%$ of f_c , while the one for $v = 93$ is $\approx 60\%$ larger than f_c . This results in a dispersion-like structure in f^v . It should be emphasized that this is again remarkably different from the other dips in $I^v(\omega)$ ($v < 55$) that show the same (constant) enhancement factor f_c as their neighbor states.

5.3.2 Combined influence of trap and atomic interaction

In view of the important question how the efficiency of photoassociation can be improved, Figure 5.9 reveals that besides the use of a tight trap a large scattering length is also favorable. The photoassociation rate (away from the dips) is enhanced by orders of magnitude, if a_{sc} varies from $a_{\text{sc}} = +50 a_0$ to $a_{\text{sc}} = +2020 a_0$! In view of the already discussed fact that the results for the overall spectrum I^v differ for $a_{\text{sc}} > 0$ and $a_{\text{sc}} < 0$ only by the position of the dips, it is evident that photoassociation (or corresponding Raman transitions) are much more efficient, if $|a_{\text{sc}}|$ is very large.

In order to understand the dependence of the FC factors of the vibrational final states on the scattering length it is instructive to look at the variation of the initial-state wave function with a_{sc} for large R values. This is shown in Figure 5.11 for $\omega = 2\pi \times 100$ kHz. While a large attractive interaction ($a_{\text{sc}} \ll 0$) leads to a very confined wave function for the first trap-induced bound state, a large repulsive interaction ($a_{\text{sc}} \gg 0$) does not only result in a node (responsible for the photoassociation window discussed above), but also to a push of the outermost lobe to larger R values. This push is of course counteracted by the confinement of the trap. However, only the highest lying final states probe the very large R range. As is apparent from Figure 5.2 the final states $v \leq 92$ probe almost completely the range $R \leq 1000 a_0$. Within this R interval the absolute value of the initial-state wave function increases with the absolute value of a_{sc} . As a consequence, the corresponding FC factors and I^v should increase with $|a_{\text{sc}}|$. An exception to this is the already discussed occurrence of the photoassociation window

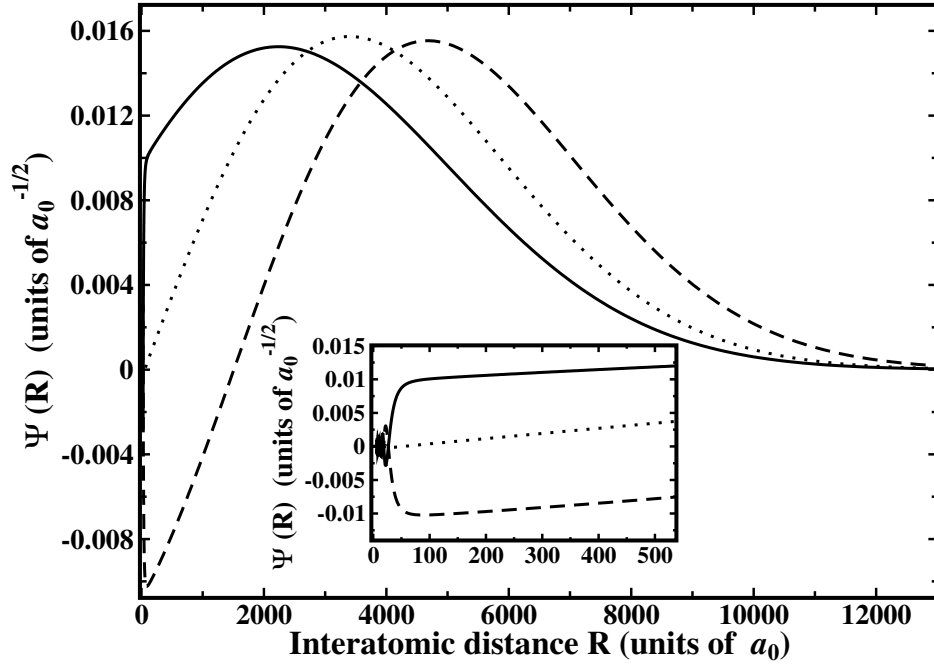


Figure 5.11: Wave functions of the initial state describing two Li atoms in a trap with frequency $\omega = 2\pi \times 100$ kHz for different masses that yield the scattering lengths $a_{\text{sc}} = -2030 a_0$ (solid), $a_{\text{sc}} = +50 a_0$ (dots), and $a_{\text{sc}} = +2020 a_0$ (dashes). The insert shows the small R range on an enlarged scale.

(spectral dip) that occurs for a positive scattering length, if the position of the node is probed by the final-state wave function. Consequently, one expects for the low-lying final states (in fact for almost all except the very high-lying ones and the ones at the dip position) that an increase of $|a_{\text{sc}}|$ leads to an increased photoassociation rate.

An evident question is of course, whether the enhancements due to the use of tighter traps and tuning of a_{sc} can be used in a constructive fashion? In order to investigate this question, one can introduce another enhancement factor

$$g^v(\omega, a_{\text{sc}}) = \frac{I^v(\omega, a_{\text{sc}})}{I^v(\omega_{\text{ref}}, a_{\text{sc,ref}})} \quad (5.7)$$

with $a_{\text{sc,ref}} = 0 a_0$ (and $\omega_{\text{ref}} = 2\pi \times 1$ kHz as before). Clearly, a cut through $g^v(\omega, a_{\text{sc}})$ for constant a_{sc} is equal to $f^v(\omega)$. A cut for constant ω describes on the other hand the relative enhancement of the photoassociation rate as a function of a_{sc} .

The function $g^v(\omega, a_{\text{sc}})$ depends of course on the vibrational state v , but as was discussed before, most of the states show a constant enhancement

factor f_c . Thus it is most interesting to investigate $g_c(\omega, a_{sc})$ that is defined as the g function for vibrational states for which the relation $f^v = f_c$ is valid. This excludes the states in the cut-off regime and those at or very close to the photoassociation window. Figure 5.12 shows $g_c(\omega, a_{sc})$ as a function of a_{sc} for

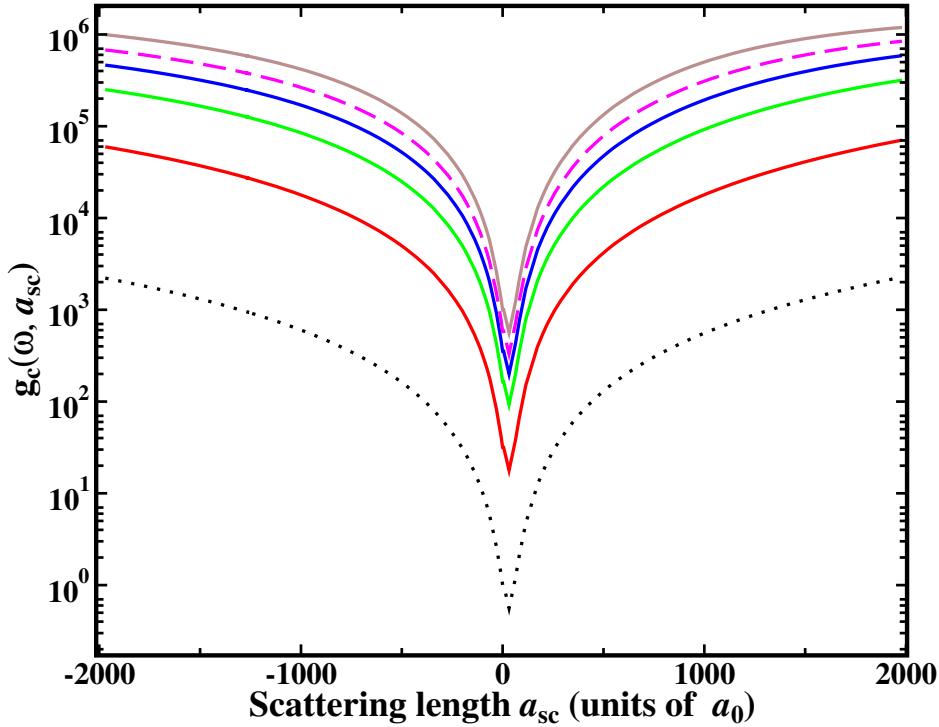


Figure 5.12: Enhancement factor g_c (Equation (5.7)) in the constant (v -independent) regime as a function of a_{sc} for trap frequencies $\omega = 2\pi \times 1$ kHz (black dots), $\omega = 2\pi \times 10$ kHz (red), $\omega = 2\pi \times 30$ kHz (green), $\omega = 2\pi \times 50$ kHz (blue), $\omega = 2\pi \times 70$ kHz (magenta dashes), and $\omega = 2\pi \times 100$ kHz (brown).

different trap frequencies. The important finding is that $g_c(\omega, a_{sc})$ increases as a function of ω and $|a_{sc}|$. In fact, within the shown ranges of ω and a_{sc} the function $g_c(\omega, a_{sc})$ rises by 6 orders of magnitude, if the maximum values of ω ($2\pi \times 100$ kHz) and a_{sc} ($\pm 2000 a_0$) are considered. A more detailed analysis shows that the enhancement is almost equally distributed among the two parameters, i. e., a factor 10^3 stems from the variation of ω and about the same factor from varying a_{sc} . Thus the enhancement of the photoassociation rate due to the two different physical parameters occurs practically independently of each other, at least in the rather large parameter range considered. It should be emphasized that these ranges are realistically achievable in present-day experiments. It is interesting to note that this finding is not

only very encouraging with respect to the possible enhancement of photoassociation rates and related molecule production schemes, but it shows also that the influence of the parameters scattering (a_{sc}) and characteristic length scale of an isotropic harmonic trap ($a_{\text{ho}} = \sqrt{1/(\mu\omega)}$) on the photoassociation process is very different from the one observed for the energy. In energy-related discussions (like the one on the validity of the pseudopotential approximation in [83]) it was found that the ratio $|a_{\text{sc}}/a_{\text{ho}}|$ determines the behavior. In the present case, both parameters and not only their ratio are important. In fact $|a_{\text{sc}}/a_{\text{ho}}|$ would imply a complete cancellation of enhancement if both values a_{sc} and a_{ho} are simultaneously switched to respective $C \cdot a_{\text{sc}}$ and $C \cdot a_{\text{ho}}$ ones.

5.4 Pseudopotential approximation in a harmonic trap

As a simplified model, the pseudopotential approximation is widely used in photoassociation studies. This approximation is very valuable because it leads to an analytically solvable problem for two atoms placed in a harmonic trap. In the present work, realistic potentials have been adopted. This allows to check the range of applicability of the pseudopotential approximation in which the interaction between particles is described by a simple contact potential. Indeed, the comparison with the simplified model shows that it often provides reasonable estimates for the trap-induced enhancement of the photoassociation rate even if the predicted absolute rates are completely erroneous. In this section the results obtained using realistic atomic interaction are compared to those of the pseudopotential approximation.

The bound state of two atoms in a harmonic trap when the atom-atom interaction $V_{\text{int}}(R)$ is approximated by a regularized contact potential

$$V_{\text{int}}(R) = \frac{4\pi}{2\mu} a_{\text{sc}} \delta^3(\vec{R}) \frac{\partial}{\partial R} R \quad (5.8)$$

with energy-independent scattering length a_{sc} , was first derived analytically by Busch *at al.* [95]. The bound states with integer quantum number n_t are expressed as

$$\Psi_{a_{\text{sc}}}^{n_t}(R) = \frac{1}{2} \pi^{-3/2} A R e^{-\bar{R}^2/2} \Gamma(-\nu) U(-\nu, \frac{3}{2}, \bar{R}^2), \quad (5.9)$$

where $\bar{R} = R/a_{\text{ho}}$. A is a normalization constant with the dimension $[1/\sqrt{\text{m}^3}]$ and ν is an effective quantum number for the relative motional eigenstate,

$\nu = \frac{E_{a_{sc}}^{n_t}}{2\omega} - \frac{3}{4}$. The energy eigenvalues are given by the roots of the equation

$$\frac{\Gamma(-x/2 + 3/4)}{\Gamma(-x/2 + 1/4)} = \frac{1}{\sqrt{2\xi}}, \quad (5.10)$$

where $x = E_{a_{sc}}^{n_t}/\omega$ and $\xi = a_{sc}/a_{ho}$.

The initial-state wave function $\Psi^{10'}(R; \omega)$ of two ${}^6\text{Li}$ atoms interacting through the $a^3\Sigma_u^+$ potential and the pseudopotential wave function $\Psi_{a_{sc}}^0$ with the physical (trap-free) value of the scattering length $a_{sc} = -2030 a_0$ are plotted together in Figure 5.13 for the case of a trap frequency $\omega = 2\pi \times 10\text{kHz}$.

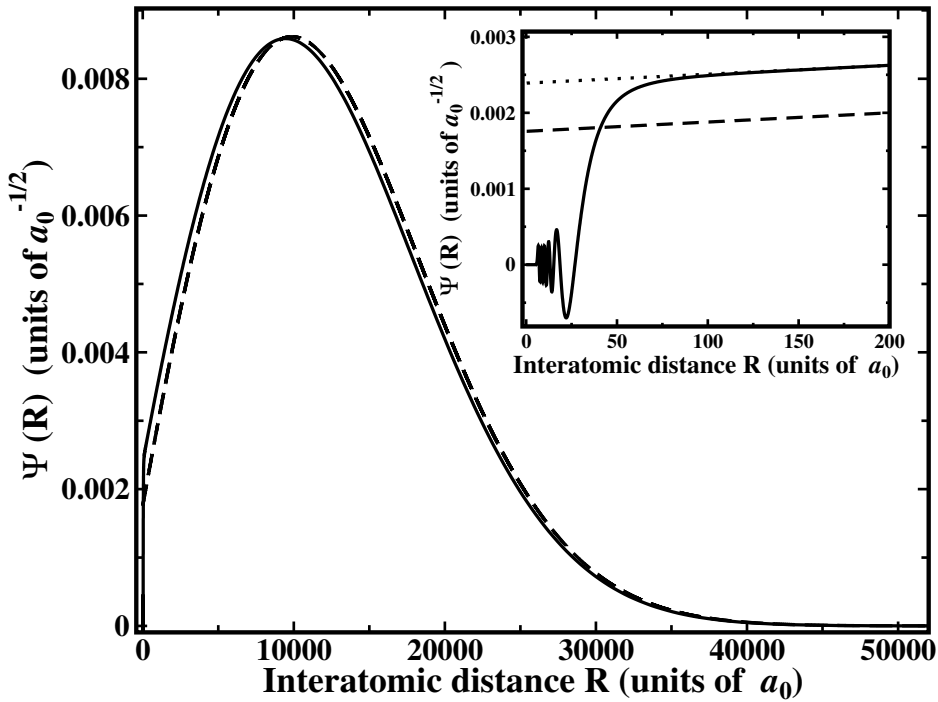


Figure 5.13: Wave functions of the first trap-induced bound state ($\omega = 2\pi \times 10\text{kHz}$) of two ${}^6\text{Li}$ atoms interacting through the full $a^3\Sigma_u^+$ potential (solid), a pseudopotential with the energy-independent (trap-free) scattering length $a_{sc} = -2030 a_0$ (dashes), and one with the energy-dependent value $a_E = -2872 a_0$ (dots). The inset shows the short R range on an enlarged scale.

As expected, the wave function $\Psi_{a_{sc}}^0$ fails completely for short internuclear separations, since it does not reproduce any nodal structure at all. In addition, $\Psi_{a_{sc}}^0$ exhibits a wrong behavior at $R = 0$ where it is non-zero. In the long-range part $\Psi_{a_{sc}}^0$ agrees better with the correct wave function. There the main difference is an obvious phase shift between the two functions. This

phase shift is a consequence of the confining potential and vanishes in the absence of the trap ($\omega \rightarrow 0$). The physical reason for the phase shift is the non-zero ground-state energy in the trap (zero-point energy and motion) due to the Heisenberg uncertainty principle. As a consequence, the scattering of the two atoms in a trap differs from the trap-free case even at zero temperature. Figure 5.13 shows that a pseudopotential approximation using an energy-dependent scattering length a_E leads to a highly improved description of two particles confined in an isotropic harmonic trap [83, 97].

While the scattering length is defined in the limit $E \rightarrow 0$, an energy-dependent scattering length can be introduced by extending its original asymptotic definition in terms of the phase shift for s -wave scattering $\delta_0(E)$ to non-zero collision energies. This yields $a_E = -\tan\delta_0(E)/k$ with $k = \sqrt{2\mu E}$. Clearly, the evaluation of $\delta_0(E)$ requires to solve the complete scattering problem and thus also a_E can only be obtained from the solution for the correct atom-atom interaction potential.

After determination of the ground-state energy of two ${}^6\text{Li}$ atoms from a full calculation (using the realistic interaction potential), this energy is used in Equation (5.10) to find a_E , which is then substituted in the Equation (5.9) in place of a_{sc} [131]. The energy-dependent scattering length a_E is found to be equal to $-2872 a_0$ for two ${}^6\text{Li}$ atoms in a trap with frequency $\omega = 2\pi \times 10\text{kHz}$. The resulting wave function is also shown in Figure 5.13, together with the correct one and the one obtained for $a_{\text{sc}} = -2030 a_0$. Clearly, the agreement with the correct wave function is very good for large R . For $R > 150 a_0$ the wave function obtained for $a_E = -2872 a_0$ is not distinguishable from the correct one. Only in the inset of Figure 5.13 that shows the wave functions at short internuclear separations one sees a deviation. It is due to the absence of any nodal structure and the wrong behavior at $R \rightarrow 0$ of the pseudopotential wave function. In fact, at short distances ($\lesssim 40 a_0$) the introduction of an energy-dependent scattering length that corrects the phase shift leads to an even larger error compared to the use of a_{sc} .

The validity of the pseudopotential approximation using an energy-dependent scattering length was discussed before. Blume and Greene [83] found that the applicability of this approximation depends on the ratios β_6/a_{ho} and $|a_{\text{sc}}/a_{\text{ho}}|$ where $\beta_6 = (2\mu C_6)^{1/4}$ is the characteristic length scale of the interaction potential in the case of a leading C_6/R^6 van der Waals potential. For two ${}^6\text{Li}$ atoms in a trap with $\omega = 2\pi \times 100\text{kHz}$ interacting via the $a^3\Sigma_u^+$ potential those ratios are 0.02 and 0.59, respectively. These validity criteria are, however, based solely on energy arguments. In other words, if those ratios are sufficiently smaller than 1, the energy obtained by means of Equation (5.10) with a_{sc} should agree well with the correct energy. In

the present example of ${}^6\text{Li}$ the ratio between the correct first trap-induced energy $E^{10'}$ and $E_{a_{\text{sc}}}^{n_i=0}$ obtained with the energy-independent pseudopotential is $E^{10'}/E_{a_{\text{sc}}}^0 = 0.96$ for $\omega = 2\pi \times 10$ kHz and $E^{10'}/E_{a_{\text{sc}}}^0 = 0.92$ for $\omega = 2\pi \times 100$ kHz. By construction, the energy $E_{a_{\text{E}}}^{n_i=0}$ agrees completely with $E^{10'}$.

5.4.1 I^v in pseudopotential approximation

Figure 5.14 shows $I^v(\omega)$ within the pseudopotential approximation with energy-independent scattering length compared to the spectrum obtained for the realistic atom-atom interaction, both for a trap frequency $\omega = 2\pi \times 10$ kHz. The two results disagree completely for $v \leq 60$. For higher lying vi-

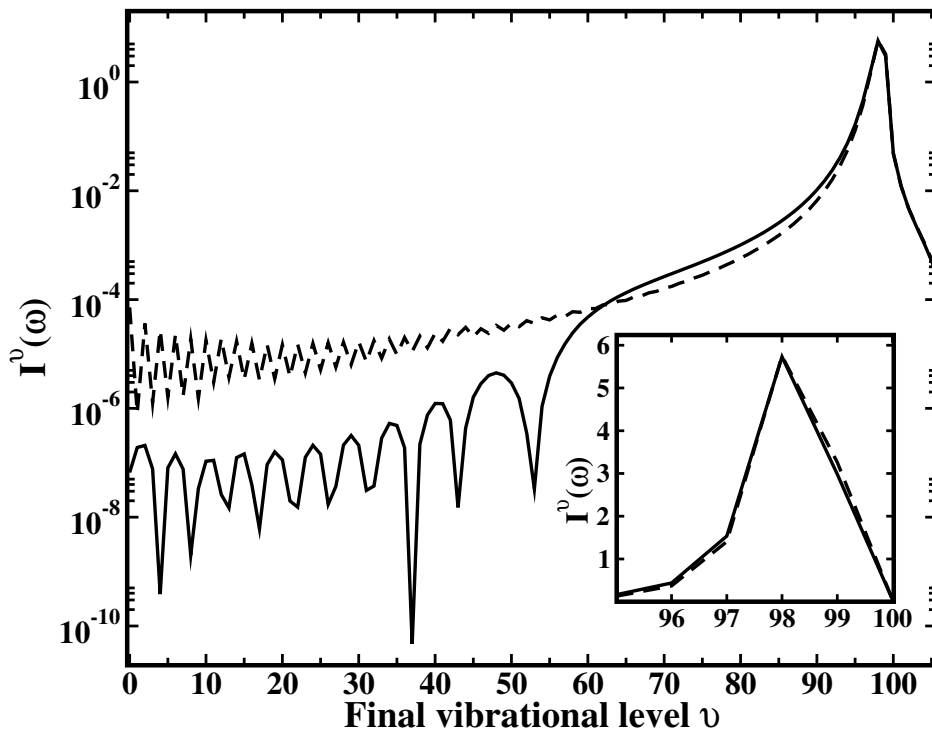


Figure 5.14: Squared photoassociation transition moments $I^v(\omega)$ for ${}^6\text{Li}$ in a $\omega = 2\pi \times 10$ kHz trap calculated with the molecular interaction potential (solid) or within the energy-independent pseudopotential approximation (dashes).

brational states ($v > 60$) the agreement is reasonable. For the highest lying states ($v \geq 95$) very good agreement is found even on a linear scale (inset of Figure 5.14). Adopting the energy-dependent scattering length yields quantitative agreement already for $v \geq 75$, but again a complete disagreement for $v \leq 60$.

The breakdown of the pseudopotential approximation (with energy-independent or dependent scattering lengths) for describing photoassociation to the low-lying vibrational states is a direct consequence of the wrong short-range behavior of the pseudopotential wave functions. From the definition of $I^v(\omega)$ it follows that the pseudopotential approximation fails, if the final-state vibrational wave function has a substantial amplitude in the R range where the initial-state wave function is strongly influenced by the atom-atom interaction. An estimate for this R range is the already mentioned effective-range parameter $\beta_6 = (2\mu C_6)^{1/4}$. Since for large v the final-state wave function is dominated by its outermost lobe whose position is in turn close to the classical outer turning point R_{out} , the pseudopotential approximation should be valid for $R_{\text{out}} > \beta_6$. In the case of ${}^6\text{Li}$ one finds $\beta_6 = 62.5 a_0$. According to Figure 5.2 the pseudopotential approximation should only be applicable for $v > 70$.

The pseudopotential approximation was used already in [82] for an analysis of the photoassociation rate change due to scattering-length modification. However, that investigation focused on very high lying vibrational states close to or even above the trap-free dissociation limit. For transitions to those states the R dependence of the electronic transition dipole moment can safely be ignored. Hence, it is sufficient to concentrate on the Franck-Condon (FC) factors. In Figure 5.15 the squares of these factors are shown as a function of the scattering length for $90 \leq v \leq 98$ and trap frequency $\omega = 2\pi \times 100$ kHz. As in [82] the pseudopotential approximation is used for the initial state. The final-state wave function is obtained by a full numerical calculation whereas an approach based on quantum defect theory (QDT) was used in [82]. Furthermore, Na_2 was considered in [82] while the present study deals with Li_2 .

For the states $90 \leq v \leq 93$ shown in Figure 5.15(a) the dependence on a_{sc} in a 100 kHz trap is very similar to the one found in [82]. The rather regular variation with a_{sc} is due to the fact that the final-state wave function probes the flat part of the initial-state wave function, as can be seen in the inset of Figure 5.15(a) where the wave function for $v = 92$ is shown together with the initial-state wave function for three different values of a_{sc} . The initial-state wave function varies almost linearly with a_{sc} in the Franck-Condon window of the $v = 92$ final state. According to the discussion in Section 5.2.5, the states $v \geq 90$ belong to the cut-off regime, but for $v \leq 93$ the enhancement factor f^v is still close to its value f_c in the constant regime (see Figures 5.4 and 5.7). The minima of the FC^2 factors for $a_{\text{sc}} \gg 0$ are a consequence of the dip discussed in Section 5.3.1. Since the nodal position R_x moves towards larger R if a_{sc} increases, the minimum in the FC^2 factors moves towards a larger value of a_{sc} if v increases. While the pseudopotential

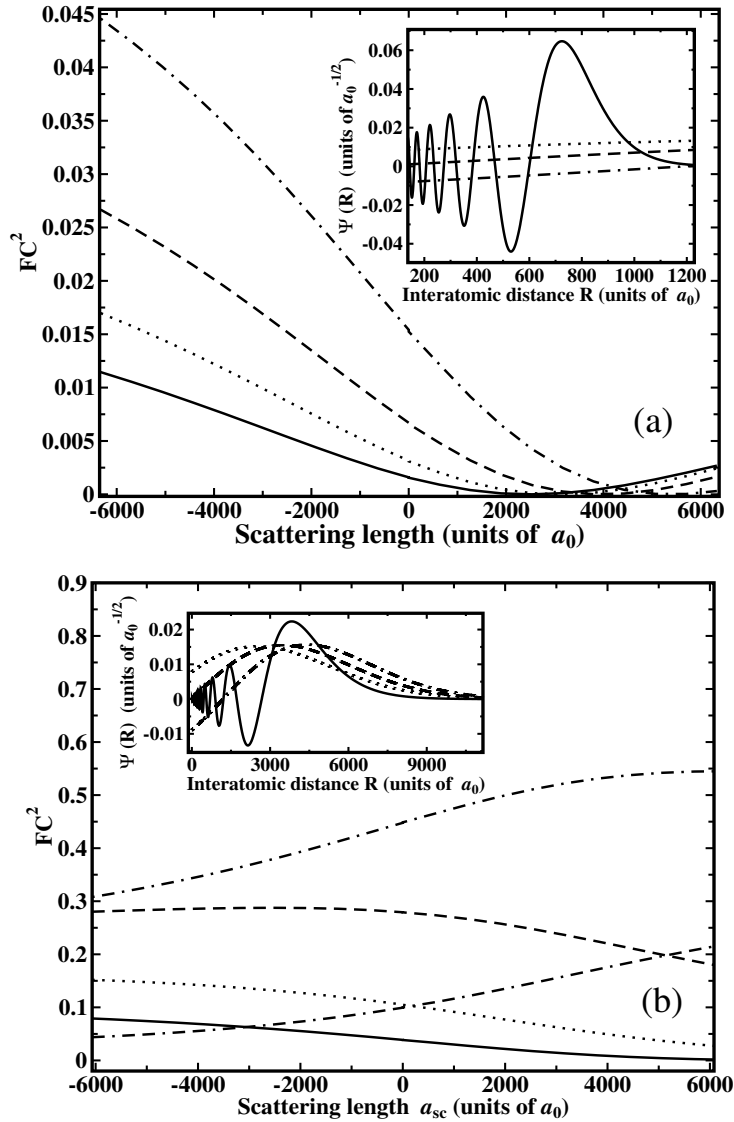


Figure 5.15: (a) Squared Franck-Condon factors between the final vibrational states $v = 90$ (solid), 91 (dots), 92 (dashes), or 93 (chain) of the $1^3\Sigma_g^+$ state and the initial-state pseudopotential wave functions as a function of the scattering length a_{sc} . The trap frequency is $\omega = 2\pi \times 100$ kHz. The inset shows the $v = 92$ final-state wave function together with the pseudopotential wave functions for $a_{sc} = -2000 a_0$ (dots), $a_{sc} = 0$ (dashes), $a_{sc} = +2000 a_0$ (chain). (b) As (a), but for $v = 94$ (solid), 95 (dots), 96 (dashes), 97 (chain), $v=98$ (dot-dash-dash). The inset shows the $v = 97$ final-state wave function and the pseudopotential wave functions for $a_{sc} = -2000 a_0$ (dots), $a_{sc} = 0$ (dashes), $a_{sc} = +2000 a_0$ (chain).

approximation is capable to predict the existence of the dip for $a_{\text{sc}} \gg 0$, its position is not necessarily correctly reproduced in a trap. This is due to the fact that the pseudopotential overestimates the trap-induced shift of the outermost node position. For example, if the mass of Li is varied such that $a_{\text{sc}} = +850 a_0$ is obtained, a 100 kHz trap shifts R_x to $\approx +810 a_0$ (Figure 5.8) and the dip occurs at $v = 92$ (Figure 5.7). On the other hand, the pseudopotential approximation (with $a_{\text{sc}} = +850 a_0$) yields $R_x \approx +580 a_0$ and the dip occurs for $v = 90$. This error in the prediction of R_x increases with a_{sc} .

The final states $94 \leq v \leq 98$ whose FC^2 factors are shown in Figure 5.15(b) probe the non-linear part of the initial-state wave function (close to the trap boundary). Consequently, the dependence on a_{sc} differs from the one found in [82]. For $90 \leq v \leq 92$ the FC^2 factors are first decreasing and then increasing if a_{sc} varies from $-6000 a_0$ to $+6000 a_0$. For $93 \leq v \leq 96$ the FC^2 factors are purely decreasing. Finally, for $v = 97$ and 98 the FC^2 factors are increasing with a_{sc} .

In view of the fact that the scattering length of a given atom pair may be known (e. g., from some measurement), but the corresponding atom-atom interaction potential is unknown, it is of course interesting to investigate whether the pseudopotential approximation allows to predict the enhancement factor also in the constant regime, i. e., whether it correctly reproduces $f_c(\omega)$. Hence, a simple estimate is possible for the effect of a tight trap on the photoassociation rate in the constant regime that covers most of the spectrum. In order to determine $f_c(\omega)$ it is sufficient to analyze the ratio of the initial-state wave function $\Psi_{a_{\text{sc}}}^0$ for the trap frequencies ω and ω_{ref} . This comparison may be done at any arbitrary internuclear separation R_{lin} provided it belongs to the linear regime. The result is

$$f_c^{\text{pseudo}}(\omega) = \left[\frac{\Psi_{a_{\text{sc}}}^0(R_{\text{lin}}; \omega)}{\Psi_{a_{\text{sc}}}^0(R_{\text{lin}}; \omega_{\text{ref}})} \right]^2. \quad (5.11)$$

A very special and simple choice which guarantees that R_{lin} belongs to the linear regime is $R_{\text{lin}} = 0$. With this value of R_{lin} it can be found from the analysis of $\Psi_{a_{\text{sc}}}^0$

$$f_c^{\text{pseudo}}(\omega) = \left[\frac{A(\omega)}{A(\omega_{\text{ref}})} \right]^2 \frac{\omega_{\text{ref}}}{\omega}, \quad (5.12)$$

where $A(\omega)$ is the normalization factor fulfilling $|A(\omega)|^2 = \sqrt{2\omega} \pi \xi^2 \frac{\partial E}{\partial \xi}$ [95]. Depending on the level of approximation either a_{sc} or a_E may be used in the evaluation of A . An even simpler estimate is obtained if the atom-atom

interaction potential is completely ignored in the initial state. The harmonic-oscillator eigenfunctions at $R = R_{\text{lin}} = 0$ yield

$$f_c^{\text{ho}}(\omega) = \left(\frac{\omega}{\omega_{\text{ref}}} \right)^{3/2}. \quad (5.13)$$

In Figure 5.16 the enhancement factors $f_c(\omega)$ calculated at different levels of approximation are shown as a function of the trap frequency ω . The results

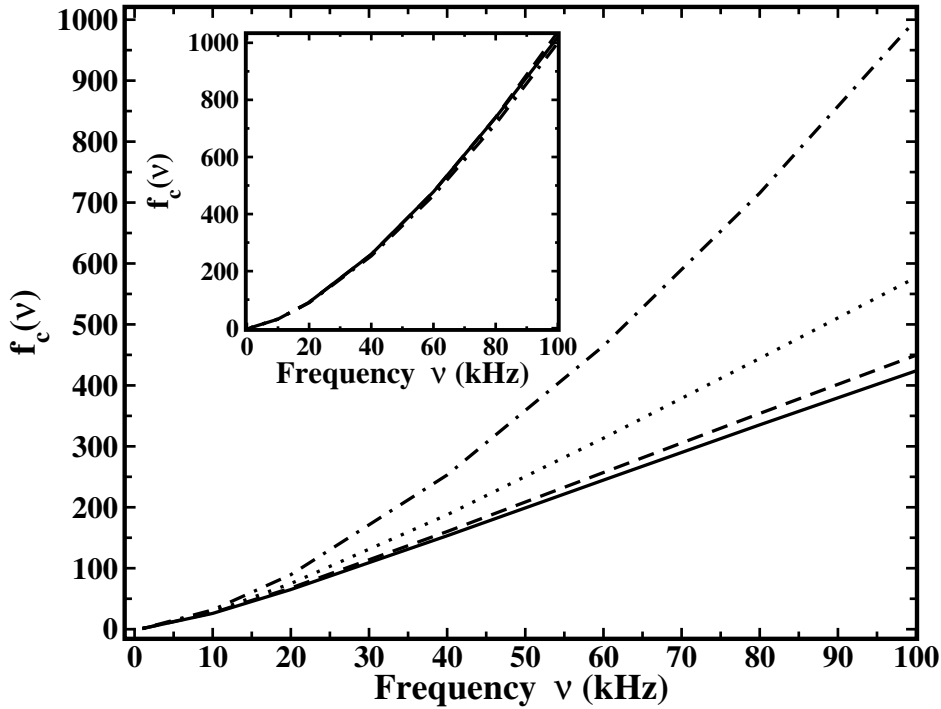


Figure 5.16: Dependence of the enhancement factor f_c on the trap frequency $\nu = \omega/(2\pi)$ for ${}^6\text{Li}_2$ using the molecular (solid), the energy-independent (dots) and energy-dependent (dashes) pseudopotential, or the harmonic-oscillator (chain) wave functions. The inset shows the same curves for ${}^{39}\text{K}_2$.

obtained for ${}^6\text{Li}$ and ${}^{39}\text{K}$ are compared to each other. In the latter case the scattering length $a_{\text{sc}} = +90 a_0$ has a much smaller absolute value than for ${}^6\text{Li}$ ($a_{\text{sc}} = -2030 a_0$). Consequently, the atom-atom interaction is expected to be less important. This is confirmed by Figure 5.16. The results obtained for $f_c(\omega)$ with the aid of the different approximations discussed above are in a very good agreement with the correct result for of ${}^{39}\text{K}$. Even the simple harmonic-oscillator model predicts the enhancement factor in the constant regime very accurately.

It should be emphasized that the correct prediction of the enhancement factor by the simplified approximation works although the prediction of the rates is completely wrong (Figure 5.14) in this constant regime (small v). For a large absolute value of the scattering length (like for ${}^6\text{Li}$), i. e., for a strong atom-atom interaction, the frequency dependence of $f_c(\omega)$ predicted by the simplified models is not very accurate. In fact, the simple harmonic-oscillator model clearly overestimates the enhancement factor for large ω . The pseudopotential approximation yields much better results, especially if the energy-dependent scattering length a_E is used.

Since Equation (5.12) is useful for obtaining an estimate of the enhancement factor $f_c(\omega)$ but the procedure to calculate $\frac{\partial E}{\partial \xi}$ required for obtaining $A(\omega)$ is rather complicated, it is interesting to test whether $A(\omega)$ can alternatively be evaluated from an expansion of the energy E at $\xi = 0$. Using the relation $\frac{\partial x}{\partial \xi} = \left(\frac{\partial \xi}{\partial x}\right)^{-1}$ it is straightforward to determine an expansion for the scaled energy

$$x(\xi) = \frac{3}{2} + \sum_{n=0}^{\infty} \frac{1}{(n+1)!} \left. \frac{\partial^{(n)} F(x)}{\partial x^{(n)}} \right|_{x=3/2} \xi^{n+1} \quad (5.14)$$

with

$$F(x) = - \frac{2\sqrt{2} \Gamma\left[\frac{3}{4} - \frac{x}{2}\right]}{\Gamma\left[\frac{1}{4} - \frac{x}{2}\right] \psi\left[\frac{1}{4} - \frac{x}{2}\right] - \psi\left[\frac{3}{4} - \frac{x}{2}\right]} \quad (5.15)$$

and the digamma function ψ . The zero- and first-order terms of the expansion (5.14) are from Busch *et al.* [95]. Using Equations (5.14) and (5.12)

$$f_c^{\text{pseudo}}(\omega) = \frac{\sum_{n=0}^{\infty} \frac{1}{n!} \left. \frac{\partial^{(n)} F(x)}{\partial x^{(n)}} \right|_{x=3/2} \xi^n}{\sum_{n=0}^{\infty} \frac{1}{n!} \left. \frac{\partial^{(n)} F(x)}{\partial x^{(n)}} \right|_{x=3/2} \xi_{\text{ref}}^n} \left(\frac{\omega}{\omega_{\text{ref}}}\right)^{\frac{3}{2}} \quad (5.16)$$

is obtained with $\xi_{\text{ref}} = \frac{a_{\text{sc}}}{a_{\text{ho,ref}}}$. Note, Equation (5.16) can also be used for the evaluation of $g_c(\omega, a_{\text{sc}})$ if ξ_{ref} is replaced by $\tilde{\xi}_{\text{ref}} = \frac{a_{\text{sc,ref}}}{a_{\text{ho,ref}}}$ in the denominator.

5.5 Conclusion and discussion

Summary of the results

The influence of a tight isotropic harmonic trap on the photoassociation process has been investigated for alkali atoms. It is found that for most of the

states (the ones in the constant regime) there is an identical enhancement as the trap frequency increases. This enhancement can reach 3 orders of magnitude for trap frequencies of about 100 kHz as they are reported in literature. While the enhancement itself agrees at least qualitatively with the concept of confinement of the initial-state wave function, also trap-induced suppressed photoassociation is possible. In fact, as a simple sum rule confirms, any enhancement must be accompanied by suppression. The physical origin of this suppression is the trap-induced confinement of the initial-state wave function of relative motion within a radius that is smaller than the mean internuclear separation of the least bound vibrational states in the electronic target state. Since in the present calculation both initial and final state are exposed to the same harmonic trap, this result may appear surprising. While the explanation is based on the different long-range behaviors of the two involved electronic states, the effect itself may be very interesting in terms of, e. g., quantum information.

Consider for example an optical lattice as trapping potential. The initial (unbound) atom pair is (for sufficient trap depths) located within a single lattice site (Mott insulator state). In the photoassociated state it could, however, reach into and thus communicate with the neighbor site, if the lattice parameters are appropriately chosen. Such a scenario could be used for a controlled logical operation (two-qubit gate) like the CNOT. Since the latter forms together with single-qubit gates a universal gate, this could provide a starting point for a quantum computer. Alternatively, it may be interesting to use the fact that if a single spot with the dimension of the trap length a_{ho} or a specific site in an optical lattice can be addressed, then the atoms would only respond, if they are in their (unbound) initial state. If they are in the photoassociated excited state, they would on the other hand be located outside the trap and thus would not respond. For this it is already sufficient, if they are (predominantly) located in the classically forbidden regime. Also, modifying the trap frequency it is possible to block the photoassociation process on demand. The trap frequency is then varied in such a fashion that a specific final state resonantly addressed with a laser with sufficiently small bandwidth belongs either to the constant or to the cut-off regime.

A further important finding is that the influence of a tight trap on the photoassociation spectra (as a function of the final vibrational state) for different alkali atoms is structurally very similar, independent whether photoassociation starts from the singlet or triplet ground state. Also the type of interaction (strong or weak as well as repulsive or attractive) does not lead to a substantial modification of the trap influence. The only exception is a strong repulsive interaction that leads to a pronounced window in the photoassociation spectrum. The reason is the position of the last node in

the initial-state wave function that in this case is located at a relatively large value of R and leads to a cancellation effect in the overlap with the final state. The nodal position depends strongly on a_{sc} , but only for very tight traps also on ω . As has been discussed previously [129, 130], the position of the window may be used for a scattering-length determination. This will also approximately work for not too tight traps, but the trap influence has to be considered for very tight ones. Alternatively, the window provides a control facility, since the transition to a single state can be selectively suppressed. In very tight traps this effect is not only more pronounced, but in addition the transitions to the neighbor states are further enhanced. This could open up a new road to control in the context of the presently on-going discussion of using femtosecond lasers for creating non-stationary wave packets in the electronic excited state [132–134]. One of the problems encountered in this approach is the difficulty to shape the wave packet, since the high-lying vibrational states that have a reasonable transition rate are energetically very closely spaced and thus the shape of the wavepacket is determined by the Franck-Condon factors that cannot easily be manipulated but strongly increase as a function of v .

In view of the question how to enhance photoassociation or related association schemes (like Raman-based ones) the investigation of the enhancement factors $g^v(\omega, a_{sc})$, especially their values in the constant regime ($g_c(\omega, a_{sc})$) are most important. It shows that not only increasing the tightness of the trap (enlarging ω) leads to an enhancement of the photoassociation rate, but a similar effect can be achieved by increasing the interaction strength $|a_{sc}|$. Most interestingly, these two enhancement factors work practically independently of each other, i. e., it is possible to use both effects in a constructive fashion and to obtain a multiplicative overall enhancement factor. For a 100 kHz trap and a scattering length $|a_{sc}|$ of the order of 2000 an enhancement factor (uniform for all states in the constant regime) of 5 to 6 orders of magnitude is found compared to the case of a shallow 1 kHz trap and $|a_{sc}| = 0$. On the other hand, the highest lying states are less enhanced or can even be suppressed due to the trap. However, these states are less practical for the purpose of creating molecules in their electronic ground state, since they have very long vibrational periods and (as is discussed below) short radiative lifetimes. Usually, the Franck-Condon factors with the bound vibrational levels of the electronic ground state are also very small. From a practical point of view these highest lying states are disadvantageous, since they are close to the dissociation threshold and thus a very narrow photoassociation laser pulse would be required in order to prevent substantial photoinduced dissociation.

A comparison of the results obtained for the realistic atom-atom interac-

tion potential with the ones obtained using the approximate pseudopotential approximation or ignoring the interaction at all shows that these approximations yield only for the transitions to very high lying vibrational states a good estimate of the photoassociation rate. Nevertheless, despite the complete failure of predicting the rates to low lying states, these models allow to determine the enhancement factor in the constant regime. For weakly interacting atoms (small $|a_{\text{sc}}|$) already the pure harmonic-oscillator model (ignoring the atomic interaction) leads to a reasonable prediction of the trap-induced enhancement factor $f_c(\omega)$. However, the trap-induced shift of the position of the photoassociation window that occurs for large repulsive interactions is often strongly overestimated by the pseudopotential approximation.

Influence of higher order atomic structures on the results

In the construction of the potential curves the fine and hyperfine interactions were excluded and thus it is of course of interest whether their inclusion changes the conclusions. Since these interactions become important at internuclear separations at which the spin-orbit coupling and hyperfine splitting is comparable to the energy difference between the potential curves, only the long-range part and thus the high-lying vibrational states are affected. Therefore, fine and hyperfine effects modify the results obtained with either realistic (but non-relativistic) or pseudopotentials in the same way. Potential curves that include spin-orbit coupling can be constructed for alkali dimers following the recipe in [135]. We have repeated the calculation of the PA rates for the $0_g^-(1/2)$ state of ${}^6\text{Li}_2$ obtained this way. Although the absolute rates of the states above about $v = 77$ change, the overall effect of a tight trap remains unchanged. As before, a long constant regime is followed by a cut-off for the highest lying states. It is interesting to note that this is true, although the $0_g^-(1/2)$ has the peculiar property to possess R^{-6} behavior. This is a consequence of a cancellation effect between the involved R^{-3} terms. However, the new effective C_6 coefficient is orders of magnitude larger than the usual C_6 which leads to a much shallower potential of the $0_g^-(1/2)$ excited state compared to the electronic ground state. The crossing point introduced in Section 5.2.5 for $0_g^-(1/2)$ is $R_c \approx +3400 a_0$ and thus four times larger than the one of the electronic ground state.

The inclusion of hyperfine interaction for the first excited electronic state of alkali dimers is known to lead to a very complicated spectrum [40, 136]. From a comparison of the atomic hyperfine coupling of ${}^6\text{Li}$ with the vibrational spacings one expects hyperfine interactions to distort the spectrum drastically for the vibrational states $v > 96$. For lower lying states the hyperfine coupling should, however, only lead to a corresponding splitting of

the different spectral peaks [41]. In the latter case the results obtained in this work remain directly valid, but for the integral over the complete set of sidebands.

Since the goal of the present work is the investigation of the effect of tight traps on the photoassociation rate and not a quantitative prediction of a specific transition, we did not attempt to perform a full resolution of the hyperfine-coupled states close to the dissociation threshold (in the trap-free case). Instead, the range of affected vibrational levels was confirmed by composing a so-called van Vleck potential (as described in [137]) using the already discussed $0_g^-(1/2)$ and the closest lying $0_u^-(1/2)$ state. The obtained hyperfine-coupled potential curves agree until about $R = 1000 a_0$ with the original ones that do not include hyperfine interaction. From Figure 5.2 it is clear that only the states $v > 95$ should then be affected by hyperfine interaction. At about the same vibrational level the vibrational period becomes comparable to the radiative lifetime (the atomic lifetime of the 2^2P state is about 27 ns). Consequently, the peaks corresponding to transitions to different vibrational states will necessarily overlap, and even in an experiment with an infinitely narrow laser light it is not possible to individually excite a single vibrational state.

Therefore, we do not attempt to resolve this spectral regime in detail. However, the sum rule derived in Section 5.2.2 allows to predict that the main conclusions of this work are not modified due to hyperfine interaction or radiative lifetime. Since the derivation of the sum rule does not depend on the properties of the final states (they must only form a complete set), the total sum remains constant. Since the rates to the low-lying states that are practically not modified by hyperfine interaction are enhanced by the trap, this enhancement must be compensated by a decrease of the rates to the remaining highest lying states. Clearly, even if the hyperfine interaction (or radiative corrections) modifies the individual rates to the highest lying vibrational states, the sum of the rates to these states must decrease and thus show the predicted cut-off behavior. In view of the discussed experimental difficulty to resolve these states due to the radiative lifetime, a more detailed information may anyhow be of minor practical importance. Note, these very high-lying states are also of minor relevance for schemes that attempt to produce molecules in their electronic ground state, since their limited radiative lifetime does not allow them to reach to sufficiently small internuclear distances. It may be noted that other atoms like the earth alkalines show simpler spectra due to the absence of hyperfine interaction which simplifies the full theoretical treatment of photoassociation [138]. While some aspects like the sum rule can directly be applied to these systems, their different long-range behavior requires a more detailed study, if the influence of a trap

on photoassociation should be treated in detail.

Accounting for the real trapping situation

It is also important to stress that the results in this work were obtained for isotropic harmonic traps with the same trapping potential seen by both atoms. In this case center-of-mass and relative motion can be separated and in both coordinates an isotropic harmonic trap potential (with different trap lengths due to the different total and reduced masses) is encountered. As is discussed, e. g., in [97, 139] where a numerical and an analytical solution are respectively derived for the case of atoms interacting via a pseudopotential, a similar separation of center-of-mass and relative motion is possible for axially symmetric (cigar or pancake shaped) harmonic traps.

In reality, the traps for alkali atoms are of course not strictly harmonic. Since the present work focuses, however, for the initial atom pair on the lowest trap induced state the harmonic approximation should in most cases be well justified. Independently on the exact way the trap is formed (e. g., by a far off-resonant focused Gaussian laser beam or by an optical lattice), the lowest trap-induced state agrees usually well with the one obtained in the harmonic approximation, if the zero-point energy is sufficiently small. This requirement sets of course an upper scale to the applicability of the harmonic approximation with respect to the trap frequency. If ω is too large, the atom pair sees the anharmonic part of the trap. (Clearly, the trap potential must also be sufficiently deep to support trap-induced bound states, i. e., to allow for Mott insulator states in the case of an optical lattice).

An additional problem arises from the anharmonicity of a real trap: the anharmonic terms lead to a non-separability of the relative and the center-of-mass motion. In fact, a recent work discusses the possibility of using this coupling of the two motions for the creation of molecules [79]. Again, a tighter trap is expected to lead to a stronger coupling and thus finally to a breakdown of the applicability of the harmonic model.

For the final state of the considered photoassociation process there exists on the first glance an even more severe complication. Usually, the two atoms will not feel the same trapping potential, since they populate different electronic states. In the case of traps whose action is related to the induced dipole moment (which is the case for optical potentials generated with the aid of lasers that are detuned from an atomic transition), the two atoms (in the case of Li the ones in the 2^2S and the 2^2P state) will in fact see potentials with opposite sign. If the laser traps the ground-state atoms, it repels the excited ones. In the alternative case of an extremely far-off resonant trap the trapping potential is proportional to the dynamic

polarizability of the atoms. In the long-wavelength limit (as is realized, e. g., in focused CO₂ lasers [140]) the dynamic polarizability approaches the static one, $\lim_{\lambda \rightarrow \infty} \alpha(\lambda) = \alpha_{st}$. The static polarizabilities do not necessarily have opposite signs for the ground and the excited electronic state of an alkali atom, but in many cases different values. Then the trapping potentials for the initial and final states of the photoassociation process are different. The Li system appears to be a counter example, since for ⁶Li₂ the average polarizability of the $a^3\Sigma_u^+$ (2s+2s) state is predicted to be equal to $\bar{\alpha} = \alpha_{zz} = \alpha_{xx} = 2\alpha_0(2s) = 2 \times 165 = 330 a_0$. For the $1^3\Sigma_g^+$ (2s+2p_z) state one has $\alpha_{zz} = \alpha_0(2s) + \alpha_{zz}(2p_z) = 285 a_0$ and $\alpha_{xx} = \alpha_0(2s) + \alpha_{xx}(2p_z) = 292 a_0$ yielding an average polarizability $\bar{\alpha} \approx 290 a_0$ [141]. Thus the trapping potentials are expected to be very similar. This is not the case for, e. g., ⁸⁷Rb₂ where the average polarization for the $a^3\Sigma_u^+$ state is $670 a_0$ and for $1^3\Sigma_g^+$ it is $1698 a_0$ [142].

It was checked that the use of very different values of ω for determining the initial and final state wave functions does not influence the basic findings of the present work. The reason is simple. Besides the very least bound states (and of course the trap-induced ones) the final states are effectively protected by the long-range interatomic potential from seeing the trap. However, if the two atoms are exposed to different trap potentials, a separation of center-of-mass and relative motion is again not possible, even in the fully harmonic case (a fact that was, e. g., overlooked in [80]). One would again expect that this coupling increases with the difference in the trap potentials of the two involved states.

Improvement of the photoassociation efficiency by tuning atom-atom interactions

Different interaction strengths occur naturally for different alkali atoms as is well known and also evident from the explicit examples of ⁶Li, ⁷Li, and ³⁹K that were discussed in this work. According to the findings of this work the choice of a proper atom pair (with large $|a_{sc}|$) enhances the achievable photoassociation yield quite dramatically. Clearly, for practical reasons it is usually not easy to change in an existing experiment the atomic species, since the trap and cooling lasers are adapted to a specific one. In addition, the naturally existing alkali species provide only a fixed and limited number of interaction strengths.

The tunability of the interaction strength on the basis of Feshbach resonances, especially magnetic ones, marked a very important corner-stone in the research area of ultracold atomic gases. The findings of the present work strongly suggest that this tunability could be used to improve the efficiency

of photoassociation (and related) schemes. However, it has to be emphasized that it is not at all self-evident that the independence of the scattering-length variation and the one of the trap frequency as it occurs in the model used in this work is applicable to (magnetic) Feshbach resonances. Furthermore, the present work considered only the single-channel case while the proper description of a magnetic Feshbach resonance requires a multi-channel treatment. Noteworthy, a strong enhancement of the photoassociation rate by at least 2 orders of magnitude while scanning over a magnetic Feshbach resonance was predicted on the basis of a multichannel calculation for a specific ^{85}Rb resonance already in [90]. An experimental confirmation followed very shortly thereafter [143]. The explanation for the enhancement given in [90] is, however, based on an increased admixture of bound-state contribution to the initial continuum state in the vicinity of the resonance. This is evidently different from the reason for the enhancement due to large values of $|a_{\text{sc}}|$ discussed in the present work.

Chapter 6

Reaching the absolute lowest state via photoassociation

In contrast to homonuclear systems, in heteronuclear systems the presence of a dipole moment allows transitions from two free ground-state atoms interacting via the ground triplet or singlet potential to the different vibrational levels of the same ground triplet or singlet potential. This may be done via one-photon stimulated radiative photoassociation. The lowest possible molecular ground state is very important for investigation of physical phenomena, because in this state fundamental properties of atoms and molecules can be more easily studied. In view of the very important question of how the efficiency of photoassociation can be improved, results of the previous Chapter 5 reveal that the use of a large scattering length is favorable. This conclusion is based on a study of the photoassociation into final excited states, and moreover the investigation is made in the framework of the single-channel approximation. Whether the conclusion still holds for transitions to the final ground states is, however, questionable. Besides, the enhancement of the photoassociation rate for large scattering lengths should be further checked, if real multi-channel solutions are adopted. As was discussed in Chapter 3, the correct theoretical description of a magnetic Feshbach resonance requires a multi-channel scattering treatment. In Chapter 4, it was shown on the basis of multi-channel solutions that the reduction of the channel number to one can still conserve essential physics. This statement can be further checked by considering relevant physical observables, like the photoassociation rate, and the consequences of this approximation for the photoassociation spectrum should also be understood. In this chapter, the photoassociation to the lowest state is considered. A strong enhancement of the photoassociation rate around a Feshbach resonance is observed, and its reasons are discussed. For this specific study, the applicability of the single-channel approach is further

tested.

6.1 Reaching the lowest state of ${}^6\text{Li}-{}^{87}\text{Rb}$

For two ultracold atoms the stimulated one-step photoassociation rate $\Gamma_{\downarrow}^v(a_{\text{sc}})$ down to lower vibrational states within the same electronic state (DPA) is proportional to the intensity \mathcal{I} of the association laser and to the squared dipole transition moment [129]

$$I^v(a_{\text{sc}}) = \left| \int_0^{\infty} \Phi^v(R) D(R) \Phi^{\epsilon}(R; a_{\text{sc}}) dR \right|^2 . \quad (6.1)$$

The rate is proportional to the PA laser intensity \mathcal{I} , and thus equal to

$$\Gamma_{\downarrow}^v(a_{\text{sc}}) = 4\pi^2 \mathcal{I} I^v(a_{\text{sc}}) . \quad (6.2)$$

In Equation (6.1) $\Phi^{\epsilon}(R; a_{\text{sc}})/R$ and $\Phi^v(R)/R$ are the wave functions of the initial and final states of the DPA process, respectively. The latter is the bound vibrational state v . The initial wave function Φ^{ϵ} depends on the collision energy ϵ of the two atoms and on the s -wave scattering length a_{sc} . Since the radial density is proportional to $|\Psi|^2$, it is convenient to discuss $\Psi(R)$ instead of the true vibrational wave function $\Psi(R)/R$. This will be done in the following where $\Psi(R)$ is for simplicity called vibrational wave function. In Equation (6.1), $D(R)$ is the (R -dependent) electronic transition dipole matrix element.

Equation (6.1) is only valid within the dipole approximation, as it was already discussed for the rate for the PA process in Section 5.2.1. It is supposed to be applicable, if the photon wavelength is much larger than the spatial extension of the atomic or molecular system. The shortest photoassociation laser wavelength corresponds to the transition to the lowest vibrational state. Although the spatial extension of the initial state is infinite and so the dipole approximation is only valid for the final state, it is still possible to neglect the higher-order effects for the purposes of the present study. It is noteworthy that the integral of Equation (6.1) is finite, as it contains a finite wave function $\Phi^v(R)$ as a factor.

The deepest bound vibrational levels of the ${}^6\text{Li}-{}^{87}\text{Rb}$ dimer belong to the singlet $X^1\Sigma^+$ electronic state. The DPA rate will be determined for the transition into the lowest bound vibrational level of this electronic state. In order to compare the multi-channel or single-channel approaches, the photoassociation rates for this transition will be compared considering different approximations for the initial wave function Φ^{ϵ} .

6.1 Reaching the lowest state of ${}^6\text{Li}-{}^{87}\text{Rb}$

For symmetry reasons, the transitions between singlet and triplet electronic states are forbidden, for the presently considered interactions. Therefore, only singlet components of the multi-channel wave function Φ^ϵ contribute to the rate, if a transition to the $X^1\Sigma^+$ electronic state is considered. Hence, integrals of Equation (6.1) are non-zero only for the $|S_1\rangle$ and $|S_2\rangle$ states of the multi-channel solution. The influence of the resonant magnetic field may be studied using the broad and narrow resonances presented in Chapter 3. As was shown in that chapter, in the presence of the resonant magnetic field, the amplitude of the wave function for the $|S_1\rangle$ state is strongly enhanced in the vicinity of the broad resonance, while the one for the $|S_2\rangle$ state stays almost unperturbed for all B values around the resonance, and even in the off-resonant case (Figure 3.7). Therefore, the main contribution to the rate (6.2) is coming from the ϕ_{S_1} function for the broad resonance. For the completeness of study the photoassociation will be also considered for the mentioned narrow resonance.

It is noteworthy that, although the coupling between different channels breaks the orthogonality of the multi-channel wave functions, this is just a slight disturbance. The integral (6.1) differs from zero mainly because it contains $D(R)$ as a factor. In order to calculate the absolute rates Γ_\downarrow^v , the most accurate electronic transition dipole matrix elements must be used. Data for $D(R)$ of ${}^6\text{Li}-{}^{87}\text{Rb}$ are given by Aymar and Dulieu in [144].

The DPA process for the multi-channel and single-channel cases are illustrated in Figure 6.1. The comparison of the multi-channel wave function ϕ_{S_1}

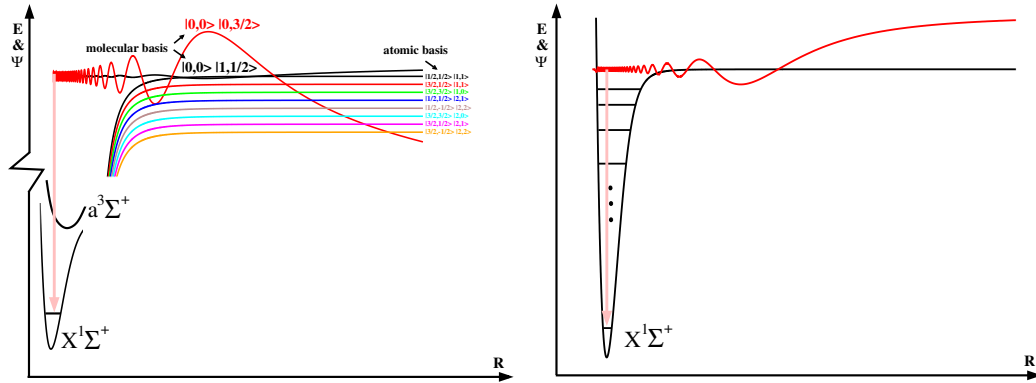


Figure 6.1: Schematic representation (not to scale) of the DPA process in a magnetic field for the ${}^6\text{Li}-{}^{87}\text{Rb}$: (a) transition to a deeply bound vibrational level of the $X^1\Sigma^+$, starting from mixture of the $|S_1\rangle$ and $|S_2\rangle$ molecular states, (b) two free atoms interacting via a pure singlet electronic state, scattering with almost zero energy and transiting to a deeply bound vibrational level.

and the single-channel φ^w solutions (where the φ^w function is obtained by the variation of the long-range van der Waals part of the interatomic interaction potential) showed (Section 4.2.2) that they do not differ structurally. The functions match if the φ^w wave function is multiplied by the proper constant C^w (Equation 4.11). If the 1%-2% difference around $R \sim 20 a_0$ is ignored, then the absolute rates Γ_{\downarrow}^v calculated using the single-channel and multi-channel approaches differ by $(C^w)^2$. However, in order to find C^w , the multi-channel solution must be available. This makes the single-channel solution useless for the calculation of the absolute rate. However, in cases where the relative rate is of practical importance, it can be calculated using both approaches (single-channel or multi-channel). The relative and absolute rates within the single-channel approach are studied presently considering an alternative s -variation (variation of the inner wall of the atom-atom interaction potential). In this case, the single-channel wave function does not only differ from appropriate multi-channel one by the $(C^s)^2$ prefactor but is also modified at the interatomic distances relevant for the Γ_{\downarrow}^v calculation.

A change of a_{sc} leads to an increase or decrease of Γ_{\downarrow}^v . In order to quantify the magnitude of this change, an enhancement or suppression factor may be introduced [100]

$$g^v(a_{sc}) = \frac{\Gamma_{\downarrow}^v(a_{sc})}{\Gamma_{\downarrow}^v(a_{sc}^{\text{ref}})} = \frac{I^v(a_{sc})}{I^v(a_{sc}^{\text{ref}})} \quad (6.3)$$

It describes the relative enhancement [$g^v > 1$] or suppression [$g^v < 1$] of the DPA rate at a given a_{sc} vs. a reference scattering length a_{sc}^{ref} , for a specific final state v . Although it may appear to be most natural to choose $a_{sc}^{\text{ref}} = 0$, a large non-zero value offers some advantages. In this case, $I^v(a_{sc}^{\text{ref}})$ is not very small, therefore large numerical errors are avoided.

In order to investigate the general trend of $I^v(a_{sc})$ a linear function may be adopted instead of the full electronic transition dipole matrix element $D(R)$. Figure 6.2(a) presents the squared dipole transition moments for the broad I_B^0 and narrow I_N^0 resonances of the multi-channel approach as well as for the single-channel approximation with s -variation I_s^0 for $D(R) \sim R$.

As is seen from Figure 6.2(a), all three squared dipole transition moments have the same trend, but larger values are observed for the broad resonance of the multi-channel case. As is seen from Figure 6.2(a), the single-channel approximation results in the smallest values. There is also a pronounced minimum for small a_{sc} in all three rates. For I_B^0 the minimum is located at $\sim -22 a_0$, for I_N^0 at $\sim -19 a_0$, and for I_s^0 at $\sim 95 a_0$. The shift between the minima for broad vs. narrow resonance is entirely due to the different amplitudes of the initial functions corresponding to the same value of the scattering length. This shift is very small and, therefore, the difference in amplitudes

affects the minimum location only slightly. For the single-channel approximation the minimum in I_s^0 is shifted relative to the multi-channel minima towards larger values. This is mainly due to the fact that the initial wave function obtained using the s -variation is deformed at small internuclear distances (Figure 4.3(b)). Although the narrow resonance shows the largest rate, in an experiment the DPA process is more efficient for the broad resonance because three-body losses can be minimized in this case.

Figure 6.2(b) shows the suppression factors g^0 corresponding to the squared dipole transition moments presented in Figure 6.2(a). The value $a_{\text{sc}}^{\text{ref}} = 15000 a_0$ is chosen as the reference scattering length. As is evident from

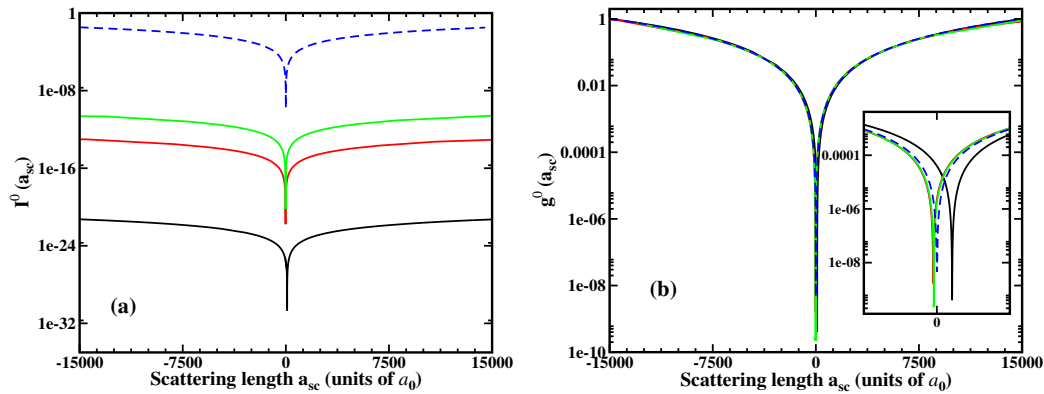


Figure 6.2: (a) The squared dipole transition moments I^0 and (b) suppression factor g^0 as functions of the scattering length for the multi-channel solutions around the narrow (green solid) and broad (red solid) resonances, the single-channel approximation being obtained by s -variation (black solid). The blue dashed line corresponds to a simple estimate given by Equation (6.4). (The inset in figure (b) shows the small a_{sc} range on an enlarged scale.)

Figure 6.2(b), all approaches show almost the same behavior. They differ only in a narrow range of small scattering lengths, as is highlighted by the inset in Figure 6.2(b). This small mismatch corresponds to that in I^0 values, and occurs due to the above mentioned difference in the amplitude and structure of the initial wave functions. Additionally, Figure 6.2 contains the simple estimate [93, 129] for g^0

$$g^0(a_{\text{sc}}) \approx \frac{\sin^2(\arctan[-ka_{\text{sc}}])}{\sin^2(\arctan[-ka_{\text{sc}}^{\text{ref}}])} \quad (6.4)$$

based on the renormalization of the free-solution (3.14). As can be seen from Figure 6.2(a), the general trend of I^0 is reproduced correctly but the amplitude is wrong because Equation (6.4) implies that an approximate depen-

dence for I^0 is used instead of Equation (6.2). In spite of this, Figure (6.2)(b) shows that the function g^0 is reproduced accurately.

6.2 Conclusion

As a result of the I^v and g^v analysis, it turns out that neither the details of the interatomic nor magnetic-field interactions are relevant either for the g^0 calculation or for the analysis of the $I^0(a_{sc})$ trend. Additional investigations show that the relative rates g^v for transition into all other $v \neq 0$ levels of the singlet and even triplet states are equal to g^0 obtained above. Except for a slight shift for small a_{sc} (Figure (6.2)), g^v values appear to be state independent, which means that all final levels v of the DPA process belong to the *constant regime* introduced for the PA process in Section 5.2.4. A simple single-channel model turns out to be adequate to calculate the relative enhancement of the photoassociation process. In view of the very important question how to optimize the efficiency of DPA, Figure 6.2 reveals that the use of a large scattering length is favorable.

To conclude the applicability of the single-channel approach for the DPA or PA study, not only s variation and μ variation, but also all other v -variational schemes derived in Chapter 4 are sufficient for the $I^v(a_{sc})$ study. Although only s variation and μ variation are analyzed in this thesis, this conclusion can be drawn from the shape of the wave functions of the remaining v -variational schemes. Different $I^v(v; a_{sc}^{fix})$ for a fixed scattering length a_{sc}^{fix} in the constant regime are smoothly changing minima and maxima (Chapter 5, Figure 5.4(a)). However, the function $I^v(v; a_{sc}^{fix})$ obtained by the single-channel approach is quantitatively modified compared to the multi-channel result. The smallest modification of the function shape is observed for the w variation where the nodal structure is slightly perturbed and only amplitudes can deviate significantly. Larger modifications, and even strong changes, in the minima and maxima positions can occur if the J -, μ -, and s -variational schemes are used. Nevertheless, the general structure of $I^v(v; a_{sc}^{fix})$ is still reproduced even with these approximations. It should, however, be remembered that the single-channel approach cannot be relied upon, if absolute values of $I^v(a_{sc})$ are important, because the amplitudes of the wave functions are not determined accurately and the matching constant C^v for the single-channel wave function must be used. Only if vibrational levels of higher excited state are considered where the outer-turning points are beyond the intermediate range ($\sim 20 a_0$ for ${}^6\text{Li}$ - ${}^{87}\text{Rb}$ singlet state), the mentioned matching constant is no longer needed. In this case, all the single-channel schemes (except the w -variation) produce quantitatively correct results because the

long-range part of the wave function is correct.

Since all single-channel variational schemes appear to have nodal structure errors at some range, care must be exercised when using them for studies of dynamical properties implying the solution of the time-dependent Schrödinger equation. If, e. g., the extreme case where the single-channel approach with a pseudopotential is considered, the nodal structure is altogether absent. With this approximation, only the long-range part of the wave function is correct, but it completely fails at short range. Hence, the repulsion of the wave packet from the zero point of R results in an error with accumulative character.

Chapter 7

Theoretical approach for two atoms in a 3D optical lattice

In Chapter 5 the influence of the external confinement on the photoassociation process was analyzed for isotropic harmonic traps with the same trapping potential seen by both atoms. In this case, the center-of-mass and relative motions can be separated and in both coordinates an isotropic harmonic trap potential is encountered. In reality, the traps are of course not strictly harmonic and in such approximation some important features of the real trap can be lost. For example, in the case of an optical lattice formed by superimposing orthogonal standing light waves, the correct sinusoidal potential exhibits an energy band with a spread of energies while the harmonic potential possesses a discrete equidistant spectrum. Due to the anharmonicity of a real trap the separability of the relative and the center-of-mass motions is lost. In fact, even within the harmonic approximation, the different trapping potentials experienced by the two atoms lead to a coupling of center-of-mass and relative motion. This situation occurs, e. g., for heteronuclear atom pairs or two atoms of the same kind but in different electronic states. In order to tackle these problems a theoretical approach has been developed in this work that allows an investigation of two atoms, trapped in a 3D optical lattice of the \sin^2/\cos^2 form and interacting via a realistic central potential. With this choice of an anharmonic trapping potential and interaction potential type, the full 6D problem must be solved. In this chapter, a theoretical approach is developed that allows this problem to be solved exactly. Furthermore, this chapter provides the mathematical description of the developed theoretical approach. Also the full consideration of the lattice symmetry and possible indistinguishability of atoms is presented. The development of the method is carried out in such a way as to minimize the need for numerical calculations. Where available, analytical results are provided.

7.1 Trapping potential

If an atom is placed into a laser field, the atomic energy levels are shifted due to the dynamical Stark effect. If the detuning of the light field with respect to the transition frequency is positive (“red detuned”), the excited state shifts upwards and the ground state shifts downwards by the same amount. In the case of negative detuning (“blue detuning”), the shifts are opposite. The magnitude of the energy shift depends on the detuning, the laser intensity, and the transition strength between the two levels. This energy shift may be regarded as an effective potential

$$V(\vec{r}) = -\frac{1}{2} \alpha \langle \vec{E}(\vec{r}, t)^2 \rangle \quad (7.1)$$

in which the atom moves. In Equation (7.1) α is the polarizability that depends generally on the laser frequency. Its sign depends on the detuning. If the time-averaged field varies with position, the shift of the energy due to the field gives rise to a dipole force on the atom. If the frequency of the light is tuned to the red the dipole force pulls the atom towards the intensity maxima of the field. In the case of the blue detuning the atoms are repelled from the intensity maxima.

Depending on the value of the detuning the laser field can be classified as *far-off-resonant* or *resonant* (almost zero detuning). In case of far-off-resonant laser field the detuning is very far from any atomic resonance. These fields are very suitable for the construction of a periodic OL. If a laser field forms a standing wave in space, the atoms placed in this field experience a periodic potential. If three independent laser fields are turned on along three spatial directions, a three-dimensional lattice potential is formed,

$$\hat{V}_{\text{trap},j} = \sum_{c=x,y,z} V_c^j \sin^2(k_c c_j) \quad . \quad (7.2)$$

Here V_c^j is the potential depth acting on the particle j (along the direction c) and it is equal to the product of the laser intensity I_c and the polarizability of the particle j . $k_c = 2\pi/\lambda_c$ is the wave vector and λ_c is the wavelength of the laser creating the lattice potential along the coordinate c . The OL period is $\lambda_c/2$.

7.1.1 Outline of the exact theoretical description

The Hamiltonian describing the interaction of two atoms with coordinate vectors \vec{r}_1 and \vec{r}_2 trapped in a three-dimensional optical lattice is given by

$$\hat{H}(\vec{r}_1, \vec{r}_2) = \hat{T}_1(\vec{r}_1) + \hat{T}_2(\vec{r}_2) + \hat{U}(\vec{r}_1, \vec{r}_2) + \hat{V}_{\text{trap},1}(\vec{r}_1) + \hat{V}_{\text{trap},2}(\vec{r}_2) \quad (7.3)$$

where \hat{T}_j is the kinetic energy operator for particle j , \hat{U} is the atom-atom interaction potential, and $\hat{V}_{\text{trap},j}$ is the trapping potential for particle j in the form of Equation (7.2).

A direct solution of the Schrödinger equation with the Hamiltonian given in the form of Equation (7.3) is complicated, since \hat{U} depends in general on all six coordinates describing the two-particle system, even if the atom-atom interaction is central, i. e., $\hat{U} = \hat{U}(r)$ with $r = |\vec{r}_1 - \vec{r}_2|$. For realistic interatomic interaction potentials, there is no separability and this leads to very demanding six-dimensional integrals. Therefore, it is more convenient to treat the two-particle problem in COM and REL motion coordinates. If spherical coordinates are adopted, a central interaction potential leads to a dependence on the radial coordinate only.

On the other hand, the formulation of the two-particle problem in COM and REL coordinates complicates the treatment of the trapping potential, because its separability in Cartesian coordinates is lost in the COM and REL coordinate system. However, performing a Taylor expansion of the sinusoidal trapping potential (7.2) around the origin simplifies the problem drastically, because the angular parts for matrix elements of the corresponding eigenproblem can be analytically integrated for the case of a central interatomic interaction potential. For two identical atoms in the same state, the use of the harmonic approximation for the trapping potential even leads to complete separability in COM and REL coordinates [83]. If the true atom-atom interaction is further replaced by a δ -function pseudopotential, the Schrödinger equation possesses an analytical solution for both isotropic and anisotropic harmonic traps [95, 139]. It is noteworthy that, even within the harmonic approximation, the separability is lost, if the two atoms experience different trapping potentials. This is the case, if a heteronuclear system or two identical atoms in different electronic states are considered.

After performing the Taylor expansion of the sinusoidal trapping potential (7.2) around the origin, the transformation of the Hamiltonian (7.3) into the COM and REL coordinate systems leads to a Hamiltonian of the form

$$\hat{H}(\vec{R}, \vec{r}) = \hat{h}_{\text{COM}}(\vec{R}) + \hat{h}_{\text{REL}}(\vec{r}) + \hat{W}(\vec{R}, \vec{r}) \quad (7.4)$$

with

$$\hat{h}_{\text{COM}}(\vec{R}) = \hat{t}(\vec{R}) + \hat{v}_{\text{OL}}(\vec{R}), \quad (7.5)$$

$$\hat{h}_{\text{REL}}(\vec{r}) = \hat{T}(\vec{r}) + \hat{V}_{\text{OL}}(\vec{r}) + \hat{U}(r) \quad . \quad (7.6)$$

It is worth emphasizing that in the present formulation only the truly non-separable terms (represented by products of COM and REL coordinates) are

left in the coupling term \hat{W} . All separable terms of the OL potential are included into the COM and REL Hamiltonians \hat{h}_{COM} and \hat{h}_{REL} respectively.

In the first step, the eigenstates and eigenvalues of the COM and REL Hamiltonians are obtained independently of each other by means of a numerical solution of the corresponding stationary Schrödinger equations,

$$\hat{h}_{\text{COM}} |\psi_i\rangle = \varepsilon_i |\psi_i\rangle \quad (7.7)$$

and

$$\hat{h}_{\text{REL}} |\phi_i\rangle = \epsilon_i |\phi_i\rangle \quad . \quad (7.8)$$

The wavefunctions $\psi(\vec{R})$ and $\phi(\vec{r})$ are then used to form the configuration state functions $\Phi_k(\vec{R}, \vec{r}) = \psi_{i_k}(\vec{R}) \phi_{j_k}(\vec{r})$. The stationary Schrödinger equation with the full Hamiltonian is given in Equation (7.4). The equation

$$\hat{H} |\Psi_i\rangle = \mathcal{E}_i |\Psi_i\rangle \quad , \quad (7.9)$$

is then solved by expanding Ψ as $\Psi(\vec{R}, \vec{r}) = \sum_k \tilde{C}_k \Phi_k(\vec{R}, \vec{r})$. Insertion of this expansion into Equation (7.9) leads to a matrix eigenvalue problem (Appendix A), which is solved numerically and yields the energies \mathcal{E}_i and eigenvector coefficients \tilde{C}_k . The detailed realization of this approach is described in the following.

7.2 Spherical harmonics approach (SHA)

7.2.1 Center-of-mass and relative motion coordinate systems

The transformation from absolute (ABS) coordinates of two particles $\{\vec{r}_1, \vec{r}_2\}$ to the COM and REL motion coordinates in the Cartesian frame $\{\vec{R}, \vec{r}\}$ is

$$\begin{aligned} \vec{r} &= \vec{r}_1 - \vec{r}_2 \quad , \\ \vec{R} &= \mu_1 \vec{r}_1 + \mu_2 \vec{r}_2 \quad , \end{aligned} \quad (7.10)$$

and the reverse transformation is

$$\begin{aligned} \vec{r}_1 &= \vec{R} + \mu_2 \vec{r} \quad , \\ \vec{r}_2 &= \vec{R} - \mu_1 \vec{r} \end{aligned} \quad (7.11)$$

where $\mu_1 = m_1/(m_1 + m_2)$ and $\mu_2 = m_2/(m_1 + m_2)$. The transformation from COM and REL motion coordinates in, the Cartesian frame to COM

and REL motion coordinates in the spherical frame $\{R, \Theta, \Phi, r, \theta, \phi\}$ with azimuthal $\{\phi, \Phi\} \in [0, 2\pi]$ and polar $\{\theta, \Theta\} \in [0, \pi]$ coordinates is

$$\begin{aligned} x &= \varrho \cos(\varphi) \sin(\vartheta) \quad , \\ y &= \varrho \sin(\varphi) \sin(\vartheta) \quad , \\ z &= \varrho \cos(\vartheta) \quad . \end{aligned} \quad (7.12)$$

and the reverse transformation is

$$\begin{aligned} \varrho &= \sqrt{x^2 + y^2 + z^2} \quad , \\ \vartheta &= \arctan\left(\frac{\sqrt{x^2 + y^2}}{z}\right) \quad , \\ \varphi &= \arctan\left(\frac{y}{x}\right) \quad . \end{aligned} \quad (7.13)$$

In Equations (7.12) and (7.13), ϱ , φ , and ϑ are respective radial or angular parts of the COM and REL motion coordinates in spherical frame.

A two-step transformation of coordinates

$$\{\vec{r}_1, \vec{r}_2\} \xrightarrow{\text{I}} \{\vec{R}, \vec{r}\} \xrightarrow{\text{II}} \{R, \Theta, \Phi, \rho, \theta, \phi\} \quad (7.14)$$

must be applied to the Hamiltonian of Equation (7.3) in order to formulate the problem in a form as presented in Section 7.1.1. The transformations of Equations (7.10)-(7.11) are also used to analyze solutions in different coordinate system. The system of two atoms in a 3D space, as well as different coordinate systems, is presented in Figure 7.1.

7.2.2 Hamiltonians and trial functions

The eigenvectors of the Hamiltonians \hat{h}_{COM} , \hat{h}_{REL} , and \hat{H} (Equations (7.7)-(7.9)) can be presented as a sum of products of B splines and spherical harmonics Y . The B splines describe the radial motion and the spherical harmonics describe the angular motion. Hence, the eigenvector of the \hat{h}_{REL} Hamiltonian is

$$\phi(r, \theta, \phi) = \sum_{\alpha=1}^{N_r} \sum_{l=0}^{N_l} \sum_{m=-l}^l c_{\alpha lm} \cdot B_{\alpha}(r) \cdot Y_l^m(\theta, \phi) \quad (7.15)$$

where N_r and N_l are the number of B splines and orbital quantum numbers l respectively. In the same spirit, the eigenvector of the \hat{h}_{COM} Hamiltonian is

$$\psi(R, \Theta, \Phi) = \sum_{\beta=1}^{N_R} \sum_{L=0}^{N_L} \sum_{M=-L}^L C_{\beta LM} \cdot B_{\beta}(R) \cdot Y_L^M(\Theta, \Phi) \quad (7.16)$$

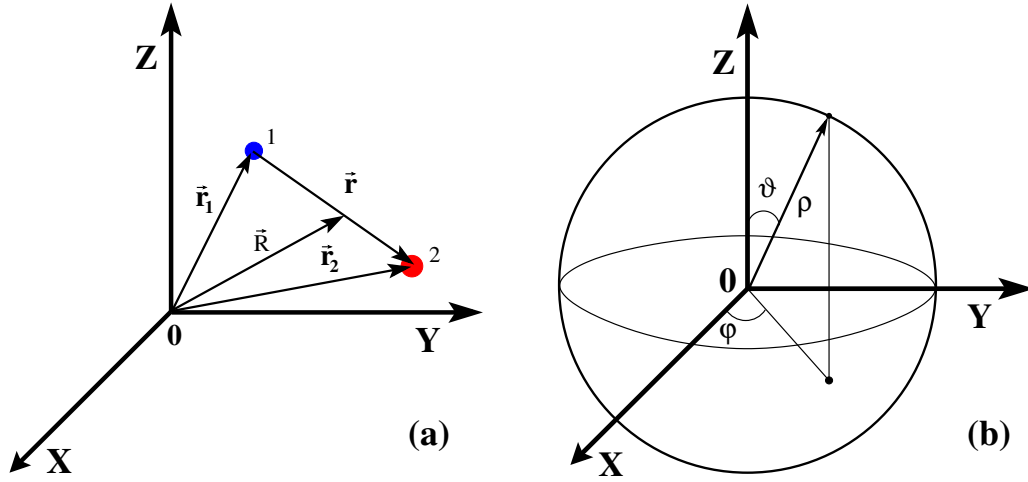


Figure 7.1: (a) Two different particles in ABS and COM-REL coordinate systems in the Cartesian frame. (b) A spherical coordinate system, with the azimuthal φ and polar ϑ angles.

where N_R and N_L are the number of B splines and orbital quantum numbers L respectively. In electronic structure calculations, the atomic basis functions of the diatomic problem are called orbitals. Similarly, different functions of Equations (7.15) and (7.16) will also be called *orbitals* with respective orbital indices (a) and (b). Different products of the COM and REL orbitals can form a *configuration*. The wave function of the exact Hamiltonian \hat{H} can be written as a superposition of configurations,

$$\begin{aligned}
 \Psi(r, \theta, \phi, R, \Theta, \Phi) &= \sum_{\mathbf{a}} \sum_{\mathbf{b}} \mathbb{K}_{\mathbf{ab}} \phi^{(\mathbf{a})}(r, \theta, \phi) \cdot \psi^{(\mathbf{b})}(R, \Theta, \Phi) \\
 &= \sum_{\mathbf{a}} \sum_{\mathbf{b}} \mathbb{K}_{\mathbf{ab}} \sum_{\alpha=1}^{N_r} \sum_{l=0}^{N_l} \sum_{m=-l}^l c_{\alpha lm}^{(\mathbf{a})} \cdot B_{\alpha}(r) \cdot Y_l^m(\theta, \phi) \\
 &\quad \times \sum_{\beta=1}^{N_R} \sum_{L=0}^{N_L} \sum_{M=-L}^L C_{\beta LM}^{(\mathbf{b})} \cdot B_{\beta}(R) \cdot Y_L^M(\Theta, \Phi) \quad . \quad (7.17)
 \end{aligned}$$

Here $\mathbb{K}_{\mathbf{ab}}$ are the expansion coefficients for different configurations. The substitution of the wave functions of Equations (7.15), (7.16) and (7.17) into respectively, the Hamiltonians of Equations (7.8), (7.7) and (7.9) leads to the

differential equations

$$\left[-\frac{1}{2\mu} \frac{\partial^2}{\partial r^2} + \frac{1}{2\mu} \frac{\hat{I}_{\text{REL}}^2}{r^2} + \hat{U}(r) + \hat{V}_{\text{OL}}(r, \theta, \phi) \right] \phi^{(\mathbf{a})}(r, \theta, \phi) = \epsilon^{(\mathbf{a})} \phi^{(\mathbf{a})}(r, \theta, \phi) \quad , \quad (7.18)$$

$$\left[-\frac{1}{2M} \frac{\partial^2}{\partial R^2} + \frac{1}{2M} \frac{\hat{I}_{\text{COM}}^2}{R^2} + \hat{v}_{\text{OL}}(R, \Theta, \Phi) \right] \psi^{(\mathbf{b})}(R, \Theta, \Phi) = \epsilon^{(\mathbf{b})} \psi^{(\mathbf{b})}(R, \Theta, \Phi) \quad , \quad (7.19)$$

$$\left[\hat{T} + \hat{t} + \hat{U} + \hat{V}_{\text{OL}} + \hat{v}_{\text{OL}} + \hat{W}_{\text{OL}} \right] \Psi_i(r, \theta, \phi, R, \Theta, \Phi) = \mathcal{E}_i \Psi(r, \theta, \phi, R, \Theta, \Phi) \quad (7.20)$$

where $\hat{\mathbf{I}}_{\text{COM}}^2$ and $\hat{\mathbf{I}}_{\text{REL}}^2$ are squared operators of the angular momentum. The kinetic energy operators in COM and REL motion coordinates in the spherical frame are

$$\hat{T} = -\frac{1}{2\mu} \left(\frac{1}{r^2} \frac{\partial}{\partial r} \left(r^2 \frac{\partial}{\partial r} \right) + \frac{1}{r^2} \overbrace{\left[\frac{1}{\sin(\theta)} \frac{\partial}{\partial \theta} \left(\sin(\theta) \frac{\partial}{\partial \theta} \right) + \frac{1}{\sin^2(\theta)} \frac{\partial^2}{\partial \phi^2} \right]}^{-\hat{\mathbf{I}}_{\text{REL}}^2} \right) \quad , \quad (7.21)$$

$$\hat{t} = -\frac{1}{2M} \left(\frac{1}{R^2} \frac{\partial}{\partial R} \left(R^2 \frac{\partial}{\partial R} \right) + \frac{1}{R^2} \overbrace{\left[\frac{1}{\sin(\Theta)} \frac{\partial}{\partial \Theta} \left(\sin(\Theta) \frac{\partial}{\partial \Theta} \right) + \frac{1}{\sin^2(\Theta)} \frac{\partial^2}{\partial \Phi^2} \right]}^{-\hat{\mathbf{I}}_{\text{COM}}^2} \right) \quad (7.22)$$

where $\mu = m_1 m_2 / (m_1 + m_2)$ and $M = m_1 + m_2$ are the reduced and total mass, respectively (not to be confused with the COM index for the L projection quantum number, e. g., in Equation (7.16)). The squared operators of the angular momentum $\hat{\mathbf{I}}_{\text{COM}}^2$ and $\hat{\mathbf{I}}_{\text{REL}}^2$ commute with the Hamiltonians \hat{h}_{COM} and \hat{h}_{REL} . Therefore, ϕ and ψ are eigenfunctions of the $\hat{\mathbf{I}}_{\text{REL}}^2$ and $\hat{\mathbf{I}}_{\text{COM}}^2$ operators with eigenvalues $l(l+1)$ and $L(L+1)$ respectively. Finally, the

Schrödinger equations (7.18), (7.19) and (7.20) together with the wave functions from Equations (7.15), (7.16) and (7.17) can be transformed to a matrix eigenvalue problem (Appendix A).

The functions in Equations (7.15), (7.16) and (7.17) are scaled functions. As before, they will be used in the analysis instead of the true wave functions, while the name “wave function” will be kept for simplicity. The wave functions must satisfy the proper boundary conditions. The first condition is that the radial part must vanish at the origin. Since the problem is considered numerically, the wave functions cannot be determined at infinity, therefore they are artificially set to zero at a finite radial distance (called the box). For particles in a trap this condition is justified. For example, the wave function exponentially decays beyond the harmonic trap wall because it is steep. If continuum eigenvalues are considered, then the box variation changes the density of states and the continuum can thus be modeled properly. The boundary conditions at zero and at the box are achieved by excluding the first and the last B spline, respectively. Therefore, the summation in Equations (7.15), (7.16) and (7.17) must be changed into $\sum_{\alpha=2}^{N_r-1}$ and $\sum_{\beta=2}^{N_R-1}$.

7.2.3 Description of the trapping potential

The optical lattice potential of the form in Equation (7.2), for two heteronuclear particles in COM and REL motion coordinates in Cartesian frame, is

$$\hat{V}_{\text{OL}}(\vec{r}_1, \vec{r}_2) = \sum_{i=1}^2 \sum_{c=\{x,y,z\}} V_c^i \sin^2\{k_c[R_c + (-1)^{i-1}\mu_{\eta_i}r_c]\} \quad (7.23)$$

where $\eta_i = i + (-1)^{i-1}$. Using trigonometric relations the OL potential can be written in the more suitable form

$$\hat{V}_{\text{OL}}(\vec{r}_1, \vec{r}_2) = \frac{1}{2} \sum_{i=1}^2 \sum_{c=\{x,y,z\}} V_c^i (1 + (-1)^{\eta_i} \sin(2k_c R_c) \sin(2k_c r_c \mu_{\eta_i}) - \cos(2k_c R_c) \cos(2k_c r_c \mu_{\eta_i})) \quad (7.24)$$

Equation (7.24) can be split into pure COM and REL coordinates and the coupling [79] for the case of two identical particles in the same ground state and if they are situated in a cubic lattice with equal intensities and k numbers

along each of the spatial directions

$$\hat{V}_{\text{OL}} = 2V_0 \sum_{c=\{x,y,z\}} \sin^2\left(\frac{kr_c}{2}\right) , \quad (7.25)$$

$$\hat{v}_{\text{OL}} = 2V_0 \sum_{c=\{x,y,z\}} \sin^2(kR_c) , \quad (7.26)$$

$$\hat{W} = -4V_0 \sum_{c=\{x,y,z\}} \sin^2(kR_c) \sin^2\left(\frac{kr_c}{2}\right) . \quad (7.27)$$

Generally this splitting is not possible. In order to implement the separation of the original Hamiltonian (7.3) into parts as given by Equations (7.4), the Taylor expansion of Equation (7.24) must be performed around the origin of the COM and REL motion coordinates (R_c and r_c)

$$\begin{aligned} & \sin(2k_c R_c) \sin(2k_c r_c \mu_{\eta_s}) = \\ & \sum_{j=0}^{\infty} \sum_{i=0}^{\infty} \frac{(-1)^{i+j}}{(2i+1)!(2j+1)!} (2k_c)^{2i+1} (2k_c \mu_{\eta_s})^{2j+1} R_c^{2i+1} r_c^{2j+1} , \end{aligned} \quad (7.28)$$

$$\begin{aligned} & \cos(2k_c R_c) \cos(2k_c r_c \mu_{\eta_s}) = \\ & \sum_{t=0}^{\infty} \sum_{k=0}^{\infty} \frac{(-1)^{k+t}}{(2k)!(2t)!} (2k_c)^{2k} (2k_c \mu_{\eta_s})^{2t} R_c^{2k} r_c^{2t} . \end{aligned} \quad (7.29)$$

Since the problem is considered numerically, the infinite sum must be truncated. If the expansion is restricted to the $(2n)$ th order with $n = 1, 2, 3, \dots$, infinite summations are changed according to the rules

$$\begin{aligned} & 2i + 1 + 2j + 1 \leq 2n , \\ & i \leq n - 1 - j \quad \text{while} \quad j \leq n - 1 , \\ & 2k + 2t \leq 2n , \\ & k \leq n - t \quad \text{while} \quad t \leq n . \end{aligned} \quad (7.30)$$

Hence, the OL potential can be approximated by the $(2n)$ th order Taylor expansion as

$$\begin{aligned} \hat{V}_{\text{OL}}(\vec{r}_1, \vec{r}_2) \approx & \frac{1}{2} \sum_{s=1}^2 \sum_{c=\{x,y,z\}} V_c^s [1 + \\ & (-1)^{\eta_s} \left. \sum_{j=0}^{n-1} \sum_{i=0}^{n-1-j} \mathbb{C}_{ijcs}^{\sin} R_c^{2i+1} r_c^{2j+1} - \sum_{t=0}^n \sum_{k=0}^{n-t} \mathbb{C}_{tkcs}^{\cos} R_c^{2k} r_c^{2t} \right] \end{aligned} \quad (7.31)$$

where the coefficients

$$\mathbb{C}_{ijcs}^{\sin} = \frac{(-1)^{i+j}}{(2i+1)!(2j+1)!} (2k_c)^{2i+1} (2k_c \mu_{\eta_s})^{2j+1} \quad , \quad (7.32)$$

$$\mathbb{C}_{tkcs}^{\cos} = \frac{(-1)^{k+t}}{(2k)!(2t)!} (2k_c)^{2k} (2k_c \mu_{\eta_s})^{2t} \quad (7.33)$$

are introduced for compactness of Equation (7.31).

The splitting of the potential $\hat{V}_{\text{OL}}(\vec{r}_1, \vec{r}_2)$ of Equation (7.23) into the COM, REL and coupling parts becomes now straightforward:

$$\hat{v}_{\text{OL}} = \frac{1}{2} \sum_{s=1}^2 \sum_{c=\{x,y,z\}} V_c^s [1 - \mathbb{C}_{00cs}^{\cos}] \equiv 0 \quad , \quad (7.34)$$

$$\begin{aligned} \hat{v}_{\text{OL}}(R, \Theta, \Phi) &= -\frac{1}{2} \sum_{s=1}^2 \sum_{c=\{x,y,z\}} V_c^s \sum_{k=1}^n \mathbb{C}_{0kcs}^{\cos} R_c^{2k} \\ &\stackrel{n \rightarrow \infty}{=} \sum_{s=1}^2 \sum_{c=\{x,y,z\}} V_c^s \sin^2(k_c R_c) \quad , \end{aligned} \quad (7.35)$$

$$\begin{aligned} \hat{V}_{\text{OL}}(r, \theta, \phi) &= -\frac{1}{2} \sum_{s=1}^2 \sum_{c=\{x,y,z\}} V_c^s \sum_{t=1}^n \mathbb{C}_{t0cs}^{\cos} r_c^{2t} \\ &\stackrel{n \rightarrow \infty}{=} \sum_{s=1}^2 \sum_{c=\{x,y,z\}} V_c^s \sin^2(k_c r_c \mu_{\eta_s}) \quad , \end{aligned} \quad (7.36)$$

$$\begin{aligned} \hat{W}(R, \Theta, \Phi, r, \theta, \phi) &= \\ &\frac{1}{2} \sum_{s=1}^2 \sum_{c=\{x,y,z\}} V_c^s \left[(-1)^{\eta_s} \sum_{j=0}^{n-1} \sum_{i=0}^{n-1-j} \mathbb{C}_{ijcs}^{\sin} R_c^{2i+1} r_c^{2j+1} - \right. \\ &\quad \left. \sum_{t=1}^n \sum_{k=1}^{n-t} \mathbb{C}_{tkcs}^{\cos} R_c^{2k} r_c^{2t} \right] \\ &\stackrel{n \rightarrow \infty}{=} \frac{1}{2} \sum_{s=1}^2 \sum_{c=\{x,y,z\}} V_c^s \left[(-1)^{\eta_s} \sin(2k_c R_c) \sin(2k_c r_c \mu_{\eta_s}) - \right. \\ &\quad \left. \sum_{t=1}^n \sum_{k=1}^{n-t} \mathbb{C}_{tkcs}^{\cos} R_c^{2k} r_c^{2t} \right] \quad . \end{aligned} \quad (7.37)$$

If $n = 1$ in the second term of Equation (7.37), the summation is defined by

$\sum_{t=1}^1 \sum_{k=1}^0$. The limits in the second sum do not indicate the inverse summation from 1 to 0, but rather indicate the absence of the summation. If the infinite summation is introduced again, as is shown in Equations (7.35)-(7.37), a surprising result occurs, namely, for \hat{V}_{OL} and \hat{v}_{OL} and partly for \hat{W} , the \sin^2 form is restored. However, this does not make the problem easier. Although analytical solutions for the \sin^2 -like lattice exists, the boundary conditions are not the same and the presence of the interparticle interaction requires a further transformation to the spherical frame where \sin^2 -like lattice again has a complicated non-separable argument.

7.2.4 Expansion of the trap with spherical harmonics

The use of spherical harmonics as basis functions and the expansion of the trapping potential in terms of spherical harmonics lead to an analytical form of the matrix elements. Any function of angular arguments can be represented as

$$F(\theta, \phi) = \sum_{l=0}^{\infty} \sum_{m=-l}^l \mathbb{Y}_{lm} Y_l^m(\theta, \phi) \quad (7.38)$$

where the projection coefficients \mathbb{Y}_{lm} are

$$\mathbb{Y}_{lm} = (-1)^m A_{l-m} \int_0^{\pi} d\theta \int_0^{2\pi} d\phi \sin(\theta) F(\theta, \phi) P_l^{-m}(\cos(\theta)) e^{-\mathbf{I}m\phi} \quad . \quad (7.39)$$

Here \mathbf{I} stands for imaginary unit and A_{l-m} is defined in Equation (E.1). For each Cartesian coordinate there exist projection coefficients \mathbb{Y}_{lmt}^c . For the Cartesian coordinates x, y and z in the $2t$ power these coefficients are given

by

$$\mathbb{Y}_{lmt}^x = (-1)^m A_{l-m} \times \int_0^\pi d\theta \int_0^{2\pi} d\phi \sin(\theta) \cos^{2t}(\phi) \sin^{2t}(\theta) P_l^{-m}(\cos(\theta)) e^{-\mathbf{I}m\phi} \quad , \quad (7.40)$$

$$\mathbb{Y}_{lmt}^y = (-1)^m A_{l-m} \times \int_0^\pi d\theta \int_0^{2\pi} d\phi \sin(\theta) \sin^{2t}(\phi) \sin^{2t}(\theta) P_l^{-m}(\cos(\theta)) e^{-\mathbf{I}m\phi} \quad , \quad (7.41)$$

$$\mathbb{Y}_{lmt}^z = (-1)^m A_{l-m} \times \int_0^\pi d\theta \int_0^{2\pi} d\phi \sin(\theta) \cos^{2t}(\theta) P_l^{-m}(\cos(\theta)) e^{-\mathbf{I}m\phi} \quad . \quad (7.42)$$

The integrals in Equations (7.40), (7.41) and (7.42) can be calculated analytically. Consider, for example, the integral of Equation (7.40). The application of the Euler formula for the $\cos^{2t}(\phi)$ term and the use of Equation (E.2) lead to straightforward derivation of \mathbb{Y}_{lmt}^x . The transition to the new integration variable $\xi = \cos(\theta)$ changes the integration limits from $[0, \pi]$ to $[-1, 1]$. The integral is non-zero only, if the integrand becomes symmetric in the interval $[-1, 1]$ after transformation. The associated Legendre function $P_l^m(x)$ is even if $l + |m|$ is even and odd otherwise. Since the summation index k of Equation (E.2) is integer and $0 \leq k \leq 2t$, the relation $-2t \leq m \leq 2t$ is valid and m is always even. Therefore, the integral is non-zero only if l is even. Additionally, the natural restrictions on l and m quantum numbers are $l \geq 0$ and $|m| \leq l$. Another important fact is that the functions $P_{l>2t}^{|m| \leq l, |m| \leq 2t}(x)$ are oscillatory in the interval $[-1, 1]$ and the symmetry of the integrand causes the contribution of negative and positive parts to cancel out, leading to zero integral. Hence, one more restriction on l is that $l \leq 2t$. Finally, Equation (E.3) for the integral over the associated Legendre function together with Equations (E.6), (E.7) and (E.8) must also be used. Summarizing all the above mentioned steps and restrictions on the indices, the analytical form of the \mathbb{Y}_{lmt}^x is

$$\mathbb{Y}_{lmt}^x = (-1)^{\frac{l+m}{2}} 2^{-\frac{m}{2}-t+2} A_{l-m} \pi \binom{2t}{t + \frac{m}{2}} \frac{(t - \frac{m}{2})!(t + \frac{m}{2})!(l - m - 1)!!}{(t - \frac{l}{2})!(\frac{l}{2} + \frac{m}{2})!(2t + l + 1)!!} \quad ,$$

$$l, m \text{ even}, \quad -2t \leq m \leq 2t, \quad |m| \leq l, \quad l \leq 2t \quad . \quad (7.43)$$

It is useful to know the combinations of the indices leading to non-zero integrals because the computation becomes efficient and fast.

The derivation of \mathbb{Y}_{lmt}^y is similar to \mathbb{Y}_{lmt}^x and results in

$$\mathbb{Y}_{lmt}^y = (-1)^{\frac{m}{2}} \mathbb{Y}_{lmt}^x \quad (7.44)$$

with the same limitations for the indices. In order to derive the \mathbb{Y}_{lmt}^z coefficients, Equations (E.4) and (E.9) must be used. The result of the derivation is

$$\mathbb{Y}_{lmt}^z = A_{l0} (-1)^{\frac{l}{2}} \pi \delta_{m,0} \frac{2^{\frac{l}{2}+2} (2t-1)!!}{(l+2t+1)!!} \prod_{i=0}^{l/2-1} (-t+i) \quad ,$$

$$l \text{ even, } l \leq 2t \quad . \quad (7.45)$$

The coupling potential \hat{W} of Equation (7.37) consists of two types of terms, i. e., those with even powers and those with odd powers. The expansion coefficients for the $R_c^{2k} r_c^{2t}$ terms are the same as for the potentials \hat{V}_{OL} and \hat{V}_{OL} (Equations (7.43), (7.44) and (7.45)). The expansion coefficients for the terms $R_c^{2i+1} r_c^{2j+1}$ are different. For these terms there are three more coefficients that must be found,

$$\tilde{\mathbb{Y}}_{lmj}^x = (-1)^m A_{l-m} \times \int_0^\pi d\theta \int_0^{2\pi} d\phi \sin(\theta) \cos^{2j+1}(\phi) \sin^{2j+1}(\theta) P_l^{-m}(\cos(\theta)) e^{-\mathbf{Im}\phi} \quad , \quad (7.46)$$

$$\tilde{\mathbb{Y}}_{lmj}^y = (-1)^m A_{l-m} \times \int_0^\pi d\theta \int_0^{2\pi} d\phi \sin(\theta) \sin^{2j+1}(\phi) \sin^{2j+1}(\theta) P_l^{-m}(\cos(\theta)) e^{-\mathbf{Im}\phi} \quad , \quad (7.47)$$

$$\tilde{\mathbb{Y}}_{lmj}^z = (-1)^m A_{l-m} \times \int_0^\pi d\theta \int_0^{2\pi} d\phi \sin(\theta) \cos^{2j+1}(\theta) P_l^{-m}(\cos(\theta)) e^{-\mathbf{Im}\phi} \quad . \quad (7.48)$$

The integrals in Equations (7.46), (7.47) and (7.48) can also be calculated analytically. Consider for example the integral in Equation (7.46). The

application of the Euler formula for the $\cos^{2j+1}(\phi)$ term and the use of Equations (E.2) and (E.5) leads to straightforward derivation of \tilde{Y}_{lmj}^x ,

$$\tilde{Y}_{lmj}^x = (-1)^m A_{l-m} (-1)^{\frac{l-m}{2}} \frac{\pi}{2^{2j}} \times$$

$$\binom{2j+1}{j+\frac{m+1}{2}} \frac{2^{\frac{2j+3-m}{2}} \left(\frac{2j+1-m}{2}\right)! \left(\frac{2j+1+m}{2}\right)! (l-m-1)!!}{(2j+l+2)!! \left(\frac{2j+1-l}{2}\right)! \left(\frac{m+l}{2}\right)!},$$

$$l, m \text{ odd, } -2j-1 \leq m \leq 2j+1, \quad l \leq 2j+1 \quad . \quad (7.49)$$

Likewise, the derivation of \tilde{Y}_{lmj}^y is similar to \tilde{Y}_{lmj}^x , and results in

$$\tilde{Y}_{lmj}^y = \mathbf{I} (-1)^{\frac{m-3}{2}} \tilde{Y}_{lmj}^x \quad (7.50)$$

with the same limitations on the indices as for \tilde{Y}_{lmj}^x . Finally, \tilde{Y}_{lmj}^z is

$$\tilde{Y}_{lmj}^z = A_{l0} 4\pi \delta_{m,0} (-2)^{\frac{l-1}{2}} \frac{(2j+1)!!}{(2j+l+2)!!} \prod_{i=0}^{\frac{l-3}{2}} (-j+i) \quad (7.51)$$

The OL potential expressed in terms of the spherical harmonics has the

following final form

$$\hat{V}_{\text{OL}}(r, \theta, \phi) = -\frac{1}{2} \sum_{s=1}^2 \sum_{c=\{x,y,z\}} V_c^s \sum_{t=1}^n \mathbb{C}_{t0cs}^{\text{cos}} r^{2t} \times \sum_{l=0,\{2\}}^{2t} \sum_{m=-l,\{2\}}^l \mathbb{Y}_{lmt}^c Y_l^m(\theta, \phi) \quad , \quad (7.52)$$

$$\hat{v}_{\text{OL}}(R, \Theta, \Phi) = -\frac{1}{2} \sum_{s=1}^2 \sum_{c=\{x,y,z\}} V_c^s \sum_{k=1}^n \mathbb{C}_{0kcs}^{\text{cos}} R^{2k} \sum_{L=0,\{2\}}^{2k} \sum_{M=-L,\{2\}}^L \mathbb{Y}_{LMk}^c Y_L^M(\Theta, \Phi) \quad , \quad (7.53)$$

$$\begin{aligned} \hat{W}_{\text{OL}}(R, \Theta, \Phi, r, \theta, \phi) = & \frac{1}{2} \sum_{s=1}^2 \sum_{c=\{x,y,z\}} V_c^s \left[(-1)^{\eta_s} \sum_{j=0}^{n-1} \sum_{i=0}^{n-1-j} \mathbb{C}_{ijcs}^{\text{sin}} R^{2i+1} r^{2j+1} \times \right. \\ & \sum_{l=1,\{2\}}^{2j+1} \left[\tilde{\mathbb{Y}}_{l0j}^c Y_l^0(\theta, \phi) + \sum_{m=-l,\{2\}}^l \tilde{\mathbb{Y}}_{lmj}^c Y_l^m(\theta, \phi) \right] \times \\ & \sum_{L=1,\{2\}}^{2i+1} \left[\tilde{\mathbb{Y}}_{L0i}^c Y_L^0(\Theta, \Phi) + \sum_{M=-L,\{2\}}^L \tilde{\mathbb{Y}}_{LMi}^c Y_L^M(\Theta, \Phi) \right] - \\ & \sum_{t=1}^n \sum_{k=1}^{n-t} \mathbb{C}_{tkcs}^{\text{cos}} R^{2k} r^{2t} \sum_{l=0,\{2\}}^{2t} \sum_{m=-l,\{2\}}^l \mathbb{Y}_{lmt}^c Y_l^m(\theta, \phi) \times \\ & \left. \sum_{L=0,\{2\}}^{2k} \sum_{M=-L,\{2\}}^L \mathbb{Y}_{LMk}^c Y_L^M(\Theta, \Phi) \right] . \quad (7.54) \end{aligned}$$

where, e. g., $\sum_{l=0,\{2\}}^{2t}$ stands for $\sum_{l=0,2,4,\dots}^{2t}$. In Equation (7.54), $\tilde{\mathbb{Y}}_{l0j}^x = \tilde{\mathbb{Y}}_{l0j}^y = 0$ and $\tilde{\mathbb{Y}}_{lmj}^z = 0$ for $m \neq 0$.

7.2.5 Alternative lattice potential \cos^2

Among the variety of the optical lattice geometries the \sin^2 form is the most widespread one. The use of the \sin^2 for the present method has advantages. The 22nd order of the Taylor expansion results in a triple-well potential (Figure 7.2(a)). This form was, e. g., used for Bose-Hubbard model study [145], where the present method was further tested. It is also very useful to consider

the alternative lattice form \cos^2 , because the very important in physics the double-well geometry of the trap [146] is easier obtained with this geometry. The 13th-order expansion of the \cos^2 potential already leads to double-well geometry (Figure 7.2(b)). Double-well potentials are especially interesting in the context of quantum information studies.

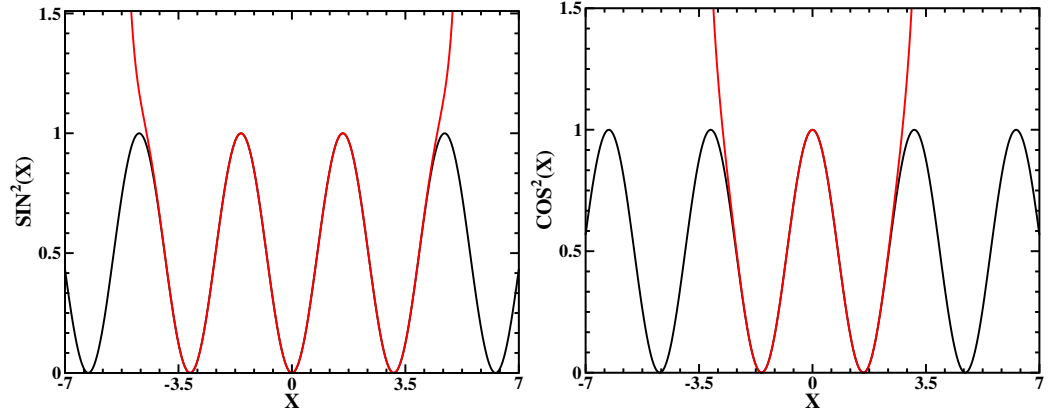


Figure 7.2: (a) The $\sin^2(x)$ function (black) together with 22nd order Taylor expansion (red). (b) The $\cos^2(x)$ function (black) together with 13th order Taylor expansion (red).

The OL potential of the \cos^2 form is

$$\hat{V}_{\text{OL}}(\vec{r}_1, \vec{r}_2) = \sum_{s=1}^2 \sum_{c=\{x,y,z\}} V_c^s \sin^2(k_c c_s + \frac{\pi}{2}) \quad . \quad (7.55)$$

Using trigonometric relations the OL potential can be written in the more suitable form

$$\hat{V}_{\text{OL}}(\vec{r}_1, \vec{r}_2) = \frac{1}{2} \sum_{s=1}^2 \sum_{c=\{x,y,z\}} V_c^s (1 + (-1)^s \sin(2k_c R_c) \sin(2k_c r_c \mu_{\eta_s}) + \cos(2k_c R_c) \cos(2k_c r_c \mu_{\eta_s})) \quad . \quad (7.56)$$

After a derivation similar to the case of the \sin^2 potential the splitting of the

OL into COM and REL motion in Cartesian frame becomes

$$\hat{v}_{\text{OL}} = \sum_{s=1}^2 \sum_{c=\{x,y,z\}} V_c^s, \quad (7.57)$$

$$\hat{v}_{\text{OL}}(R, \Theta, \Phi) = \frac{1}{2} \sum_{s=1}^2 \sum_{c=\{x,y,z\}} V_c^s \sum_{k=1}^n \mathbb{C}_{0kcs}^{\cos} R_c^{2k}, \quad (7.58)$$

$$\hat{V}_{\text{OL}}(r, \theta, \phi) = \frac{1}{2} \sum_{s=1}^2 \sum_{c=\{x,y,z\}} V_c^s \sum_{t=1}^n \mathbb{C}_{t0cs}^{\cos} r_c^{2t}, \quad (7.59)$$

$$\begin{aligned} \hat{W}(R, \Theta, \Phi, r, \theta, \phi) = \\ \frac{1}{2} \sum_{s=1}^2 \sum_{c=\{x,y,z\}} V_c^s \left[(-1)^s \sum_{j=0}^{n-1} \sum_{i=0}^{n-1-j} \mathbb{C}_{ijcs}^{\sin} R_c^{2i+1} r_c^{2j+1} + \right. \\ \left. \sum_{t=1}^n \sum_{k=1}^{n-t} \mathbb{C}_{tkcs}^{\cos} R_c^{2k} r_c^{2t} \right]. \end{aligned} \quad (7.60)$$

Equations (7.57)-(7.60) are analogous to Equations (7.34)-(7.37) for the \sin^2 -like potential.

7.2.6 Overlap and Hamiltonian matrices

The variational Rayleigh-Ritz-Galerkin approach (Appendix A) leads to the set of Equations (A.8). In this approach the integrals of the respective matrix elements must be calculated. The angular part for COM and REL motion is calculated analytically. The radial part of the problem is solved numerically.

The indices for matrix elements are denoted as $I = \{LM\beta\}$, $i = \{lm\alpha\}$ and $\mathbb{I} = \{\mathbf{(a)}, \mathbf{(b)}\}$ where orbital indices of the REL motion $\mathbf{(a)} \equiv i$ and for the COM motion $\mathbf{(b)} \equiv I$.

Overlap matrix

The overlap matrices S of the uncoupled COM and REL motion problems are not equal to the unity matrix

$$\begin{aligned} S_{ij} &= \int_0^{\rho_r} dr B_\alpha(r) B_{\alpha'}(r) \int_0^\pi d\theta \int_0^{2\pi} d\phi \sin[\theta] Y_l^{m*}(\theta, \phi) Y_{l'}^{m'}(\theta, \phi) \\ &= \int_0^{\rho_r} dr B_\alpha(r) B_{\alpha'}(r) \delta_{ll'} \delta_{mm'} \end{aligned} \quad (7.61)$$

and

$$S_{IJ} = \int_0^{\rho_R} dR B_\beta(R) B_{\beta'}(R) \delta_{LL'} \delta_{MM'} \quad . \quad (7.62)$$

In Equations (7.61) and (7.62), ρ_r and ρ_R are box boundaries. The overlap matrix of the coupled problem is unitary due to orthogonality of the orbitals

$$S_{\mathbb{I}\mathbb{J}} = \langle \mathbb{I} | \mathbb{J} \rangle = \delta_{\mathbb{I}\mathbb{J}} \quad . \quad (7.63)$$

Kinetic energy part of the Hamiltonian matrix

Since $\hat{I}_{\text{REL}}^2 Y_l^m(\theta, \phi) = l(l+1) Y_l^m(\theta, \phi)$ and $\hat{I}_{\text{COM}}^2 Y_L^M(\Theta, \Phi) = L(L+1) Y_L^M(\Theta, \Phi)$, the kinetic energy part of the Hamiltonian matrix is

$$\begin{aligned} T_{ij} &= -\frac{1}{2\mu} \int_0^{\rho_r} dr B_{\alpha'}(r) \frac{\partial^2}{\partial r^2} B_\alpha(r) \delta_{ll'} \delta_{mm'} + \\ &\quad \frac{1}{2\mu} l(l+1) \int_0^{\rho_r} dr r^{-2} B_\alpha(r) B_{\alpha'}(r) \delta_{ll'} \delta_{mm'} \\ &= -\frac{1}{2\mu} \left(\frac{\partial B_\alpha(r)}{\partial r} B_{\alpha'}(r) \Big|_0^{\rho_r} - \int_0^{\rho_r} dr \frac{\partial B_\alpha(r)}{\partial r} \frac{\partial B_{\alpha'}(r)}{\partial r} - \right. \\ &\quad \left. \frac{1}{2\mu} l(l+1) \int_0^{\rho_r} dr r^{-2} B_\alpha(r) B_{\alpha'}(r) \right) \delta_{ll'} \delta_{mm'} \\ &= \frac{1}{2\mu} \left(\int_0^{\rho_r} dr \frac{\partial B_\alpha(r)}{\partial r} \frac{\partial B_{\alpha'}(r)}{\partial r} + \right. \\ &\quad \left. l(l+1) \int_0^{\rho_r} dr r^{-2} B_\alpha(r) B_{\alpha'}(r) \right) \delta_{ll'} \delta_{mm'} \end{aligned} \quad (7.64)$$

and

$$\begin{aligned} t_{IJ} &= \frac{1}{2M} \left(B'_1(0) B_1(0) + \int_0^{\rho_R} dR \frac{\partial B_\beta(R)}{\partial R} \frac{\partial B_{\beta'}(R)}{\partial R} + \right. \\ &\quad \left. (L+1) \int_0^{\rho_R} dR R^{-2} B_\beta(R) B_{\beta'}(R) \right) \delta_{LL'} \delta_{MM'} \quad . \end{aligned} \quad (7.65)$$

Interparticle interaction

The matrix elements of the interparticle interaction potential are

$$[U_{12}]_{ij} = \int_0^{\rho_r} dr U_{12}(r) B_\alpha(r) B_{\alpha'}(r) \delta_{ll'} \delta_{mm'} \quad . \quad (7.66)$$

Expansion terms

The product of two spherical harmonics can be expressed as a sum of products between one spherical harmonic and 3j-Wigner symbols

$$Y_l^m(\theta, \phi) Y_{l_t}^{m_t}(\theta, \phi) = \sum_{l_t, m_t} \sqrt{\frac{(2l_t + 1)(2l + 1)(2l_t + 1)}{4\pi}} \times \\ \begin{pmatrix} l_t & l & l_t \\ m_t & m & m_t \end{pmatrix} \begin{pmatrix} l_t & l & l_t \\ 0 & 0 & 0 \end{pmatrix} Y_{l_t}^{m_t^*}(\theta, \phi) \quad (7.67)$$

together with

$$Y_{l_t}^{m_t^*}(\theta, \phi) = (-1)^{m_t} Y_{l_t}^{-m_t}(\theta, \phi) \quad . \quad (7.68)$$

The Gaunt coefficient [147, 148] may be obtained as

$$\int_0^\pi d\theta \int_0^{2\pi} d\phi \sin(\theta) Y_l^m(\theta, \phi) Y_{l_t}^{m_t}(\theta, \phi) Y_{l'}^{m'^*}(\theta, \phi) \\ = \sum_{l_t, m_t} (-1)^{m_t} \sqrt{\frac{(2l_t + 1)(2l + 1)(2l_t + 1)}{4\pi}} \begin{pmatrix} l_t & l & l_t \\ m_t & m & m_t \end{pmatrix} \begin{pmatrix} l_t & l & l_t \\ 0 & 0 & 0 \end{pmatrix} \times \\ \underbrace{\int_0^\pi d\theta \int_0^{2\pi} d\phi \sin(\theta) Y_{l_t}^{-m_t}(\theta, \phi) Y_{l'}^{m'^*}(\theta, \phi)}_{\delta_{l_t l'} \delta_{-m_t m'}} \\ = (-1)^{m'} \sqrt{\frac{(2l_t + 1)(2l + 1)(2l' + 1)}{4\pi}} \begin{pmatrix} l_t & l & l' \\ m_t & m & -m' \end{pmatrix} \begin{pmatrix} l_t & l & l' \\ 0 & 0 & 0 \end{pmatrix} \quad . \quad (7.69)$$

Making use of Equation (7.69), the angular part of the matrix elements can be calculated straightforwardly for both coupled and uncoupled motions

$$\begin{aligned}
 [\text{V}_{\text{OL}}]_{ij} &= -\frac{1}{2} \sum_{s=1}^2 \sum_{c=\{x,y,z\}} V_c^s \sum_{t=1}^n \mathbb{C}_{t0cs}^{\text{cos}} \int_0^{\rho_r} r^{2t} B_\alpha(r) B_{\alpha'}(r) \\
 &\times \sum_{l_t=0, \{2\}}^{2t} \sum_{m_t=-l_t, \{2\}}^{l_t} \mathbb{Y}_{l_t m_t}^c (-1)^{m'} \sqrt{\frac{(2l_t+1)(2l+1)(2l'+1)}{4\pi}} \\
 &\times \begin{pmatrix} l_t & l & l' \\ m_t & m & -m' \end{pmatrix} \begin{pmatrix} l_t & l & l' \\ 0 & 0 & 0 \end{pmatrix} \quad (7.70)
 \end{aligned}$$

and

$$\begin{aligned}
 [\text{V}_{\text{OL}}]_{IJ} &= -\frac{1}{2} \sum_{s=1}^2 \sum_{c=\{x,y,z\}} V_c^s \sum_{k=1}^n \mathbb{C}_{0kcs}^{\text{cos}} \int_0^{\rho_R} r^{2k} B_\beta(R) B_{\beta'}(R) \\
 &\times \sum_{L_k=0, \{2\}}^{2k} \sum_{M_k=-L_k, \{2\}}^{L_k} \mathbb{Y}_{L_k M_k}^c (-1)^{M'} \sqrt{\frac{(2L_k+1)(2L+1)(2L'+1)}{4\pi}} \\
 &\times \begin{pmatrix} L_k & L & L' \\ M_k & M & -M' \end{pmatrix} \begin{pmatrix} L_k & L & L' \\ 0 & 0 & 0 \end{pmatrix} . \quad (7.71)
 \end{aligned}$$

Since in the coupled problem the $\hat{h}_{\text{COM}} + \hat{h}_{\text{REL}}$ part of the Hamiltonian is diagonal,

$$[\hat{h}_{\text{COM}} + \hat{h}_{\text{REL}}]_{\mathbb{I}\mathbb{J}} = \langle \mathbb{I} | \hat{h}_{\text{COM}} + \hat{h}_{\text{REL}} | \mathbb{J} \rangle = [\epsilon^{(\mathbf{a})} + \epsilon^{(\mathbf{b})}] \delta_{\mathbb{I}\mathbb{J}} , \quad (7.72)$$

only the coupling elements of the lattice potential must be calculated. They

are given as

$$\begin{aligned}
 W_{\mathbb{I}\mathbb{J}} = & \frac{1}{2} \sum_{s=1}^2 \sum_{c=\{x,y,z\}} V_c^s \left[(-1)^{\eta_s} \sum_{j=0}^{n-1} (-1)^j \frac{(2k_c \mu_{\eta_s})^{2j+1}}{(2j+1)!} \times \right. \\
 & \sum_{\alpha=1}^{N_r} \sum_{l=0}^{N_l} \sum_{m=-l}^l c_{\alpha l m}^{(\mathbf{a})} \sum_{\alpha'=1}^{N_r} \sum_{l'=0}^{N_l} \sum_{m'=-l'}^l c_{\alpha' l' m'}^{(\mathbf{a}')} \int_0^\infty r^{2j+1} B_\alpha(r) B_{\alpha'}(r) dr \times \\
 & \sum_{l_j=1, \{2\}}^{2j+1} \left[\left(\tilde{\mathbb{Y}}_{l_j 0 j}^c \begin{pmatrix} l_j & l & l' \\ 0 & m & m' \end{pmatrix} + \sum_{m_j=-l_j, \{2\}}^{l_j} \tilde{\mathbb{Y}}_{l_j m_j j}^c \begin{pmatrix} l_j & l & l' \\ m_j & m & -m' \end{pmatrix} \right) \times \right. \\
 & \left. S_{l_j l l'}^{m'} \begin{pmatrix} l_j & l & l' \\ 0 & 0 & 0 \end{pmatrix} \right] \times \\
 & \sum_{i=0}^{n-1-j} (-1)^i \frac{(2k_c)^{2i+1}}{(2i+1)!} \sum_{\beta=1}^{N_R} \sum_{L=0}^{N_L} \sum_{M=-L}^L C_{\beta L M}^{(\mathbf{b})} \times \\
 & \sum_{\beta'=1}^{N_R} \sum_{L'=0}^{N_L} \sum_{M'=-L'}^L C_{\beta' L' M'}^{(\mathbf{b}')} \int_0^\infty R^{2i+1} B_\beta(R) B_{\beta'}(R) dR \times \\
 & \sum_{L_i=1, \{2\}}^{2i+1} \left[\left(\tilde{\mathbb{Y}}_{L_i 0 i}^c \begin{pmatrix} L_i & L & L' \\ 0 & M & M' \end{pmatrix} + \sum_{M_i=-L_i, \{2\}}^{L_i} \tilde{\mathbb{Y}}_{L_i M_i i}^c \begin{pmatrix} L_i & L & L' \\ M_i & M & -M' \end{pmatrix} \right) \times \right. \\
 & \left. S_{L_i L L'}^{M'} \begin{pmatrix} L_i & L & L' \\ 0 & 0 & 0 \end{pmatrix} \right] - \\
 & \sum_{t=1}^n (-1)^t \frac{(2k_c \mu_{\eta_s})^{2t}}{(2t)!} \sum_{\alpha=1}^{N_r} \sum_{l=0}^{N_l} \sum_{m=-l}^l c_{\alpha l m}^{(\mathbf{a})} \times \\
 & \sum_{\alpha'=1}^{N_r} \sum_{l'=0}^{N_l} \sum_{m'=-l'}^l c_{\alpha' l' m'}^{(\mathbf{a}')} \int_0^\infty r^{2t} B_\alpha(r) B_{\alpha'}(r) dr \times \\
 & \sum_{l_t=0, \{2\}}^{2t} \sum_{m_t=-l_t, \{2\}}^{l_t} \mathbb{Y}_{l_t m_t t}^c S_{l_t l l'}^{m'} \begin{pmatrix} l_t & l & l' \\ m_t & m & -m' \end{pmatrix} \begin{pmatrix} l_t & l & l' \\ 0 & 0 & 0 \end{pmatrix} \times \\
 & \sum_{k=1}^{n-t} (-1)^k \frac{(2k_c)^{2k}}{(2k)!} \sum_{\beta=1}^{N_R} \sum_{L=0}^{N_L} \sum_{M=-L}^L C_{\beta L M}^{(\mathbf{b})} \sum_{\beta'=1}^{N_R} \sum_{L'=0}^{N_L} \sum_{M'=-L'}^L \times \\
 & C_{\beta' L' M'}^{(\mathbf{b}')} \int_0^\infty R^{2k} B_\beta(R) B_{\beta'}(R) dR \times \\
 & \sum_{L_k=0, \{2\}}^{2k} \sum_{M_k=-L_k, \{2\}}^{L_k} \mathbb{Y}_{L_k M_k k}^c S_{L_k L L'}^{M'} \begin{pmatrix} L_k & L & L' \\ M_k & M & -M' \end{pmatrix} \begin{pmatrix} L_k & L & L' \\ 0 & 0 & 0 \end{pmatrix} \left. \right] \quad (7.73)
 \end{aligned}$$

where $S_{bcd}^a = (-1)^a \sqrt{\frac{(2b+1)(2c+1)(2d+1)}{4\pi}}$.

Not all of the matrix elements need to be considered, some of them are zero. The reason to this is that the Hamiltonian of two atoms in a sinusoidal lattice potential possesses a certain symmetry. This symmetry will be described in the following section.

7.3 Symmetry of the system

The Hamiltonian of two atoms trapped in a \sin^2 -like potential is invariant under the symmetry operations of the D_{2h} point group. The D_{2h} group has subgroups C_s , C_1 , C_2 , C_{2v} , and C_{2h} . The D_{2h} has eight irreducible representations. This symmetry is widespread in electronic structure calculations [149].

The following Hamiltonians are equivalent

$$\begin{aligned} H(x, y, z) &= H(-x, -y, -z) = H(-x, y, z) = H(x, -y, z) = \\ H(x, y, -z) &= H(-x, -y, z) = H(x, -y, -z) = H(-x, y, -z) \quad . \quad (7.74) \end{aligned}$$

This invariance of the Hamiltonian is described by the irreducible A_g , B_{1g} , B_{2g} , B_{3g} , A_u , B_{1u} , B_{2u} , B_{3u} representations of the group where A and B are Milliken symbols. The complete set of mutually conjugate group elements are reflections in mirror planes perpendicular to one of the axes $\sigma(xy)$, $\sigma(xz)$, $\sigma(yz)$; the clockwise rotations around the axes by an angle of π $C_2(x)$, $C_2(y)$, $C_2(z)$; the inversion of all coordinates about the center of symmetry \mathbf{I} ; and the identity operation E . The center of symmetry is the origin of the Cartesian coordinate system. The symmetry elements are illustrated in Figure 7.3. All irreducible representations of the symmetry point group may be found in the corresponding character table (Table 7.1). The symmetry properties of the system belong to a certain irreducible representation if the system changes under symmetry operations exactly as specified for that irreducible representation in the character table.

The advantage of having symmetry can be used in present work. The symmetry operations presented in Figure 7.3 in absolute coordinates must correspond to rotations in spherical coordinates. These rotations and corresponding transformations in absolute coordinates together with spherical harmonics transformations are listed in Table 7.2.

The wave functions that correspond to the respective irreducible representation can be obtained only, if three symmetry operations are applied to the initial non-symmetrized function. For example, in order to get the REL motion wave functions, which are symmetric or antisymmetric with respect

Table 7.1: Character table of the D_{2h} point group

D_{2h}	E	$C_2(z)$	$C_2(y)$	$C_2(x)$	\mathbf{I}	$\sigma(xy)$	$\sigma(xz)$	$\sigma(yz)$
A_g	1	1	1	1	1	1	1	1
B_{1g}	1	1	-1	-1	1	1	-1	-1
B_{2g}	1	-1	1	-1	1	-1	1	-1
B_{3g}	1	-1	-1	1	1	-1	-1	1
A_u	1	1	1	1	-1	-1	-1	-1
B_{1u}	1	1	-1	-1	-1	-1	1	1
B_{2u}	1	-1	1	-1	-1	1	-1	1
B_{3u}	1	-1	-1	1	-1	1	1	-1

Table 7.2: Results of the D_{2h} group operations on absolute and spherical coordinates, and corresponding transformations of the spherical harmonics

	Absolute (ax,ay,az)	Spherical ($\alpha + \theta, \beta + \phi$)	Y_l^m $Y_l^m(\theta + \alpha, \phi + \beta)$
E	(1, 1, 1)	(0+, 0+)	$Y_l^m(\theta, \phi)$
$C_2(z)$	(-1, -1, 1)	(0+, π +)	$(-1)^m Y_l^m(\theta, \phi)$
$C_2(y)$	(-1, 1, -1)	(π -, π -)	$(-1)^{l+m} Y_l^{-m}(\theta, \phi)$
$C_2(x)$	(1, -1, -1)	(π -, 2π -)	$(-1)^l Y_l^{-m}(\theta, \phi)$
\mathbf{I}	(-1, -1, -1)	(π -, π +)	$(-1)^l Y_l^m(\theta, \phi)$
$\sigma(xy)$	(1, 1, -1)	(π -, 0+)	$(-1)^{l+m} Y_l^m(\theta, \phi)$
$\sigma(xz)$	(1, -1, 1)	(0+, 2π -)	$(-1)^m Y_l^{-m}(\theta, \phi)$
$\sigma(yz)$	(-1, 1, 1)	(0+, π -)	$Y_l^{-m}(\theta, \phi)$

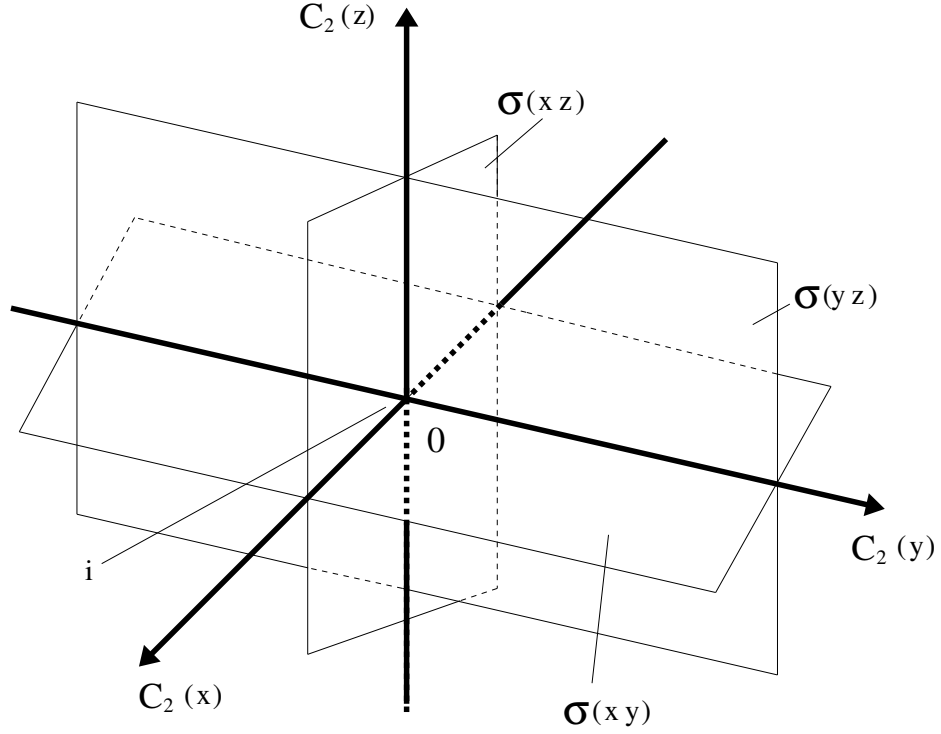


Figure 7.3: The symmetry elements of the two particles interacting by a central potential in a \sin^2 -like trap. The list is complete with the identity element E added.

to \mathbf{I} , $\sigma(xz)$, $\sigma(yz)$ operations, the respective conditions must be satisfied

$$\sum_{\alpha,l,m} c_{\alpha,l,m} B_{\alpha}(r) Y_l^m(\theta, \phi) = \pm \sum_{\alpha,l,m} c_{\alpha,l,m} B_{\alpha}(r) (-1)^l Y_l^m(\theta, \phi), \quad (7.75)$$

$$\sum_{\alpha,l,m} c_{\alpha,l,m} B_{\alpha}(r) Y_l^m(\theta, \phi) = \pm \sum_{\alpha,l,m} c_{\alpha,l,m} B_{\alpha}(r) Y_l^{-m}(\theta, \phi) \quad , \quad (7.76)$$

$$\sum_{\alpha,l,m} c_{\alpha,l,m} B_{\alpha}(r) Y_l^m(\theta, \phi) = \pm \sum_{\alpha,l,m} c_{\alpha,l,m} B_{\alpha}(r) (-1)^m Y_l^{-m}(\theta, \phi) \quad (7.77)$$

where \pm corresponds to gerade/ungerade situations. In Equations (7.75), (7.76) and (7.77), the properties of the spherical harmonics in Table 7.2 are adopted.

Hence, the respective symmetric and antisymmetric solutions are

$$\varphi_{\mathbf{i}^+}(r, \theta, \phi) = \sum_{\alpha} B_{\alpha}(r) \sum_{l=0, \{2\}} \sum_{m=-l}^l c_{\alpha lm} Y_l^m(\theta, \phi) \quad , \quad (7.78)$$

$$\varphi_{\mathbf{i}^-}(r, \theta, \phi) = \sum_{\alpha} B_{\alpha}(r) \sum_{l=1, \{2\}} \sum_{m=-l}^l c_{\alpha lm} Y_l^m(\theta, \phi) \quad , \quad (7.79)$$

$$\begin{aligned} \varphi_{\sigma^+(yz)}(r, \theta, \phi) &= \sum_{\alpha} \sum_{l=0} c_{\alpha l 0} B_{\alpha}(r) Y_l^0(\theta, \phi) + \\ &\frac{1}{\sqrt{2}} \sum_{\alpha} \sum_{l=1} \sum_{m=1}^l c_{\alpha lm} B_{\alpha}(r) (Y_l^m(\theta, \phi) + Y_l^{-m}(\theta, \phi)) \quad , \end{aligned} \quad (7.80)$$

$$\begin{aligned} \varphi_{\sigma^-(yz)}(r, \theta, \phi) &= \frac{1}{\sqrt{2}} \sum_{\alpha} \sum_{l=1} \sum_{m=1}^l c_{\alpha lm} B_{\alpha}(r) \times \\ &(Y_l^m(\theta, \phi) - Y_l^{-m}(\theta, \phi)) \quad , \end{aligned} \quad (7.81)$$

$$\begin{aligned} \varphi_{\sigma^+(xz)}(r, \theta, \phi) &= \sum_{\alpha} \sum_{l=0} c_{\alpha l 0} B_{\alpha}(r) Y_l^0(\theta, \phi) + \\ &\frac{1}{\sqrt{2}} \sum_{\alpha} \sum_{l=1} \sum_{m=1}^l c_{\alpha lm} B_{\alpha}(r) (Y_l^m(\theta, \phi) + (-1)^m Y_l^{-m}(\theta, \phi)) \quad , \end{aligned} \quad (7.82)$$

$$\begin{aligned} \varphi_{\sigma^-(xz)}(r, \theta, \phi) &= \frac{1}{\sqrt{2}} \sum_{\alpha} \sum_{l=1} \sum_{m=1}^l c_{\alpha lm} B_{\alpha}(r) \times \\ &(Y_l^m(\theta, \phi) - (-1)^m Y_l^{-m}(\theta, \phi)) \end{aligned} \quad (7.83)$$

where, e. g., the index \mathbf{i}^+ (\mathbf{i}^-) means that the wave function $\varphi_{\mathbf{i}^+}$ ($\varphi_{\mathbf{i}^-}$) is symmetric (antisymmetric) with respect to the inversion operation. The consistent application of the symmetry operations \mathbf{I} , $\sigma(xz)$, $\sigma(yz)$ result in eight linearly independent functions. For example, one of these operations is

$$\begin{aligned} \varphi_{\mathbf{i}^- \sigma^-(xz) \sigma^-(yz)}(r, \theta, \phi) &= \frac{1}{\sqrt{2}} \sum_{\alpha} \sum_{l=1, \{2\}} \sum_{m=2, \{2\}}^l c_{\alpha lm} B_{\alpha}(r) \times \\ &(Y_l^m(\theta, \phi) - Y_l^{-m}(\theta, \phi)) \quad . \end{aligned} \quad (7.84)$$

According to the character table (Table 7.1) of D_{2h} these eight functions can

be attributed to the respective irreducible group representations

$$\begin{aligned} \varphi_{A_g} = & \sum_{\alpha} \sum_{l=0,\{2\}} C_{\alpha l 0} B_{\alpha}(r) Y_l^0(\theta, \phi) + \\ & \frac{1}{\sqrt{2}} \sum_{\alpha} \sum_{l=2,\{2\}} \sum_{m=2,\{2\}}^l C_{\alpha l m} B_{\alpha}(r) (Y_l^m(\theta, \phi) + Y_l^{-m}(\theta, \phi)), \end{aligned} \quad (7.85)$$

$$\varphi_{B_{1g}} = \frac{1}{\sqrt{2}} \sum_{\alpha} \sum_{l=2,\{2\}} \sum_{m=2,\{2\}}^l C_{\alpha l m} B_{\alpha}(r) (Y_l^m(\theta, \phi) - Y_l^{-m}(\theta, \phi)), \quad (7.86)$$

$$\varphi_{B_{2g}} = \frac{1}{\sqrt{2}} \sum_{\alpha} \sum_{l=2,\{2\}} \sum_{m=1,\{2\}}^l C_{\alpha l m} B_{\alpha}(r) (Y_l^m(\theta, \phi) - Y_l^{-m}(\theta, \phi)), \quad (7.87)$$

$$\varphi_{B_{3g}} = \frac{1}{\sqrt{2}} \sum_{\alpha} \sum_{l=2,\{2\}} \sum_{m=1,\{2\}}^l C_{\alpha l m} B_{\alpha}(r) (Y_l^m(\theta, \phi) + Y_l^{-m}(\theta, \phi)), \quad (7.88)$$

$$\varphi_{A_u} = \frac{1}{\sqrt{2}} \sum_{\alpha} \sum_{l=3,\{2\}} \sum_{m=2,\{2\}}^l C_{\alpha l m} B_{\alpha}(r) (Y_l^m(\theta, \phi) - Y_l^{-m}(\theta, \phi)), \quad (7.89)$$

$$\begin{aligned} \varphi_{B_{1u}} = & \sum_{\alpha} \sum_{l=1,\{2\}} C_{\alpha l 0} B_{\alpha}(r) Y_l^0(\theta, \phi) + \\ & \frac{1}{\sqrt{2}} \sum_{\alpha} \sum_{l=3,\{2\}} \sum_{m=2,\{2\}}^l C_{\alpha l m} B_{\alpha}(r) (Y_l^m(\theta, \phi) + Y_l^{-m}(\theta, \phi)), \end{aligned} \quad (7.90)$$

$$\varphi_{B_{2u}} = \frac{1}{\sqrt{2}} \sum_{\alpha} \sum_{l=1,\{2\}} \sum_{m=1,\{2\}}^l C_{\alpha l m} B_{\alpha}(r) (Y_l^m(\theta, \phi) + Y_l^{-m}(\theta, \phi)), \quad (7.91)$$

$$\varphi_{B_{3u}} = \frac{1}{\sqrt{2}} \sum_{\alpha} \sum_{l=1,\{2\}} \sum_{m=1,\{2\}}^l C_{\alpha l m} B_{\alpha}(r) (Y_l^m(\theta, \phi) - Y_l^{-m}(\theta, \phi)). \quad (7.92)$$

Using the product table (Table 7.3), the COM and REL motion functions can be selectively combined to a configuration of the desirable symmetry. The bosonic and fermionic functions can be formed by means of the product table. In the case of homonuclear atoms the COM coordinates stay the same,

Table 7.3: Product table of the D_{2h} point group

\oplus	A_g	B_{1g}	B_{2g}	B_{3g}	A_u	B_{1u}	B_{2u}	B_{3u}
A_g	A_g	B_{1g}	B_{2g}	B_{3g}	A_u	B_{1u}	B_{2u}	B_{3u}
B_{1g}	B_{1g}	A_g	B_{3g}	B_{2g}	B_{1u}	A_u	B_{3u}	B_{2u}
B_{2g}	B_{2g}	B_{3g}	A_g	B_{1g}	B_{2u}	B_{3u}	A_u	B_{1u}
B_{3g}	B_{3g}	B_{2g}	B_{1g}	A_g	B_{3u}	B_{2u}	B_{1u}	A_u
A_u	A_u	B_{1u}	B_{2u}	B_{3u}	A_g	B_{1g}	B_{2g}	B_{3g}
B_{1u}	B_{1u}	A_u	B_{3u}	B_{2u}	B_{1g}	A_g	B_{3g}	B_{2g}
B_{2u}	B_{2u}	B_{3u}	A_u	B_{1u}	B_{2g}	B_{3g}	A_g	B_{1g}
B_{3u}	B_{3u}	B_{2u}	B_{1u}	A_u	B_{3g}	B_{2g}	B_{1g}	A_g

if two atoms are exchanged ($\vec{R} \rightarrow \vec{R} \iff \Phi \rightarrow \Phi, \Theta \rightarrow \Theta$) and only the REL coordinates are flipped ($\vec{r} \rightarrow -\vec{r} \iff \phi \rightarrow \pi + \phi, \theta \rightarrow \pi - \theta$). If the total wave function changes the sign on inversion relative to the center of the symmetry, it has a fermionic character. Otherwise, it has a bosonic character. Therefore, all gerade wave functions ($\varphi_{A_g}, \varphi_{B_{1g}}, \varphi_{B_{2g}}$ and $\varphi_{B_{3g}}$) are bosonic and all ungerade wave functions ($\varphi_{A_u}, \varphi_{B_{1u}}, \varphi_{B_{2u}}$ and $\varphi_{B_{3u}}$) are fermionic. The configurations that form the bosonic (fermionic) wave function must be symmetric (antisymmetric) under the $\mathbf{i} \oplus E$ operation.

7.4 Conclusion

A numerical approach is developed, which in principle allows an exact description of two atoms trapped in a 3D optical lattice, if the interatomic interaction potential is central (isotropic) and can be given in terms of a single potential curve. However, an extension to non-central (e.g., dipolar) interactions is straightforward with the present approach. The use of spherical harmonics together with B -splines as basis functions and the expansion of the trap in terms of spherical harmonics leads to an analytical form of the matrix elements for the trap. The possible zero matrix elements are considered explicitly, which makes the approach computationally efficient. Additionally, the D_{2h} symmetry of the lattice is taken into account, which further simplifies the computation and helps to classify the solutions.

Since the present approach was formulated rather generally, it immedi-

ately forms the basis for further investigations. This includes, e. g., the consideration of highly anisotropic, asymmetric (disordered), or multiple-well lattice geometries [146]. First results for triple-well potentials have recently been used for the determination of Bose-Hubbard parameters and an investigation of the validity of the Bose-Hubbard model itself [145]. Further extensions of the approach should also allow the study of the case of a pair of atoms or molecules interacting by non-centric, e. g., dipolar interactions, or atoms in the presence of electric field. A study of collisions of a single atom and an ion in trapping potentials [150, 151] is also straightforward with the present approach. Finally, it is planned to extend the method for studies of the time-dependent dynamics of atomic pairs in time-varying lattices.

Chapter 8

Anharmonicity and coupling effects in optical lattices

The main motivation for the development of the numerical approach presented in Chapter 7 was the study of anharmonicity and coupling effects arising in real lattices. Since this approach is formulated and implemented rather generally, the investigation of, e.g., multiple-well lattice geometries is straightforward. However, in order to explore the effects of anharmonicity and coupling, the consideration of a single site of the optical lattice is sufficient in sufficiently deep lattices. In this chapter, the detailed analysis of anharmonicity and coupling of center-of-mass and relative coordinates is presented for heteronuclear dimers in a single site of an optical lattice in terms of energy values and wave functions. Deviations from the harmonic approximation due to effects of anharmonicity and coupling are quantified and analyzed for different heteronuclear systems, confinement strengths, and interatomic interaction regimes.

8.1 Model system

8.1.1 Trap parameters

Despite the already mentioned breakdown of the harmonic approximation especially for heteronuclear systems it is still convenient to introduce the mean harmonic-oscillator frequencies ω_{ho} and Ω_{ho} of a single lattice site for

the REL and COM motion respectively,

$$\omega_{\text{ho}} = k \sqrt{2 \frac{V_1 \mu_2^2 + V_2 \mu_1^2}{\mu}} , \quad (8.1)$$

$$\Omega_{\text{ho}} = k \sqrt{2 \frac{V_1 + V_2}{M}} . \quad (8.2)$$

In Equations (8.1) and (8.2) μ and M denote the reduced mass and total mass of the two particles respectively, μ_j is defined as $\mu_{1,2} = \mu/m_{2,1}$ where m_j is the mass of atom j , and $V_j = I_0 \cdot \alpha_j$ is the optical lattice depth that is equal to the product of the laser intensity I_0 (for an isotropic geometry $I_0 = I_x = I_y = I_z$) and the polarizabilities α_j of atom j . Finally, one has $k = k_x = k_y = k_z$ for an isotropic geometry of the lattice. This isotropy is in fact assumed in Equations (8.1) and (8.2). For identical particles of mass m Equation (8.1) reduces to the well-known relation $\omega_{\text{ho}} = k\sqrt{2V_0/m}$ [79].

Some parameters of the trap chosen in the present study were motivated by the recent experiment reported in [96]. Therein a three-dimensional optical lattice generated by lasers with wavelength $\lambda = \lambda_x = \lambda_y = \lambda_z$ of 1030 nm was used for the trapping of ultracold bosonic ^{87}Rb and fermionic ^{40}K atoms. The two different lattice depths $V_{\text{Rb}} = 40 E_r^{\text{Rb}}$ and $V_{\text{K}} = 27.5 E_r^{\text{Rb}}$ were considered where the individual recoil energy is defined, e.g., as $E_r^{\text{Rb}} = k^2/(2m_{\text{Rb}})$. Since the static dipole polarizabilities of rubidium and potassium are different, $\alpha_{\text{Rb}} = 324$ a. u. and $\alpha_{\text{K}} = 301$ a. u. [152], the two atoms experience different potentials: $V_{\text{K}} = 37.2 E_r^{\text{Rb}}$ and $V_{\text{K}} = 25.5 E_r^{\text{Rb}}$ for $40 E_r^{\text{Rb}}$ and $27.5 E_r^{\text{Rb}}$ respectively. The mean harmonic-oscillator frequencies (8.1) are $\omega_{\text{ho}}(40 E_r^{\text{Rb}}) = 2\pi \times 35.7$ kHz and $\omega_{\text{ho}}(27.5 E_r^{\text{Rb}}) = 2\pi \times 30$ kHz. While most of the results of this work are obtained for these frequencies, some other values are also considered in order to investigate the influence of the trap frequency more generally.

8.1.2 Interatomic interaction potential

The interaction between rubidium and potassium atoms is modeled using the BO potential of the $a^3\Sigma^+$ electronic state describing the interaction of two spin-polarized atoms. In general the atom-atom interaction potentials are only known numerically. For the short-range part V_{SR} of the potential in between $R \in [1.588 a_0, 18.2 a_0]$ the data of [153] are used (a_0 is the Bohr radius). The data points at $R = 17.6 a_0$ and $R = 16.99998 a_0$ have been omitted, because their inclusion results in a non-smooth potential curve. The long range part V_{LR} of the $a^3\Sigma^+$ electronic state is constructed in a similar way as was done by Zemke *et al.* [154]. Therefore, this long range

part is defined as $V_{\text{LR}}(r) = D_e + \Delta V_{\text{disp}}(r) + \Delta V_{\text{ex}}(r)$ for $R \geq 18.6 a_0$ where $\Delta V_{\text{disp}}(r) = -C_6/r^6 - C_8/r^8 - C_{10}/r^{10}$ and the dispersion coefficients C_n are the values of Derevianko and co-workers [155, 156] except $C_6 = 4292 \pm 19$ a.u. which was taken from [157]. The exchange interaction is given by $\Delta V_{\text{ex}}(r) = -Cr^\alpha e^{-\beta r}$ with $C = 0.00231382$, $\alpha = 5.25603$, $\beta = 1.11892$ as given in [154]. To merge the short- and the long-range parts the short-range part is raised up by half of the value $\delta_{\text{merge}} = V_{\text{SR}}(18.2 a_0) - V_{\text{LR}}(18.6 a_0)$. According to [154] the $a^3\Sigma^+$ state supports 32 bound states and the interaction of the atoms via the $a^3\Sigma^+$ potential is strong and repulsive. The same amount of bound states and the same character of the interaction are observed in the present calculation using the potential curve constructed the way described above.

In order to study the influence of different masses, polarizabilities, different interaction potentials, and also to check the generality of the conclusions of this work other systems are also analyzed. In particular, the heteronuclear ${}^6\text{Li}-{}^7\text{Li}$ and ${}^6\text{Li}-{}^{133}\text{Cs}$ pairs interacting via their respective $a^3\Sigma^+$ electronic state are considered. The potential curves for ${}^6\text{Li}-{}^7\text{Li}$ and ${}^6\text{Li}-{}^{133}\text{Cs}$ were constructed according to [100] and [158], respectively.

8.1.3 Manipulation of the interatomic interaction

In the limit of zero collision energy the interaction between two atoms can be characterized by their s -wave scattering length a_{sc} , as was discussed in Chapter 2. The sign of a_{sc} determines the type of interaction (repulsive or attractive) and the absolute value determines the interaction strength. Experimentally it is difficult to accurately measure the scattering length. For example, there is no agreement about the value of the triplet scattering length for the ${}^{87}\text{Rb}-{}^{40}\text{K}$ dimer. According to the ongoing discussion [157, 159–161] the value $-185(4) a_0$ appears to be the most reliable one. A standard way to match the calculated scattering length with the experimental value is a smooth shift of the inner wall of the BO potential as is described in [154]. This procedure can also be used for an effective variation of the scattering length, since a systematic variation of the inner wall allows to shift the least bound (lb) state supported by the potential curve as is shown in Figure 8.1. If the least bound state is close to the dissociation threshold or moves even into the dissociative continuum, the scattering length and thus the interaction between the ultracold atoms are strongly influenced, as was already discussed in Chapter 4. Therefore, a small variation of the inner wall of the potential can modify the interatomic interaction potential from strongly repulsive to strongly attractive. This procedure is adopted for studies in the present chapter in order to investigate the influence of the interatomic interaction potential. The scattering length is only well-defined for zero-energy scatter-

ing and thus the underlying concept is in principle not applicable to trapped particles with a non-vanishing zero-point energy. Therefore, the scattering-length values (for a given inner-wall shift) are determined for the trap-free situation. In this case a_{sc} can be uniquely determined from the analysis of the shape of the zero-energy scattering wave function [36].

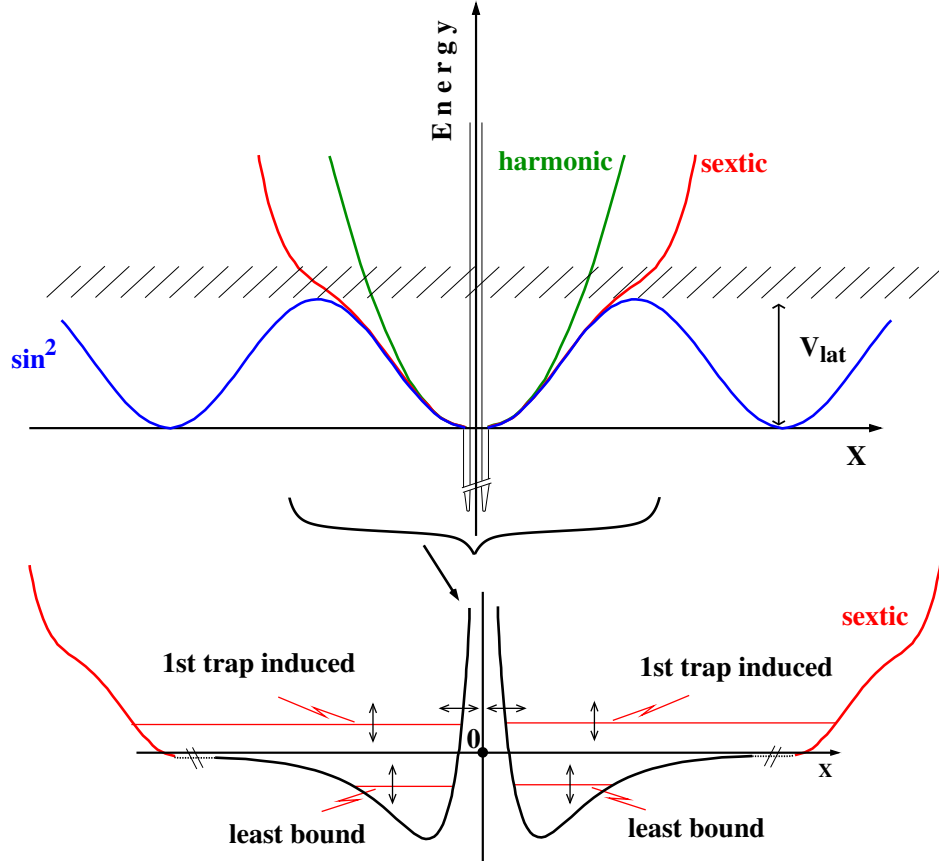


Figure 8.1: Sketch (not to scale) of a cut through the potential surfaces along the x direction ($y = z = 0$) for a system of two *identical* atoms if one of them is positioned at the zero of x . The upper graph shows the \sin^2 potential together with the harmonic (green) and sextic (red) approximations. While the harmonic and sextic potentials support solely bound states, the energy spectrum of the \sin^2 potential is partly discrete (for a sufficiently deep value of V_{lat}) and partly continuous. The lower graph shows the range of small x values on an enlarged scale. A very tiny variation of the inner wall of the interaction potential leads to a relatively large shift of the least bound and the first trap-induced states.

Ignoring the formal problems of defining a scattering length within a trap (that will be discussed in some more detail below), it is often considered useful

to introduce a dimension-free interaction parameter ξ that reflects the relative magnitude of the interaction strength with respect to the confinement by the trap. If this confinement is approximated within the harmonic approximation, the interaction parameter is naturally defined as $\xi = a_{\text{sc}}/a_{\text{ho}}$ where a_{ho} is the characteristic length of a harmonic potential given by $a_{\text{ho}} = 1/\sqrt{\mu\omega_{\text{ho}}}$. For a heteronuclear atom pair ω_{ho} is again the mean harmonic frequency defined in Equation (8.1).

Experimentally, a strong variation of the interaction strength can be realized with the help of MFR [162, 163]. The MFR technique was also used to tune the interatomic interaction from strongly repulsive to strongly attractive in the already mentioned experiments with atoms in the optical lattices [56, 94, 96]. In general, the correct theoretical description of a MFR requires a multi-channel scattering treatment which in the present case would have to incorporate also the optical lattice. In the analysis of the experiments described in [56, 94, 96] it is, however, assumed that it is possible to model the MFR in an effective two-channel picture [36]. Within this model it is straightforward to relate the applied magnetic field to a scattering-length value (Equation (9.2) below).

8.1.4 Computational details

The eigenfunctions of the Hamiltonians \hat{h}_{COM} and \hat{h}_{REL} are obtained by expressing both $\psi(\vec{R})$ and $\phi(\vec{r})$ as a linear combination of products of radial B -spline functions times spherical harmonics, as was discussed in the previous Chapter 7. The corresponding Schrödinger equations are solved numerically using the Rayleigh-Ritz-Galerkin approach [164] which leads to an algebraic eigenproblem.

In general, the lattice leads to a coupling of the angular momenta. Therefore, the spherical harmonics are no eigensolutions of the angular part. Due to the cubic trap geometry used in the experiment in [96] and also for the present calculations, the coupling of different spherical harmonics is weak. In fact, the orbitals $\psi(\vec{R})$ and $\phi(\vec{r})$ describing the states relevant to this work are almost converged, even if only $l = 0$ is considered. However, the coupling term \hat{W} in the Hamiltonian (7.4) leads to a stronger angular momentum coupling. Good convergence was found in the CI calculation, if all spherical harmonics up to $l = 3$ (and thus also $-3 \leq m \leq +3$) were included in the calculation of the orbitals $\psi(\vec{R})$ and $\phi(\vec{r})$.

The required number of B splines and their knot sequence depend strongly on the behavior of the wave function ($\psi(\vec{R})$ or $\phi(\vec{r})$) that should be described. In the context of ultracold collisions the main interest is put on the energetically low-lying COM orbitals $\psi(\vec{R})$ that possess a small number of nodes.

For the results discussed in this work, about 70 B splines were found to be sufficient to obtain convergence. Evidently, more complicated or highly anisotropic trap geometries (like double or triple wells [145]) require larger expansions.

The numerical description of the REL orbitals $\phi(\vec{r})$ is more demanding, if one is interested in the most weakly bound states or the low-lying dissociative states. The BO curves of alkali-metal atom dimers support often a large number of bound states (e.g., the $^{87}\text{Rb}-^{40}\text{K}$ system possesses in the $a^3\Sigma^+$ state already 32 bound states for $l = 0$). The very long-ranged, weakly bound states consist therefore of a highly oscillatory inner part (covering the so-called molecular regime and providing the orthogonality to all lower lying bound states) and a rather smooth long-range part. Correspondingly, it is practical to use two different knot sequences for the B splines. In the present case convergence was found if 200 B splines expanded on a linear knot sequence covering the interval $0 \leq r \leq 20 a_0$ are used together with about 70 B splines for the remaining r range. The latter 70 B splines are expanded on a knot sequence in which the separation between the knot points increases in a geometric fashion.

Converged CI calculations were found, if they comprised configurations built from about 120 REL and 60 COM orbitals. After taking symmetry into account this amounts to about 1060 configurations forming the CI expansion for the states of interest in this work.

8.2 Numerical results

8.2.1 Energy spectrum of the $^{87}\text{Rb}-^{40}\text{K}$ system

The description of an optical lattice beyond the harmonic approximation is in the present work achieved by extending the Taylor expansion of the \sin^2 potential beyond the harmonic (1st order and thus quadratic) term. In principle, one should seek for convergence with respect to the expansion length, but there are some practical reasons why a simple convergence study as a function of the expansion length causes problems. First of all, even-order expansions like the 2nd order one which leads to polynomials with a degree of up to 4 (quartic potential) support an infinite number of bound states with negative energy, since they tend to $-\infty$ for x approaching either $+\infty$ or $-\infty$. However, these bound states with negative energies are unphysical, since they do not exist in the case of the (original) positive definite \sin^2 potential. The 3rd order expansion that leads to polynomials up to a degree of 6 (sextic potential) supports on the other hand (like all odd-order expansions) only

bound states with positive energy values.

A comparison of this sextic potential with the \sin^2 potentials shows that the sextic potential reproduces extremely well a single site of the \sin^2 potential and thus of the optical lattice (Figure 8.1). Therefore, the sextic potential is a good choice for the investigation of the effects of anharmonicity on the bound states in a single site of an optical lattice. Evidently, the sextic potential cannot reproduce effects that are due to tunneling between neighbor potential wells. Therefore, extended (energetically higher lying) bound states in the optical lattice that are markedly affected by tunneling are not well reproduced by a sextic potential. Noteworthy, even in this case a simple convergence study will, however, not work. For example, the 5th order and thus next odd-order expansion shows a triple-well structure, but the two outer wells have a depth and width that differs pronouncedly from the correct shape (and the central well). This leads to completely wrongly described states in these outer wells and may thus show wrong tunneling behavior for the states in the middle well, especially in the case of resonant tunneling. Since the present study concentrates on the anharmonicity effects within a single site of an optical lattice, only the sextic potential and, for comparison, the harmonic one are considered. Effects that are due to tunneling between neighbor wells and thus include more than single-well potentials are investigated in a separate work [145].

The potential seen by the two atoms in an optical lattice contains, of course, in addition to the trap potential also the interatomic interaction potential that in the present case is described by a Born-Oppenheimer potential curve (and appears only in the REL coordinates). As is sketched in Figure 8.1, the interatomic interaction dominates the short-range part of the potential and leads in the case of alkali-metal atoms to a large number of bound molecular states. Since the trap potential is compared to the variation of the BO curve almost constant in the range of the molecular bound states, especially the lower lying of these states will in practice not be influenced by the optical lattice. The largest possible effect of the optical lattice on the molecular bound states is expected to occur for the energetically highest lying one, the least bound (lb) state.

Due to the large spatial extension of the trap states of typical experimentally realized optical lattices these trap-induced states are expected to be only weakly influenced by the molecular potential. However, an immediate consequence of the existence of the molecular bound states below the trap-induced ones is the nodal structure at short distances that is imprinted on the wavefunctions and leads to the required orthogonality of the eigenstates. The energetically lowest lying and thus first trap-induced (1ti) state possesses thus exactly one more node than the lb state. In the experiments

most closely related to the present work [94, 96] the transition energy between the lb and the 1ti state has been measured by either rf dissociation or association, respectively. This transition energy was called binding energy, but it should be kept in mind that its definition does not coincide with the standard definition of a molecular binding energy which is given by the energy difference between a molecular bound state and the (lowest) dissociation limit. In the present case the existence of the optical lattice leads to a discretization of the dissociation continuum and thus to an additional energy shift due to the zero-point energy of the trap.

If the coupling \hat{W} of REL and COM coordinates is ignored, the energies E_{lb} and $E_{1\text{ti}}$ of the least bound and the 1st trap-induced state, respectively, are obtained from the eigenvalues of Equations (7.7) and (7.8) as

$$E_{\text{lb}}^{(n)} \equiv E_{(1,\text{lb})}^{(n)} = \varepsilon_1^{(n)} + \epsilon_{\text{lb}}^{(n)} \quad , \quad (8.3)$$

$$E_{1\text{ti}}^{(n)} \equiv E_{(1,1\text{ti})}^{(n)} = \varepsilon_1^{(n)} + \epsilon_{1\text{ti}}^{(n)} \quad (8.4)$$

where n specifies the expansion length describing the optical lattice: $n = 2$ for a harmonic and $n = 6$ for a sextic trap. In accordance with the underlying assumption of an ultracold gas, the system is assumed to be in its lowest state with respect to translational motion, i. e., in the COM ground state with energy ε_1 . The corresponding wavefunctions are given by $\Phi_{\text{lb}}(\vec{R}, \vec{r}) = \psi_1(\vec{R})\phi_{\text{lb}}(\vec{r})$ and $\Phi_{1\text{ti}}(\vec{R}, \vec{r}) = \psi_1(\vec{R})\phi_{1\text{ti}}(\vec{r})$.

After the inclusion of the coupling of REL and COM motion the wavefunctions Φ are no longer eigenstates of the Hamiltonian, but are used as a basis for expanding the full wavefunctions Ψ that are obtained together with their energies \mathcal{E} by solving the Schrödinger Equation (7.9). The state Ψ with a dominant contribution from Φ_{lb} ($\Phi_{1\text{ti}}$) is then identified as least bound (1st-trap-induced) state with energy $\mathcal{E}_{\text{lb}}^{(n)}$ ($\mathcal{E}_{1\text{ti}}^{(n)}$), where n stands again for the order of the Taylor expansion of the optical-lattice potential.

In Figure 8.2 the energies of the least bound and the 1st trap-induced state are shown for ^{87}Rb - ^{40}K as a function of the trap-free scattering length (Section 8.1.3) for different levels of approximation ranging from the separable harmonic one to the fully coupled sextic solution. The trapping parameters were chosen in accordance with the corresponding experiment [96]. Clearly, the energies for the different approximations differ most for large positive scattering lengths and thus in the case of a strong repulsive interaction between the atoms.

A comparison of the results for the least bound and the first trap-induced states reveals that the energy of the former is almost unaffected by the anharmonicity of the trap and COM-REL coupling. Although this state is at least in the strongly repulsive part of the spectrum long ranged, it “feels” the

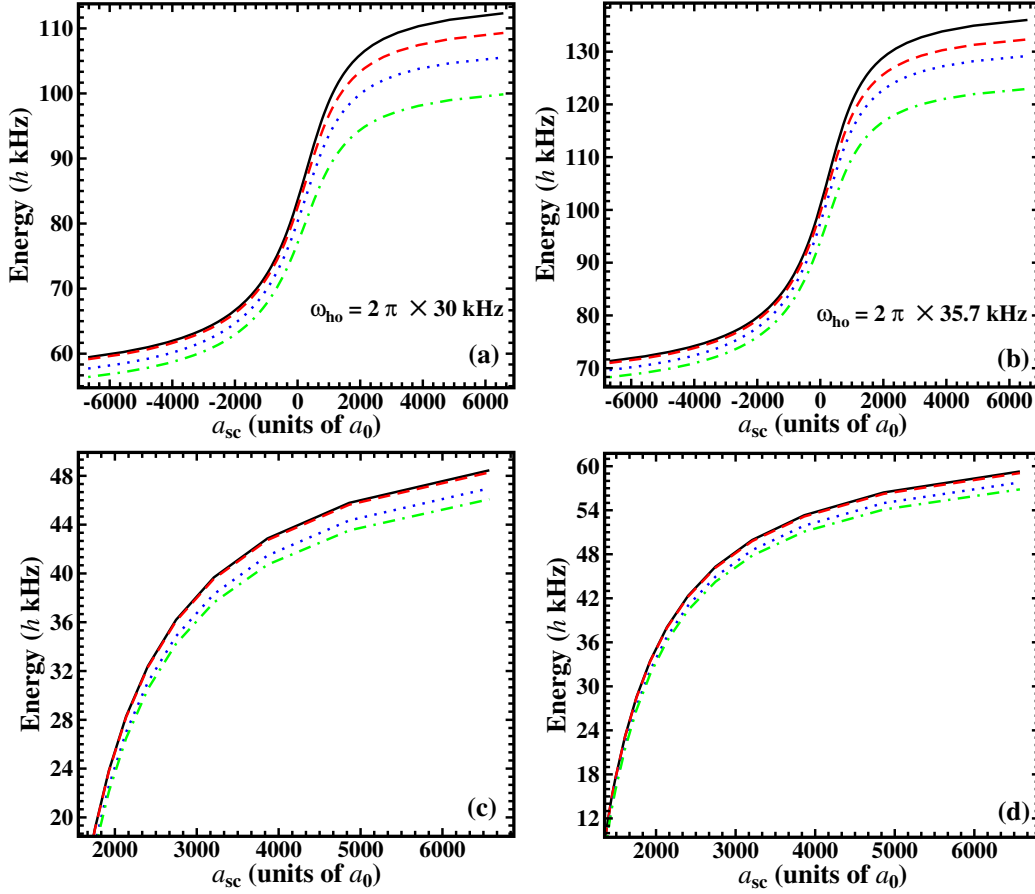


Figure 8.2: Energies of the 1st trap-induced (a-b) and least bound (c-d) states of ^{87}Rb - ^{40}K dimers in a single site of an optical lattice ($\lambda = 1030$ nm) for the potential depths (a) and (c) $V_{\text{Rb}} = 27.5 E_r^{\text{Rb}}$ and (b) and (d) $V_{\text{Rb}} = 40.0 E_r^{\text{Rb}}$ at different levels of approximation as a function of the trap-free scattering length (Section 8.1.3). The energies obtained with a full CI calculation for a sextic potential ($\mathcal{E}^{(6)}$, green chain) and a harmonic one ($\mathcal{E}^{(2)}$, red dashes) are compared to the corresponding sextic ($E^{(6)}$, blue dots) and harmonic ($E^{(2)}$, black solid) energies that are obtained, if the coupling between COM and REL motion is neglected. (Note, the sum $\frac{3}{2}(\omega_{\text{ho}} + \Omega_{\text{ho}})$ corresponds to $E^{(2)}(a_{\text{sc}} = 0) = 100.65$ kHz.)

anharmonic form of the trapping potential very weakly. This state remains thus sufficiently deeply localized in the trap potential and the harmonic approximation works still reasonably well; even for the rather strong repulsive interaction expressed by the scattering length $a_{\text{sc}} \approx 6500 a_0$. The energy change of the first trap-induced state due to the anharmonicity and REL-COM coupling is on the other hand much more pronounced. This change is thus predominantly defining the modification of the binding energy due to

the trap.

If the results for different levels of approximation are compared with each other, a clear ordering is visible. Independent of the scattering length and thus the interaction strength as well as its type (repulsive or attractive) the uncoupled harmonic energy $E^{(2)}$ is lowered, if the COM-REL coupling is included ($\mathcal{E}^{(2)}$). Note, this coupling exists even within the harmonic approximation for a heteronuclear diatomic molecule like RbK, since the two atoms possess different masses and polarizabilities and experience therefore different trap potentials. As a consequence, COM and REL motions do not separate. Only for diatomic systems made from two atoms in the same electronic state (or in some accidental situation) this coupling of COM and REL motion vanishes within the harmonic approximation.

An even larger reduction of the energy is observed, if only the anharmonicity is considered as is reflected by $E^{(6)}$ in which the coupling of COM and REL motion is ignored. For the considered system the effect of anharmonicity is thus a larger correction to the separable harmonic approximation than the one due to the coupling of COM and REL motion. A further energy reduction is found, if both effects are considered which leads to $\mathcal{E}^{(6)}$. Interestingly, the energy reduction indicated by $\mathcal{E}^{(6)}$ is larger than the sum of the energy reductions obtained separately for $\mathcal{E}^{(2)}$ and $E^{(6)}$. The coupling of COM and REL motion is thus enhanced, if the more realistic sextic potential is considered instead of the harmonic one.

In order to quantitatively describe the different effects of the trapping potential the energy differences

$$\Delta_{\text{geom}} = E_i^{(2)} - E_i^{(6)} \quad , \quad (8.5)$$

$$\Delta_{\text{coup}}^{(n)} = E_i^{(n)} - \mathcal{E}_i^{(n)} \quad , \quad (8.6)$$

$$\Delta_{\text{tot}} = E_i^{(2)} - \mathcal{E}_i^{(6)} = \Delta_{\text{geom}} + \Delta_{\text{coup}}^{(6)} \quad (8.7)$$

may be introduced, where $i = \{\text{lb}, \text{1ti}\}$. Δ_{geom} characterizes the effect of anharmonicity of the optical lattice based on the uncoupled solutions. $\Delta_{\text{coup}}^{(n)}$ is a measure of the coupling between COM and REL motion within the harmonic ($n = 2$) or sextic ($n = 6$) potential. Finally, Δ_{tot} specifies the energy difference between the simple harmonic approximation (in which the coupling of COM and REL motion is ignored) and the full solution of two atoms in a single site of an optical lattice (within the sextic approximation).

As is evident from Figure 8.2, the effect is largest for the strongly repulsive regime. This is due to a rise of the energy level to the region of higher anharmonicity of the trapping potential. Moreover, the state in this point is also long-ranged due to the strong repulsive interaction. Numerical values of

Table 8.1: The effect of the trapping potential on the energy spectrum of the 1st trap-induced state of ^{87}Rb - ^{40}K for the trapping parameters of the experiment reported in [96]. The Δ values defined by Equations (8.5)-(8.7) are given in units of h^{-1}/kHz and calculated at $a_{\text{sc}} = 6500 a_0$.

$V_{\text{Rb}}(E_r^{\text{Rb}})$	Δ_{geom}	$\Delta_{\text{coup}}^{(2)}$	$\Delta_{\text{coup}}^{(6)}$	Δ_{tot}
27.5	6.797	3.022	5.665	12.462
40.0	6.828	3.689	6.243	13.071

the differences Δ (8.5-8.7) for ^{87}Rb - ^{40}K , the experimental trap parameters in [96], and $a_{\text{sc}} = 6500 a_0$ are given in Table 8.1.

For the considered system the value Δ_{tot} and thus the total energy between the uncoupled and the coupled harmonic approximation amounts to about 13 kHz for $a_{\text{sc}} = 6500 a_0$. An effect of this size should be visible in the experiment in [96] with a claimed resolution of 1.7 kHz but would not be resolvable with a ten times worse resolution as it occurs for a ten times shorter rf-pulse as was used, e. g., in [94].

In an analysis of the influence of the interaction strength as is performed in this work it is important to stay within the restrictions of a single-site model. The parameter variation has to avoid situations in which tunneling or even over-the-barrier transfer of atoms between different sites of a physical optical lattice can occur, since this range is clearly not adequately described with a harmonic or sextic potential with infinite walls. For example, for a very large positive scattering length the large repulsive interaction shifts the lowest-lying atom-pair state (1st trap-induced state) above the barrier of a true optical lattice. While this physical lattice would not support any bound states, the harmonic or sextic potentials would still possess an infinite number of them. As is discussed in Section 8.2.3, it was always checked that the wave functions remain well localized within the boundaries of a single site of the optical lattice for the parameters used in this study.

8.2.2 Comparison with ^6Li - ^{133}Cs and ^6Li - ^7Li dimers

In order to obtain a more complete picture of the anharmonicity and the coupling effects other systems were analyzed. Besides the already considered ^{87}Rb - ^{40}K pair (example of large masses and polarizabilities) other experimentally relevant alkali metal dimers like ^6Li - ^{133}Cs (small mass and polarizability of ^6Li and for ^{133}Cs both characteristics are large) and ^6Li - ^7Li (small masses and polarizabilities of both elements) are investigated.

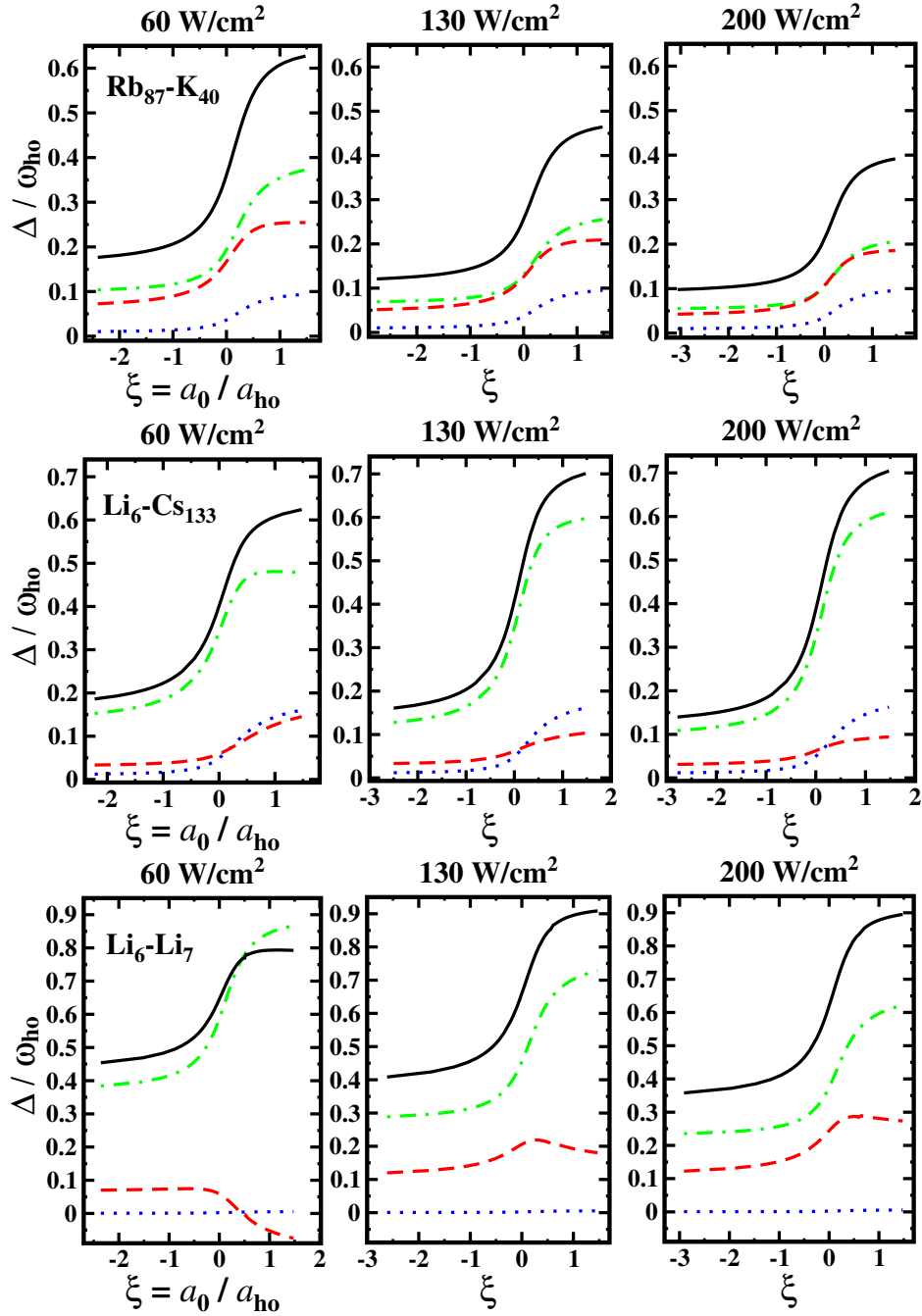


Figure 8.3: The energy differences (Equations (8.5-8.7)) $\Delta_{\text{coupl}}^{(2)}$ (blue dots), $\Delta_{\text{coupl}}^{(6)}$ (red dashes), Δ_{geom} (green chain), Δ_{tot} (black solid) (in multiples of ω_{ho} , both in atomic units) for different alkali metal dimers and intensities of the lattice laser (as specified in the graphs). The wavelength of the trap laser is 1030 nm. (The laser intensity 200 W/cm^2 corresponds to a $30 E_r^{\text{Rb}}$ lattice depth for the $^{87}\text{Rb}\text{-}^{40}\text{K}$ dimer.)

Figure 8.3 shows the differences Δ (8.5-8.7) as a function of the scaled interaction parameter ξ (Section 8.1.3) for different lattice depths obtained by the laser intensity variation for the three mentioned systems. As is evident from Figure 8.3, the harmonic coupling difference $\Delta_{\text{coup}}^{(2)}$ is not influenced by the lattice depth, because the coupling depends only on the polarizabilities and the masses and is of the form $(\mu_2\alpha_1 - \mu_1\alpha_2)$. Therefore, $\Delta_{\text{coup}}^{(2)}$ is largest for ${}^6\text{Li}$ - ${}^{133}\text{Cs}$ and smallest for ${}^6\text{Li}$ - ${}^7\text{Li}$ as is clear from Figure 8.3. Beyond the harmonic approximation the mass, polarizability, laser intensity, and k -vector dependence are mathematically non-trivial in the framework of the present approach. As a result, the different Δ values have a behavior which is difficult to predict *a priori*. For example, while the total difference Δ_{tot} decreases with the laser intensity for ${}^{87}\text{Rb}$ - ${}^{40}\text{K}$ and increases for the other two systems, the values Δ_6 and Δ_{geom} change their behavior not only with the laser intensity but also when going from one dimer to the other. Most noteworthy, the Δ values for ${}^6\text{Li}$ - ${}^7\text{Li}$ are not smaller than for the other pairs although this system is almost homonuclear.

Another peculiar feature of the ${}^6\text{Li}$ - ${}^7\text{Li}$ dimer compared to the other considered ones is the occurrence of negative values for $\Delta_{\text{coup}}^{(6)}$ in the case of large positive values of ξ and the laser intensity of 60 W cm^{-2} . This leads to a smaller value of Δ_{tot} compared to Δ_{geom} for these parameters. Clearly, the conclusions obtained for the generic ${}^{87}\text{Rb}$ - ${}^{40}\text{K}$ system are not always transferable to other alkali metal dimers.

8.2.3 Wave-function analysis

Radial pair densities

An alternative analysis of the anharmonicity and COM-REL coupling effects is possible from the wave functions of the first trap induced and the least bound state. Since the probability density for finding a two-particle separation to lie in between r and $r + dr$ is determined by the radial pair density

$$\rho(r) = \iiint\iiint |\chi_i(\vec{R}, \vec{r})|^2 dV_R r^2 d\Omega_r \quad , \quad (8.8)$$

it is convenient to discuss radial pair densities instead of the wave functions. In Equation (8.8) the function $|\chi_i\rangle$ stands for $|\Psi_i\rangle$ or $|\Phi_i\rangle$ depending on the considered approximation, dV_R is the COM volume element, and Ω_r is the angular part of the REL motion coordinates.

The energy spectrum of the first trap induced and the least bound states for the wide range of the interaction regimes was presented in Figure 8.2. However, the three asymptotic interaction situations, i. e., strong attraction ($a_{\text{sc}} \rightarrow -\infty$), the almost zero interaction ($a_{\text{sc}} \rightarrow 0$) and the strong repulsion

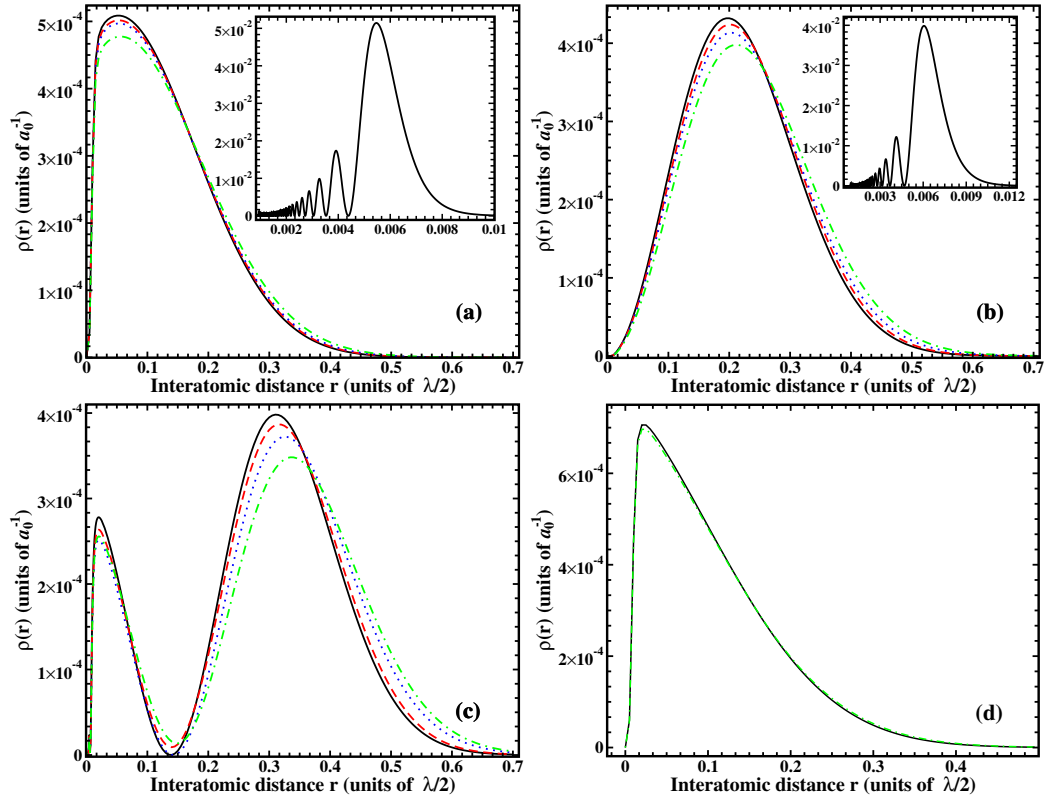


Figure 8.4: Radial pair densities of the 1st trap-induced state of the ^{87}Rb - ^{40}K system in a 3D cubic lattice of $40 E_r^{\text{Rb}}$ depth and the laser wavelength λ of 1030 nm in the uncoupled harmonic (black solid), the harmonic with coupling (red dashes), the uncoupled sextic (blue dots), and the sextic with coupling (green chain) approximations for the three interaction regimes: a) strongly attractive, b) almost zero interaction, c) strongly repulsive, d) strongly repulsive but for the least bound-state. (The insets show the densities for the least bound-state.)

($a_{\text{sc}} \rightarrow +\infty$) are found sufficient for the wave function analysis. Figure 8.4 shows the radial pair densities at the different levels of approximation for the three interaction regimes. As is evident from Figure 8.4, a large attractive interaction leads to a very confined function for the first trap-induced bound state while a large repulsive interaction does not only result in a node but also in a shift of the outermost lobe to larger interatomic distances. This shift is counteracted by the confinement of the trap. Remind, for the trap-free situation in the strongly repulsive regime the wave function crosses the internuclear axis exactly at the value of the scattering length. Evidently, the behavior of the density for almost zero interaction is only determined by the trap.

As is apparent from Figure 8.4 the inclusion of the anharmonicity and the coupling leads to more extended pair densities. For all interaction regimes the following behavior is found. The effect is smallest for the harmonic coupling correction. A larger effect is found for the sextic non-coupled case which is strengthened by the sextic coupling. Effectively, the particles experience a more extended trap, if a more complete description of the problem is achieved. Such an effect is expected for the harmonic-to-sextic uncoupled description, since the harmonic trap is tighter than the sextic one as is evident from the sketch in Figure 8.1. While this is expected for the inclusion of the anharmonicity, this is not immediately clear for the coupling.

The least bound state in the strongly repulsive regime is very long-ranged as the inset of Figure 8.4(c) shows. This distance is almost comparable with the extension of the first trap-induced state for the strongly attractive regime. Nevertheless, the influence of the anharmonicity and the coupling on the least bound state is almost absent, because the state is energetically deeply bound and therefore does almost not probe the anharmonicity of the lattice.

In the considered parameter ranges the radial pair densities approach zero clearly before the interatomic distance reaches the boundary of a single lattice site, i. e., for $r < \lambda/2$, as can be seen from Figure 8.4. Therefore, tunneling or a distribution of the dimer over more than a single lattice site does not occur and the present single-site model is applicable. Furthermore, effects of the artificial infinite walls of the harmonic or sextic potentials should not be a problem. However, the radial pair densities provide only an indication for the applicability of the single-site approximation, since it is still possible that the dimer as a whole may be distributed over more than one site. This can only be excluded from an analysis of the total wave function including the COM motion as is done in the next section.

Wave function in absolute coordinates

It is instructive to analyze the full wave function or corresponding particle density also in absolute coordinates of the laboratory space (ABS). They supply the complete information about the dimer and provide pictures of the COM and REL motion simultaneously. This is evidently not the case for the radial pair density (Figure 8.4) that is averaged over the COM motion and over the angular part of the REL motion. Thus it does not reveal whether the pair as a whole moves through the lattice. Note, while the radial pair density provides nevertheless a rather easy to interpret picture of the underlying physics, this is far less the case for its angular part. The reason is that the anisotropic (egg-box like) shape of the (cubic) optical lattice does not trivially show up in the REL coordinate system. An analysis

in the lab frame is, however, also non-trivial, since the functions depend on six spatial coordinates. Use of the cubic symmetry reduces the size of the symmetry non-equivalent space, but it is still impractical to consider the complete multidimensional function. Instead, some insight may be gained from selected cuts. Although a number of cuts was analyzed in this work, only the results for cuts along the x coordinate of both atoms and thus for $y_i = z_i = 0$ (for both particles i) are shown and discussed.

In order to quantitatively describe the different effects of the trapping potential it is again useful to consider not the wave functions at different levels of approximation themselves, but their respective differences. Similarly to the energy differences defined in Equations (8.5-8.7), the wave-function differences

$$\Delta F_{\text{geom}}(\vec{r}_1, \vec{r}_2) = \Phi_i^{(2)}(\vec{r}_1, \vec{r}_2) - \Phi_i^{(6)}(\vec{r}_1, \vec{r}_2) \quad , \quad (8.9)$$

$$\Delta F_{\text{coup}}^{(n)}(\vec{r}_1, \vec{r}_2) = \Phi_i^{(n)}(\vec{r}_1, \vec{r}_2) - \Psi_i^{(n)}(\vec{r}_1, \vec{r}_2) \quad , \quad (8.10)$$

$$\Delta F_{\text{tot}}(\vec{r}_1, \vec{r}_2) = \Phi_i^{(2)}(\vec{r}_1, \vec{r}_2) - \Psi_i^{(6)}(\vec{r}_1, \vec{r}_2) \quad (8.11)$$

may be introduced. Cuts through these difference functions ΔF are shown in Figure 8.5 for the first trap-induced state and the almost non-interacting case ($a_{\text{sc}} \approx 0$). The sign convention used in Equations (8.9-8.11) means that positive maxima in Figure 8.5 correspond to the case that the wave functions in lower order of approximation have a larger amplitude than those in the higher one. (This choice is, of course, arbitrary and basically motivated by the fact that it leads to positive maxima in the center of the plots which is more suitable for optical reasons.)

The diagonal $x_{\text{Rb}} = x_{\text{K}}$ defines the REL coordinate axis. The wavefunctions and therefore also their differences ΔF are strictly zero along the REL axis, since the molecular interaction potential rises exponentially to infinity for $r \rightarrow 0$. Note, even for $a_{\text{sc}} = 0$ the atoms interact in the present approach, since the scattering length characterizes only the effective long-range interaction. In the case of the often adopted δ -type pseudopotential description the interaction vanishes completely for $a_{\text{sc}} = 0$ and the wavefunction does not vanish around $r = 0$. Slightly away from the REL axis the wavefunction shows rapid oscillations due to the nodal structure that is again a consequence of the realistic interatomic interaction potential used in the present work. They are, however, not resolved in Fig 8.5, as these oscillations occur in a very small ($\sim 10^{-3} \lambda/2$) r range compared to the one displayed.

The COM axis is defined by $x_{\text{Rb}} = -\mu_{\text{K}}/\mu_{\text{Rb}} x_{\text{K}}$. Since ^{87}Rb - ^{40}K is heteronuclear, the COM axis is rotated from the $x_{\text{Rb}} = -x_{\text{K}}$ diagonal and is thus for better readability explicitly indicated in the graphs. Another con-

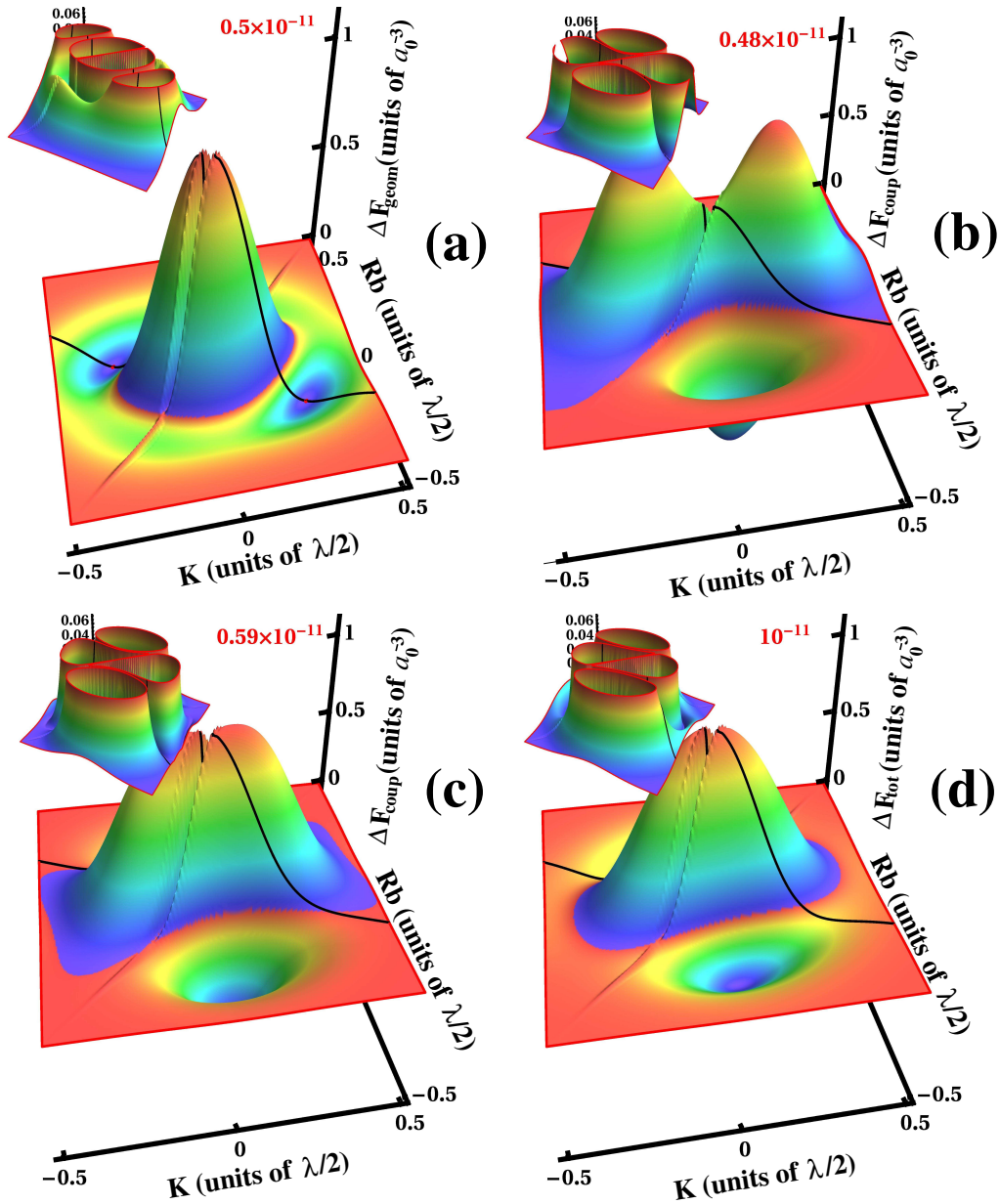


Figure 8.5: Cuts of ΔF (defined in Equations (8.9-8.11)) along the x direction ($y_{\text{Rb}} = y_{\text{K}} = z_{\text{Rb}} = z_{\text{K}} = 0$) for the 1st trap-induced state and almost non-interacting ^{87}Rb - ^{40}K atoms in a 3D cubic lattice ($40 E_r^{\text{Rb}}$, $\lambda = 1030$ nm): a) $\Delta F_{\text{geom}}(x_{\text{Rb}}, x_{\text{K}})$ b) $\Delta F_{\text{coup}}^{(2)}(x_{\text{Rb}}, x_{\text{K}})$ c) $\Delta F_{\text{coup}}^{(6)}(x_{\text{Rb}}, x_{\text{K}})$ d) $\Delta F_{\text{tot}}(x_{\text{Rb}}, x_{\text{K}})$. The differences ΔF are given in atomic units, downscaled by the corresponding factors given in red. The black lines indicate the COM axis ($x_{\text{Rb}} = -\mu_{\text{K}}/\mu_{\text{Rb}} x_{\text{K}}$). The insets show $|\Delta F|$ (on an enlarged scale).

sequence of the heteronuclear character is the elliptical shape that would be circular in the case of a homonuclear system.

Figure 8.5(a) characterizes the geometrical effect of the anharmonicity of an optical lattice. Effectively, the sextic trap is more extended than the harmonic one. This leads to the decrease of the density at the center of the potential and an increased probability at the potential edges. Therefore, the probability to find Rb and K atoms at a larger distance from the center of the optical lattice is higher for an anharmonic trap compared with a harmonic one. Note, this probability redistribution is not homogeneous. For example, for $x_K \approx 0.3 \lambda/2$ and $x_{Rb} \approx -0.1 \lambda/2$ a pronounced minimum of the function ΔF_{geom} exists, as is evident from Figure 8.5(a). This behavior in the ABS space is a direct consequence of the different COM and REL motion trapping depths. The COM of the system is more confined. Hence, the density shift in the direction of the COM axis is larger than for the REL one, as is better seen in the inset of Figure 8.5(a). In the inset one notices also that there exist small minima at the places where both atoms are close together ($r \approx 0$), but away from the center of the lattice site. In general, ΔF_{geom} is rather symmetric with respect to the COM and REL axes.

Figure 8.5(b) shows the effect of the coupling of COM and REL motion within the harmonic approximation. For its understanding it is important to keep in mind that the definition of coupling between the different degrees of freedom depends on the adopted coordinate system. In the present work it is defined by the Hamiltonian in Equation (7.4) and thus the coupling of COM and REL coordinates. While this is a natural choice for discussions of, e. g., the radial pair density, its meaning is less transparent for a discussion of wave functions in ABS coordinates of the two atoms. An evident example is the case of two truly non-interacting atoms in a harmonic trap. Even for a heteronuclear atom pair the problem separates in ABS coordinates, as was already mentioned in Section 7.1.1. However, treating this system in COM and REL coordinates the coupling term \hat{W} in Equation (7.4) and thus also the difference $\Delta F_{\text{coup}}^{(2)}$ is non-zero, but the latter reflects the non-separability due to the adopted coordinate system.

A comparison of $\Delta F_{\text{coup}}^{(2)}$ shown in Figure 8.5(b) with the one obtained from the analytically known harmonic solutions in either ABS or REL and COM coordinates for truly non-interacting particles (see, e. g., [165]) confirms that the structures in Figure 8.5(b) for the ^{87}Rb - ^{40}K dimer with the long-range interaction being tuned to be almost vanishing are similar. In contrast to the case of the geometry effect visible in Figure 8.5(a) the maxima and minima in Figure 8.5(b) have a more similar magnitude (the maxima being about 16% larger in absolute value than the minima) and, clearly, they also originate from the different effects discussed above. Furthermore, they

are located away from the center of the optical-lattice site. In fact, they are found, if one of the two atoms is located closely to the center and the other one is separated by about the most likely separation (about $0.2 \lambda/2$, Figure 8.4 (b)). The maxima (minima) are connected with the lighter K (heavier Rb) atom being close to the center. The anti-clockwise rotation of the maxima and minima around the origin is due to the heteronuclear character and reflects the coupling term in ABS coordinates, i. e., $\Delta F_{\text{coup}}^{(2)} \sim e^{-\gamma x_{\text{K}} x_{\text{Rb}}}$ (where γ is some constant). Also the different widths of the maxima and minima is a consequence of the heteronuclear character of ^{87}Rb - ^{40}K . While the off-centered minima of ΔF_{geom} are centered on the COM axis, the COM axis appear to separate the minima and maxima of $\Delta F_{\text{coup}}^{(2)}$, although it does not define a strict nodal plane.

The sextic coupling effect presented in Figure 8.5(c) is similar to the harmonic one in Figure 8.5(b). However, the two maxima are now almost connected (if there were not the strict node on the REL axis) and form more a kind of plateau. The minima are less pronounced and as a consequence, the absolute values of the maxima are now about 40% larger than the ones of the minima.

Figure 8.5(d) presents the complete effect of anharmonicity and coupling of the optical lattice. Compared to the previously discussed ΔF functions the shown ΔF_{tot} is in shape most similar to $\Delta F_{\text{coup}}^{(6)}$ in Figure 8.5(c). However, the two maxima at the corners of the plateau appear now to be merged with the central peak due to the new scale (and are basically only separated by the node along the REL axis). As a consequence, the density of the exact sextic solution is reduced at the center of the lattice compared with the uncoupled harmonic approximation. In fact, as is evident from the equality $\Delta F_{\text{tot}} = \Delta F_{\text{geom}} + \Delta F_{\text{coup}}^{(6)}$ (compare Equation (8.7)), the merging of the two maxima is simply a consequence of the superposition of the structures of $\Delta F_{\text{coup}}^{(6)}$ and ΔF_{geom} . Note the correspondingly almost by a factor 2 larger amplitude of ΔF_{tot} compared to the other wavefunction differences. Since the minima of ΔF_{geom} and $\Delta F_{\text{coup}}^{(6)}$ appear at rather different places, their relative importance diminishes in comparison to the maxima. This leads to an about 66% larger absolute value of the maxima compared to the minima in the case of ΔF_{tot} . However, the additivity leads to an effective broadening of the minima of ΔF_{tot} in direction of the COM axis compared to the minima found for $\Delta F_{\text{coup}}^{(6)}$.

To conclude the almost non-interacting case, the optical lattice is in the coupled sextic description effectively more extended than in the uncoupled harmonic one. As a consequence of this anharmonicity the wave-function amplitude at the center of the lattice site decreases and is redistributed to the edges of the potential. As a consequence of the coupling, the decrease of the

wave-function amplitude stretches further out along a diagonal in between the COM and REL axes close to the axis defined by the Rb atom being located at the center of the lattice site ($x_{\text{Rb}} = 0$). On the other hand, the coupling leads also to minima (increased amplitude) along a diagonal between the COM and REL axes, but close to the $x_{\text{K}} = 0$ axis. As a consequence of the heteronuclear character of the ^{87}Rb - ^{40}K dimer, the two diagonals are rotated with respect to the two corresponding $x = 0$ axes.

Figure 8.6 characterizes the anharmonicity and coupling effect in the strongly interacting regimes. The most evident difference between the (almost) non-interacting case and the strongly interacting situations is the pronounced squeezing of the central peak along the COM axis. This is easily seen by comparing the geometry effect characterized by ΔF_{geom} in Figures 8.6(a) and (b) with Figure 8.5(a). Connected with this squeezing is an increase of the maxima by a factor of almost 6 (strong repulsion) or more than 8 (strong attraction). The additional lobe occurring for strongly repulsive interaction at large distances leads to two further maxima on the COM axis (one for a positive and one for a negative value of x_{K}) for ΔF_{geom} (Figure 8.6(b)), indicating a corresponding difference between the uncoupled harmonic and sextic solutions that occurs also at the outer lobes. The minima on the COM axis are in this case shifted to larger distances from the REL axis. This is not the case for a strong attractive interaction, but there the amplitude of the minimum is even smaller than in the attractive case where it is already of less relative importance compared to the central maxima than in the non-interacting case. On the other hand, the minima on the REL axis that had been very weak compared to the ones on the COM axis for the non-interacting case are in the strongly interacting cases much more pronounced, but also squeezed into a narrow regime close to the REL axis.

As for the almost non-interacting case (Figure 8.5(d)), the total differences ΔF_{tot} for the strongly interacting cases (Figures 8.6(c) and (d)) differ from their ΔF_{geom} counterparts by the occurrence of two minima along diagonals between the COM and REL axes for $x_{\text{K}} \approx 0$. While the also coupling-induced maxima for $x_{\text{Rb}} \approx 0$ lead for the non-interacting case to a broad central peak, they appear in the strongly interacting case as shoulders. The reason is the massive squeezing of the central peak already discussed for ΔF_{geom} . The additional maxima along the COM axis in the case of strong repulsion lead to a rather structured difference surface ΔF_{tot} in this case. Another interesting effect visible from Figure 8.6(d) is the enormous increase of the central maximum when comparing ΔF_{tot} with ΔF_{geom} . For both the almost non-interacting and the strongly attractive case there is an approximate increase by a factor of 2, but in the strongly repulsive case there is a factor of more than 6.

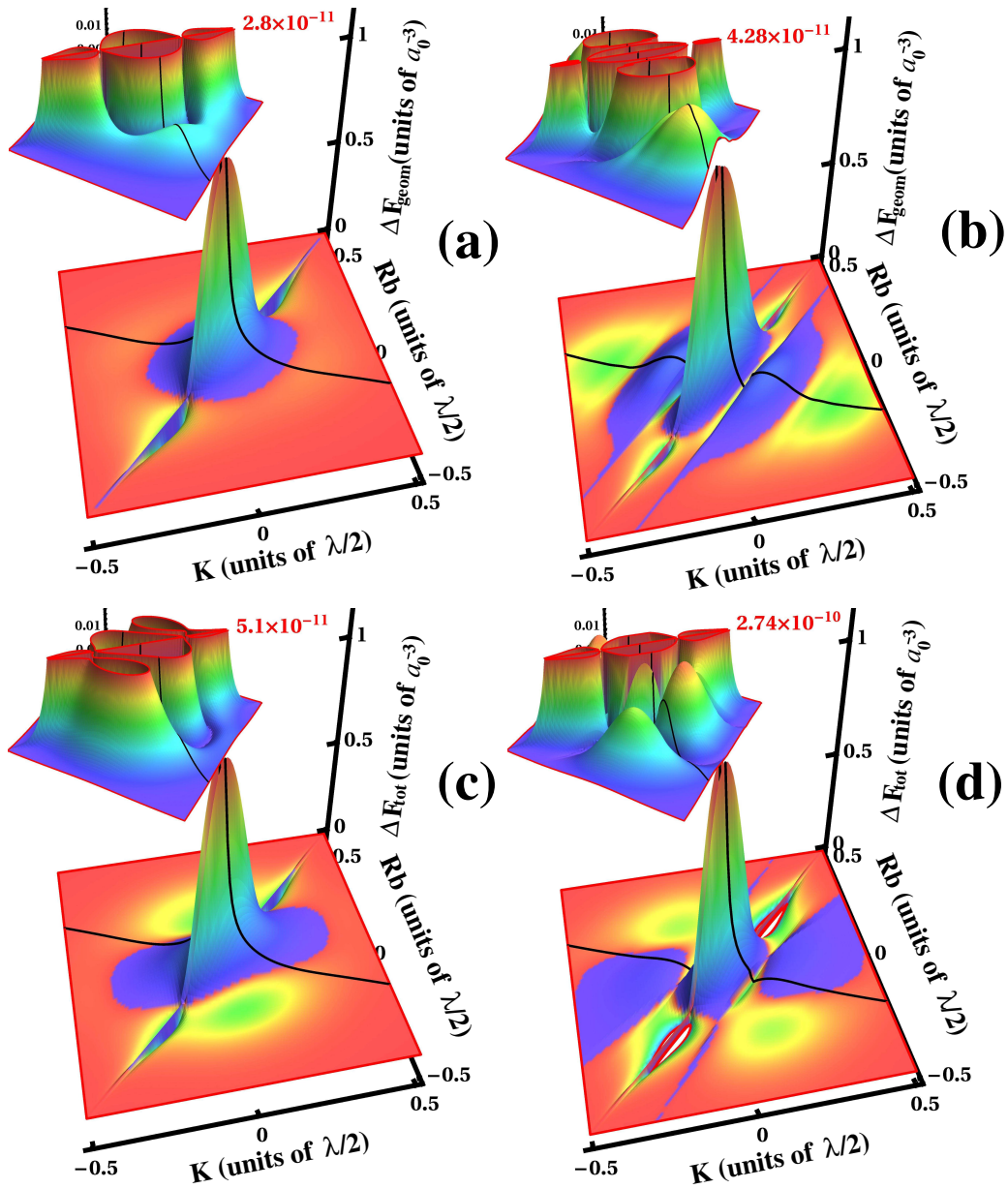


Figure 8.6: Cuts through the differences ΔF as in Figure 8.5, but a) $\Delta F_{\text{geom}}(x_{\text{Rb}}, x_{\text{K}})$ and c) $\Delta F_{\text{tot}}(x_{\text{Rb}}, x_{\text{K}})$ for strongly attractively interacting particles ($a_{\text{sc}} = -6600 a_0$); b) $\Delta F_{\text{geom}}(x_{\text{Rb}}, x_{\text{K}})$ and d) $\Delta F_{\text{tot}}(x_{\text{Rb}}, x_{\text{K}})$ for strongly repulsively interacting particles ($a_{\text{sc}} = +6600 a_0$).

Compared to the analysis of the radial pair densities in Section 8.2.3 it is evident that the absolute wave-function analysis reveals much more subtle details. In the case of radial pair densities there was the clear trend that improving the level of description leads to an increasing shift of probability from the maxima towards large separations. Similarly, the energies were uniformly lowered. (Remind, however, that the energy analysis for ${}^6\text{Li}{}^7\text{Li}$ showed that such a uniform trend is not found for all heteronuclear systems.) The cuts through the full wave functions show that the effects of coupling and anharmonicity are not as trivial. Most importantly, they indicate that there is a lot of changes of the wave functions for short internuclear separations where, e. g., a pseudopotential approach is questionable. The relative importance of this regime of interatomic separations is, however, reduced, if an average over the angles is performed; simply because it scales with the radial part of the volume element, r^2 . This is also the reason why the energies are not very sensitive to this short-range regime and thus the pseudopotential approach may rather successfully predict also energy differences between different levels of approximation.

The wave functions (not their differences) were also used in order to assure that the parameters chosen in this work allow a discussion in terms of a single site of an optical lattice. Different cuts through the wave functions (in different directions relative to the optical lattice) never indicated a substantial wave function amplitude close to the boundaries of the single lattice site.

8.3 Conclusion

A detailed analysis of anharmonicity and coupling of center-of-mass and relative coordinates in terms of energy values and wave functions was performed for heteronuclear dimers in a single site of an optical lattice. It is explained, why such a single site is optimally described by a sextic potential, if a finite Taylor expansion is used. The effects of deviations from the harmonic approximation and of the coupling were quantified and analyzed for different heteronuclear systems, confinement strengths and interatomic interaction regimes. The influence of the lattice is found to be always much stronger for the first trap-induced state than for the least bound state. As a consequence, binding energies are modified by the lattice mainly by the modification of the first trap-induced state.

While the energy deviations from the harmonic uncoupled approximation is for all three considered generic heteronuclear dimers largest for strong repulsive interaction, the relative size (and even sign) of the energy change

due to coupling or anharmonicity varies for the different dimers. The same is true for the influence of the trap depth. A deeper lattice can lead to smaller or larger energy differences between the harmonic uncoupled or the full coupled solution. While the analysis of the radial pair densities shows that the lattice mainly influences the maxima located at large interatomic separations, the analysis of cuts through the wave functions in absolute coordinates reveals non-negligible changes also at short interatomic distances. This may have important consequences for the validity of pseudopotential approximations.

Chapter 9

Ultracold heteronuclear molecules in a 3D optical lattice

A natural application of the theoretical approach developed in Chapter 7 is to model the experimental results of C. Ospelkaus *et al.* [96]. In that experiment, radio frequency association was used to create molecules from fermionic ^{40}K and bosonic ^{87}Rb atoms in a 3D cubic optical lattice close to the Feshbach resonance. The binding energy of the heteronuclear molecules was measured as a function of the applied magnetic field strength. In this chapter, the theoretical predictions of the present work are checked against the experimental data as well as against subsequent theoretical studies [98].

9.1 Comparison to experiment

Figure 9.1 shows the experimental data for a lattice with depth $V_{\text{Rb}} = 40 E_r^{\text{Rb}}$ and wavelength $\lambda = 1030 \text{ nm}$. Note, the binding energies measured in the experiment are not the usual ones. In free space, real molecules (RM) close to the Feshbach resonance exist only on the repulsive side of the resonance ($a_{\text{sc}} > 0$). The binding energy measured in a trap-free situation is the one relative to the threshold energy of the continuum. In the presence of an external optical lattice, this continuum is discretized, and there is instead a first, trap-induced state. On the attractive side of the resonance ($a_{\text{sc}} < 0$), the energy of this state is lowered relative to the field-free position. This leads to confinement-induced molecules (CIM) [94]. In the experiment reported in [96], the binding energy of the RM and CIM in a trap were measured. For $a_{\text{sc}} > 0$, the excitation energy of the repulsively interacting bound pair (RIP) [70], where repulsion between bosons and fermions shifts the two-particle ground state towards a higher energy, was also measured. The cor-

responding RM, CIM and RIP branches are denoted in Figure 9.1, in which the experimental results of [96] are reproduced for comparison.

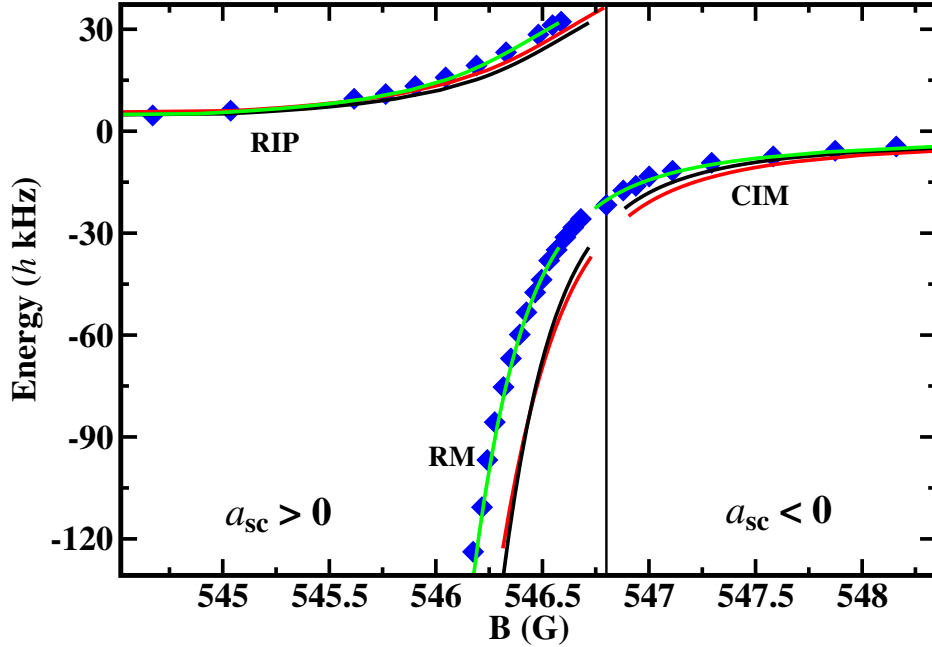


Figure 9.1: The experimentally measured binding energy (diamonds) of ^{87}Rb - ^{40}K in an optical lattice ($40 E_r^{\text{Rb}}$, λ of 1030 nm) together with the theoretically calculated ones for the sextic potential and the energy-independent (black solid) or energy-dependent (red solid) scattering length and the Feshbach resonance parameters $B_0 = 546.8$ G and $\Delta B = -3$ G. The figure also shows the binding energy for the sextic trap and the energy-independent scattering length for the alternative value $B_0 = 546.66$ G (green solid). (All theoretical curves are full CI solutions.)

In order to compare the experimentally measured binding energies with the theoretically calculated ones, a proper mapping must be applied. Figure 9.2 outlines the procedure specifying how the binding energies were determined in the model. The scattering length $a_{\text{bg}} = -185 a_0$ is chosen as the B -field-free background scattering length. The energy of the first trap-induced state obtained with the full sextic solution at a_{bg} is chosen as energy zero and is marked explicitly in Figure 9.2. A variation of the scattering length leads to energy shifts of the least bound and the first trap-induced states relative to this energy zero. The binding energy is a function of this shift, as is indicated by the arrows in Figure 9.2. Specifically, the binding energy as a function of the scattering length may be obtained from the present

theoretical data with help of the relation [36, 105, 166]

$$\mathbf{E}_b^{(n)}(a_{sc}; i) = \mathbf{E}_{1ti}^{(n)}(a_{bg}) - \mathbf{E}_i^{(n)}(a_{sc}) \quad (9.1)$$

where i and n are, as in Chapter 8, $i = \{lb, 1ti\}$ and $n = \{2, 6\}$. Furthermore, \mathbf{E} stands for the state energy at a given level of approximation $\mathbf{E} = \{E, \mathcal{E}\}$. This definition of a binding energy results in three different branches. While the first trap-induced state is responsible for the RIP and the CIM branch, the least bound state is responsible for the RM part. The corresponding branches are indicated in Figure 9.1 and in the sketch of Figure 9.2.

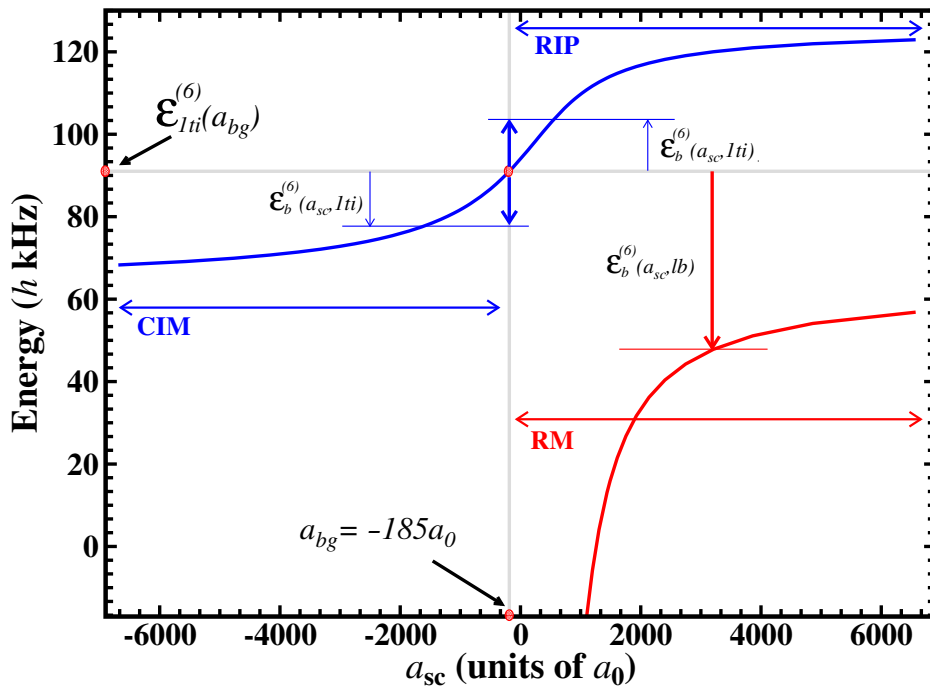


Figure 9.2: Sketch of the procedure for obtaining binding energies from the model. The 1st trap-induced (blue) and least bound (red) state energies obtained with a full CI calculation for the sextic potential (the same as in Figure 8.2(b)) are shown. While the energy-offset of the first trap-induced level (blue arrows) relative to the energy zero ($\mathcal{E}_{1ti}^{(6)}(a_{bg})$) is responsible for the confinement phenomena, the energy offset of the least bound state (red arrow) is responsible for the pure molecular ones.

Experimentally, the binding energies were measured as functions of the magnetic field while theoretically calculated energies are functions of the interaction strength represented by the scattering length (see Section 8.1.3 for details). To provide a B dependence of the theoretical data, a_{sc} is mapped

onto the magnetic field using a two-channel approximation [36] with the aid of

$$a_{\text{sc}}(B) = a_{\text{bg}} \left(1 - \frac{\Delta B}{B - B_0} \right) \quad (9.2)$$

where ΔB is the resonance width and B_0 is the resonance position. Equation (9.2) gives in turn for the B field as a function of a_{sc}

$$B(a_{\text{sc}}) = \Delta B \left(1 - \frac{a_{\text{sc}}}{a_{\text{bg}}} \right)^{-1} + B_0 \quad . \quad (9.3)$$

The a_{sc} values obtained from theory are inserted into Equation (9.3) to determine the B dependence of the energy.

Figure 9.1 shows the binding energy obtained from the full sextic solution $\mathcal{E}^{(6)}$ for the experimental parameters of the trap and magnetic field Feshbach resonance parameters $\Delta B = -3$ G [161] and $B_0 = 546.8$ G [65]. As is evident from Figure 9.1, the model does not perfectly agree with the experiment. Some possible reasons of the disagreement are discussed in the following paragraph.

9.1.1 Reasons for deviation between theory and experiment

Equation (9.2) is derived for the lattice-free situation under the assumption that the collision between two atoms can be approximated by a two-channel scattering model. In general, as was already mentioned in Chapter 3, the correct theoretical description requires a multi-channel scattering treatment which in the present case would also have to incorporate the optical lattice. Moreover, the present model uses an “artificial” variation of the scattering length (see Section 8.1.3), and the a_{sc} values obtained from this variation are the ones of a single-channel approach.

Even assuming the validity of Equation (9.2), there is another important factor influencing the comparison of theory and experiment. The values of the scattering length a_{sc} and a_{bg} of Equation (9.2) are determined in a lattice-free situation. In the presence of a trap, these values must be revised and adjusted to the trap parameters. It was shown in [83] that the use of an energy-dependent scattering length a_{sc}^E gives almost correct energy levels for two harmonically trapped atoms. The evaluation of a_{sc}^E requires the solution of the complete scattering problem, and thus a_{sc}^E can only be obtained with the knowledge of the solution for the realistic atom-atom interaction potential. Eventually, the trap-free values of the scattering length a_{sc} and a_{bg} must be substituted by appropriate energy-dependent scattering length

a_{sc}^E values. However, the problem is that the energy-dependent scattering length approach is so far developed only for the harmonic approximation, for s -wave collisions, and the uncoupled problem. An anharmonic, e. g., “sextic”, energy-dependent scattering length concept as well as any other extensions of it do so far not exist to the author’s knowledge.

In view of the absence of an a_{sc}^E beyond the uncoupled harmonic approximation, the following procedure was adopted. The energy-dependent values of the scattering length are obtained using a solution for the pseudopotential energy and valid for a harmonic trap [82]

$$\frac{\Gamma\left(-\frac{1}{2}\frac{\epsilon_{1\text{ti}}^{(2)}}{\omega_{\text{ho}}} + \frac{3}{4}\right)}{\Gamma\left(-\frac{1}{2}\frac{\epsilon_{1\text{ti}}^{(2)}}{\omega_{\text{ho}}} + \frac{1}{4}\right)} = \frac{a_{\text{ho}}}{a_{\text{sc}}^E \sqrt{2}} \quad , \quad (9.4)$$

where Γ is a gamma function. The energy of the REL motion obtained for the *harmonic* trap are imposed into Equation (9.4) and the a_{sc}^E values are obtained. The new values of the scattering length obtained with this manipulation are used for the mapping of the binding energies of $\mathcal{E}^{(6)}$ with the help of Equation (9.2). Figure 9.1 shows the result of this procedure. As is seen from the figure the shift of the spectral curve for the case of the energy-dependent scattering length along the B -axis is not big, but the curve is shifted along itself for the RIP branch and is tilted towards the other ones in immediate proximity to the resonance. This may be seen as an indication that the energy dependence of the scattering length (properly included) does not have too big an effect, but the approximate implementation is certainly not conclusive and thus cannot exclude possible significance.

Another important reason of the mismatch between theory and experiment could be an insufficient knowledge of the resonance parameters [98]. It turns out to be sufficient to change the center of the Feshbach resonance to the value $B_0 = 546.66$ G to match the experimental and the theoretical data. A variation of B_0 of this size is well within the experimental uncertainty with which the resonance parameters are known [65]. The result obtained with this modified value of B_0 is also shown in Figure 9.1. Remarkably, if both parameters B_0 and ΔB are used together to fit the experimental curve, it leads to a larger error than if only the parameter B_0 is varied (in the discussion in the following subsection, especially Figure 9.4). While a variation of ΔB and B_0 shifts the theoretical data along the magnetic-field axis, the variation of a_{bg} leads in addition to a shift along the energy axis, since it changes the B-field-free energy zero.

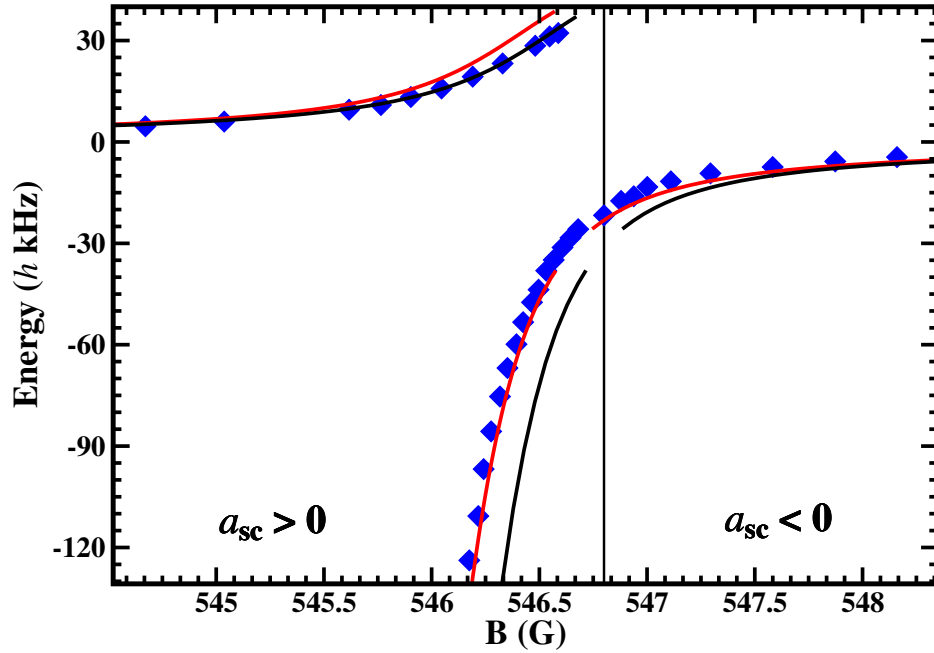


Figure 9.3: As Figure 9.1, but using a *harmonic* potential, an energy-independent scattering length, and the Feshbach-resonance positions $B_0 = 546.8$ G (black solid) or $B_0 = 546.66$ G (red solid).

Finally, one may address the question whether despite the degree of uncertainty, the effect of the anharmonicity and coupling is visible in the experiment [96]. Figure 9.3 shows the binding energies obtained from the harmonic approximation. While the harmonic approximation predicts the binding energy of the repulsively interacting pair part of the spectrum correctly, for other parts it results in a disagreement. A variation of the MFR parameters does not lead to a simultaneous matching of all spectral branches. Therefore, it is possible to conclude that, in the experiment [96], effects of anharmonicity and coupling (and thus deviations from a simple uncoupled harmonic model) were very probably detected.

9.2 Comparison to a previous theoretical investigation

The effects of anharmonicity and coupling of COM and REL motion in a single site of an optical lattice were also the subject of a recent theoretical study by Deuretzbacher *et al.* [98]. The approach therein differs from the present

one, since (i) it does not use the full interatomic interaction potential but resorts to the pseudopotential approximation, (ii) a different partitioning of the Hamiltonian is adopted, and (iii) different basis functions (eigensolutions of the harmonic oscillator) were adopted.

The two independently developed approaches provide the possibility of further checking whether theory has achieved a sufficient accuracy to investigate the small deviations from the simple uncoupled harmonic approximation claimed to be found in the experiment in [96]. A consequence of difference (i) between the two approaches is, furthermore, the ability to investigate the adequacy of the pseudopotential adopted in [98]. As a consequence of (iii), the approach in [98] can only be applied to very deep lattices and an extension to multiple-site lattices or even to shallow lattices is not straightforward. The reason is the rather strong spatial confinement of the harmonic-oscillator solutions. As a consequence, it needs an impractically large number of basis functions in order to cover an extended spatial regime. Since anharmonicity and coupling effects are different for shallower lattices as is discussed in Section 8.2.2, the tunneling effects may also play an important role [167, 168]. Within the present approach, calculations for multiple-wells and shallow lattices are straightforward and were already recently performed [145].

The spatial compactness of the harmonic-oscillator eigenfunctions is, on the other hand, evident from the convergence study with respect to the Taylor expansion of the optical lattice performed in [98]. As was discussed in Section 8.2.1, such a study does not make sense, since, e. g., even-order expansions lead to unphysical continua. Clearly, only a basis that does not explore the corresponding regime of the configuration space (like the one used in [98]) can avoid any signs of these unphysical continua.

Table 9.1 shows a comparison of some energies and energy differences obtained with the numerical approach by Deuretzbacher *et al.* [98] and the present one, for a large positive scattering length ($a_{\text{sc}} = 6500 a_0$). The results obtained with the two approaches do not differ very much in the case of all of the three considered alkali-metal dimers. The agreement between the energy differences is overall slightly better than the one of the absolute energies. The comparison seems to confirm the proper numerical implementation of both numerical approaches. Most importantly, it demonstrates that, for the calculation of energy shifts as well as anharmonic and coupling effects in a single site of an optical lattice, the pseudopotential approach remains valid; at least to a very good approximation.

It is presently not possible to attribute the remaining differences to the different atomic interaction potential or some remaining numerical uncertainty. Note, the different interaction potential influences the results in two ways. First, the δ -type pseudopotential does not properly account for the

Table 9.1: Influence of different levels of approximation on the energy of the 1st trap-induced state for three heteronuclear systems. All results are obtained for $a_{\text{sc}} = 6500 a_0$ (or $\xi(\text{RbK}) = 3.34$, $\xi(\text{LiCs}) = 3.76$, $\xi(\text{LiLi}) = 3.24$), lattice depths of $V_1 = V_2 = 10 E_{\text{r,rel}}$ where $E_{\text{r,rel}} = k^2/(2\mu)$, and a wavelength $\lambda = 1000$ nm.

atom pair	$E_{1\text{ti}}^{(2)}$	Δ_2	$\mathcal{E}_{1\text{ti}}^{(6)} - \mathcal{E}_{1\text{ti}}^{(2)}$	Δ_{tot}
^{87}Rb - ^{40}K [present]	3.79	-0.12	-0.29	-0.41
[98]	3.74	-0.12	-0.27	-0.39
^6Li - ^{133}Cs [present]	2.93	-0.38	-0.22	-0.60
[98]	2.88	-0.35	-0.22	-0.57
^6Li - ^7Li [present]	3.93	-0.01	-0.30	-0.31
[98]	3.92	-0.01	-0.29	-0.30

short-range part of the interaction. Second, the mapping of the energy to a corresponding interaction strength is different in the two approaches. In the pseudopotential approach the scattering length is simply a parameter that enters the interaction potential, while in the present approach it is extracted from the resulting wave function as was described in Section 8.1.3. As a consequence, there is a finite range in which a_{sc} can be varied within the present approach.

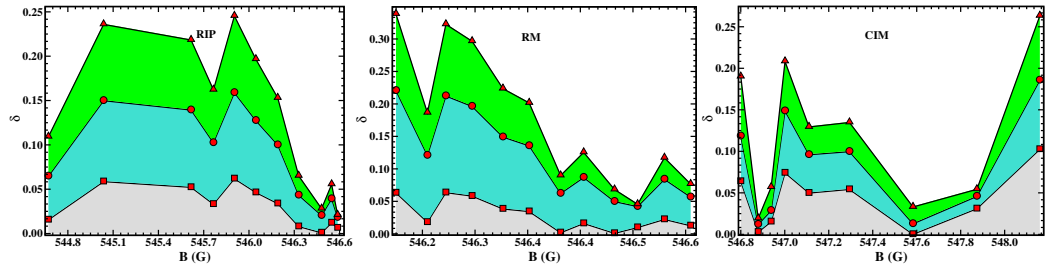


Figure 9.4: The relative error defined in Equation (9.5) for the alternative Feshbach parameters $B_0 = 546.660$ G, $\Delta B = -3$ G (squares), $B_0 = 546.669$ G, $\Delta B = -2.92$ G (circles), and $B_0 = 546.66$ G, $\Delta B = -2.92$ G (triangles).

Comparable to the present finding (Section 9.1.1) the binding-energy spectrum of ^{87}Rb - ^{40}K calculated by Deuretzbacher *et al.* [98] does not agree very well with the experimental one in [96], if the previously experimentally determined Feshbach-resonance parameters ($B_0 = 546.8$ G, $\Delta B = -3$ G) are used. Deuretzbacher *et al.* [98] proposed that, with the aid of the calculation, it is in fact possible to improve on the MFR parameters. Such a fit (with the

energy-independent scattering length) yielded the new resonance parameters $B_0 = 546.669$ G and $\Delta B = -2.92$ G [98]. This has to be contrasted with the present fit that yields the new resonance position $B_0 = 546.660$ G, but an unchanged width ($\Delta B = -3$ G), as was discussed in Section 8.1.3. Thus there is a similar (though slightly larger) trend for B_0 , but disagreement with the results of Deuretzbacher *et al.* [98] with respect to ΔB .

In view of the different fit results, it is important to investigate in more detail their sensitivity to the fit parameters. The quality of the fit depends on the agreement between the calculated binding energy ($\mathcal{E}^{(6)}(B)$) and the experimental one (E_{exp}). It is thus given by the relative error

$$\delta(B) = \left| \frac{E_{\text{exp}}(B) - \mathcal{E}^{(6)}(B)}{E_{\text{exp}}(B)} \right|. \quad (9.5)$$

Figure 9.4 shows $\delta(B)$ for three sets of MFR parameters: (i) $B_0 = 546.660$ G and $\Delta B = -3$ G (optimal fit parameters, this work), (ii) $B_0 = 546.669$ G and $\Delta B = -2.92$ G (optimal fit parameters from Deuretzbacher *et al.* [98]), and (iii) $B_0 = 546.660$ G and $\Delta B = -2.92$ G (optimal fit parameter found in this work for B_0 , but ΔB from [98]). As is evident from Figure 9.4, any variation of either ΔB or B_0 from their optimal values results in an increased error for all energy branches and all magnetic fields. Clearly, the fit shows a well defined minimum and thus there is no ambiguity in the fit parameters as could occur, e. g., in the case of very shallow minima where the outcome of the fit may be strongly influenced by small numerical inaccuracies.

Provided the fit fidelity of Deuretzbacher *et al.* [98] is comparable to the present one, i. e., a fit with the binding energies they calculated using the optimal fit parameters of the present work would disagree with the experiment in a similarly pronounced fashion as shown in Figure 9.4, it is presently impossible to conclude whether theory has already reached the level of accuracy that is required for an improved determination of MFR parameters. While both fits appear to indicate a smaller value of B_0 compared to the one previously extracted from experiment, the deviation between both fits is only about half as small as the improvement claimed by Deuretzbacher *et al.* [98]. Clearly, such a result is, from a statistical point of view, inconclusive. In the case of the width ΔB the present finding agrees even fully to the previously determined experimental value and thus disagrees with the result of the fit of Deuretzbacher *et al.* [98].

In order to obtain a more conclusive result it is vital to investigate whether the differences between the results of Deuretzbacher *et al.* [98] and the present ones are solely due to the use of the pseudopotential approximation or the more realistic interatomic interaction potential in the two studies. If this were

the case, the fit results of the present study should be regarded as the more accurate ones. Furthermore, this would be an important example for the need to consider the interatomic interaction on a more accurate level than the one provided by the pseudopotential approximation. Since the implementation of the pseudopotential is due to the singular behavior of the δ function non-trivial in the context of the present approach, such an investigation has to be postponed to a separate work. Clearly, more experimental data (for different heteronuclear systems) would also be very important for gaining a deeper insight and it is hoped that the present work stimulates such experimental activities.

Finally, there are two further uncertainties in the determination of the MFR parameters from a fit like the one of Deuretzbacher *et al.* [98] or in the present work. They are related to the way in which the mapping of the theoretical data onto the magnetic field is performed. As already mentioned, this mapping is usually based on the assumption of validity of Equation (9.3) and thus on the assumption that the B -field mapping of the multichannel MFR can be performed based solely on a scattering-length variation. Even in this case there is, however, the problem of the proper determination of the energy-dependent scattering length in an optical lattice which is so far unknown. The use of a_{sc}^E extracted from the harmonic uncoupled energies for the mapping of the full sextic energy results effectively in a shift of the energy-independent curve, as is seen in Figure 9.1. However, both the energy-dependent and energy-independent a_{sc} discussed in this work utilize the same harmonic energy curve ignoring also the coupling to the COM motion. How the situation would change, if a_{sc}^E for a non-harmonic solution would be used, is difficult to predict, since the other curves in Figure 8.2 not only differ in shape, but are also shifted relative to each other and contain the COM part. The overall good agreement of the theoretical binding energies (with fitted MFR parameters) to the experimental data does, of course, suggest that these uncertainties have a small influence, but this may be a pure coincidence.

Both the investigation of the appropriateness of the B -field mapping and the question of the possibility of defining an energy-dependent scattering length beyond the uncoupled harmonic approximation requires a theoretical approach for the treatment of two atoms in an optical lattice as the one presented in this work and is presently pursued. The results of the previous sections are valid independently of these uncertainties. Different interaction regimes are experimentally accessible within the validity regime of a single-potential-curve treatment even for the same dimer, by considering different isotopes or electronic states. However, the simplicity of experimental tunability as is found for magnetic Feshbach resonances is then, of course, lost.

9.3 Conclusion

The results of the theoretical approach developed in Chapter 7 are also compared to a recent experiment in which the binding energies of ^{87}Rb - ^{40}K have been measured as a function of an external magnetic field tuned close to a magnetic Feshbach resonance. The assumptions necessary for such a comparison are carefully discussed. It is found that very good agreement between experiment and theory can only be reached if the previously experimentally determined resonance parameters are modified. Since this needed modification is within the error bars within which the parameters had previously been determined, this is not only reasonable, but may even indicate the possibility of more accurately determining the width and position of magnetic Feshbach resonances in ultracold atomic gases, as was proposed recently in a comparable theoretical study. However, the resonance parameters determined in the previous study based on the pseudopotential approximation differ from the ones found in the present work. Whether this deviation is due to the pseudopotential approximation is difficult to judge at this moment. If this were the case, then the found breakdown of the pseudopotential approximation would, of course, be a very interesting finding. A further investigation is therefore of great interest, and the present work stimulates hopefully also further experimental work in this direction. Since the influence of anharmonicity and coupling becomes more important for less deep optical lattices and for excited trap levels corresponding experiments like the ones in [64, 167, 169] are expected to provide further tests of the approach.

Chapter 10

Summary and outlook

The subject of this investigation was ultracold atomic and molecular physics as it occurs, e. g., in Bose-Einstein condensates of dilute gases. To simulate the fully correlated motion in such ultracold many-body systems, a *B*-spline based configuration-interaction approach was developed. In this approach, the mean-field solutions were used in the subsequent configuration-interaction calculation. Furthermore, the two-body interparticle interaction potential was adopted in the form of the pseudopotential. It was concluded that, with this choice of the two-body model interaction, the proposed approach does not converge. The mean-field study showed that two-body collisions are dominant in ultracold dilute atomic gases. The observed divergence also showed that the correct choice of the interparticle interaction description is very important. These facts have motivated the detailed study of the two-body physics of the remaining part of the thesis. The two-body problem has been investigated in more detail using different levels of approximation. In this context, the collision of two atoms in the presence of a resonant magnetic field, the problem of the influence of tight harmonic traps on the photoassociation of atoms, and the physics of two atoms in optical lattices were investigated in more detail.

In order to describe collisions of two atoms the multi-channel problem was studied. For this the interactions like the hyperfine, the exchange, or the Zeeman ones were properly taken into account. The full multi-channel problem was analyzed numerically for the Feshbach resonances in collisions between generic ${}^6\text{Li}$ and ${}^{87}\text{Rb}$ atoms in the absolute ground-state mixture in presence of static magnetic field. The radial wave functions of the collisional ground-state were analyzed in detail in on-resonant and off-resonant situations. It was observed that depending on the distance between two particles the set of the interacting states is preferably considered in either of asymptotically free (atomic) basis or in of the triplet/singlet (molecular) basis. While

the atomic basis is convenient for the description of the long-range part of the wave function, the molecular basis is suitable for the short-range part.

In many systems the multi-channel approach cannot be solved or adopted for practical reasons. In order to overcome this problem, effective single-channel schemes were developed. The single-channel schemes developed here are based on an artificial variation of the two-body Hamiltonian. In this case the atom-atom interaction potential can be varied in numerous ways. The strong-repulsive inner wall, the exchange part, and the long-range van der Waals part may be modified separately in a controllable manner. These procedures were called *s*-, *J*- and *w*-variational schemes. Additionally, the μ -variational scheme was used, that denotes the mass variation if the kinetic energy operator is modified. For short interatomic distances variational schemes obtained by manipulating the mass or the short-range part of the interaction potential led to wave functions that disagree in the nodal structure with the appropriate exact multi-channel solution. None of the single-channel wave functions gave correct amplitudes. In order to find the correction factor at short distances, the multi-channel solution must be available. On the other hand, the variation of the long-range part of the interaction potential via variation of a van der Waals coefficient resulted in quantitative agreement of the single-channel solution with the full solution at short range. At long-range distances the *m*-, *J*-, and *s*-variational schemes gave correct behavior of the wave function and the *w*-variation fails. For these distances, the multiplication by a correction constant C^v is not needed.

The influence of a tight isotropic harmonic trap on photoassociation of two ultracold alkali-metal atoms forming a homonuclear diatomic molecule was investigated using realistic atomic interaction potentials. The systematic analysis was done for a generic ${}^6\text{Li}_2$ dimer. The generality of the conclusions made for ${}^6\text{Li}_2$ were checked considering alternative dimers in diverse electronic states. Two photoassociation regimes were identified: the constant and cut-off ones. For states in the constant regime an identical enhancement was found as the trap frequency increases. This enhancement can reach 3 orders of magnitude for trap frequencies of about 100 kHz. While the enhancement itself agrees at least qualitatively with the concept of confinement of the initial-state wave function, trap-induced suppressed photoassociation is also possible for states in the cut-off regime. A simple sum rule was derived, confirming that any enhancement must be accompanied by suppression. The physical origin of this suppression is the trap-induced confinement of the initial-state wave function of relative motion within a radius that is smaller than the mean internuclear separation of the least bound vibrational states in the electronic target state. Additionally, a useful rule of thumb was found which predicts up to which final vibrational level the constant regime can

be expected. A further important finding was that the influence of a tight trap on the photoassociation spectra (as a function of the final vibrational state) for different alkali atoms is structurally very similar, independently of whether photoassociation starts from a singlet or triplet state. Also the type of interaction (strong or weak as well as repulsive or attractive) did not lead to a substantial modification of the trap influence. The only exception was a strong repulsive interaction that led to a pronounced window in the photoassociation spectrum. The reason is the position of the last node in the initial-state wave function that in this case is located at a relatively large value of interatomic distance and leads to a cancellation effect in the overlap with the final state. In view of the very important question how to optimize the efficiency of photoassociation, the present investigation revealed that not only increasing the tightness of the trap leads to an enhancement of the photoassociation rate, but a similar effect can be achieved by increasing the interaction strength. Most interestingly, these two enhancement factors work practically independent of each other, i. e. it is possible to use both effects in a constructive fashion and to obtain a multiplicative overall enhancement factor. On the other hand, the states in the cut-off regime are less enhanced or can even be suppressed due to the trap. A comparison of the results obtained for the realistic atom-atom interaction potential with the ones obtained using the approximate pseudopotential approximation or ignoring the interaction at all showed that these approximations only yield a good estimate of the photoassociation rate for the transitions to very high-lying vibrational states. Nevertheless, despite the complete failure to predict the rates of low-lying states, these models still allow the determination of the enhancement factor in the constant regime.

Photoassociation was considered within the single-channel approximation. The consequences of not using full multi-channel solutions can be summarized in the following. All presently developed single-channel schemes are sufficient for the general description of the photoassociation process. Although only s variation and μ variations were analyzed explicitly in this work, this conclusion can be drawn from the shape of the wave functions of the remaining v -variational schemes. However, the photoassociation spectrum obtained by the single-channel approach is quantitatively modified compared to the multi-channel result. The smallest modification of the function shape is expected for the w -variation where the nodal structure is slightly perturbed and only amplitudes can deviate significantly. A larger modification and even strong changes in the minima and maxima positions can occur if J -, μ -, and s -variational schemes are used. Nevertheless, the general structure of the photoassociation spectrum is still reproduced even with these approximations. It should, however, be remembered that the single-channel

approach cannot be relied upon, if the absolute values of photoassociation rate are of importance, because the amplitudes of the wave functions are not determined accurately and the matching constant C^v for the single-channel wave function must be used. Only if vibrational levels of higher excited state are considered, where the outer-turning points are beyond the intermediate range ($\sim 20 a_0$ for ${}^6\text{Li}$ - ${}^{87}\text{Rb}$ singlet state), the mentioned matching constant is no longer needed. In this case all the single-channel schemes (except the w-variation) produce quantitatively correct results because the long-range part of the wave function is correct.

Finally, a numerical approach is developed, which in principle allows an exact description of two atoms trapped in a 3D optical lattice if the interatomic interaction potential is central (isotropic) and can be given in terms of a single potential curve. A detailed analysis of anharmonicity and coupling of center-of-mass and relative coordinates in terms of energy values and wave functions was performed for heteronuclear dimers in a single site of an optical lattice. It is explained why such a single site is optimally described by a sextic potential, if a finite Taylor expansion is used. The effects of deviations from the harmonic approximation and the coupling were quantified and analyzed for different heteronuclear systems, confinement strengths and interatomic interaction regimes. The influence of the lattice is found to be always much stronger for the first trap-induced state than for the least bound state. As a consequence, binding energies are modified by the lattice mainly by the modification of the first trap-induced state.

The results of the theoretical approach developed here are also compared to a recent experiment in which the binding energies of ${}^{87}\text{Rb}$ - ${}^{40}\text{K}$ have been measured as a function of an external magnetic field tuned close to a magnetic Feshbach resonance. The assumptions necessary for such a comparison are carefully discussed. It is found that very good agreement between experiment and theory can be reached only, if the previously experimentally determined resonance parameters are modified. Since this needed modification is within the error bars with which the parameters had been determined before, this is not only reasonable, but may even indicate the possibility of more accurately determining the width and position of magnetic Feshbach resonances in ultracold atomic gases, as was proposed recently in a comparable theoretical study. However, the resonance parameters determined in another theoretical study performed in parallel to the present one that is based on the pseudopotential approximation differ from the ones found in the present work. Whether this deviation is due to the pseudopotential approximation is difficult to judge at this moment. If this were the case, the then found breakdown of the pseudopotential approximation would, of course, be a very interesting finding. Since the present approach was rather generally formu-

lated, it immediately suggests further investigations. This includes, e. g., the consideration of highly anisotropic, asymmetric (disordered), or multiple-well lattice geometries. First results for triple-well potentials have recently been used for the determination of Bose-Hubbard parameters and an investigation of the validity of the Bose-Hubbard model itself. Further extensions of the approach should also allow to study the case of a pair of atoms or molecules interacting by non-centric, e. g., dipolar interactions. Finally, it is planned to extend the method for studies of the time-dependent dynamics of atomic pairs in time-varying lattices.

Appendix A

Rayleigh-Ritz-Galerkin approach

An efficient numerical method for solving a multidimensional stationary Schrödinger equation

$$\hat{H}|\psi\rangle = E|\psi\rangle \quad (\text{A.1})$$

with boundary conditions for $|\psi\rangle$, is the variational or Rayleigh-Ritz-Galerkin (RRG) approach [164]. This method is used in the present thesis for solving eigenproblems. In this method the approximate wave function is constructed as a linear combination of a finite number N of basis functions $|i\rangle$

$$|\psi\rangle \approx \sum_i^N C_i \cdot |i\rangle \quad (\text{A.2})$$

Therefore the problem can approximately be written in terms of the Lagrange form functional as

$$\mathbb{E}[\psi] \approx \sum_{i=1}^N \sum_{j=1}^N (C_i^* C_j H_{ij} - E C_i^* C_j S_{ij}) = \mathbf{C}^\dagger \mathbf{H} \mathbf{C} - E \mathbf{C}^\dagger \mathbf{S} \mathbf{C} \quad (\text{A.3})$$

with the $N \times N$ matrices

$$H_{ij} \equiv \langle i | \hat{H} | j \rangle, \quad \text{and} \quad S_{ij} \equiv \langle i | \hat{S} | j \rangle. \quad (\text{A.4})$$

The minima of the functional or solutions of the Schrödinger equation may be found by equating the derivatives of \mathbb{E} in Equation (A.3) to zero

$$\frac{\partial \mathbb{E}[\psi]}{\partial C_i^*} = 0, \quad \text{and} \quad \frac{\partial \mathbb{E}[\psi]}{\partial C_i} = 0, \quad (\text{A.5})$$

which gives rise to the matrix equations

$$\mathbf{H}\mathbf{C} = E\mathbf{S}\mathbf{C} \quad \text{and} \quad \mathbf{C}^\dagger\mathbf{H} = E\mathbf{C}^\dagger\mathbf{S} \quad . \quad (\text{A.6})$$

These equations are equivalent because the matrices \mathbf{H} and \mathbf{S} are Hermitian and the multipliers E are therefore real. Hence, the approximate solution of the Schrödinger equation is obtained by solving the generalized matrix eigenvalue equation

$$\mathbf{H}\mathbf{C} = E\mathbf{S}\mathbf{C} \quad , \quad (\text{A.7})$$

or in a form of the Galerkin set of equations [170]

$$\sum_{i=1}^N (C_i H_{ji} - E C_i S_{ji}) = 0 \quad , \quad (\text{A.8})$$

which is more suitable for the numerical implementation. The variational method ensures that the obtained solutions approach the exact ones, if the configuration space is systematically increased. As the expansion basis approaches completeness (forming an orthonormal basis of Hilbert space), the solution vector converges to the exact one.

Appendix B

B splines

The numerical implementation of all physical problems of the present work uses *B* splines. The *B* splines constitute a set of piecewise polynomial functions on the domain $[a, b]$. The corresponding *B*-spline basis is specified by giving a knot sequence $\{t_i\}$, $i = 1, 2, \dots$ defined in a continuous chain of segments where the *B*-spline functions are defined. The i th *B*-spline basis function of the order k (degree $k - 1$) is defined as

$$\begin{aligned} B_{i,k}(t) &= \frac{t - t_i}{t_{i+k-1} - t_i} B_{i,k-1}(t) + \frac{t_{i+k} - t}{t_{i+k} - t_{i+1}} B_{i+1,k-1}(t), \\ B_{i,1}(t) &= \begin{cases} 1, & t_i \leq t < t_{i+1}, \\ 0, & \text{otherwise.} \end{cases} \end{aligned} \quad (1)$$

The *B*-spline functions constitute a complete set of basis functions that approximates a given wave function in the range of interest. The use of *B* splines offers many advantages. The eigenvectors of the Schrödinger equation are smooth functions and are thus well represented as piecewise polynomials. Furthermore, the polynomial structure makes the integrals simple and subject to an efficient calculations using Gaussian quadratures. The oscillations are included by appropriate placing the knot points. Zero boundary conditions can be straightforwardly implemented. Using the advantage of the strong localization (compactness) it is possible to create a compact set of basis functions, saving the computational resources. The derivative \mathcal{B} of a *B* spline is again a function of *B* splines and can be obtained using the recurrence relation

$$\mathcal{B}_{i,k}(t) = \frac{k-1}{t_{i+k-1} - t_i} B_{i,k-1}(t) + \frac{k-1}{t_{i+k} - t_{i+1}} B_{i+1,k-1}(t). \quad (\text{B.1})$$

Finally, a *B*-spline basis allows systematic control of the convergence using few parameters.

A proper choice of the knot sequence helps to reach a faster convergence. For example, a non-uniform knot sequence is preferable for the radial problem with the Born-Oppenheimer potential describing the interparticle interaction. The region where the wave function has a richer structure must have

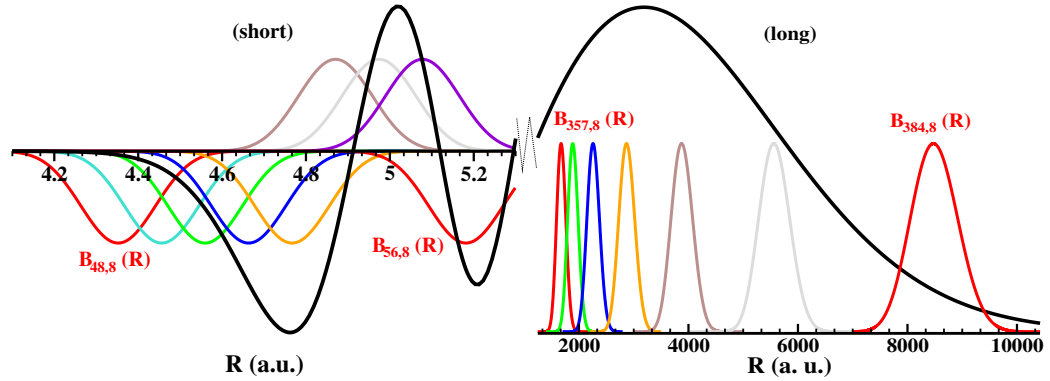


Figure B.1: Approximation of the first trap-induced wave function of two atoms in a harmonic trap interacting via realistic interatomic potential. The wave function (black) is shown together with the B splines (colored). The region where the inner part is oscillating rapidly (“short”) and the long-range region where the trap is dominant (“long”) are presented.

a dense knot sequence, while the remaining region can be spanned using a geometrical grid. This is illustrated in Figure B.1 where the first trap-induced eigensolution for the two atoms in a harmonic trap interacting via realistic Born-Oppenheimer potential is approximated by B splines.

Another great advantage of the B -spline basis is that the resulting matrices have band structure as shown in Figure B.2. This makes it possible to use fast diagonalization techniques, which is computationally efficient both in terms of space and time consumption.

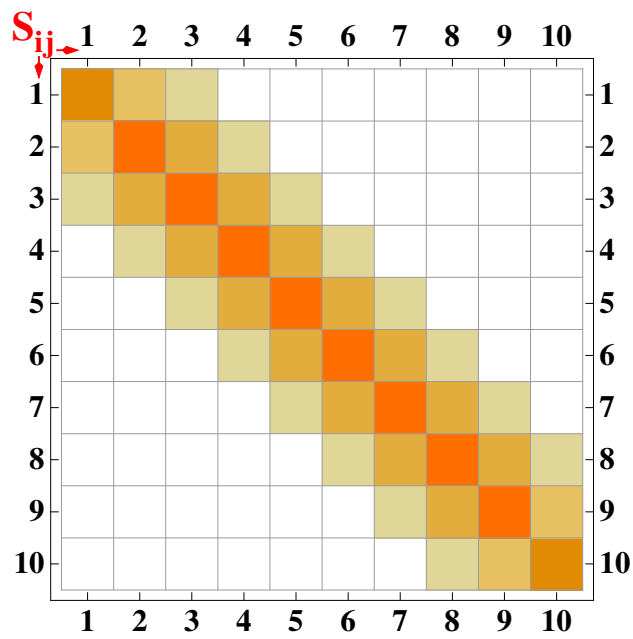


Figure B.2: S -matrix calculated with ten B splines. White color corresponds to zero matrix elements. Colored squares indicate non-zero elements. The matrix is symmetric.

Appendix C

Pseudopotential approximation with B splines

In this appendix the numerical approach for the pseudopotential approximation with B splines is given, as the complement to Chapter 5. It is known that the scattering function in the low energy limit asymptotically behaves like $C(1 - \frac{a}{R})$ where C is a normalization factor. Then multiplying by R the scaled function $C(R - a_{sc})$ may be obtained. Since the scaled function is non-zero at zero, its expansion with B splines leads to several non-independent expansion coefficients. This dependence can be established using the boundary conditions:

$$\left. \frac{\psi'(R)}{\psi(R)} \right|_{R \rightarrow 0} = \frac{C}{C(0 - a_{sc})} = -\frac{1}{a_{sc}} \quad . \quad (\text{C.1})$$

Using Equation (C.1) and the expansion of ψ in B splines

$$\psi(r) = \sum_{\alpha=1}^N C_{\alpha} B_{\alpha}(r) \quad , \quad (\text{C.2})$$

it can be found that the coefficients C_1 and C_2 are not independent,

$$\frac{C_1 B_1'(0) + C_2 B_2'(0)}{C_1 B_1(0)} = -\frac{1}{a} \quad , \quad (\text{C.3})$$

therefore $C_1 = D \cdot C_2$, where

$$D = \frac{a B_1'(0)}{a B_1'(0) + 1} \quad , \quad (\text{C.4})$$

and $B_2'(0) = -B_1'(0)$ and $B_1(0) = 1$. Finally, a new basis can be introduced,

$$\psi(r) = \sum_{\alpha=2}^N C_\alpha \mathbb{B}_\alpha(r), \quad (\text{C.5})$$

with $\mathbb{B}_2 = D \cdot B_1(r) + B_2(r)$ and $\mathbb{B}_\alpha(r) = B_\alpha(r)$ for $\alpha > 2$. In the new basis the kinetic energy term contains an extra element, which was zero before. The matrix elements involved in the eigenvalue problem are determined as follows.

Matrix elements are the same as for the problem with a realistic potential, but with some additional terms. These terms are explicitly indicated in the following equations. The kinetic energy matrix elements are

$$\begin{aligned} \mathbb{T}_{22} &= \frac{1}{2\mu} \left(\mathbb{B}_2(0)\mathbb{B}_2'(0) + \int_0^\rho dr \mathbb{B}_2'(r)\mathbb{B}_2'(r) \right) \\ &= \frac{1}{2\mu} \underbrace{\left(D(D-1)B_1'(0) + D^2 \int_0^\rho dr B_1'(r)B_1'(r) + 2D \int_0^\rho dr B_1'(r)B_2'(r) \right)}_{\text{add}} \\ &\quad + \frac{1}{2\mu} \int_0^\rho dr B_2'(r)B_2'(r) \\ \\ \mathbb{T}_{2 \ 3 \leq \alpha \leq k} &= \frac{1}{2\mu} \left(\int_0^\rho dr \mathbb{B}_2'(r)B_\alpha'(r) \right) = \frac{D}{2\mu} \underbrace{\int_0^\rho dr B_1'(r)B_\alpha'(r)}_{\text{add}} \\ &\quad + \frac{1}{2\mu} \int_0^\rho dr B_2'(r)B_\alpha'(r) \end{aligned} \quad (\text{C.6})$$

The centrifugal term is zero here because for the s -wave $l = 0$. The matrix

elements for the trap are

$$\begin{aligned}
\mathbb{V}_{22} &= \int_0^\rho dr \cdot r^{2t} \mathbb{B}_2(r) \mathbb{B}_2(r) \\
&= \underbrace{D^2 \int_0^\rho dr \cdot r^{2t} B_1(r)^2 + 2D \int_0^\rho dr \cdot r^{2t} B_1(r) B_2(r)}_{\text{add}} + \int_0^\rho dr \cdot r^{2t} B_2(r)^2 \\
\mathbb{V}_{2 \ 3 \leq \alpha \leq k} &= \underbrace{D \int_0^\rho dr \cdot r^{2t} B_1(r) B_\alpha(r)}_{\text{add}} + \int_0^\rho dr \cdot r^{2t} B_2(r) B_\alpha(r)
\end{aligned} \tag{C.7}$$

Finally, the overlap matrix elements are

$$\begin{aligned}
\mathbb{S}_{22} &= \int_0^\rho dr \mathbb{B}_2(r) \mathbb{B}_2(r) = \underbrace{D^2 \int_0^\rho dr B_1(r)^2 + 2D \int_0^\rho dr B_1(r) B_2(r)}_{\text{add}} \\
&\quad + \int_0^\rho dr B_2(r)^2 \\
\mathbb{S}_{2 \ 3 \leq \alpha \leq k} &= \underbrace{D \int_0^\rho dr B_1(r) B_\alpha(r)}_{\text{add}} + \int_0^\rho dr B_2(r) B_\alpha(r)
\end{aligned} \tag{C.8}$$

The solutions of the Schrödinger equation for the relative motion in a harmonic trap using different approximations for the interaction potential are shown in Figure C.1. As is evident from the figure the solutions are reproduced numerically correctly with the implemented approach even for those regimes where the pseudopotential approximation breaks down.

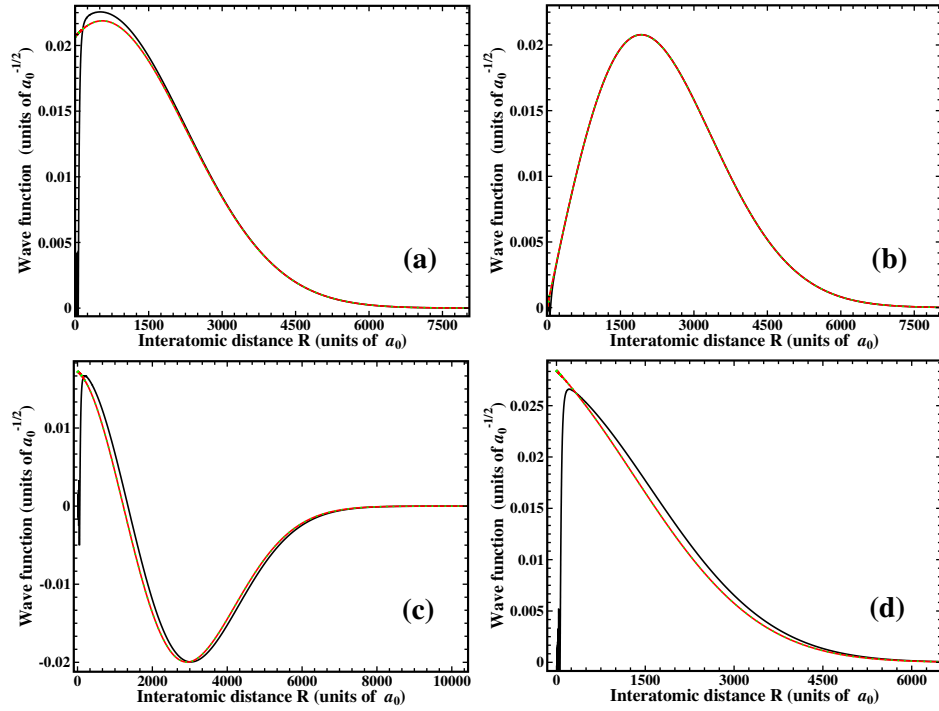


Figure C.1: Wave functions calculated for ^{87}Rb - ^{40}K in harmonic trap of $\omega_{\text{ho}} = 2\pi \times 35\text{kHz}$ frequency using realistic Born-Oppenheimer (black) potential and pseudopotential (red) together with analytical solution for the pseudopotential given in Equation (5.9) (green dots). Wave functions belong to different interaction regimes; (a) strongly attractive, (b) almost non-interacting particles, (c) and (d) strongly repulsive regimes. Figures (a) to (c) show the first trap induced state and (c) shows the least bound state.

Appendix D

Born-Oppenheimer approximation

Calculations of the present thesis assume the Born-Oppenheimer approximation for the description of interatomic interactions to be valid. The non-relativistic Hamiltonian of a diatomic system consisting of two nuclei A and B each with one valence electron using the effective model potential for core electrons can be given as

$$\hat{H}(\vec{R}, \vec{r}_1, \vec{r}_2) = \underbrace{-\frac{1}{2m_e} \sum_{i=1}^2 \nabla_i^2 - \sum_{I=A}^B \sum_{i=1}^2 \frac{Z_I e^2}{r_{Ii}} + \frac{e^2}{r_{12}} + \frac{Z_A Z_B e^2}{R}}_{\hat{H}_e(\vec{r}_1, \vec{r}_2; R)} - \underbrace{\sum_{I=A}^B \frac{1}{2M_I} \nabla_I^2}_{N^+ \text{ kin. en.}} . \quad (\text{D.1})$$

In Equation (D.1) m_e and M_I are the electronic and nuclear masses respectively, Z_I is the nuclear charge, r_{12} is the distance between the two electrons and R is the distance between the nuclei (in a coordinate system with the origin in the nuclear center of mass $\vec{R} = \vec{R}_A - \vec{R}_B$). $\hat{H}_e(\vec{r}_1, \vec{r}_2; R)$ denotes the electronic part of the Hamiltonian. For a fixed internuclear position R it depends on the electronic coordinates only and electronic wave function satisfies the electronic wave equation

$$\hat{H}_e(\vec{r}_1, \vec{r}_2; R) \psi_q(\vec{R}; \vec{r}_1, \vec{r}_2) = E_q(R) \psi_q(\vec{R}; \vec{r}_1, \vec{r}_2) , \quad (\text{D.2})$$

where $E_q(R)$ are eigenvalues of the specific electronic configuration q and the ψ_q form a complete orthonormal set of electronic states $\{q\}$. The complete

set ψ_q may be used to construct the exact eigenvalues of the Hamiltonian of Equation (D.1)

$$\Psi(\vec{R}, \vec{r}_1, \vec{r}_2) = \sum_q F_q(\vec{R}) \psi_q(\vec{R}; \vec{r}_1, \vec{r}_2) \quad . \quad (\text{D.3})$$

The substitution of the wave function (D.3) and Hamiltonian (D.1) into the Schrödinger equation leads to a set of coupled differential equations. In spherical coordinates it can be written as

$$\sum_q \left\langle \psi_s \left| -\frac{1}{2\mu} \frac{1}{R^2} \frac{\partial}{\partial R} \left(R^2 \frac{\partial}{\partial R} \right) + \frac{\vec{N}^2}{2\mu R^2} \right| \psi_q \right\rangle F_q(\vec{R}) + [E_s(R) - E] F_s(\vec{R}) = 0 \quad ,$$

$$s = 0, 1, 2, \dots \quad , \quad (\text{D.4})$$

where \vec{N} is the orbital angular momentum of the relative nuclear motion.

The mass of the electrons is much smaller than the mass of the nuclei, while the forces acting on electrons and nuclei are of comparable magnitude. Hence, the nuclear motion is usually very slow compared with the electronic motion. As a consequence, the electronic wave function varies slowly with respect to \vec{R} and $\frac{\partial \psi_q}{\partial R} \approx 0$. In addition, it is sufficient to retain only the diagonal term $\langle \psi_s | \vec{N}^2 | \psi_s \rangle$ of the kinetic energy due to rotational motion. These approximations allow the nuclear wave equation to be obtained by solving

$$-\frac{1}{2\mu} \left[\frac{1}{R^2} \frac{\partial}{\partial R} \left(R^2 \frac{\partial}{\partial R} \right) - \frac{K(K+1)}{R^2} \right] F_s(\vec{R}) + [E_s(R) - E] F_s(\vec{R}) = 0 \quad . \quad (\text{D.5})$$

Here $K = N + L$ is the total orbital angular momentum of the whole molecule, L being the orbital angular momentum of the electrons. In Equation (D.5) the kinetic energy due to rotational motion was approximated as $\frac{K(K+1)}{2\mu R^2}$ because $\vec{K}^2 \Psi_s = K(K+1) \Psi_s$ and $L_z \Psi_s = \pm \Lambda \Psi_s$, so the equation

$$\begin{aligned} \langle \psi_s | \vec{N}^2 | \psi_s \rangle &= \langle \psi_s | \vec{K}^2 + \vec{L}^2 - 2\vec{K} \cdot \vec{L} | \psi_s \rangle \\ &= K(K+1) - \Lambda^2 + \langle \psi_s | L_x^2 + L_y^2 | \psi_s \rangle \end{aligned} \quad (\text{D.6})$$

is valid. In Equation (D.6) the last two terms $\langle \psi_s | L_x^2 + L_y^2 | \psi_s \rangle$ are small in comparison with $2\mu E_s(R) R^2$ and may be omitted.

Finally, if the nuclear-motion wave function is expressed in terms of the product of a radial and angular function with $\Lambda = 0$, the nuclear wave equation becomes

$$\begin{aligned}
 & -\frac{1}{2\mu} \left[\frac{1}{R^2} \frac{\partial}{\partial R} \left(R^2 \frac{\partial}{\partial R} \right) - \frac{K(K+1)}{R^2} \right] F_{s,v,K}(R) \\
 & + [E_s(R) - E_{s,v,K}] F_{s,v,K}(R) = 0, \tag{D.7}
 \end{aligned}$$

where $F_{s,v,K}(R)$ is the radial function for a given electronic state s . The nuclear motion (e.g., rotation, vibration) “sees” a potential $E_s(R) = V_s(R)$ from the speedy electrons. Example potentials for singlet $X^1\Sigma_g^+$ and triplet $a^3\Sigma_g^+$ states of a homonuclear system were shown in Figure 3.3. The two potentials differ due to the exchange interaction (Equation (3.5)), which prevents the electronic wave functions from overlapping, if the atoms are sufficiently close and the outer electrons have parallel spins, i. e., they are in the triplet state. This is a consequence of the Pauli exclusion principle, which forbids two fermions to be in the same quantum state. Thus, the triplet potential is much less attractive than the singlet potential, as is clear from Figure 3.3.

Appendix E

Auxiliary relations

$$Y_l^m(\theta, \phi) = \sqrt{\frac{2l+1}{4\pi} \frac{(l-m)!}{(l+m)!}} P_l^m(\cos(\theta)) e^{im\phi} = A_{lm} P_l^m(\cos(\theta)) e^{im\phi} \quad . \quad (\text{E.1})$$

$$(a+x)^n = \sum_{k=0}^n \binom{n}{k} x^k a^{n-k}, \quad n \in \text{Integers} \quad . \quad (\text{E.2})$$

$$\begin{aligned} & \int_{-1}^1 (1-x^2)^{\lambda-1} P_\nu^\mu dx \\ &= \frac{\pi 2^\mu \Gamma(\lambda + \frac{1}{2}\mu) \Gamma(\lambda - \frac{1}{2}\mu)}{\Gamma(\lambda + \frac{1}{2}\nu + \frac{1}{2}) \Gamma(\lambda - \frac{1}{2}\nu) \Gamma(-\frac{1}{2}\mu + \frac{1}{2}\nu + 1) \Gamma(-\frac{1}{2}\mu - \frac{1}{2}\nu + \frac{1}{2})}, \\ & \text{with } [2\text{Re}\lambda > |\text{Re}\mu|] \quad . \end{aligned} \quad (\text{E.3})$$

$$\int_0^1 x^\lambda P_{2m}(x) dx = \frac{(-1)^m \Gamma[m - \frac{1}{2}\lambda] \Gamma[\frac{1}{2} + \frac{1}{2}\lambda]}{2\Gamma[-\frac{1}{2}\lambda] \Gamma[m + \frac{3}{2} + \frac{1}{2}\lambda]}, \quad \text{with } [\text{Re}\lambda > -1] \quad . \quad (\text{E.4})$$

$$\int_0^1 x^\lambda P_{2m+1}(x) dx = \frac{(-1)^m \Gamma[m + \frac{1}{2} - \frac{1}{2}\lambda] \Gamma[1 + \frac{1}{2}\lambda]}{2\Gamma[\frac{1}{2} - \frac{1}{2}\lambda] \Gamma[m + 2 + \frac{1}{2}\lambda]}, \quad \text{with } [\text{Re}\lambda > -2] \quad . \quad (\text{E.5})$$

$$\Gamma\left[n + \frac{1}{2}\right] = \frac{\sqrt{\pi}}{2^n} (2n-1)!!, \quad n \geq 0 \in \text{Integers} \quad . \quad (\text{E.6})$$

$$\Gamma\left[\frac{1}{2} - n\right] = (-1)^n \frac{2^n \sqrt{\pi}}{(2n - 1)!!}, \quad n \geq 0 \in \text{Integers} \quad . \quad (\text{E.7})$$

$$\Gamma[x + 1] = x\Gamma[x] \quad . \quad (\text{E.8})$$

$$P_l^{-m} = (-1)^m \frac{(l - m)!}{(l + m)!} P_l^m \quad . \quad (\text{E.9})$$

Abbreviations

Abkürzung	Erklärung
AB	atomic basis
ABS	absolute, laboratory space
BEC	Bose-Einstein condensate
BMF	beyond-mean-field
BO	Born-Oppenheimer
CI	configuration interaction
CIM	confinement-induced molecule
COM	center-of-mass
DPA	dump photoassociation
EPA	enhanced photoassociation
FC	Franck-Condon
FOPA	Feshbach-optimized photoassociation
GGPE	Ginzburg-Gross-Pitaevskii equation
HFE	Hartree-Fock equation
MB	molecular basis
MI	Mott insulator
MFR	magnetic Feshbach resonance
MFT	mean-field theory
OL	optical lattice
PA	photoassociation
QDT	quantum defect theory
REL	relative
RIP	repulsively interacting bound pair
RM	real molecule
RRG	Rayleigh-Ritz-Galerkin
SHA	spherical harmonics approach
SPA	suppressed photoassociation
STIRAP	stimulated Raman adiabatic passage
TFA	Thomas-Fermi approximation
VP	variational principle

Acknowledgments

During my PhD study I met many people who contributed to my scientific and human growth. Among them I would like to thank, first of all, my supervisor PD Dr. Alejandro Saenz, who helped me through many scientific discussions and with helping me with the organization of my life in Germany. Alejandro was always generous with suggestions and ready to provide explanations at any time, even when extremely busy.

Some special words are for my Byelorussian friend and colleague, Yulian Vanne, who started his PhD at the same time as me. I enjoyed discussions with him about science, politics, and personal life. A better friend, one more ready to talk and help, I can hardly imagine.

I would also like to recall all the other members of my research group, with whom I enjoyed discussions and fruitful working atmosphere: Manohar Awasthi, Irina Dumitriu, Armin Luhr. Thanks to Armin, I learned at last to speak at least some German. Also, I gratefully acknowledge my neighbors from the experimental groups, Optische Metrologie and Nano Optics. It was a great pleasure to work among friends in such an opened and stimulating atmosphere.

I would like also thank those colleagues with whom I had the chance to work together on several projects. Philipp-Immanuel Schneider investigated the Bose-Hubbard model together with me. He is always full of ideas and is very quick in realizing them. Also, Alexandr Leonov and Martin Athanasiou studied two-body dynamics in optical lattices with me. These guys are brilliant scientists.

I am also grateful to Prof. Dr. Matthias Bollhoefer who supported me in applying JADAMILU, a software package for large-scale computations, to making my calculations.

Special thanks to my wife, Anastasia, who made a great contribution in supporting me at the time of writing the dissertation. I do not know how without her love and care I could have made it through my PhD.

Last but not least, I want to acknowledge my friends who one way or another influenced my personal and academic growth: Sergei Zhukovsky, Sergei

Sosnovsky, Grigoriy Astrakharchick, Anastasia Loman, and Igor Litvin.

I would also like to especially thank Dr. Charles Stewart for helping me with English.

Bibliography

- [1] A. Einstein. Quantentheorie des einatomigen idealen gases. *Sitzungsber. Kgl. Preuss. Akad. Wiss.*, 261, 1924.
- [2] M. H. Anderson, J. R. Ensher, M. R. Matthews, C. E. Wieman, and E. A. Cornell. Observation of Bose-Einstein condensation in a dilute atomic vapor. *Science*, 269:198, 1995.
- [3] Vladan Vuletić and Steven Chu. Laser cooling of atoms, ions, or molecules by coherent scattering. *Phys. Rev. Lett.*, 84:3787, 2000.
- [4] V. Boyer, S. Murdoch, Y. Le Coq, G. Delannoy, P. Bouyer, and A. Aspect. Multifrequency evaporative cooling to Bose-Einstein condensation in a high magnetic field. *Phys. Rev. A*, 62:021601, 2000.
- [5] K. B. Davis, M. O. Mewes, M. R. Andrews, N. J. van Druten, D. S. Durfee, D. M. Kurn, and W. Ketterle. Bose-Einstein condensation in a gas of sodium atoms. *Phys. Rev. Lett.*, 75:3969, 1995.
- [6] C.C. Bradley, C.A. Sackett, J.J. Tollet, and R.G. Hulet. Evidence of Bose-Einstein condensation in an atomic gas with attractive interactions. *Phys. Rev. Lett.*, 75:1687, 1995.
- [7] G. Modugno, G. Ferrari, G. Roati, R.J. Brecha, A. Simoni, and M. Inguscio. Bose-Einstein condensation of potassium atoms by sympathetic cooling. *Science*, 294:1320, 2001.
- [8] T. Weber, J. Herbig, M. Mark, H.-C. Nägerl, and R. Grimm. Bose-Einstein condensation of cesium. *Science*, 299:232, 2003.
- [9] Thomas C. Killian, Dale G. Fried, Lorenz Willmann, David Landhuis, Stephen C. Moss, Thomas J. Greytak, and Daniel Kleppner. Cold collision frequency shift of the 1s-2s transition in hydrogen. *Phys. Rev. Lett.*, 81:3807, 1998.

- [10] Dale G. Fried, Thomas C. Killian, Lorenz Willmann, David Landhuis, Stephen C. Moss, Daniel Kleppner, and Thomas J. Greytak. Bose-Einstein condensation of atomic hydrogen. *Phys. Rev. Lett.*, 81:3811, 1998.
- [11] A. Robert, O. Sirjean, A. Browaeys, J. Poupard, S. Nowak, D. Biron, C. I. Westbrook, and A. Aspect. A Bose-Einstein condensate of metastable atoms. *Science*, 292:461, 2001.
- [12] F. Pereira Dos Santos, J. Lonard, Junmin Wang, C. J. Barrelet, F. Perales, E. Rasel, C.S. Unnikrishnan, M. Leduc, and C. Cohen-Tannoudji. Bose-Einstein condensation of metastable helium. *Phys. Rev. Lett.*, 86:3459, 2001.
- [13] Yosuke Takasu, Kenichi Maki, Kaduki Komori, Tetsushi Takano, Kazuhito Honda, Mitsutaka Kumakura, Tsutomu Yabuzaki, and Yoshiro Takahashi. Spin-singlet Bose-Einstein condensation of two-electron atoms. *Phys. Rev. Lett.*, 91:040404, 2003.
- [14] Axel Griesmaier, Jörg Werner, Sven Hensler, Jürgen Stuhler, and Tilman Pfau. Bose-Einstein condensation of chromium. *Phys. Rev. Lett.*, 94:160401, 2005.
- [15] S. Jochim, M. Bartenstein, A. Altmeyer, G. Hendl, S. Riedl, C. Chin, J. Hecker Denschlag, R. Grimm, C. Zhu, A. Dalgarno, and A. Derevianko. Bose-Einstein condensation of molecules. *Science*, 302:2101, 2003.
- [16] M. W. Zwierlein, C. A. Stan, C. H. Schunck, S. M. F. Raupach, S. Gupta, Z. Hadzibabic, and W. Ketterle. Observation of Bose-Einstein condensation of molecules. *Phys. Rev. Lett.*, 91:250401, 2003.
- [17] C. A. Regal, C. Ticknor, J. L. Bohn, and D. S. Jin. Creation of ultracold molecules from fermi gas of atoms. *Nature*, 424:47, 2003.
- [18] Markus Greiner, Cindy A. Regal, and Deborah S. Jin. Emergence of a molecular Bose-Einstein condensate from a Fermi gas. *Nature*, 426:537, 2003.
- [19] M. A. Kasevich. Coherence with atoms. *Science*, 298:1363, 2002.
- [20] M. R. Andrews, C. G. Townsend, H.-J. Miesner, D. S. Durfee, D. M. Kurn, and W. Ketterle. Observation of interference between two Bose condensates. *Science*, 275:637, 1997.

- [21] I. Bloch, T. W. Hänsch, and T. Esslinger. Measurement of the spatial coherence of a trapped Bose gas at the phase transition. *Science*, 403:166, 2000.
- [22] F. Minardi, C. Fort, P. Maddaloni, M. Modugno, and M. Inguscio. Time-domain atom interferometry across the threshold for Bose-Einstein condensation. *Phys. Rev. Lett.*, 87:170401, 2001.
- [23] Immanuel Bloch, Theodor W. Hänsch, and Tilman Esslinger. Atom laser with a cw output coupler. *Phys. Rev. Lett.*, 82:3008–3011, 1999. doi: 10.1103/PhysRevLett.82.3008.
- [24] P. L. Kapitza. Viscosity of liquid helium below the λ -point. *Nature*, 141:74, 1938.
- [25] N. Bogolubov. Theory of superfluidity. *Sov. Phys. JETP*, 11:23, 1947.
- [26] J. M. Vogels, K. Xu, C. Raman, J. R. Abo-Shaeer, and W. Ketterle. Experimental observation of the Bogoliubov transformation for a Bose-Einstein condensed gas. *Phys. Rev. Lett.*, 88:060402, 2002.
- [27] C. Raman, M. Köhl, R. Onofrio, D. S. Durfee, C. E. Kuklewicz, Z. Hadzibabic, and W. Ketterle. Evidence for a critical velocity in a Bose-Einstein condensed gas. *Phys. Rev. Lett.*, 83:2502–2505, 1999.
- [28] J. R. Abo-Shaeer, C. Raman, J. M. Vogels, and W. Ketterle. Observation of vortex lattices in Bose-Einstein condensates. *Science*, 292:476, 2001.
- [29] M. Cristiani, O. Morsch, J. H. Müller, D. Ciampini, and E. Arimondo. Experimental properties of Bose-Einstein condensates in one-dimensional optical lattices: Bloch oscillations, Landau-Zener tunneling, and mean-field effects. *Phys. Rev. A*, 65:063612, 2002.
- [30] B. P. Anderson and M. A. Kasevich. Macroscopic quantum interference from atomic tunnel arrays. *Science*, 282:1686, 1998.
- [31] S. Burger, F. S. Cataliotti, C. Fort, F. Minardi, M. Inguscio, M. L. Chiofalo, and M. P. Tosi. Superfluid and dissipative dynamics of a Bose-Einstein condensate in a periodic optical potential. *Phys. Rev. Lett.*, 86:4447, 2001.
- [32] Philipp Treutlein, Peter Hommelhoff, Tilo Steinmetz, Theodor W. Hänsch, and Jakob Reichel. Coherence in microchip traps. *Phys. Rev. Lett.*, 92:203005, 2004.

- [33] N. D. Lemke, A. D. Ludlow, Z. W. Barber, T. M. Fortier, S. A. Diddams, Y. Jiang, S. R. Jefferts, T. P. Heavner, T. E. Parker, and C. W. Oates. Spin-1/2 optical lattice clock. *Phys. Rev. Lett.*, 103:063001, 2009.
- [34] C. A. Regal, C. Ticknor, J. L. Bohn, and D. S. Jin. Creation of ultracold molecules from fermi gas of atoms. *Nature*, 424:47, 2003.
- [35] S. Inouye, M. R. Andrews, J. Stenger, H.-J. Miesner, D. M. Stamper-Kurn, and W. Ketterle. Observation of Feshbach resonances in a Bose-Einstein condensate. *Nature*, 392:151, 1998.
- [36] Thorsten Köhler, Krzysztof Góral, and Paul S. Julienne. Production of cold molecules via magnetically tunable Feshbach resonances. *Rev. Mod. Phys.*, 78:1311, 2006.
- [37] Paul S. Julienne. Condensed-matter physics: Really cool molecules. *Nature*, 424:24–25, 2003.
- [38] P. D. Lett, K. Helmerson, W. D. Phillips, L. P. Ratliff, S. L. Rolston, and M. E. Wagshul. Spectroscopy of Na₂ by photoassociation of laser-cooled Na. *Phys. Rev. Lett.*, 71:2200, 1993.
- [39] A. Fioretti, D. Comparat, A. Crubellier, O. Dulieu, F. Masnou-Seeuws, and P. Pillet. Formation of cold Cs₂ molecules through photoassociation. *Phys. Rev. Lett.*, 80:4402, 1998.
- [40] Kevin M. Jones, Eite Tiesinga, Paul D. Lett, and Paul S. Julienne. Ultracold photoassociation spectroscopy: Long-range molecules and atomic scattering. *Rev. Mod. Phys.*, 78:483, 2006.
- [41] E. R. I. Abraham, W. I. McAlexander, C. A. Sackett, and Randall G. Hulet. Spectroscopic determination of the s-wave scattering length of lithium. *Phys. Rev. Lett.*, 74:1315, 1995.
- [42] E. Tiemann, H. Knöckel, and H. Richling. Long-range interaction at the asymptote $3s + 3p$ of Na₂. *Eur. Phys. J. D*, 37:323, 1996.
- [43] A. Fioretti, C. Amiot, C.M. Dion, O. Dulieu, M. Mazzoni, G. Smirne, and C. Gabbanini. Cold rubidium molecule formation through photoassociation: A spectroscopic study of the 0_g^- long-range state of ⁸⁷Rb₂. *Eur. Phys. J. D*, 15:189, 2001.
- [44] R. F. Gutterres, C. Amiot, A. Fioretti, C. Gabbanini, M. Mazzoni, and O. Dulieu. Determination of the ⁸⁷Rb $5p$ state dipole matrix element

- and radiative lifetime from the photoassociation spectroscopy of the $\text{Rb}_2 0_g^-(P_{3/2})$ long-range state. *Phys. Rev. A*, 66:024502, 2002.
- [45] K.-K. Ni, S. Ospelkaus, M. H. G. de Miranda, A. Pe'er, B. Neyenhuis, J. J. Zirbel, S. Kotochigova, P. S. Julienne, D. S. Jin, and J. Ye. A high phase-space-density gas of polar molecules. *Science*, 322:231, 2008.
- [46] Jeremy M. Sage, Sunil Sainis, Thomas Bergeman, and David DeMille. Optical production of ultracold polar molecules. *Phys. Rev. Lett.*, 94: 203001, 2005.
- [47] J. Deiglmayr, A. Grochola, M. Repp, K. Mörtlbauer, C. Glück J. Lange, O. Dulieu, R. Wester, and M. Weidemüller. Formation of ultracold polar molecules in the rovibrational ground state. *Phys. Rev. Lett.*, 101: 133004, 2008.
- [48] Matthieu Viteau, Amodsen Chotia, Maria Allegrini, Nadia Bouloufa, Olivier Dulieu, Daniel Comparat, and Pierre Pillet. Optical pumping and vibrational cooling of molecules. *Science*, 321:232–234, 2008.
- [49] Maciej Lewenstein. Atomic and molecular physics: Polar molecules in topological order. *Nature*, 2:309, 2006.
- [50] A. Micheli, G. K. Brennen, and P. Zoller. A toolbox for lattice-spin models with polar molecules. *Nature*, 2:341–347, 2006.
- [51] D. DeMille. Quantum computation with trapped polar molecules. *Phys. Rev. Lett.*, 88:067901, 2002.
- [52] Eric R. Hudson, H. J. Lewandowski, Brian C. Sawyer, and Jun Ye. Cold molecule spectroscopy for constraining the evolution of the fine structure constant. *Phys. Rev. Lett.*, 96:143004, 2006.
- [53] Immanuel Bloch. Ultracold quantum gases in optical lattices. *Nature Physics*, 1:23, 2005.
- [54] D. Jaksch, C. Bruder, J. I. Cirac, C. W. Gardiner, and P. Zoller. Cold Bosonic atoms in optical lattices. *Phys. Rev. Lett.*, 81:3108, 1998.
- [55] M. Greiner, O. Mandel, T. Esslinger, T.W. Hänsch, and I. Bloch. Exploring phase coherence in a 2D lattice of Bose-Einstein condensates. *Nature*, 415:39, 2002.

- [56] Michael Köhl, Henning Moritz, Thilo Stöferle, Kenneth Günter, and Tilman Esslinger. Fermionic atoms in a three dimensional optical lattice: Observing fermi surfaces, dynamics, and interactions. *Phys. Rev. Lett.*, 94:080403, 2005.
- [57] Kevin E. Strecker, Guthrie B. Partridge, Andrew G. Truscott, and Randall G. Hulet. Formation and propagation of matter-wave soliton trains. *Nature*, 417:150, 2002.
- [58] L. Khaykovich, F. Schreck, G. Ferrari, T. Bourdel, J. Cubizolles, L. D. Carr, Y. Castin, and C. Salomon. Formation of a matter-wave bright soliton. *Science*, 296:1290, 2002.
- [59] A. Görlitz, J. M. Vogels, A. E. Leanhardt, C. Raman, T. L. Gustavson, J. R. Abo-Shaeer, A. P. Chikkatur, S. Gupta, S. Inouye, T. Rosenband, and W. Ketterle. Realization of Bose-Einstein condensates in lower dimensions. *Phys. Rev. Lett.*, 87:130402, 2001.
- [60] S. Richard, F. Gerbier, J. H. Thywissen, M. Hugbart, P. Bouyer, and A. Aspect. Momentum spectroscopy of 1D phase fluctuations in Bose-Einstein condensates. *Phys. Rev. Lett.*, 91:010405, 2003.
- [61] P. O. Fedichev, Yu., Kagan, G. V. Shlyapnikov, and J. T. M. Walraven. Influence of nearly resonant light on the scattering length in low-temperature atomic gases. *Phys. Rev. Lett.*, 77:2913, 1996.
- [62] D. Jaksch, H.-J. Briegel, J. I. Cirac, C. W. Gardiner, and P. Zoller. Entanglement of atoms via cold controlled collisions. *Phys. Rev. Lett.*, 82:1975–1978, 1999. doi: 10.1103/PhysRevLett.82.1975.
- [63] M. Greiner, O. Mandel, T. Esslinger, T.W. Hänsch, and I. Bloch. Quantum phase transition from a superfluid to a mott insulator in a gas of ultracold atoms. *Nature*, 415:39–44, 2002.
- [64] L. Fallani, J. E. Lye, V. Guarrera, C. Fort, and M. Inguscio. Ultracold atoms in a disordered crystal of light: Towards a Bose glass. *Phys. Rev. Lett.*, 98:130404, 2007.
- [65] S. Ospelkaus, C. Ospelkaus, L. Humbert, K. Sengstock, and K. Bongs. Tuning of heteronuclear interactions in a degenerate Fermi-Bose mixture. *Phys. Rev. Lett.*, 97:120403, 2006.
- [66] David R. Meacher. Optical lattices – crystalline structure bound by light. *Contemporary Physics*, 39:329, 1998.

BIBLIOGRAPHY

- [67] Maciej Lewenstein, Anna Sanpera, Veronica Ahufinger, Bogdan Damski, Aditi Sen, and Ujjwal Sen. Ultracold atomic gases in optical lattices: mimicking condensed matter physics and beyond. *Advances in Physics*, 56:243, 2007.
- [68] J. Hubbard. Electron correlations in narrow energy bands. *Proc. R. Soc. London A*, 276:238, 1963.
- [69] Immanuel Bloch, Jean Dalibard, and Wilhelm Zwerger. Many-body physics with ultracold gases. *Rev. Mod. Phys.*, 80:885, 2008.
- [70] K. Winkler, G. Thalhammer, F. Lang, R. Grimm, J. Hecker, Denschlag, A. J. Daley, A. Kantian, H. P. Büchler, and P. Zoller. Repulsively bound atom pairs in an optical lattice. *Nature*, 441:853–856, 2006.
- [71] P. W. Anderson. Absence of diffusion in certain random lattices. *Phys. Rev.*, 109:1492–1505, 1958. doi: 10.1103/PhysRev.109.1492.
- [72] B. Damski, J. Zakrzewski, L. Santos, P. Zoller, and M. Lewenstein. Atomic bose and Anderson glasses in optical lattices. *Phys. Rev. Lett.*, 91:080403, 2003. doi: 10.1103/PhysRevLett.91.080403.
- [73] Robert Roth and Keith Burnett. Phase diagram of bosonic atoms in two-color superlattices. *Phys. Rev. A*, 68:023604, 2003. doi: 10.1103/PhysRevA.68.023604.
- [74] T. Schulte, S. Drenkelforth, J. Kruse, W. Ertmer, J. Arlt, K. Sacha, J. Zakrzewski, and M. Lewenstein. Routes towards Anderson-like localization of Bose-Einstein condensates in disordered optical lattices. *Phys. Rev. Lett.*, 95:170411, 2005. doi: 10.1103/PhysRevLett.95.170411.
- [75] Nicolas Bilas and Nicolas Pavloff. Propagation of a dark soliton in a disordered Bose-Einstein condensate. *Phys. Rev. Lett.*, 95:130403, 2005. doi: 10.1103/PhysRevLett.95.130403.
- [76] Tobias Paul, Patricio Leboeuf, Nicolas Pavloff, Klaus Richter, and Peter Schlagheck. Nonlinear transport of Bose-Einstein condensates through waveguides with disorder. *Phys. Rev. A*, 72:063621, 2005. doi: 10.1103/PhysRevA.72.063621.
- [77] U. Schlöder, T. Deuschle, C. Silber, and C. Zimmermann. Autler-townes splitting in two-color photoassociation of ^6Li . *Phys. Rev. A*, 68:051403(R), 2003.

- [78] D. Jaksch, V. Venturi, J. I. Cirac, C. J. Williams, and P. Zoller. Creation of a molecular condensate by dynamically melting a Mott insulator. *Phys. Rev. Lett.*, 89:040402, 2002.
- [79] E. L. Bolda, E. Tiesinga, and P. S. Julienne. Ultracold dimer association induced by a far-off-resonance optical lattice. *Phys. Rev. A*, 71:033404, 2005.
- [80] Christiane P. Koch, Françoise Masnou-Seeuws, and Ronnie Kosloff. Creating ground state molecules with optical Feshbach resonances in tight traps. *Phys. Rev. Lett.*, 94:193001, 2005.
- [81] Tim Rom, Thorsten Best, Olaf Mandel, Artur Widera, Markus Greiner, Theodor W. Hänsch, and Immanuel Bloch. State selective production of molecules in optical lattices. *Phys. Rev. Lett.*, 93:073002, 2004.
- [82] B. Deb and L. You. Model study on the photoassociation of a pair of trapped atoms into an ultralong-range molecule. *Phys. Rev. A*, 68:033408, 2003.
- [83] D. Blume and Chris H. Greene. Fermi pseudopotential approximation: Two particles under external confinement. *Phys. Rev. A*, 65:043613, 2002.
- [84] K. Bergmann, H. Theuer, and B. W. Shore. Coherent population transfer among quantum states of atoms and molecules. *Rev. Mod. Phys.*, 70:1003, 1998.
- [85] K. Winkler, F. Lang, G. Thalhammer, v. d. Straten, R. Grimm, and J. Hecker Denschlag. Coherent optical transfer of Feshbach molecules to a lower vibrational state. *Phys. Rev. Lett.*, 98:043201, 2007.
- [86] S. Ospelkaus, A. Pe'er, K.-K. Ni, J. J. Zirbel, B. Neyenhuis, S. Kotochigova, P. S. Julienne, J. Ye, and D. S. Jin. Efficient state transfer in an ultracold dense gas of heteronuclear molecules. *Nature*, 4:622, 2008.
- [87] Johann G. Danzl, Elmar Haller, Mattias Gustavsson, Manfred J. Mark, Russell Hart, Nadia Bouloufa, Olivier Dulieu, Helmut Ritsch, and Hanns-Christoph Nägerl. Quantum gas of deeply bound ground state molecules. *Science*, 321:1062, 2008.
- [88] M. Korek, Y. A. Moghrabi, and A. R. Allouche. Theoretical calculation of the excited states of the KCs molecule including the spin-orbit interaction. *J. Chem. Phys.*, 124:094309, 2006.

- [89] Philippe Pellegrini, Marko Gacesa, and Robin Côté. Giant formation rates of ultracold molecules via Feshbach-optimized photoassociation. *Phys. Rev. Lett.*, 101:053201, 2008.
- [90] F. A. van Abeelen, D. J. Heinzen, and B. J. Verhaar. Photoassociation as a probe of Feshbach resonances in cold-atom scattering. *Phys. Rev. A*, 57:R4102, 1998.
- [91] M. Junker, D. Dries, C. Welford, J. Hitchcock, Y. P. Chen, and R. G. Hulet. Photoassociation of a Bose-Einstein condensate near a Feshbach resonance. *Phys. Rev. Lett.*, 101:060406, 2008.
- [92] John Weiner, Vanderlei S. Bagnato, Sergio Zilio, and Paul S. Julienne. Experiments and theory in cold and ultracold collisions. *Rev. Mod. Phys.*, 71:1, 1999.
- [93] R. Côté, A. Dalgarno, Y. Sun, and R. G. Hulet. Photoabsorption by ultracold atoms and the scattering length. *Phys. Rev. Lett.*, 74:3581, 1995.
- [94] Thilo Stöferle, Henning Moritz, Kenneth Günter, Michael Köhl, and Tilman Esslinger. Molecules of Fermionic atoms in an optical lattice. *Phys. Rev. Lett.*, 96:030401, 2006.
- [95] Thomas Busch, Berthold-Georg Englert, Kazimierz Rzazewski, and Martin Wilkens. Two cold atoms in a harmonic trap. *Found. of Phys.*, 28:549, 1998.
- [96] C. Ospelkaus, S. Ospelkaus, L. Humbert, P. Ernst, K. Sengstock, and K. Bongs. Ultracold heteronuclear molecules in a 3D optical lattice. *Phys. Rev. Lett.*, 97:120402, 2006.
- [97] E. L. Bolda, E. Tiesinga, and P. S. Julienne. Pseudopotential model of ultracold atomic collisions in quasi-one- and two-dimensional traps. *Phys. Rev. A*, 68:032702, 2003.
- [98] F. Deuretzbacher, K. Plassmeier, D. Pfannkuche, F. Werner, C. Ospelkaus, S. Ospelkaus, K. Sengstock, and K. Bongs. Heteronuclear molecules in an optical lattice: Theory and experiment. *Phys. Rev. A*, 77:032726, 2008.
- [99] Johan Mentink and Servaas Kokkelmans. Two interacting atoms in an optical lattice site with anharmonic terms. *Phys. Rev. A*, 79:032709, 2009.

- [100] Sergey Grishkevich and Alejandro Saenz. Influence of a tight isotropic harmonic trap on photoassociation in ultracold homonuclear alkali-metal gases. *Phys. Rev. A*, 76:022704, 2007.
- [101] S. Friebel, R. Scheunemann, J. Walz, T.W. Hänsch, and M. Weitz. Laser cooling in a CO₂-laser optical lattice. *Appl. Phys. B*, 67:699, 1998.
- [102] B. D. Esry and Chris H. Greene. Validity of the shape-independent approximation for Bose-Einstein condensates. *Phys. Rev. A*, 60:1451, 1999.
- [103] E. Tiesinga, C. J. Williams, F. H. Mies, and P. S. Julienne. Interacting atoms under strong quantum confinement. *Phys. Rev. A*, 61:063416, 2000.
- [104] Z. Idziaszek and T. Calarco. Pseudopotential method for higher partial wave scattering. *Phys. Rev. Lett.*, 96:013201, 2006.
- [105] A. J. Moerdijk and B. J. Verhaar. Laser cooling and the highest bound state of the Na diatom system. *Phys. Rev. A*, 51:R4333, 1995.
- [106] Z. Idziaszek and T. Calarco. Analytical solutions for the dynamics of two trapped interacting ultracold atoms. *Phys. Rev. A*, 74:022712, 2006.
- [107] B. H. Bransden and C. J. Joachain, editors. *Physics of atoms and molecules*. Prentice Hall, England, 2003.
- [108] P. G. Burke, C. J. Noble, and V. M. Burke. R-matrix theory of atomic, molecular and optical processes. *Adv. Atom. Mol. Opt. Phys.*, 54:237, 2007.
- [109] C. Marzok, B. Deh C. Zimmermann, Ph. W. Courteille, E. Tiemann Y. V. Vanne, and A. Saenz. Feshbach resonances in an ultracold ⁷Li and ⁸⁷Rb mixture. *Phys. Rev. A*, 79:012717, 2009.
- [110] Z. Li, S. Singh, T. V. Tscherbul, and K. W. Madison. Feshbach resonances in ultracold ⁸⁵Rb-⁸⁷Rb and ⁶Li-⁸⁷Rb mixtures. *Phys. Rev. A*, 78:022710, 2008.
- [111] M.-L. Almazor, O. Dulieu, M. Elbs, E. Tiemann, and F. Masnou-Seeuws. How to get access to long range states of highly excited molecules. *Eur. Phys. J. D*, 5:237, 1999.

- [112] M.-L. Almazor, O. Dulieu, F. Masnou-Seeuws, R. Beuc, and G. Pichler. Formation of ultracold molecules via photoassociation with blue detuned laser light. *Eur. Phys. J. D*, 15:355, 2001.
- [113] M. Kemmann, I. Mistrik, S. Nussmann, H. Helm, C. J. Williams, and P. S. Julienne. Near-threshold photoassociation of $^{87}\text{Rb}_2$. *Phys. Rev. A*, 69:022715, 2004.
- [114] F. D. Colavecchia, J. P. Burke, W. J. Stevens, M. R. Salazar, G. A. Parker, and R. T. Pack. The potential energy surface for spin-aligned $\text{Li}_3(1^4\text{A}')$ and the potential energy curve for spin-aligned $\text{Li}_2(a^3\Sigma_u^+)$. *J. Chem. Phys.*, 118:5484, 2003.
- [115] C. Linton, T.L. Murphy, F. Martin, R. Bacis, and J. Verges. Fourier transform spectroscopy of the $1^3\Sigma_g^+ - a^3\Sigma_u^+$ transition of the $^6\text{Li}_2$ molecule. *J. Chem. Phys.*, 91:6036, 1989.
- [116] I. Schmidt-Mink, W. Müller, and W. Meyer. Ground- and excited-state properties of Li_2 and Li_2^+ from ab initio calculations with effective core polarization potentials. *Chem. Phys.*, 92:263, 1985.
- [117] M. Marinescu and A. Dalgarno. Dispersion forces and long-range electronic transition dipole moments of alkali-metal dimer excited states. *Phys. Rev. A*, 52:311, 1995.
- [118] Yulian V. Vanne and Alejandro Saenz. Numerical treatment of diatomic two-electron molecules using a B-spline based CI method. *J. Phys. B: At. Mol. Phys.*, 37:4101, 2004.
- [119] S. Magnier, M. Aubert-Frécon, J. Hanssen, and C. Le Sech. Two-electron wavefunctions for the ground state of alkali negative ions. *J. Phys. B: At. Mol. Phys.*, 32:5639, 1999.
- [120] I. Dumitriu, Y.V. Vanne, M. Awasthi, and A. Saenz. Photoionization of the alkali dimer cations Li_2^+ , Na_2^+ , and LiNa^+ . *J. Phys. B: At. Mol. Phys.*, 40:1821–1832, 2007.
- [121] Lyn B. Ratcliff, James L. Fish, and Daniel D. Konowalow. Electronic transition dipole moment functions for transitions among the twenty-six lowest-lying states of Li_2 . *J. Mol. Spec.*, 122:293, 1987.
- [122] Janusz Pipin and David M. Bishop. Accurate variational calculations of energies of the 2^2S , 2^2P , and 3^2D states and the dipole, quadrupole, and dipole-quadrupole polarizabilities and hyperpolarizability of the lithium atom. *Phys. Rev. A*, 45:2736, 1991.

- [123] Paul S. Julienne. Cold binary atomic collisions in a light field. *J. Res. Natl. Inst. Stand. Technol.*, 101:487, 1996.
- [124] E. R. I. Abraham, W. I. McAlexander, J. M. Gerton, R. G. Hulet, R. Côté, and A. Dalgarno. Triplet s-wave resonance in ${}^6\text{Li}$ collisions and scattering lengths of ${}^6\text{Li}$ and ${}^7\text{Li}$. *Phys. Rev. A*, 55:R3299, 1997.
- [125] A. N. Nikolov, E. E. Eyler, X. T. Wang, J. Li, H. Wang, W. C. Stwalley, and P. L. Gould. Observation of ultracold ground-state potassium molecules. *Phys. Rev. Lett.*, 82:703, 1999.
- [126] C. Amiot, J. Vergés, and C. E. Fellows. The long-range potential of the $\text{K}_2 X^1\Sigma_g^+$ ground electronic state up to 15 \AA . *J. Chem. Phys.*, 103:3350, 1995.
- [127] H. Wang, P. L. Gould, and W. C. Stwalley. Long-range interaction of the ${}^{39}\text{K}(4s)+{}^{39}\text{K}(4p)$ asymptote by photoassociative spectroscopy. i. the 0_g^- pure long-range state and the long-range potential constants. *J. Chem. Phys.*, 106:7899, 1997.
- [128] C. J. Williams, E. Tiesinga, P. S. Julienne, H. Wang, W. C. Stwalley, and P. L. Gould. Determination of the scattering lengths of ${}^{39}\text{K}$ from 1_u photoassociation line shapes. *Phys. Rev. A*, 60:4427, 2000.
- [129] R. Côté and A. Dalgarno. Photoassociation intensities and radiative trap loss in lithium. *Phys. Rev. A*, 58:498, 1998.
- [130] E. R. I. Abraham, W. I. McAlexander, J. M. Gerton, R. G. Hulet, R. Côté, and A. Dalgarno. Singlet s-wave scattering lengths of ${}^6\text{Li}$ and ${}^7\text{Li}$. *Phys. Rev. A*, 53:R3713, 1996.
- [131] E. L. Bolda, E. Tiesinga, and P. S. Julienne. Effective-scattering-length model of ultracold atomic collisions and Feshbach resonances in tight harmonic traps. *Phys. Rev. A*, 66:013403, 2002.
- [132] Wenzel Salzmann, Ulrich Poschinger, Roland Wester, Matthias Weidemüller, Andrea Merli, Stefan M. Weber, Franziska Sauer, Mateusz Plewicki, Fabian Weise, Aldo Mirabal Esparza, Ludger Wöste, and Albrecht Lindinger. Coherent control with shaped femtosecond laser pulses applied to ultracold molecules. *Phys. Rev. A*, 73:023414, 2006.
- [133] Benjamin L. Brown, Alexander J. Dicks, and Ian A. Walmsley. Coherent control of ultracold molecule dynamics in a magneto-optical trap

- by use of chirped femtosecond laser pulses. *Phys. Rev. Lett.*, 96:173002, 2006.
- [134] Christiane P. Koch, Ronnie Kosloff, and Françoise Masnou-Seeuws. Short-pulse photoassociation in rubidium below the D_1 line. *Phys. Rev. A*, 73:043409, 2006.
- [135] Olivier Dulieu, Ronnie Kosloff, Françoise Masnou-Seeuws, and Goran Pichler. Quasibound states in long-range alkali dimers: Grid method calculations. *J. Chem. Phys.*, 107:10633, 1997.
- [136] Eite Tiesinga, Kevin M. Jones, Paul D. Lett, Udo Volz, Carl J. Williams, and Paul S. Julienne. Measurement and modeling of hyperfine- and rotation-induced state mixing in large weakly bound sodium dimers. *Phys. Rev. A*, 71:052703, 2005.
- [137] Carl J. Williams, Eite Tiesing, and Paul S. Julienne. Hyperfine structure of the $\text{Na}_2 O_g^-$ long-range molecular state. *Phys. Rev. A*, 53:R1939, 1996.
- [138] Pascal Naidon and Paul S. Julienne. Optical Feshbach resonances of alkaline-earth-metal atoms in a one- or two-dimensional optical lattice. *Phys. Rev. A*, 74:062713, 2006.
- [139] Z. Idziaszek and T. Calarco. Two atoms in an anisotropic harmonic trap. *Phys. Rev. A*, 71:050701(R), 2005.
- [140] T. Takekoshi, J. R. Yeh, and R. J. Knize. Quasi-electrostatic trap for neutral atoms. *Opt. Commun.*, 114:421, 1995.
- [141] M. Mérawa and M. Rérat. Ab initio calculation of excited state dipole polarizability – application to the first $^{1,3}\Sigma_{g,u}^+$ states of Li_2 . *Eur. Phys. J. D*, 17:329, 2001.
- [142] S. Magnier and M. Aubert-Frécon. Static dipolar polarizabilities for various electronic states of alkali atoms. *J. Quant. Spec. Rad. Trans.*, 75:121, 2002.
- [143] Ph. Courteille, R. S. Freeland, D. J. Heinzen, F. A. van Abeelen, and B. J. Verhaar. Observation of a Feshbach resonance in cold atom scattering. *Phys. Rev. Lett.*, 81:69, 1998.
- [144] M. Aymar and O. Dulieu. Calculation of accurate permanent dipole moments of the lowest $^{1,3}\Sigma^+$ states of heteronuclear alkali dimers using extended basis sets. *J. Chem. Phys.*, 122:204302, 2005.

- [145] Philipp-Immanuel Schneider, Sergey Grishkevich, and Alejandro Saenz. Ab initio determination of Bose-Hubbard parameters for two ultracold atoms in an optical lattice using a three-well potential. *Phys. Rev. A*, 80:013404, 2009.
- [146] Sascha Zöllner, Hans-Dieter Meyer, and Peter Schmelcher. Few-boson dynamics in double wells: From single-atom to correlated pair tunneling. *Phys. Rev. Lett.*, 100:040401, 2008.
- [147] J. Rasch and A. C. H. Yu. Efficient storage scheme for precalculated Wigner $3j$, $6j$ and Gaunt coefficients. *SIAM J. Sci. Comput.*, 25:1416, 2003.
- [148] Didier Pinchon and Philip E. Hoggan. New index functions for storing Gaunt coefficients. *Int. J. Quant. Chem.*, 107:2186, 2007.
- [149] P. Jasik and J. E. Sienkiewicz. Calculation of adiabatic potentials of Li_2 . *Chem. Phys.*, 323:563, 2005.
- [150] Z. Idziaszek, T. Calarco, and P. Zoller. Controlled collisions of a single atom and an ion guided by movable trapping potentials. *Phys. Rev. A*, 76:033409, 2007.
- [151] Z. Idziaszek, T. Calarco, P. S. Julienne, and A. Simoni. Quantum theory of ultracold atom-ion collisions. *Phys. Rev. A*, 79:010702, 2009.
- [152] Ivan S. Lim, Markus Pernpointner, Michael Seth, Jon K. Laerdahl, Peter Schwerdtfeger, Pavel Neogrody, and Miroslav Urban. Relativistic coupled-cluster static dipole polarizabilities of the alkali metals from Li to element 119. *Phys. Rev. A*, 60:2822, 1999.
- [153] S. Rousseau, A. R. Allouche, and M. Aubert-Frécon. Theoretical study of the electronic structure of the KRb molecule. *J. Mol. Spec.*, 203:235, 2000.
- [154] Warren T. Zemke, Robin Côté, and William C. Stwalley. Analysis of the $a^3\Sigma^+$ state of KRb. *Phys. Rev. A*, 71:062706, 2005.
- [155] A. Derevianko, J. F. Babb, and A. Dalgarno. High-precision calculations of van der Waals coefficients for heteronuclear alkali-metal dimers. *Phys. Rev. A*, 63:052704, 2001.
- [156] Sergey G. Porsev and Andrei Derevianko. Accurate relativistic many-body calculations of van der Waals coefficients C_8 and C_{10} for alkali-metal dimers. *J. Chem. Phys.*, 119:844, 2003.

- [157] Francesca Ferlaino, Chiara D'Errico, Giacomo Roati, Matteo Zaccanti, Massimo Inguscio, Giovanni Modugno, and Andrea Simoni. Feshbach spectroscopy of a K-Rb atomic mixture. *Phys. Rev. A*, 73:040702(R), 2006.
- [158] Peter Sta anum, Asen Pashov, Horst Knöckel, and Eberhard Tiemann. $X\ ^1\Sigma^+$ and $a\ ^3\Sigma^+$ states of LiCs studied by fourier-transform spectroscopy. *Phys. Rev. A*, 75:042513, 2007.
- [159] J. Goldwin, S. Inouye, M. L. Olsen, B. Newman, B. D. DePaola, and D. S. Jin. Measurement of the interaction strength in a Bose-Fermi mixture with ^{87}Rb and ^{40}K . *Phys. Rev. A*, 70:021601(R), 2004.
- [160] S. Inouye, J. Goldwin, M. L. Olsen, C. Ticknor, J. L. Bohn, and D. S. Jin. Observation of heteronuclear Feshbach resonances in a mixture of Bosons and Fermions. *Phys. Rev. Lett.*, 93:183201, 2004.
- [161] M. Zaccanti, C. D'Errico, F. Ferlaino, G. Roati, M. Inguscio, and G. Modugno. Control of the interaction in a Fermi-Bose mixture. *Phys. Rev. A*, 74:041605(R), 2006.
- [162] T. Loftus, C. A. Regal, C. Ticknor, J. L. Bohn, and D. S. Jin. Resonant control of elastic collisions in an optically trapped fermi gas of atoms. *Phys. Rev. Lett.*, 88:173201, 2002.
- [163] C. A. Regal and D. S. Jin. Measurement of positive and negative scattering lengths in a Fermi gas of atoms. *Phys. Rev. Lett.*, 90:230404, 2003.
- [164] Charlotte Froese Fischer and M. Idrees. Spline methods for resonances in photoionisation cross sections. *J. Phys. B: At. Mol. Phys.*, 23:679, 1990.
- [165] A. S. Dawydow. *Quantenmechanik*. VEB Deutscher Verlag der Wissenschaften, Berlin, 1967.
- [166] Krzysztof Góral, Thorsten Köhler, Simon A. Gardiner, Eite Tiesinga, and Paul S. Julienne. Adiabatic association of ultracold molecules via magnetic-field tunable interactions. *J. Phys. B: At. Mol. Phys.*, 37:3457, 2004.
- [167] S. Fölling, S. Trotzky, P. Cheinet, M. Feld, R. Saers, A. Widera, T. Müller, and I. Bloch. Direct observation of second-order atom tunnelling. *Nature*, 448:1029, 2007.

BIBLIOGRAPHY

- [168] S. Trotzky, P. Cheinet, S. Fölling, M. Feld, U. Schnorrberger, A. M. Rey, A. Polkovnikov, E. A. Demler, M.D. Lukin, and I. Bloch. Time-resolved observation and control of superexchange interactions with ultracold atoms in optical lattices. *Science*, 319:295, 2008.
- [169] Torben Müller, Simon Fölling, Artur Widera, and Immanuel Bloch. State preparation and dynamics of ultracold atoms in higher lattice orbitals. *Phys. Rev. Lett.*, 99:200405, 2007.
- [170] B. W. Shore. Use of the Rayleigh-Ritz-Galerkin method with cubic splines for constructing single-particle bound-state radial wavefunctions: The hydrogen atom and its spectrum. *J. Phys. B: At. Mol. Phys.*, 6:1923, 1973.

List of Figures

1.1	Three-dimensional rendition of the Bose-Einstein condensate	2
1.2	Emergence of molecules in a mixture of cold gas atoms	4
1.3	Sketch of the photoassociation process	5
1.4	Optical lattice potentials	6
2.1	Numerical solution of the GGPE	17
2.2	The ground state wave functions... $\omega_\rho = 2\pi \times 100\text{Hz}$	18
2.3	The chemical potential μ ... of Figure 2.2	19
2.4	The ground state wave functions... $\omega_\rho = 2\pi \times 10\text{Hz}$	19
2.5	The chemical potential μ ... of Figure 2.4	20
2.6	Convergence of the CI expansion	21
2.7	Esry and Green's convergence check	22
3.1	An energy level diagram	28
3.2	Ground-state energies of the hyperfine states for ${}^6\text{Li}$	30
3.3	The electrostatic interaction potential	31
3.4	The dependence of E_χ on magnetic field	33
3.5	Broad and narrow resonances for the collision of the ${}^6\text{Li}$ - ${}^{87}\text{Rb}$	38
3.6	The $\psi_\chi(R)$ functions	39
3.7	The ϕ_ξ functions	40
4.1	The tuning functions f_d and f_u	46
4.2	The potentials of ${}^6\text{Li}$ - ${}^{87}\text{Rb}$ for the single-channel approach	47
4.3	Potential resonances and the single-channel functions φ^s	48
4.4	Comparison of two multi-channel singlet states at resonance	48
4.5	Comparison of $\tilde{\varphi}^J$, $\tilde{\varphi}^s$ and $\tilde{\varphi}^\mu$ with the closed channel ϕ_{S_1}	49
4.6	Comparison of the different $\tilde{\varphi}^w$ functions	51
4.7	Comparison of $\tilde{\varphi}^w$ with incoming channel ψ_{open}	52
4.8	Comparison of $\tilde{\varphi}^J$, φ^s and φ^m with incoming channel ψ_{open}	52
5.1	Sketch of the photoassociation process for ${}^6\text{Li}_2$	57
5.2	The classical outer turning points for $1^3\Sigma_g^+$ state of ${}^6\text{Li}_2$	61

LIST OF FIGURES

5.3	Wave functions of the initial $a^3\Sigma_u^+$ state of ${}^6\text{Li}_2$ for different ω	62
5.4	The $I^v(\omega)$ moments and the $f^v(\omega)$ ratio for $a_{\text{sc}} < 0$	63
5.5	Illustration of the constant photoassociation regime	67
5.6	Illustration of the cut-off photoassociation regime	70
5.7	The $I^v(\omega)$ moments and the $f^v(\omega)$ ratio for $a_{\text{sc}} > 0$	72
5.8	Explanation of the photoassociation window	73
5.9	The $I^v(\omega)$ moments for different $a_{\text{sc}} > 0$ (N^v is variable)	75
5.10	The $I^v(\omega)$ moments for different $a_{\text{sc}} > 0$ (N^v is constant)	76
5.11	Wave functions of the initial $a^3\Sigma_u^+$ state of ${}^6\text{Li}_2$ for different a_{sc}	78
5.12	Enhancement factor g_c	79
5.13	Real wave function vs pseudopotential wave function	81
5.14	The $I^v(\omega)$ moments in the pseudopotential approximation	83
5.15	Squared FC factors	85
5.16	Simple estimate for the f_c factor	87
6.1	Schematic representation of the DPA process	99
6.2	I^0 and g^0 for the multi- and single-channel solutions	101
7.1	The ABS, COM-REL and spherical coordinates	110
7.2	Double-well and triple-well traps	120
7.3	The symmetry elements of the two particles in a \sin^2 trap	128
8.1	Sketch of a cut through the potential surfaces	136
8.2	Energies of the 1st trap-induced and lb states of ${}^{87}\text{Rb}-{}^{40}\text{K}$	141
8.3	The energy differences for different alkali metal dimers	144
8.4	Radial pair densities for ${}^{87}\text{Rb}-{}^{40}\text{K}$	146
8.5	Cuts of ΔF for almost non-interacting ${}^{87}\text{Rb}-{}^{40}\text{K}$	149
8.6	Cuts of ΔF for strongly interacting ${}^{87}\text{Rb}-{}^{40}\text{K}$	153
9.1	Theory vs experiment	158
9.2	Sketch of the procedure for obtaining binding energies	159
9.3	Evidence of the measured anharmonicity and coupling effects	162
9.4	The relative error for the alternative Feshbach parameters	164
B.1	Approximation of the wave function with B splines	178
B.2	S -matrix	179
C.1	Analytical vs numerical pseudopotential wave functions	184

List of Tables

3.1	Atomic and molecular basis states of the ${}^6\text{Li}$ - ${}^{87}\text{Rb}$	36
7.1	Character table of the D_{2h} point group	127
7.2	Results of the D_{2h} group operations	127
7.3	Product table of the D_{2h} point group	131
8.1	The effect of the trapping potential on the energy spectrum	143
9.1	Approximate solutions for ${}^{87}\text{Rb}$ - ${}^{40}\text{K}$, ${}^6\text{Li}$ - ${}^{133}\text{Cs}$ and ${}^6\text{Li}$ - ${}^7\text{Li}$	164

Selbständigkeitserklärung

Hiermit erkläre ich, die vorliegende Arbeit selbständig ohne fremde Hilfe verfasst zu haben und nur die angegebene Literatur und Hilfsmittel verwendet zu haben.

Berlin, den 17.08.2009

Sergey Grishkevich